CRANFIELD UNIVERSITY

ROBERT CHRISTIE

PROPULSION SYSTEM INTEGRATION AND MODELLING SYNTHESIS

SCHOOL OF AEROSPACE, TRANSPORT AND MANUFACTURING

PhD
Academic Year: 2015–2016

Supervisor: Dr. D. G. MacManus
July 2016

CRANFIELD UNIVERSITY

SCHOOL OF AEROSPACE, TRANSPORT AND MANUFACTURING

PhD

Academic Year: 2015–2016

ROBERT CHRISTIE

Propulsion System Integration and Modelling Synthesis

Supervisor: Dr. D. G. MacManus
July 2016

Abstract

Concerns over fuel costs, along with the ever increasing requirement to reduce the impact of emissions, means that the world's airlines continue to introduce low-noise and more fuel-efficient aircraft into their fleet. Increasing the engine bypass ratio is one way to improve propulsive efficiency. However, historically an increase in the bypass ratio (BPR) has usually been associated with an increase in the fan diameter. Consequently, there can be a notable increase in the impact of the engine installation on the overall aircraft performance. For example, although the typical increase in fan diameter is generally beneficial to the uninstalled engine specific fuel consumption, the increase in the nacelle drag and weight are detrimental to the aircraft performance. There is also likely to be a stronger aerodynamic coupling between the engine and the airframe. Overall there is a risk that the gains in uninstalled engine performance are wholly or partly lost due to adverse engine-airframe installation and interference effects as well as additional nacelle weight. It is clear that the quantification of the elements of installation drag is a key aspect in the assessment of the likely developments in engine design as well as on the installation requirements for future airframe architectures.

The overall aim of this research is to determine the effect of nacelle size, weight, geometry and installation on flight efficiency. This aim has been addressed through the development of a framework which combines the engine thermodynamic model, aircraft performance, engine installation aspects and a flight trajectory approach. This framework has been

developed to assess the relative importance of various engine installation aspects on the overall flight fuel burn for a range of short-haul and long-haul configurations.

A framework (PSIMOD) to assess propulsion system integration has been developed based on an aircraft performance tool, Hermes and an engine performance model, Turbomatch. These are FORTRAN-based software which have been validated and used at Cranfield University over many years. The initial focus of this work is on the integration of these main modules to enable the overall flight characteristics and mission fuel burn to be evaluated. The system determines the engine requirements and the main aircraft characteristics at each point in a trajectory for a given mission in terms of range, cruise altitudes, payload and engine limitations. At each point in the flight the engine operating point is adjusted to ensure that the thrust requirements are met and the fuel burn is then integrated over the mission. This analysis includes airframe aerodynamics, nacelle drag, installation quality and engine performance at each point in the mission. Calculated nacelle drag is a function of engine massflow capture ratio, Mach number, Reynolds number, nacelle geometry and aircraft and engine angles of attack.

It is important to accurately model nacelle and engine weight in preliminary design as its effects on mission fuel burn are of the same order of magnitude as nacelle drag. For the short haul mission when weight increases were not modelled some engines showed an uninstalled specific fuel consumption (SFC) improvement over the baseline engine. When the additional weight of these larger engines was included in the modelling these uninstalled SFC improvements were completely negated. For the long haul mission when engine and nacelle weight increases were not modelled all engines showed an improvement in mission fuel burn over the baseline engine. However when the weight increases were modelled only the engines with a BPR=8.3 maintained a mission fuel burn improvement. This showed that for the engine design approach adopted in this paper there is an optimum increase in BPR after which further increases increase mission fuel burn.

Nacelle total local upflow angle can have a significant effect on mission fuel burn with increases in mission fuel burn of up to 2.2% seen for non-optimum nacelle offset angle. Similarly engine installation quality can have a significant effect on mission fuel burn. For a poor propulsion system integration which may have an installation drag penalty of 50% of the isolated nacelle drag mission fuel burn can increase by up to 6%. The rate of change of mission fuel burn with installation quality is a function of nacelle size.

Acknowledgements

This thesis would not exist without the help and support of many people.

My deepest thanks goes to Dr. D. MacManus for his support and guidance.

I would also like to thank the many lifelong friends I have made since coming to Cranfield.

Finally I want to thank my family for all their love and support.

Contents

List of Figures

List of Tables

Nomenclature

Roman Symbols

A	Total upflow angle
A_i	Highlight area
A_{nac}	Nacelle axial force
A_{stream}	Stream force components of the axial force
A_{surf}	Surface force components of the axial force
A_{th}	Throat area
A_x	Projected area in the x-direction
A_z	Projected area in the z-direction
An	Coefficient in the NACA-1 series profile definition
b_{naca}	Coefficient in the NACA-1 series profile definition
BP	Bernstein Polynomial
bp	Bernstein polynomial weighting coefficient
$BPR_{des,opt}$	Optimal design point BPR
c	Wing chord

$C(\psi)$	Class function
C_A	Coefficient of axial force
$C_{D,INST}$	Installation drag coefficient
$C_{D,J}$	Jet interference drag coefficient
$C_{D,nac,max}$	Nacelle drag coefficient referred to the nacelle maximum cross-sectional area
$C_{D,WBPN(powered)}$	Drag coefficient for wing, body, pylon, powered nacelle configuration
$C_{D,WBPN(TFN)}$	Drag coefficient for wing, body, pylon, through flow nacelle configuration
$C_{D,WB}$	Drag coefficient for wing, body configuration
C_{D0eng}	Coefficient of engine drag at zero incidence
C_{Deng}	Coefficient of engine drag
C_{Dieng}	Coefficient of lift independent engine drag
C_{di}	Coefficient of lift independent drag
C_D	Drag coefficient
C_{fn}	Flat plate skin friction coefficient
C_{Leng}	Coefficient of engine lift
C_L	Lift coefficient
C_M	Moment coefficient
c_{naca}	Coefficient in the NACA-1 series profile definition
C_N	Coefficient of normal force

C_P	Pressure coefficient
C_V	Velocity coefficient
C_X	Coefficient of force in the x-direction
C_Z	Coefficient of force in the z-direction
$d\phi$	Elemental force
D	Drag
$d\phi_G$	Elemental gauge force
$D_{a,datum}$	Afterbody drag at datum flow condition
$D_{a/c}$	Aircraft drag
$D_{a/f,iso}$	Isolated airframe drag
$D_{a/f}$	Airframe drag
D_a	Afterbody drag
$D_{c,datum}$	Cowl forebody drag at datum flow condition (usually MFCR=1)
D_c	Cowl forebody drag
$D_{eng,iso}$	Isolated engine drag
D_{eng}	Engine drag
D_e	Nozzle exit diameter
D_{fan}	Fan diameter
D_{Global}	Global power plant installation drag
D_{INST}	Installation drag

D_i	Highlight diameter
D_J	Jet interference drag
D_{max}	Maximum diameter
$D_{nacelle,datum}$	Nacelle drag at datum flow condition
D_{nac}	Nacelle drag
D_{spill}	Intake spillage drag
dA	Elemental area
F	Absolute stream force
f_a	Afterbody friction drag
F_G	Absolute gauge stream force
F_n	Form factor
F_s	Factor of safety
ff	Fan face
F_N	Standard net thrust
F'_N	Overall net thrust
$F'_{N,INT}$	Intrinsic net thrust
FPR	Fan Pressure Ratio
g	Acceleration due to gravity
H	Altitude
h	Horizontal offset

h_i	Horizontal offset at the beginning of a curve
h_o	Horizontal offset at the end of a curve
i	Index of summation
K	Binomial coefficient
k	Turbulent kinetic energy
k_{inst}	Installation drag factor
K_s	Spillage drag factor
L/D_{MAX}	Maximum lift to drag ratio
$L_{a/c}$	Aircraft lift
$L_{a/f,iso}$	Isolated airframe lift
$L_{a/f}$	Airframe lift
L_{axial}	Length in the axial direction
L_a	Afterbody length
$L_{eng,iso}$	Isolated engine lift
L_{eng}	Engine lift
$L_{f,max}$	Vertical offset between the start and endpoint of the forebody
L_f	Forebody length
L_{inst}	Installation lift
L_{nac}	Nacelle length
L_{nac}	Nacelle lift

L_{radial}	Length in the radial direction
L_{tot}	Total length
le	Leading edge
M	Mach number
$\dot{m}$	Mass flow rate
M_∞	Freestream Mach number
M_{DR}	Drag Rise Mach number
N	Upper bound on summation
N_1	First exponent in the class function
N_2	Second exponent in the class function
N_{eng}	Number of engines
N_g	Number of cells at mesh refinement level g
N_{nac}	Nacelle normal force
N_{stream}	Stream force components of the normal force
N_{surf}	Surface force components of the normal force
P	Static pressure
P_0	Total Pressure
P_∞	Freestream static pressure
p_{con}	Observed level of convergence
P_{pot}	Static pressure in potential flow

R	Resultant force
r	Grid refinement ratio
R_{BL}	Baseline range
Re	Reynolds number
$Re_{D_{max}/L_{nac}}$	Unit Reynolds number based on the ratio of nacelle maximum diameter to length ratio
Re_{Lnac}	Reynolds number based on nacelle length
S	Surface area
$S(\psi)$	Shape function
S_{wet}	Wetted area
sp	Stagnation point
T	Static temperature
T_0	Total temperature
T_∞	Freestream static temperature
te	Trailing edge
U	Velocity
V	Velocity
V_∞	Freestream Velocity
V_x	Velocity in the x-direction
V_z	Velocity in the z-direction
W	Massflow

$W_{F,block,des}$	Design point block fuel burn
x	Horizontal ordinate
$Y+$	Non-dimensional first cell height

Abbreviations

$ACARE$	Advisory Council for Aeronautical Research in Europe
$AIAA$	American Institute of Aeronautics and Astronautics
AR	Asymptotic Range
ARA	Aircraft Research Association
$BADA$	Base of Aircraft Data
BPD	Bypass Duct
BPR	By-Pass Ratio
BWB	Blended Wing Body
CFD	Computational fluid dynamics
CRM	Common Research Model
CST	Class Shape Transformation
dc	Drag counts
DLR	Deutsches Zentrum für Luft und Raumfahrt (German Aerospace Center)
DPW	Drag Prediction Workshop
$ENIFAIR$	Engine Integration on Future Transport Aircraft
ER	Extended Range

ESDU	Engineering Design Software and Methods Tools, formerly Engineering Sciences Data Unit
FPR	Fan Pressure Ratio
GCI	Grid Convergence Index
GE	General Electric
GEM	Geometric Engine Modeller
HBPR	High Bypass Ratio
MFCR	Mass flow capture ratio
MTOW	Maximum Take-Off Weight
NACA	National Advisory Committee for Aeronautics
NASA	National Aeronautics and Space Administration
NND	No Nacelle drag modelled
NPF	Net propulsive force
ONERA	Office National d'Etudes et de Recherches Aérospatiales (French national aerospace research centre)
PR	Pressure Ratio
PROOSIS	Propulsion Object-Oriented Simulation Software
PSI	Propulsion System Integration
PSIMOD	Propulsion System Integration Model
PW	Pratt and Whitney
RANS	Reynolds-averaged NavierStokes

$RASER$	Revolutionary Aero Space Engine Research
$S2MA$	ONERA Modane Windtunnel
SFC	Specific Fuel Consumption
SFE	Skin Friction Estimate
SRA	Strategic Research Agenda
SST	Shear Stress Transport
$T-O$	Take-Off
TET	Turbine Entry Temperature
$TETM$	Turbine Entry Temperature Matched
TFN	Through Flow Nacelle
THM	Thrust Matched
TPS	Turbine Powered Simulator
$UEET$	Ultra-Efficient Engine Technology
$VHBR$	Very High Bypass Ratio
$WATE$	Weight Analysis of Turbine Engines
WB	Wing-Body
$WBPN$	Wing-Body-Pylon-Nacelle
WBT	Wing-Body-T
$WEICO$	Weight, Dimensions and Cost
$WINM$	Weight Increase Not Modelled

WP	Work Package

Greek Symbols

α	Angle of attack
$\alpha_{air,ang}$	Aircraft angle of attack
α_{eng}	Engine incidence angle
α_w	Wing angle of attack
$\chi_{air,ang}$	Aircraft heading angle
ϵ	Angle between local relative velocity and freestream velocity vectors
η	Non-dimensional wing span
$\gamma_{air,ang}$	Aircraft flightpath angle
γ_n	Nacelle inclination angle
ν	Viscosity
ω	Specific dissipation
$\phi_{a,pot}$	Afterbody force in potential flow
$\phi_{air,ang}$	Aircraft bank angle
ϕ_a	Afterbody force
$\phi_{c,pot}$	Cowl forebody force in potential flow
ϕ_c	Cowl forebody force
ϕ_G	Gauge force
ϕ_J	Jet interference force

$\phi_{nac,pot}$	Nacelle force in potential flow
ϕ_{nac}	Nacelle force
ϕ_{post}	Post-exit force
ϕ_{pot}	Force in potential flow
ϕ_{pre}	Pre-entry force
ϕ_{spill}	Cowl suction force
ψ	Non-dimensional horizontal ordinate
ρ	Density
τ_w	Wall shear force
τ_w	Wall skin friction
Θ	Angle
$\theta_{air,ang}$	Aircraft pitch angle
θ_{nac}	Force on the nacelle imparted by internal flow
θ_{pre}	Force on the pre-entry streamtube imparted by internal flow
θ_{surf}	Local surface angle
ξ	Non-dimensional vertical ordinate

Chapter 1

Introduction

1.1 Need for accurate propulsion system drag prediction

Reducing aviation's environmental impact is one of the most important challenges facing the aerospace industry. This impact includes noise pollution, local air quality and climate change.[1] In 2001, the Advisory Council for Aeronautical Research in Europe (ACARE)[2] was founded by government and industry with the aim of making Europe's commercial aviation more affordable, cleaner, safer and quieter. ACARE's Strategic Research Agenda (SRA) identified five major challenges.[2] With respect to the environment the challenge was to meet an ever increasing demand while at the same time lessening the impact of the aviation industry on the environment at all levels.[2] One of the key findings of the SRA was that the objectives are not achievable without important breakthroughs, both in technology and in concepts of operation.[2] In 2010 ACARE developed a new vision for European aviation, looking towards 2050.[3] By 2050, taken relative to 2000, advances in aviation technology and procedures should allow a 75% reduction in CO_2 emissions and a 90% reduction in NOx emissions per passenger km as well as a 65% reduction in perceived noise.[3] Low-noise requirements imposed by regulators, mean that engine manufacturers must improve the propulsive efficiency and reduce the noise level of their

engines.[4] These environmental challenges need to be overcome by the development of new aircraft configurations or by improvements to existing ones. An accurate understanding of drag and its components its necessary for both approaches.[5]

Key aircraft design drivers include the need to reduce operating costs and the need to meet industry regulations.[5] A significant portion of an airlines direct operating costs consists of fuel expenses[6,7] (Figure 1.1(a)). In recent years there have been large fluctuations in the price of aviation fuel (Figure 1.1(b)). In the short term kerosene will remain the primary fuel for passenger aircraft. Over the next 20 years it is probable kerosene will be derived from a range of sources including crude oil, biomass and waste products. However, in all cases its is predicted that the cost of kerosene will substantially increase.[7] Reducing this cost has been a core focus of aviation technology development.[6] One key approach to improvements in fuel efficiency is to increase engine bypass ratio (BPR).[8] Increases in BPR can be achieved by decreases in core or increases in by-pass massflow. However generally fan diameter has increased. Increasing the bypass ratio can lead to increased drag from larger nacelle wetted and frontal areas as well as increased pre-entry streamtube drag. As well as increased drag it can be expected that larger engine diameters will have stronger effects on engine-airframe integration. There is then the risk that gains in fuel reduction are partly lost due to these negative effects.[9] It is clear then that the quantification of both engine installation drag and the identification of its sources is crucial at the preliminary design stage.

1.2 Novel aspects

1.2.1 Full mission analysis

Normally engine nacelles are designed at a single design point. This is usually at the end of cruise condition where spillage drag is at its greatest. This design point is selected based on experience with current nacelle designs. Some checks are then carried out to ensure

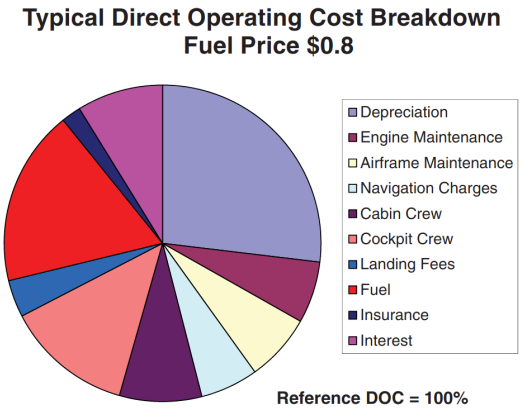

(a) Typical traditional buildup of contributions to direct operating cost of an aircraft. case for the mission of a medium-range, 150-seat aircraft [7].

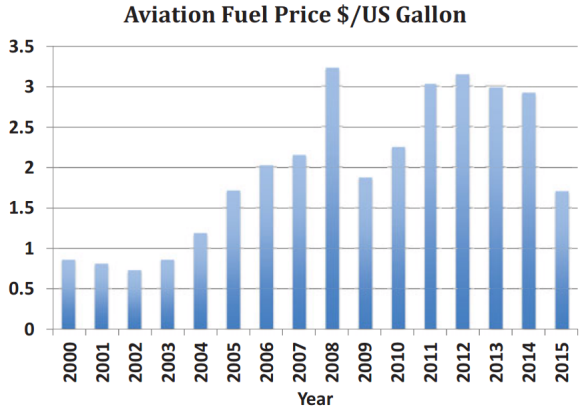

(b) Cost of aviation fuel since the year 2000 [7].

FIGURE 1.1: Aircraft operating costs

that nacelle performance is adequate in other flight stages. As engines become larger this approach may not be sufficient. It may be possible to improve propulsion system performance by taking into account nacelle performance throughout the full flight profile in the preliminary design stage. This has been achieved by the creation of a novel Propulsion System Integration Modelling (PSIMOD) framework. PSIMOD couples Cranfield University's in house engine (Turbomatch [10]) and aircraft (Hermes [11,12]) performance codes with a nacelle drag prediction model based on ESDU 81024 [13]. The ESDU drag prediction method is used to predict nacelle drag as a function of flight Reynolds number, Mach

number, nacelle shape and intake MFCR. Corrections are then applied to this drag prediction to take into account nacelle local upflow effects and nacelle and propulsion system integration effects based on CFD simulations. Nacelle drag is integrated within PSIMOD in a drag build up method at each point in the flight to allow overall mission performance to be calculated.

1.2.2 CFD compatible thrust and drag book keeping approach

The most commonly adopted thrust and drag book keeping systems in the literature rely the calculation of the force acting upon the engine pre-entry streamtube and the force exerted on the nacelle by external flow. To do this the pre-entry streamtube stagnation line on the nacelle must be extracted. This approach is not suited to automated Computational Fluid Dynamics (CFD) post-processing as this is often non-trivial. To address this issue a thrust and drag accounting methodology compatible with CFD methods has been developed known as the "modified nearfield method". Thrust and drag book keeping in the literature is normally only established for zero degrees engine incidence cases.[14] The modified nearfield method has been further developed to enable the extraction from CFD of lift and drag for ducted bodies at non-zero degrees angle of attack.

1.2.3 Nacelle performance at incidence

Knowledge of nacelle performance at incidence and in installed configurations is lacking. This project contributes to filling that knowledge gap through the building up of a database of detailed CFD calculations and the extraction of correlations between angle of attack and nacelle drag. These correlations are implemented in a propulsion system integration framework. The impact of modelling nacelle incidence on overall mission performance is assessed.

1.3 Aims and objectives

1.3.1 Research aim

The overall research aim is to develop a preliminary design framework for the assessment of powerplant aerodynamic installation effects. This framework will be used to assess the impact of nacelle size, geometry and installation on aircraft mission performance.

1.3.2 Research objectives

To address this research aim a number of objectives have been set.

1. *Develop methods for the estimation of nacelle external drag.*
2. *Develop methods for the estimation of the effects of angle of attack effects on nacelle drag.*
3. *Develop methods to assess the impact of nacelle installation effects on overall aircraft mission performance.*
4. *Generate a propulsion system integration model with defined aircraft and nacelle geometry and flight information as an input and engine net propulsive force as an output, encompassing Research Objectives 1, 2 and 3. This model will calculate nacelle drag which will then be integrated in a drag build up method at each point in a mission as part of an aircraft and engine performance model.*
5. *Use the model developed in Objective 4 to assess the sensitivity of mission fuel burn to nacelle size, position and installation for both a long haul and short haul mission.*

1.4 Publications

- A paper entitled "Aero-engine installation modelling and the impact on overall flight performance" [15] based on this research was presented at the Royal Aeronautical Society Advanced Aero Concepts, Design and Operations Conference 2014 (see Appendix A for abstract).

- A paper entitled "Aerodynamics of aero-engine installation". [16] was co-authored. The modified near-field drag extraction technique presented in this paper was developed by the author as part of the research reported on in this thesis (§4.6.1).

1.5 Overall project strategy

This work can be separated into three distinct work packages. The initial work begins with Work Package 1, (WP-1), which was the establishment of a method to estimate the external drag of an uninstalled nacelle. The outcome from this work package was a series of correlations for nacelle drag as a function of engine size, flight condition and engine angle of attack. These correlations then formed the basis of WP-2 where these correlations were used to create an uninstalled nacelle drag propulsion system integration (PSI) module. Following on from WP-1 and WP-2, WP-3 was the assessment the effect of installation on nacelle drag. This work package by extracted installation drag factors from complex full aircraft CFD as a function of nacelle size and installation position for three flight conditions which are representative of a typical mission. These factors were be extracted from mid-climb, mid-cruise and mid-descent configurations.

Chapter 2

Literature review

A review of published work relating to propulsion system integration aerodynamics is presented in this chapter. The first part of the review discusses relevant previous studies and is split into experimental and numerical studies. Secondly a review of previous studies which have investigated propulsion system integration by bringing together aircraft and engine models. The review also includes an overview of methods used to extract drag from CFD calculations or experimental measurements.

2.1 Previous studies

2.1.1 Experimental propulsion system integration studies

The simplest model of an engine for experimental or numerical studies is a representative through flow nacelle (TFN). Typically TFNs are designed to give the correct intake massflow capture ratio. However when this approach is used, jet effects are not modelled correctly. Jet effects can be more accurately simulated by using a cold air jet. Though temperature effects are not modelled the expansion of the jet exhaust can be approximated and its expansion effects assessed. One of the most widely employed tools for modelling

real engine effects in the wind tunnel is the turbine powered simulator (TPS).[17] The advantage of using a TPS over a cold air jet simulator or TFN is the ability to correctly simulate intake and exhaust flow including the correct thrust division between fan and turbine.[17]

These methods of modelling an engine are discussed in order of complexity starting with TFNs, then cold air jet simulators and finally TPSs.

2.1.1.1 Though flow nacelles

Early propulsion system integration experiments were primarily focused on aircraft aerodynamic characteristics. A lack of understanding regarding high incidence aircraft performance was highlighted in 1963 by the British Aircraft Corporation One-Eleven accident.[18] This led to a study where measurements of aerodynamic forces and moments were made for a range of aircraft configurations where nacelle size and position were varied independently[18]. It was found that the aircraft aerodynamic characteristics were dependent on the placement of the engines (Figure 2.1). The aircraft configuration consisted of aft-fuselage mounted engines and a T-tail experienced severe problems with stall.[18]

It was shown theoretically that a lower installation drag may be obtained by placing the nacelles in the underwing, rearward mounted location[19] and a large amount of experimental work was carried out to understand the aerodynamic trade-offs involved with the positioning of underwing mounted nacelles. Possible advantages of underwing-aft nacelle location were explored[20]. It was expected that such a position would disturb the flow over the suction side of the wing less and enhance wing lift by having having more favourable pressure distributions on the wing underside. It was also hoped that lower wave drag and a higher drag-divergence Mach number could be achieved through variation of the nacelle cross-sectional area[20]. These hypotheses were tested in the NASA-Langley Transonic

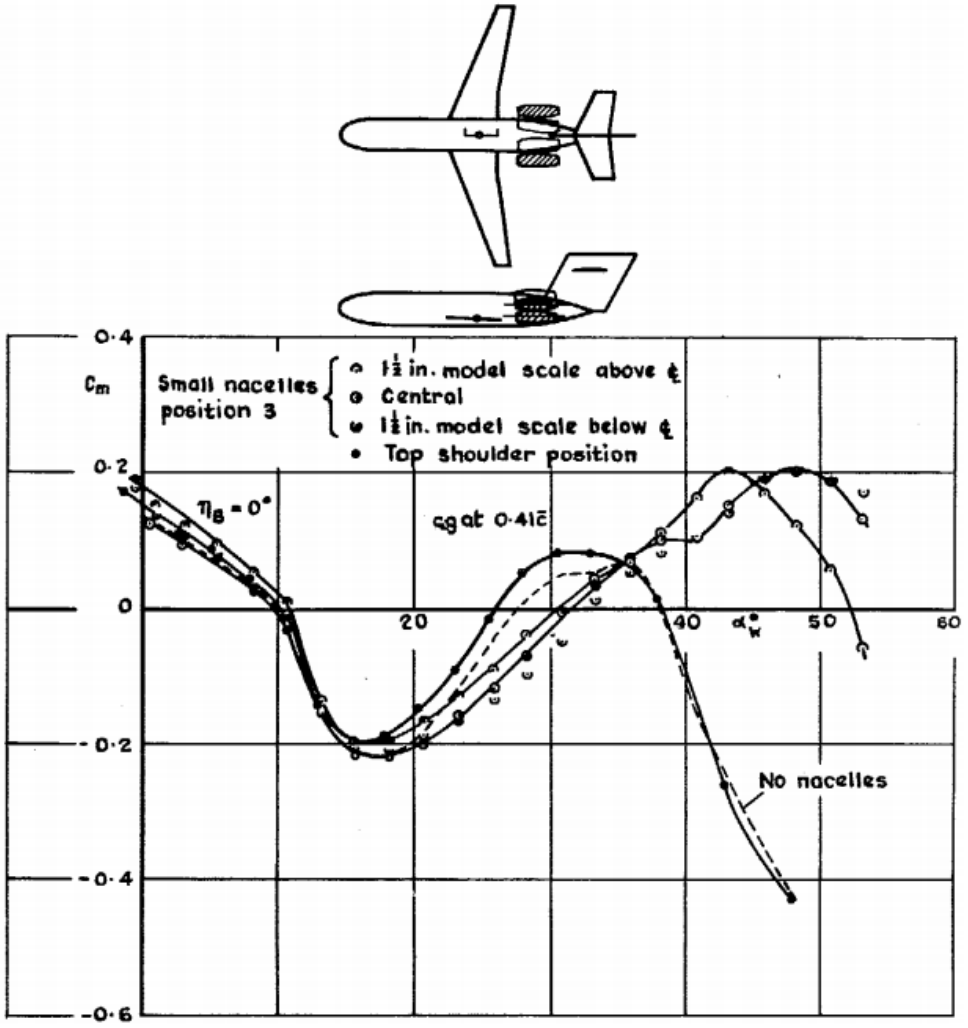

FIGURE 2.1: The effect of vertical location of nacelles on the coefficient of pitching moment.[18]

Wind Tunnel at Mach numbers ranging from 0.70 to 0.85 with aircraft incidence was varied from -2.5^o to 4.1^o. Two types of underwing-aft mounted, flow-through nacelle models were tested: one circular and one D-shaped (Figure 2.2). The D-nacelle configuration experienced the lowest drag of all those tested. Positive interference drag was calculated for every configuration, but the aft-mounted nacelles had significantly higher L/D_{MAX} than the conventional forward-mounted nacelles. At Mach number 0.80, the value for the conventional forward-mounted nacelles was about 11 percent lower. The effect of the aft-mounted nacelles on C_L was to shift the lift curve upward relative to the wing-body

only configuration, and to shift the zero-lift angle of attack to a more negative value. The opposite effect was found for the conventionally mounted nacelles. The difference in lift was mainly due to changes in pressure on the inboard wing pressure surface. Pressures in this region were increased by the presence of aft-mounted nacelles when compared to the wing-body only configuration. The conventionally mounted nacelles however caused the flow in this region to accelerate and become supersonic with a corresponding reduction in pressure[20]. These conclusions were backed up by later work[21] which found installation of nacelles in the aft under-wing position produced lift increases, as opposed to the loss in lift typical of forward wing-mounted nacelle configurations. D-shaped inlet nacelles also had the lowest nacelle installation drag.[21]

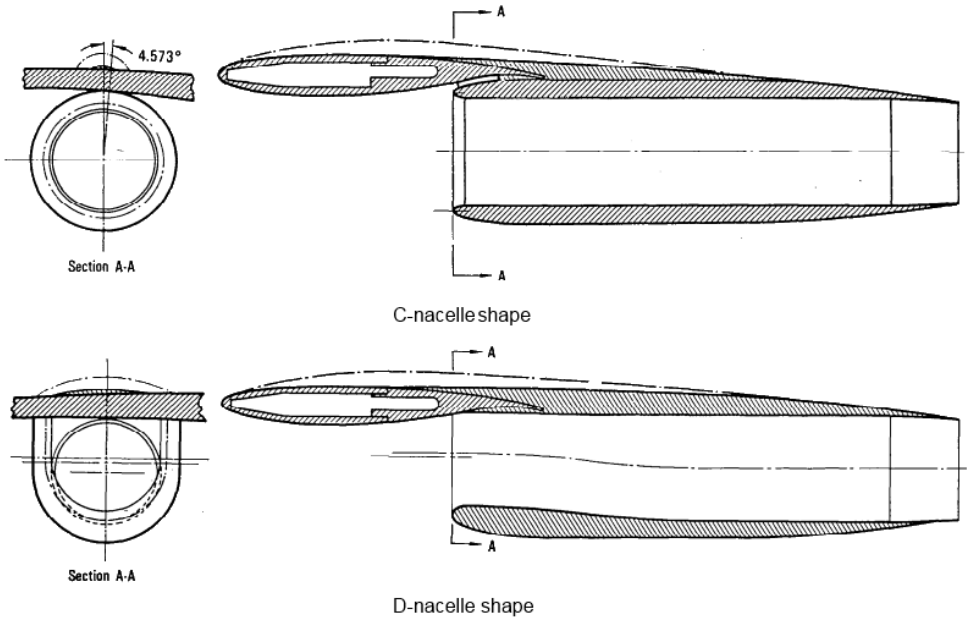

FIGURE 2.2: Underwing aft-mounted C-shape and D-shape nacelles.[20]

With supercritical wings care has to be taken over wing-pylon-nacelle integration.[22] Through careful integration design it may be possible to not only minimise adverse interference effects but to achieve a favourable negative interference effect. Efforts were made to minimise installation drag by housing the pylon structure within an antishock body.[23] It was demonstrated that antishock bodies, proposed to house the structure which required the

nacelles to be attached in the aft underwing position, could be installed on the wing without a deterioration of the longitudinal aerodynamic cruise performance at a Mach number of 0.80. At the highest test Mach number of 0.85, at which a higher shock loss occurs, one of the antishock-body/pylon configurations reduced the nacelle installation drag by approximately 80% at cruise lift.[20] Other studies have also shown that pylon design can have a major effect on installation drag.[24,25] One way of reducing the interference drag due to the pylon is to reduce local velocities and avoid separation curvature at the sides of the pylon. This can be achieved by minimising curvature at the sides of the pylon, the leading edges and along the wing lower surface.[25]

Toeing in the engine has been shown to lower installation drag.[26] The effects of toe-in angle of the under-wing, rearward-mounted nacelle and pylon were investigated across a range Mach numbers (0.70 to 0.82) and an incidence range from -2.5^o to 4.0^o. For the cruise condition minimum installed drag was achieved with a toe-in angle of 1.5^o. In agreement with previous studies[20,21] for high-wing transport aircraft the aft mounted nacelle configuration produced an increased lift when compared to wing-body model.[26] In these studies only the effect of nacelle installation location was taken into account, no consideration was made for the degradation of engine performance due to intake flow distortion.

Low-wing aircraft, more typical of modern commercial jets have a ground clearance constraint on engine installation.[27] This constraint coupled with the need to minimise engine inflow distortion are two of the main factors which lead to underwing fore mounted engines.[27] Three aircraft and underwing fore-mounted engine layouts have been investigated.[27] These consisted of a three engine configuration (two on the wing and one simulated "S" duct in the vertical tail, Figure 2.3), a four engine short pylon configuration (all wing mounted) and a four engine long pylon configuration (all wing mounted). The results of this investigation indicated that for the toe-in angles tested (0^o, 2^o, and 4^o) and cant angles tested (0^o and 3^o) there was no discernible drag difference.[27] When underwing, fore

mounted, long duct nacelles are added to a supercritical wing the magnitude and direction of flow velocities over the entire span can be changed significantly, reducing cruise lift. Care needs to be taken to ensure adequate clearance between wing and nacelles to minimise interference effects.[25]

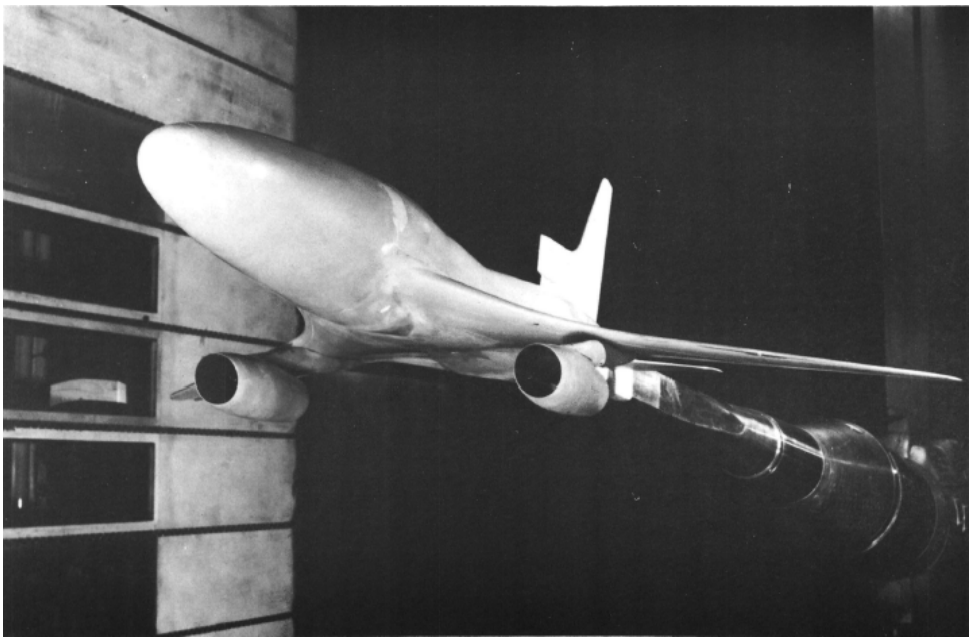

FIGURE 2.3: Three-engine advanced transport technology configuration installed in Ames 11-foot windtunnel.[27]

Efforts have been made to reduce the propulsion system drag through nacelle cowl shaping. A series of experiments were carried out at the Aircraft Research Association (ARA) Ltd, Bedford between 1968 and 1973.[28] The tests aimed to achieve favourable supercritical flow development over the nacelle exterior as previous designs had only optimised for subcritical flow. Mass flow, drag and surface pressure distributions were measured for six different nacelle shapes. Tests were carried out at Mach numbers ranging from 0.4 to 0.95 to capture both subsonic and transonic flow regimes. Some tests were carried out at an incidence of 3^o and 6^o, however this data is not recorded in the report, all data presented results from tests carried out at 0^o incidence. The intake mass flow was varied using a mass flow control plug, with the mass flow capture ratio varying from 0.2 to 1. The overall aim of the study, which was to produce favourable supercritical pressure distributions, was fulfilled. Increasing the

lip radius from that of a NACA-1 series forebody was successful in the reduction of peak velocities near the lip. This restricted spillage drag to lower values of massflow ratio.[28] Good aerodynamic performance could be achieved by the flattening of the cowl aero-line aft of the lip and by an increase in curvature near the point of maximum nacelle diameter, so long as the shock remained ahead of the region of increased curvature.[28]

Theoretically designing a nacelle to have laminar flow over much its length should result in a large reduction in propulsion system integration drag.[29] An isolated nacelle test has shown that it is possible to design a nacelle such that laminar flow is maintained over a significant length and that it is possible to install the nacelles onto a wing with a pylon without altering the extent of the laminar flow region.[29] The drag reduction for two nacelles with 60% laminar flow was approximately 9 counts at the cruise C_L of 0.45 (Figure 2.4).[29] This difference was similar in magnitude to the difference in the calculated skin friction drag. A reduction in drag of approximately 10 drag counts was achieved at the cruise C_L by the placement of the nacelles in a position foreward of the wing (Figure 2.5).[29] This was caused by a reduction of the compressibility and nacelle interference effects on the wing lower surface. Pylon design was found to have a significant effect on interference drag. Contouring the pylon so as to diminish high velocity peaks on the wing lower surface resulted in a decrease in drag of approximately 7.5 counts (Figure 2.5).[29]

2.1.1.2 DLR-F6

The DLR-F6 is a windtunnel model which was designed as a representation of a transonic transport aircraft (Figure 2.6).[30] The geometry was derived from the DLR-F4 configuration.[31] The model has been designed for a cruise Mach number of 0.75 with a lift coefficient of 0.5.[30] However this cruise Mach number is low for a modern transonic transport aircraft. A large body of experimental data is publicly available for the DLR-F6 in wing-body and wing-body-pylon-nacelle configurations (Figure 2.7). For this reason it was chosen as the

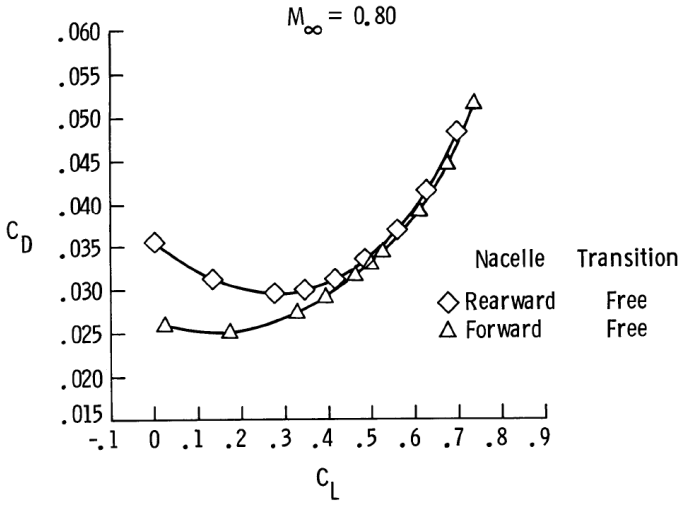

FIGURE 2.4: Effect of nacelle position on interference drag for a Mach number of 0.80 for a transport aircraft with natural laminar flow nacelles.[29]

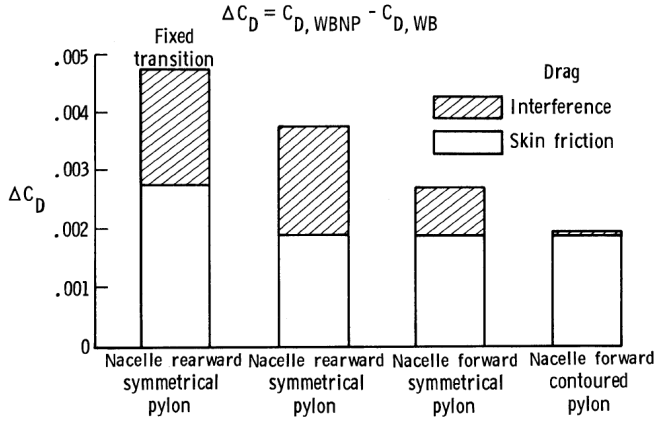

FIGURE 2.5: Installed drag for a Mach number of 0.80 and a C_L of 0.45 for a transport aircraft with natural laminar flow nacelles.[29]

test geometry for the second American Institute of Aeronautics and Astronautics Computational Fluid Dynamics Drag Prediction Workshops (AIAA CFD DPW 2).

Overall forces and moments were measured along with wing and nacelle surface distributions.[30] The wing-body-pylon-nacelle configuration had an increase in total lift at constant incidence and total drag increases at constant lift over the wing-body configuration.[30] Drag rise Mach number for the wing-body-pylon-nacelle also reduced. Analysis of the surface pressure distributions on the wing showed that the supersonic region on the wing suction surface was reduced with an upstream movement of the shock location. The presence of the pylon accelerated flow over the inboard wing pressure surface which created a local supersonic region.[32]

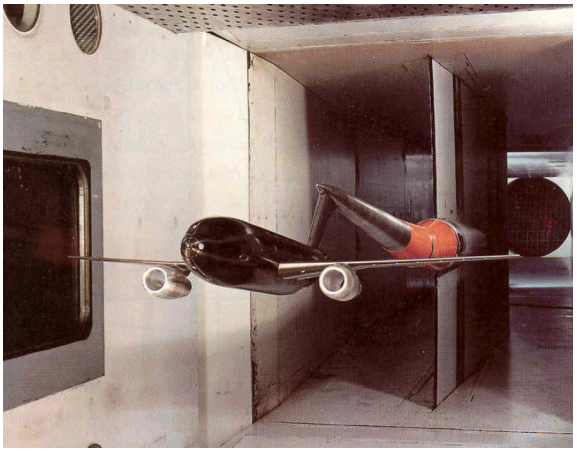

FIGURE 2.6: DLR-F6 Model in the ONERA S2MA Wind Tunnel.[33]

2.1.1.3 NASA Common Research Model (CRM)

A wide-body transport aircraft wind tunnel model known as the "Common research Model" (CRM) has been created by NASA.[34] The CRM is more representative of a modern transonic aircraft than the DLR-F6 as its supercritical wing was designed to cruise at a Mach number of 0.85 as opposed to 0.75 for the DLR-F6. For this reason coupled with

the wealth of available experimental data, the CRM replaced the DLR-F6 as the test case for the AIAA CFD DPWs from DPW 4 onwards.[35,36]

Five different CRM configurations have been tested:

- wing-body (WB)
- wing-body-pylon-throuhg-flow-nacelle (WBPN)
- wing-body-tail at three tail incidences (WBT−2, WBT0 and WBT+2)

Forces, moments and surface pressures were measured in the NASA National Transonic Facility and the NASA Ames 11-ft Transonic Wind Tunnel.[37] Nacelle-pylon interference effects were investigated. The presence of the nacelle-pylon led to an overall increase in drag and a corresponding decrease in lift. At a lift coefficient of 0.5, which corresponded to the design point of the model, the WBPN configuration had a reduced nose down pitching moment in comparison to the WB configuration.[37] Experimental data is available for three

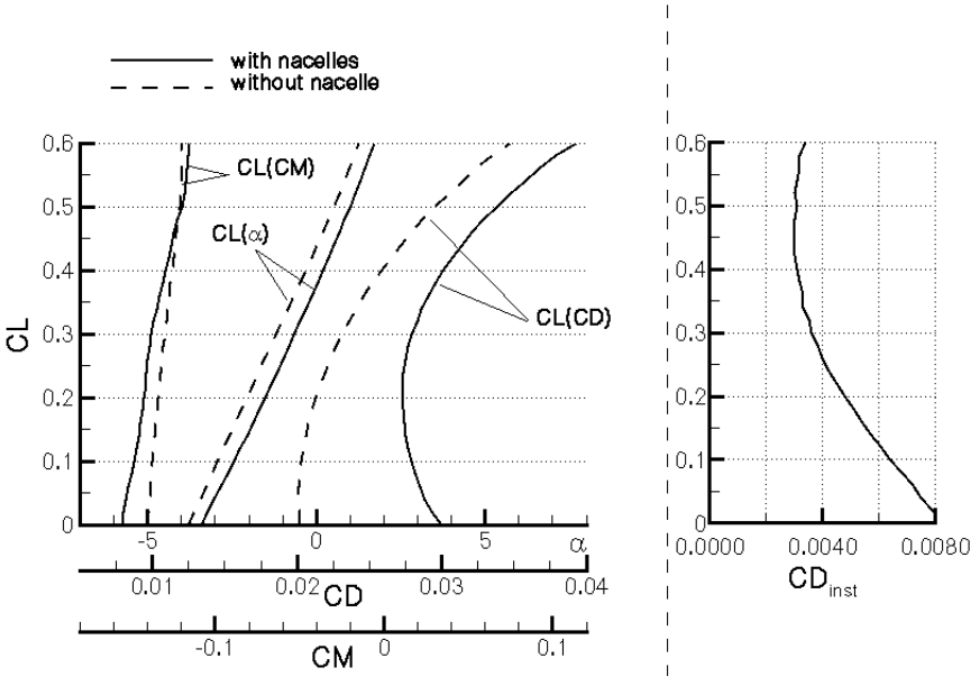

FIGURE 2.7: DLR-F6 experimental data for Mach 0.75.[30]

Reynolds numbers. The majority of the data was acquired at a wing-chord Reynolds number of 5 million. However some data is also available at a Reynolds number of 30 million, which is typical of a full-scale transport aircraft.

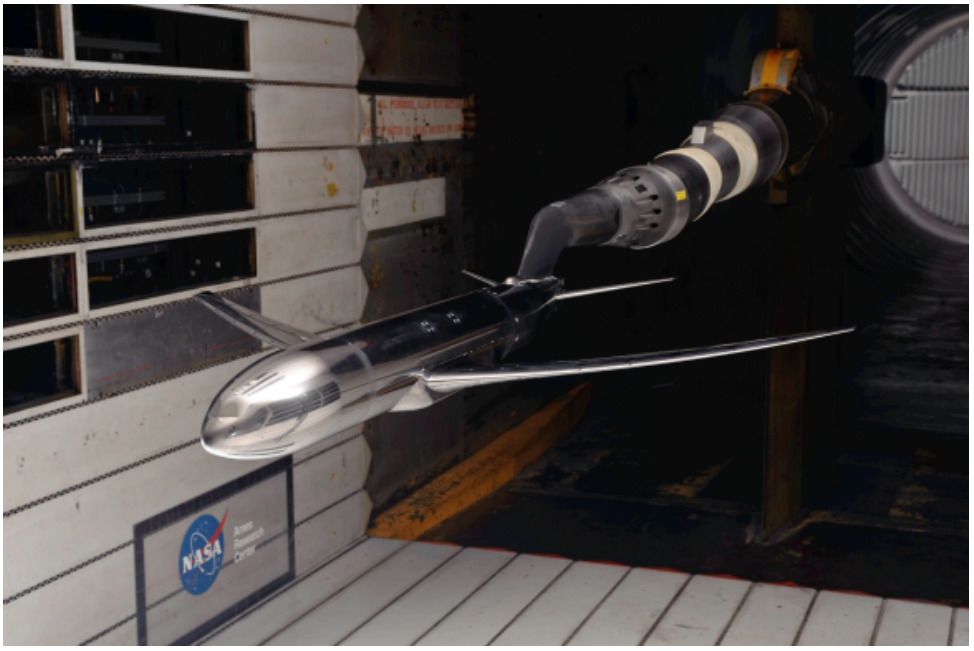

FIGURE 2.8: The Common Research Model (CRM) in the Ames 11-ft Wind Tunnel.[37]

2.1.1.4 Cold air jet simulators

One aspect of propulsion system integration that is not properly modelled by through-flow nacelles is the interaction of the jet efflux with the other aircraft components. Compressed air jets can be used to simulate the jet efflux.[38]

To determine whether jet effects would be significant for a low wing civil transport type aircraft, a series wind tunnel experiments undertaken using a wing mounted cold-air jet simulated high bypass ratio (HBPR) turbofan mounted close to a wing.[38] The presence of the through-flow nacelle and pylon led to a reduction in suction on the rear and an increase in suction on the foreward wing lower surface. The point of minimum pressure moved forward. There was little difference in data from the cold air jet nacelle at a pressure ratio (PR) of 1 and the TFN. When PR was increased to 1.5 the the pressure distribution shape remained the same. However there was an increase in the peak suction level when compared with the through-flow nacelle (Figure 2.9).[38] The increased suction due to the cold air jet occurred at about 25% of the wing chord or 43% of the pylon length on either side of the pylon. At a Mach number of 0.77 a strong shock wave was present on the inner wing.[38] However this effect was reduced with increases in incidence and there was an indication that there was a Mach-number at which the suction level no longer continues to increase. It was noted that wing interference on the inboard side of the pylon might be reduced by careful pylon shape design.[38]

The influence of cold air jets on the installation effects with changes in relative nacelle wing position has been studied.[39] The presence of the jet in some configurations caused the shock on the upper side of the wing to move upstream in agreement with previous studies.[38] Both wing drag and nacelle thrust were found to be increasing functions of the relative wing-nacelle horizontal distance. The overall effect was however always favourable with the best position being the closest coupled configuration. When the nacelle was moved vertically away from the wing there was a slight decrease in both wing drag and nacelle

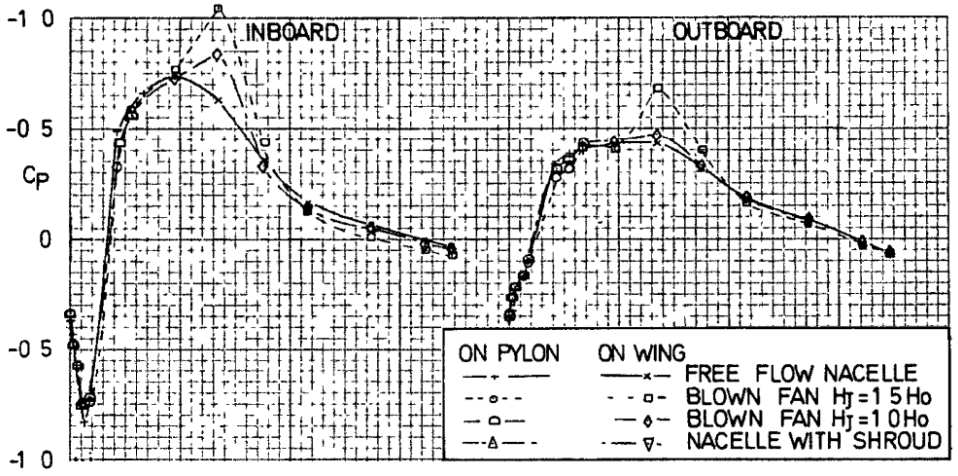

FIGURE 2.9: The influence of exhaust flow on pressures in the vicinity of the wing pylon juncture. $M = 0.75$ and $\alpha = 3.5^o$.[38]

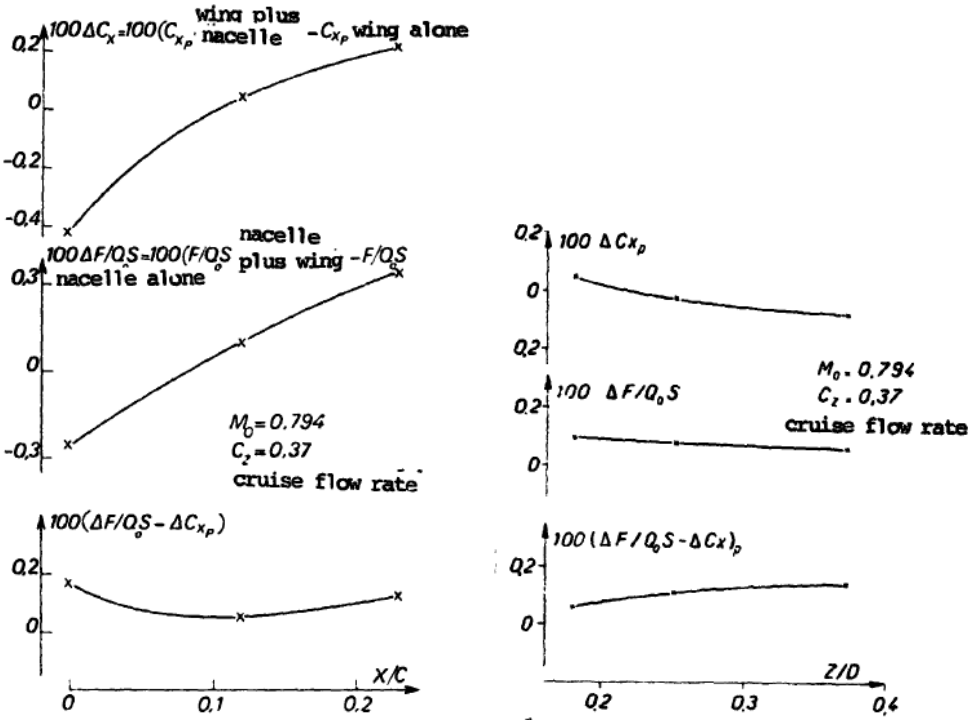

(a) Influence of relative horizontal position (b) Influence of relative vertical position

FIGURE 2.10: The influence of relative nacelle-wing position on the global interaction balance using cold air jet nacelles.[39]

thrust (Figure 2.10).[39] The overall effect was always favourable with increases in vertical offset so that the configuration with the largest offset had the best performance. However changes in overall performance when moving the nacelle vertically relative to the wing were smaller than for horizontal movements.[39]

The effects of a cold jet on the boattail pressure drag of four isolated cylindrical ejector nozzles has been studied.[40] Over a range of Mach numbers extending from 0.60 to 1.47 nozzle pressure ratio was varied from approximately 1.0 (jet off) to 11 for four isolated cylindrical ejector nozzles. Boattail angles of 10^o and 15^o were tested.

At subsonic speeds, the jet caused large reductions in drag of the 15^o boattail configurations. For values of nozzle pressure ratio much less than the design value this drag reduction was insensitive to changes in nozzle pressure ratio. However when the nozzle

pressure ratio was further increased up to and beyond the design value a further drag reduction occurred.[40] At supersonic freestream conditions, boattail pressure drag was insensitive to changes in nozzle pressure ratio until the jet approached full expansion. As the jet became underexpanded, boattail drag was significantly reduced. The trends were basically the same for both boattails except that configurations with a boattail angle of 10^o drag was affected to a lesser degree by the jet.[40]

2.1.1.5 Turbine powered simulators

Turbine driven powered simulators were used to provide representation of the inlet and exhaust flows for a four engine short-haul aircraft supercritical wing configuration.[41] Wind tunnel tests were carried out across a range of Mach numbers from 0.6 to 0.78. Both TPS and flow-through nacelles were tested so that the effects of the jet could be assessed separately from the effects of the nacelle installation. Presence of the jet can reduce interference drag. For pressure ratios from 1 to 1.37 the effect of the jet is to decrease interference drag. This was because viscous mixing of the jet flow and the external flow reduced afterbody separation. When the fan pressure ratio was further increased to 1.48, afterbody separation increased due to jet pluming which resulted in an increase in interference drag in comparison with the through flow configuration.[41]

A European cooperative research programme dealing with aerodynamic engine/airframe integration ENIFAIR, ran from 1996 to March 2000. Wind tunnel tests at high speed were carried out, the main objective of which was to determine installation and interference drag levels for different engine installation types. These wind tunnel tests were carried out with TPSs.[42] Unanticipated variation of drag with changes in engine power setting and bypass ratio was found.[43] The root cause of these findings was identified through the application of thrust and drag bookkeeping as inadequate TPS calibration. A wind tunnel correction method which allowed the effects of the interaction between flow from the jet the external flow to be corrected for was derived.

Variations in drag behaviour caused by the jet effect were investigated (Figure 2.11). In this study this was expressed as the difference in drag values calculated for the through flow nacelle and for the engine at start of cruise with a maximum thrust setting. The increases in C_D resulting from the presence of the jet was approximately 2.3% for the engine configuration in comparison to the wingbody configuration, for the ultra high bypass ratio engine this offset rose to 3.9%.[17] The wing-body-pylon-VHBR-engine configuration at the maximum thrust setting had a $C_D = 0.034$. Installation drag was calculated to be 30 aircraft drag counts which was 8.6% of the total aircraft drag for this configuration. Of these 30 aircraft drag counts, 10 drag counts were attributed to the jet effect, approximately 3% of the total aircraft drag.[17]

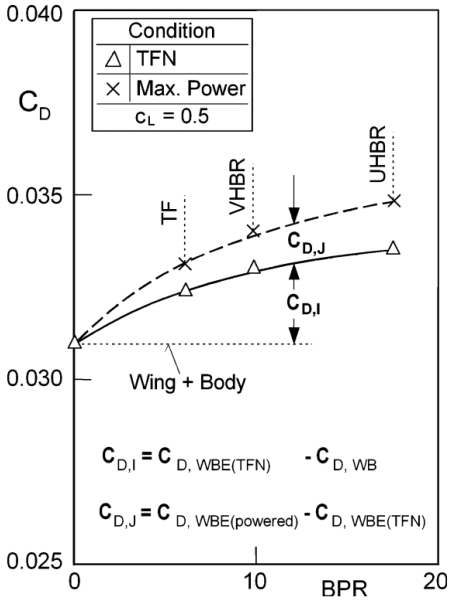

FIGURE 2.11: Variation of drag coefficient of the wing-body-pylon-engine configuration at M = 0.75 with changes in engine bypass ratio.[17]

2.1.2 Computational studies of propulsion system integration

A number of authors have applied RANS based CFD to the propulsions system problem.[16,44–52] One RANS CFD study modelled nacelle drag for a range of geometries, both 2-D and 3-D.[49] A comparison of nearfield and farfield drag extraction methodologies was carried out in comparison to the empirical ESDU nacelle drag prediction method. The farfield method was applied to the 2-D simulations but was found to be much more sensitive to the presence of shocks than the nearfield method.[49] It was concluded that this approach, for 2-D simulations at least, could not be used to calculate absolute nacelle drag values.[49] However, it could perhaps be used in an optimisation process where only overall trends were required.[49]

When simulating a powered on nacelle in conjunction with a pylon, care must be taken over thrust and drag bookkeeping.[51] A method derived from control volume theory to extract nozzle C_V from CFD calculations has been created. To illustrate this method a powered nacelle-pylon-airframe configuration was simulated with RANS CFD. At a condition of $M = 0.785$, $Re = 2.4 \times 10^7$ and $C_L = 0.55$ corresponding to a cruise condition good agreement was found with experimental data.[51] The CFD calculations overpredicted C_D by 6.1 engine drag counts.[51]

A nacelle has been modelled with RANS based CFD in order to assess its abilities to match experimental data.[52] The influence of grid refinement , near wall treatment and turbulence models was assessed. Total drag was predicted within 5% of the experimental data at zero degrees incidence.[52] This discrepancy rose to 10% at 20^o incidence.[52] The CFD method was able to capture the main flow features.[52]

A transonic civil aircraft has been modelled with RANS CFD with and without through flow nacelles (TFN).[16] A series of validation exercises were undertaken for an isolated nacelle and for the airframe-TFN configuration. In the isolated nacelle case the critical mass flow capture ratio and the drag rise Mach number (M_{DR}) were identified as key

aerodynamic performance parameters. The critical massflow capture ratio prediction was found to have an accuracy of 1.5% while the drag rise Mach number had a quoted accuracy of $\pm 0.007 M_{DR}$.[16] For the airframe-TFN configuration, discrepancies for a range of C_L from 0.1 to 0.4 of 21 aircraft drag counts between the CFD calculations and the experimental data.[16]

Two extensive sources of information on the application of CFD to the propulsion system integration problem are the Megaflow Project and the AIAA Drag Prediction Workshops. These are discussed in detail in §2.1.2.1 and §2.1.2.2.

2.1.2.1 Megaflow project

A CFD project entitled "MegaFlow" was undertaken with a focus on full aircraft aerodynamic simulations in various flight configurations including take-off, cruise and landing.[46] The main aim was to develop a computational tool which could carry out these calculations accurately and dependably while still being efficient.[46]

The DLR-F4 wing-body aircraft configuration was simulated with and without CFM-56 like nacelles installed (Figure 2.12 and 2.13).[48] Forces and moments were calculated using a structured (FLOWer) and unstructured (TAU) CFD solver. Fully turbulent CFD simulations carried out with FLOWer over predicted drag in comparison to experimentally measured values by approximately 20 aircraft drag counts. When transition was modeled this over prediction reduced to 6 aircraft drag counts.[48] When the unstructured flow solver TAU was used to carry out fully turbulent simulations instead good agreement between calculated and experimentally measured drag coefficients was found.[48]

Variation of aircraft lift coefficient with changes in installation drag was calculated for the CFM-56-like TFNs (Figure 2.13).[47] Mach number and Reynolds number were fixed at 0.75 and 3×10^6 respectively. Reasonable agreement was found with experimental results and the report concluded that variations in propulsion system installation drag due to changes

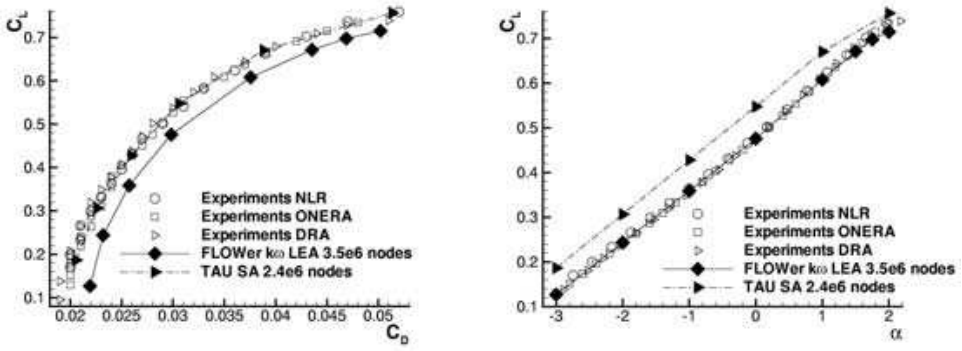

(a) (b)

FIGURE 2.12: A comparison of viscous calculations using the FLOWer and TAU solvers for the DLR-F4 wing-body configuration.[48]

in installation location and engine size can be adequately predicted with the DLR-TAU CFD solver.[47]

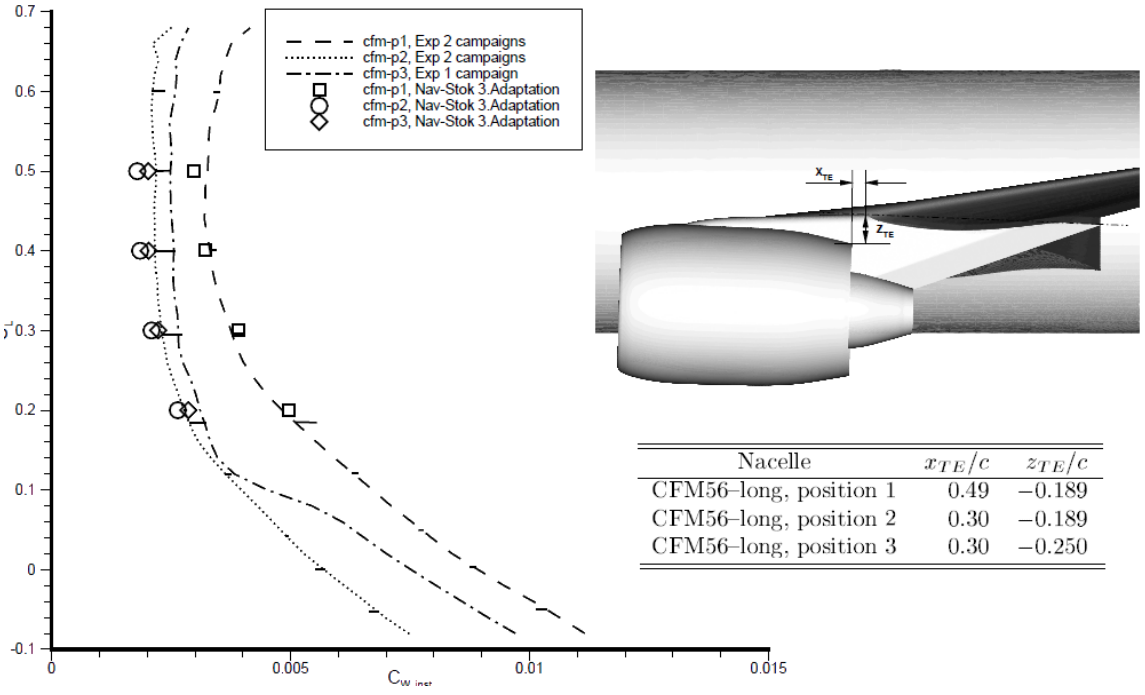

Nacelle	x_{TE}/c	z_{TE}/c
CFM56–long, position 1	0.49	−0.189
CFM56–long, position 2	0.30	−0.189
CFM56–long, position 3	0.30	−0.250

FIGURE 2.13: Aircraft lift coefficient as a function of installation drag for three different CFM56-like TFN installation positions. $M = 0.75$, $Re = 3 \times 10^6$. Symbols represent CFD calculated quantities while lines represent experimentally measured values. The DLR-TAU code used as the CFD solver.[47]

The impact of the engine power setting was also studied computationally (Figure 2.14).[45]

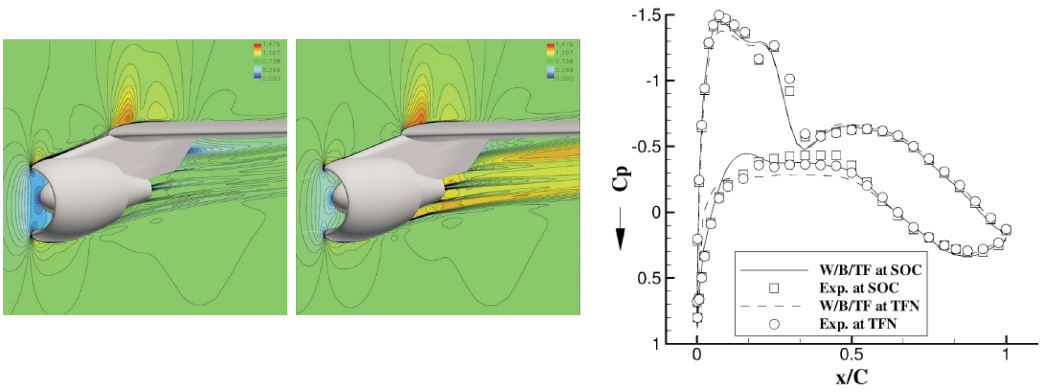

(a) TFN configuration (b) TPS configuration (c) C_P distribution, $\eta = 33\%$

FIGURE 2.14: CFD simulation of the DLR-F4 using FLOWer. $M = 0.75$, $C_L = 0.5$. The influence of engine power setting illustrated by comparing a TFN and TPS configuration, (a) and (b) contours of Mach number, (c) distribution of pressure coefficient at $\eta = 33\%$.[45]

The main consequence of employing a TPS instead of a TFN was the increase in the exhaust jet velocity. The exhaust flow can in some cases accelerated to supersonic speeds. The large velocity differential between the exhaust and nacelle external flow can result in large shear layers (Figures 2.14(a) and 2.14(b)).[45] This change in the velocity and pressure field impacts upon the performance of the wing. Figure 2.14(c) shows the variation of pressure coefficient at a wing cross-section inboard of the nacelle. The jet effect due to the TPS resulted in a lower pressure coefficient on the lower side of the wing.[45]

2.1.2.2 Drag prediction workshop series

The AIAA CFD Drag Prediction Workshop series was established to bring together parties involved in aircraft aerodynamic performance prediction, both industrial and academic, so that the state-of-the-art of computational fluid dynamics methods could be evaluated.[44] Specific focus was on assessing the ability of different numerical codes to predict aerodynamic forces and moments. Through this exercise areas which required further research and development could be identified and efforts to address them coordinated.[44]

First AIAA CFD Drag Prediction Workshop

The subject of the first AIAA CFD Drag Prediction Workshop was the DLR-F4 aircraft geometry.[53] This wing-body model is typical of civil transport aircraft which has been designed to cruise at a transonic Mach number. CFD test cases were set out for the workshop participants so that different numerical schemes and approaches could be compared.[53] Participants were also given the option of carrying out additional simulations to predict the aircraft drag rise Mach number. After the various CFD calculations were completed they were compared to experimentally measured data.[53]

Most of the experimental data consisted of wing pressure profiles.[44] With $C_L = 0.5$ Mach number was varied from 0.6 to 0.87. At a Mach number of 0.75, the model design Mach number, measurements were taken at $C_L = 0.3$, 0.4, 0.5 and 0.6.[44] In all cases the Reynolds number was fixed at 3×10^6.[44] Boundary layer trips were used to fix the boundary layer transition point. However, the major drawback with the data however is the precision of the measured drag which was given as 10 drag counts.[44]

Overall lift and minimum drag were over-predicted by the CFD methods.[44] For configurations where separation was present, i.e. at high Mach numbers and higher angles of attack, non-parabolic drag was slightly under predicted.[44] A large amount of scatter was

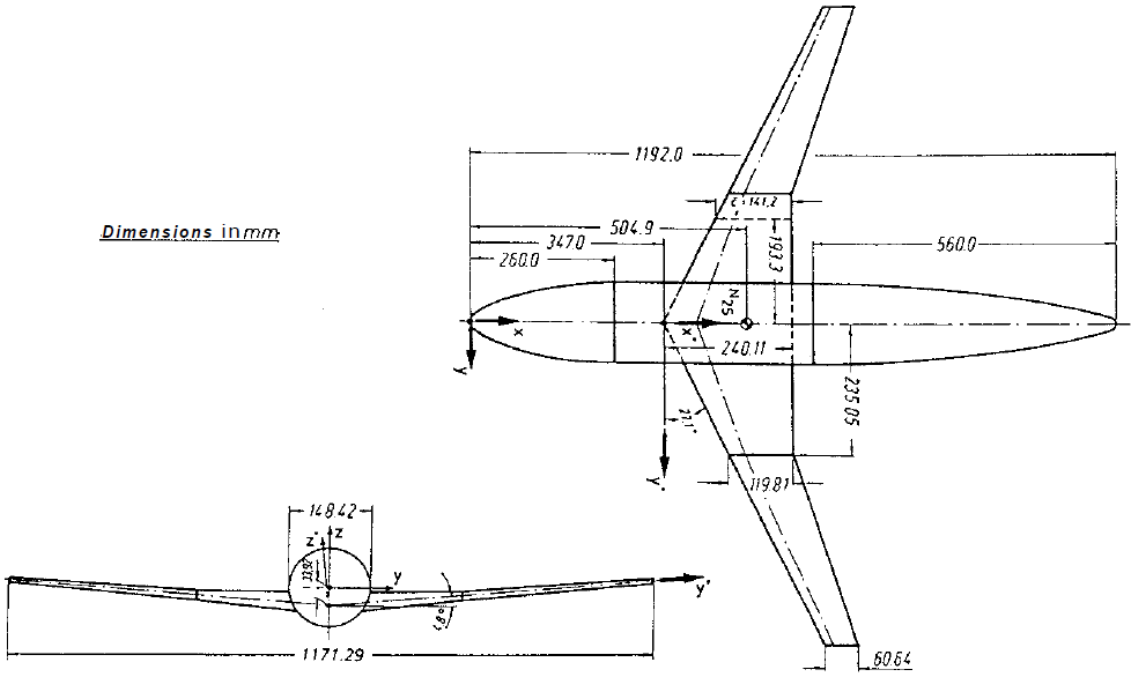

FIGURE 2.15: DLR-F4 wing-body geometry.[53]

present in the predictions. This was attributed to the various meshing codes, CFD solvers, turbulence models, etc. that were used.[44] No clear advantage was shown for any specific grid type. Though there was a large amount of scatter it was concluded that using a single code and consistent meshing and modelling techniques CFD is quite useful as an engineering tool to evaluate relative performance.[44]

Second AIAA CFD Drag Prediction Workshop

The second AIAA CFD Drag Prediction Workshop used the DLR-F6 wind tunnel model.[30] This is an A320-like wind tunnel model with two through flow nacelles (Figure 2.7). Its design Mach number is 0.75 at a Reynolds number of 3×10^6 with a lift coefficient of 0.5. The DLR-F6 is a modification of DLR-F4. The wing of the DLR-F4 was redesigned to achieve a more elliptic lift distribution and to reduce flow separation on the upper wing surface.[30] However these geometrical modifications increased the severity of flow

separations where the wing meets both the fuselage and the pylon. These separations undermined the CFD predictions and meant that conclusions could not be drawn regarding grid independence and the accuracy of drag predictions.[35]

It was decided in the next drag prediction workshop to use blind test cases and a simplified geometry which should experience less flow separation. The motivation behind using blind test cases was to better assess the CFD community's capability to predict drag, as opposed trying to match the results afterwards. The use of simpler geometries was proposed to allow the accuracy of the drag prediction with different levels of mesh independence.[35]

Third AIAA CFD Drag Prediction Workshop

A Third AIAA Drag Prediction Workshop took place to continue the work of previous AIAA Drag Prediction Workshops with the same overall objectives.[54] As was recommended by the second AIAA CFD Drag Prediction Workshop,[35] CFD studies were to be carried out "blind", with experimental data unavailable until after the CFD simulations had been completed.[54] Also the DLR-F6 model was modified by adding a wing-body fairing. This fairing was created to try to eliminate flow separation in this region (Figure 2.16). The fairing is a retro fit to DLR-F6 Model.[54]

The workshop concluded, after a large set of CFD solutions were collated, that it was obvious that several problematic issues with using CFD for accurate drag prediction still existed.[54] The level of grid-convergence was identified as an important metric. When this metric was applied to the presented cases outliers could be identified. It was concluded that the generation of consistent meshes for mesh independence studies remained a challenge, particularly when unstructured meshes are used.[54]

The FX2B fairing was used because it was supposed to remove or minimise flow separation in the wing-body junction.[54] However a large variation was found in predicted separation bubble sizes. One objective was to find out whether the pockets of flow separation found

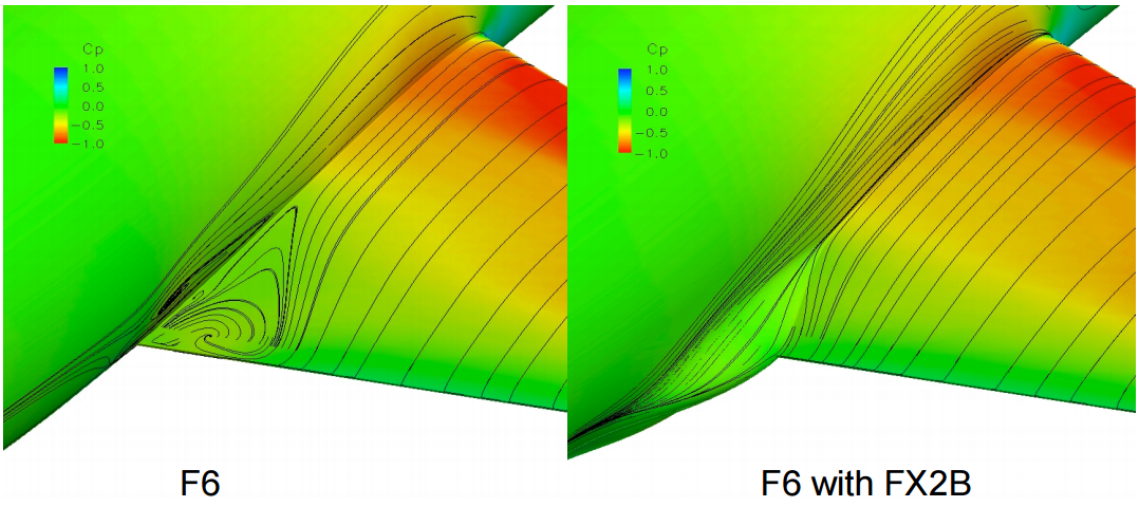

FIGURE 2.16: Surface streamlines at the wing-body junction of the DLR-F6, Mach = 0.75, CL = 0.50, RN = 5.0 million, Fully Turbulent, Spalart-Allmaras.[34]

in previous workshops was the cause of poor grid convergence seen. This hypothesis was true for some submitted cases, however for others it did not seem to cause any issues.[54]

Fourth AIAA CFD Drag Prediction Workshop

The fourth AIAA DPW[35] used the NASA Common Research Model (CRM) (§2.1.1.3) as the test geometry (Figure 2.8) instead of the DLR-F6. Three test cases were proposed, two of which were optional. The mandatory test case consisted of a mesh sensitivity study at a single aerodynamic point, and an incidence sweep.[35] These were to be carried out at a fixed-lift condition. All test cases were required to be run with fully turbulent flow.[35] Similar to the conclusions of the third DPW, it was found that there remained much room for improvement. However it was observed that there existed a core set of numerical approaches that led to similar results across all grid types. The generation of consistent grids for mesh independence studies still remained a problem.[35]

Fifth AIAA CFD Drag Prediction Workshop

The fifth AIAA DPW again used the NASA Common Research Model (CRM).[36] It mainly focused on mesh independence and the prediction of aerodynamic forces and moments for the CRM wing-body configuration. Participants also had the option of carrying out a buffet study.[36] A more substantial mesh independence study was undertaken than in previous drag prediction workshops. Improved mesh quality resulted in reduced scatter and standard deviation in the CFD results.[36]

The median predicted drag was within approximately 4 drag counts of the wind tunnel data.[36] Differences in the wind tunnel test and CFD approach were identified. The CFD approach did not take into account elastic deformation or regions of laminar flow and transition. There is therefore some uncertainty on how well they should agree. The wind tunnel results should only be used as a reference. The onset of buffet at $M = 0.85$ was also investigated. In some cases a large separation bubble at the wing-body juncture was observed. This flow phenomenon was not seen in the experimental results.[36]

2.2 Aircraft and engine modelling synthesis

A number of authors have investigated the effect of aero-engine installation on mission performance by linking engine and aircraft models.[50,55,56] However, there is a lack of literature in the preliminary design context, as is the focus of the research reported upon in this thesis. Most previous work sits more in a conceptual design context, with the focus being on the evaluation of installation effects for future technologies.[55,56]

A substantial body of work was undertaken in a study managed by Boeing Phantom Works, Seattle, through the NASA Glenn Revolutionary Aero Space Engine Research (RASER) contract.[55] This "Engine Diameter" study focused on finding the optimum BPR for a future aircraft in terms of mission fuel burn. In this context overall aircraft drag, weight,

emissions and noise were assessed. The reference aircraft was based on the 777-200ER aircraft with a composite wing and a cruise Mach number of 0.85 (Figure 2.17).[55] Two engine manufacturers provided engine information for an advanced engine incorporating future technology and three advanced "Ultra-Efficient Engine Technology" (UEET) engine designs with different BPRs (Figure 2.17). The engines on the baseline configuration were based on engine technology which was expected to be mature in 2015, i.e., ready for design into the future production of powerplants. The three General Electric (GE) UEET engine designs employed an advanced dual counter-rotating fan along with an improved compressor and turbine.[55] This allowed much larger BPR ratios to be achieved for approximately the same fan diameter when compared to the baseline engine (Table 2.1). Whereas for the Pratt and Whitney (PW) engines, increases in BPR ratio were achieved by increasing fan diameter (Table 2.1). The three PW UEET engines (Table 2.1) consisted of an advanced turbofan design (STF1171), a geared turbofan with a shortened intake and reduced nacelle diameter (STF1173) and a geared turbofan with a variable area nozzle (STF1174).[55]

GE engine:	**Baseline GE90-94B**	**GE58-F2 B7**	**GE58-F2 B6**	**GE58-F2 B5**
D_{FAN} (in)	123	100.6	108.6	123.5
BPR	7.8	7.43	9.47	13.1
$DesignFPR$	1.46	1.80	1.65	1.45
$NacelleL/D$	-	1.58	1.56	1.42
PW engine:	**Baseline PW4090**	**STF1171**	**STF1173**	**STF1174**
D_{FAN} (in)	112.9	118.5	127.9	148.7
BPR	6.2	11.5	14.3	21.5
$DesignFPR$	1.6	1.55	1.45	1.32
$NacelleL/D$	-	1.25	1.25	1.10

TABLE 2.1: Engine design points.[55]

All engine installations were positioned based on industry best practices with the nacelle top-line trailing edge location kept constant relative to the wing.[55] For each installation the wing design was re-optimised. Nacelle profile drag was calculated using "ESDU 81024 Drag of axisymmetric cowls at zero incidence for subsonic Mach numbers".[55] Industry

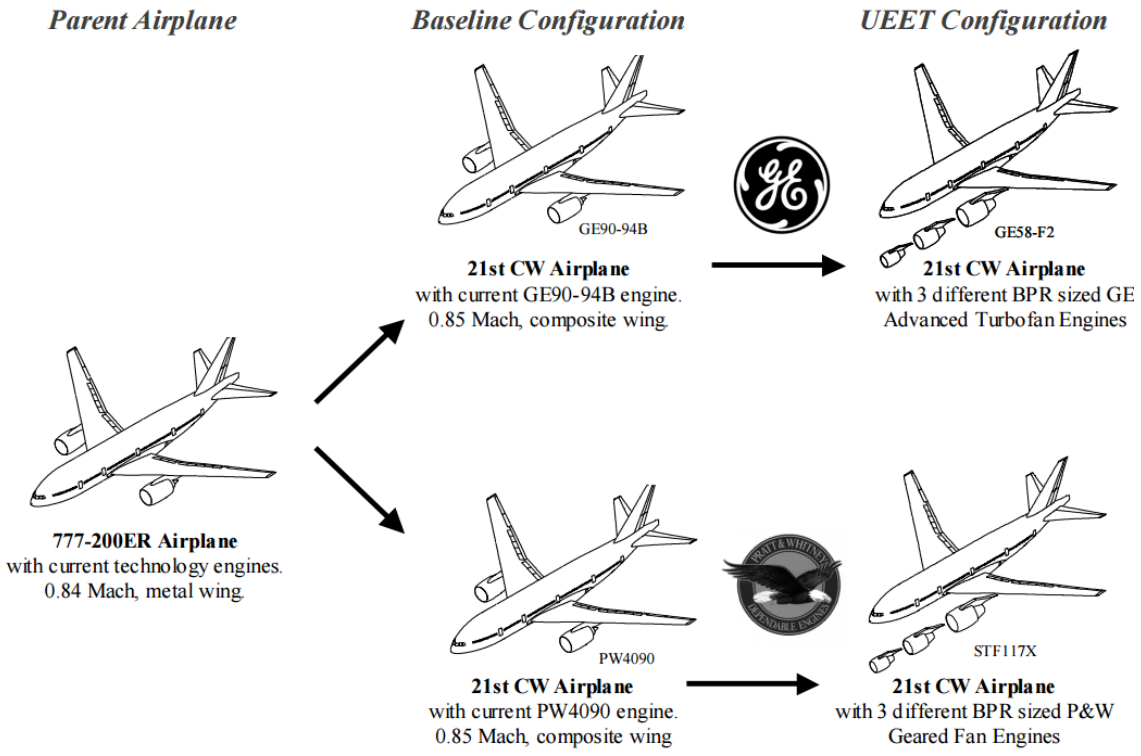

FIGURE 2.17: Airframe-engine configurations under investigation.[55]

"Handbook" methods were used to estimate pylon and interference drag. When the aircraft was resized to achieve the same mission performance, a reduction in fuel burn of 15% to 16% was estimated for the UEET engines. Optimal fan pressure ratios were found to be in line with current technologies ($1.46 \leq FPR < 1.6$).[55] The optimal GE UEET engine had a BPR of 11 while the BPR of the optimal PW UEET engine was 14.5. This optimal PW UEET engines fan diameter increased by 13.4% with respect to the baseline engine. However the fan diameter of the optimal GE engine was 6.5% smaller than the baseline.[55] These different outcomes for the engine manufacturers were due to the employed engine technology. The counter rotating fan used by the GE UEET engines resulted in higher BPRs without increasing fan diameter. This highlights the fact that technology advances in materials, airframe aerodynamics, engine architecture and cycle account for relatively large gains in mission performance[56]

Worked carried out at the Technical University of Munich in 2014[56] developed a methodology which integrates future engine design concepts into aircraft conceptual design. This methodology was demonstrated with a parametric study of two aircraft-engine configurations. Firstly a two-spool, direct-drive fan engine (Figure 2.18) was investigated in a conventional under-wing installation position.[56] Secondly an aft-fuselage mounted, two-spool, geared open rotor engine (Figure 2.18) was studied. In both cases the engines were mounted on an aircraft representative of a medium range civil transport aircraft (Figure 2.19).[56] This aircraft had characteristics similar to the Boeing 737-800 or Airbus A320-200. The baseline cruise Mach number was 0.78.

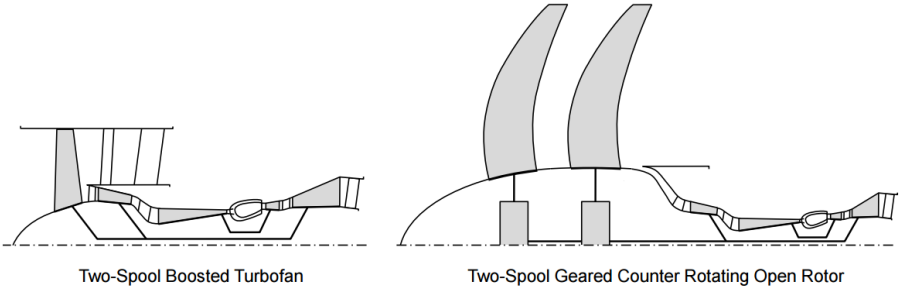

FIGURE 2.18: Schematics of the investigated engine architectures.[56]

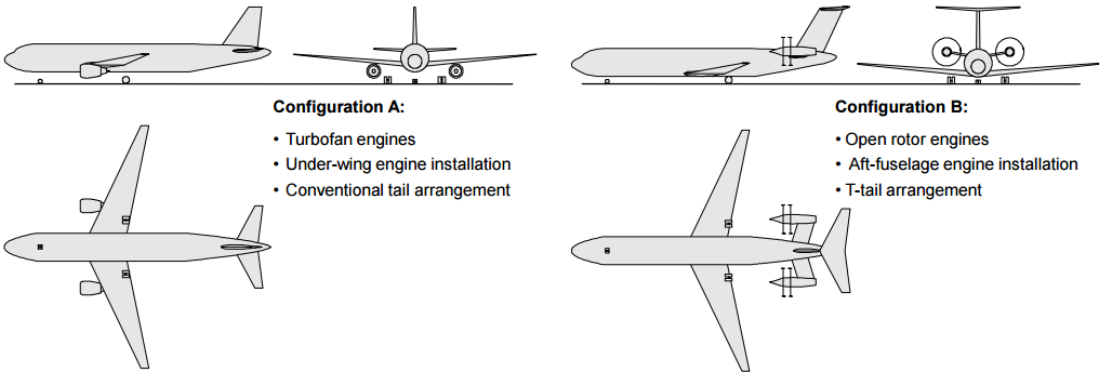

FIGURE 2.19: Airframe-engine configurations under investigation.[56]

This previous research[56] computed engine performance and nacelle drag by the use of the commercial codes GasTurb 11[57] and Piano[58], respectively. The effect of the engine installation was computed by Piano[56] , which simply assumes an increase of 10% on nacelle drag for under-wing installations and of 50% for fuselage-mounted engines. A component

build- up method based on parametric scaling of the turbo components was used for weight estimation.[56]

The performance of the under-wing turbofan configuration was investigated under four scenarios (Table 2.2).[56] Scenario 1 considered the current state of the art. Scenario 4 represented technological advances in airframe and engine design implemented through simple technology scaling parameters. While Scenario 2 and 3 consider technological advancements solely in engine and airframe design respectively in order to separate their effects.

In Scenario 1 an optimal BPR ratio of 7.1 was found.[56] When the advanced technology scaling factors were applied only to the engine (Scenario 2), the optimal BPR increased to 9.5 (Table 2.2). These engine technology scaling factors increase the aerodynamic efficiencies of the individual engine components.. It is noted that a further reduction in these losses did not lead to an significant increase in the optimal BPR.[56] In this Scenario engine mission fuel burn was reduced by 9.6% when compared to the baseline (Table 2.2). When technological advances in both engine and aircraft design were considered (Scenario 4) the reduction in mission fuel burn over the baseline scenario increases to 25.7% with the contribution of the advanced airframe approximately 20%. Overall a reduction in maximum take-off weight of 17.8% was found.[56] In Scenario 4 the optimal engine BPR increased from 7.1 to 7.2 (Table 2.2). Though this change is small it shows that to find the optimum engine BPR ratio the engine-airframe configuration must be assessed as a whole.

Scenario	$BPR_{des,opt}$ [-]	$\Delta W_{F,block,des}$ [%]	$\Delta MTOW$ [%]
State of the art existing	7.1	Baseline	Baseline
Advanced engine	9.5	-9.6	-5.6
Advanced airframe	7.2	-19.2	-14.5
Advanced airframe and engine	9.8	-25.7	-17.8

TABLE 2.2: Technology level study results at a cruise Mach number of 0.78.[56]

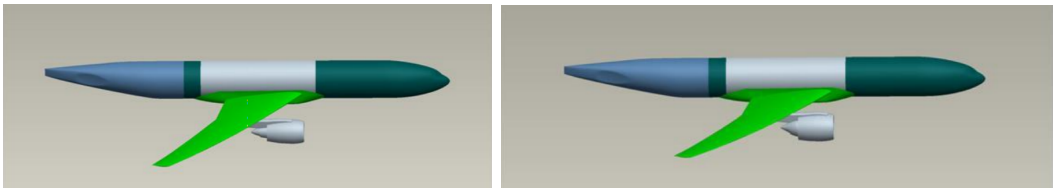

(a) Long haul aircraft with a three-spool high BPR engine incorporating an intercooler configuration.[50]

(b) Short haul aircraft with a two-shaft geared turbofan configuration.[50]

FIGURE 2.20: Investigated airframe-engine configurations.[50]

In addition to these conceptual design stage evaluations, detailed CFD work has been carried out to try to quantify propulsion system integration effects for a range of installation configurations.[50] The aim of this research was the extraction of net propulsive force as a function of engine installation location to allow mission block fuel burn to be calculated. Two aircraft-engine configurations were parametrically investigated at a cruise condition.[50] Firstly a three-spool high BPR engine incorporating an intercooler mounted under the wing of a long range aircraft was tested (Figure 2.20(a)). The second parametric study focussed on a two-shaft geared turbofan installed on a short range aircraft (Figure 2.20(b)).

Both engines were simulated in 6 under-wing installation locations which varied both horizontally and vertically.[50] A substantial effort was made in the refinement of the pylon design to improve its aerodynamic performance. In particular the junction between the nacelle and pylon was carefully designed to remove a flow separation (Figure 2.21).[50] To quantify the impact of pylon design on aerodynamic performance, aircraft drag was calculated for the original and modified pylon configurations. A reduction of 37 drag counts was achieved through the improvement of the pylon design.[50]

For both the long and short range aircraft configurations the effect of horizontal changes in the installation location on NPF dominated that of vertical movement.[50] The long range aircraft showed a 4.2% difference in cruise fuel burn between the extreme horizontal

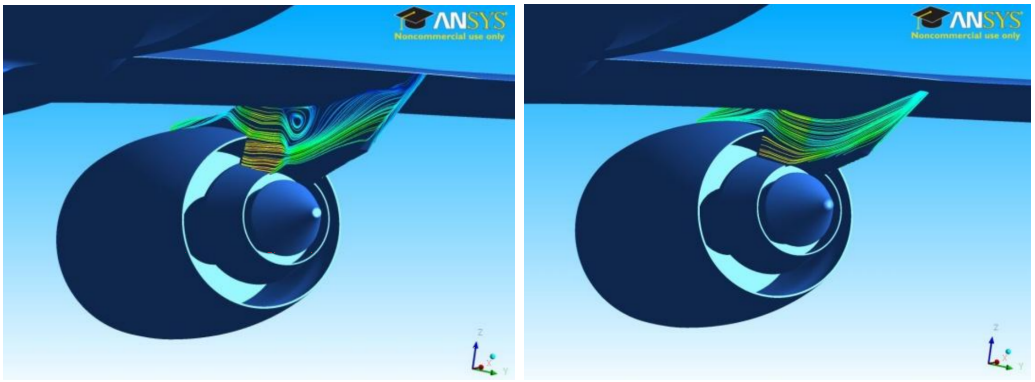

(a) Initial pylon design with surface streamlines on the inboard side highlighting a flow separation in the wing-pylon junction[50]

(b) Modified pylon design with surface streamlines on the inboard side demonstrating the removal of the previous flow separation[50]

FIGURE 2.21: Pylon design iterations[50]

installation positions (Figure 2.22(a)). This difference was 6.4% for the short haul configuration (Figure 2.22(b)). This work concluded that future work was required, specifically further CFD calculations on a more standard aircraft-engine configuration was necessary. These CFD calculations should incorporate off design conditions such as take-off, climb and descent.[50]

A number of authors have brought together aircraft and engine models as part of engine performance analysis assessments.[59–61] Previously it has been incorporated into "in-house" codes and used to evaluate optimum engine bypass ratios[59] and the impact of engine aerodynamic losses on overall mission performance.[60] One such study[59] investigated the differences in optimum bypass ratio for a business jet with aft-fuselage mounted engines with differing technology levels. An aircraft modelled was linked with the GASTURB[57] to model the engine performance. Optimum bypass ratios were estimated for two freetream Mach number conditions, $M = 0.75$ and $M = 0.9$. For the lower Mach number when a technology level equivalent to that of the 1990s was used the optimum BPR was found to range from 5 to 7.[59] When the technology level was raised that predicted for the year 2030 the optimum BPR increased to a range of 6 to 8.[59] In the case of the higher freestream Mach number, 0.9, lower optimum bypass ratios were predicted. Estimated optimum BPR

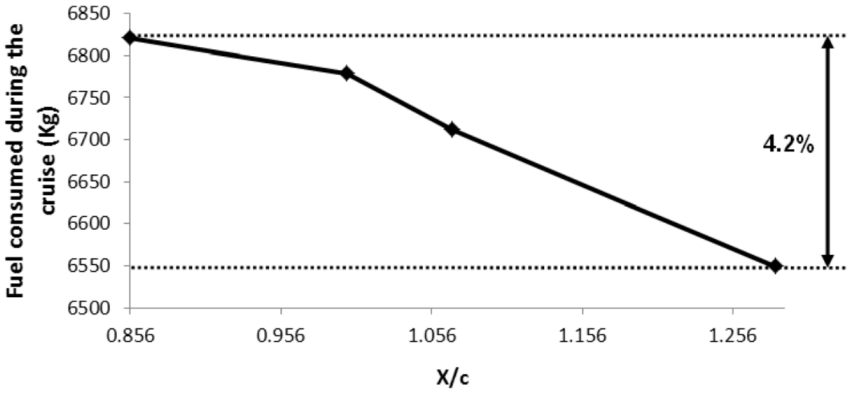

(a) Changes in cruise fuel burn as a function of horizontal installation location for the long range aircraft.[50]

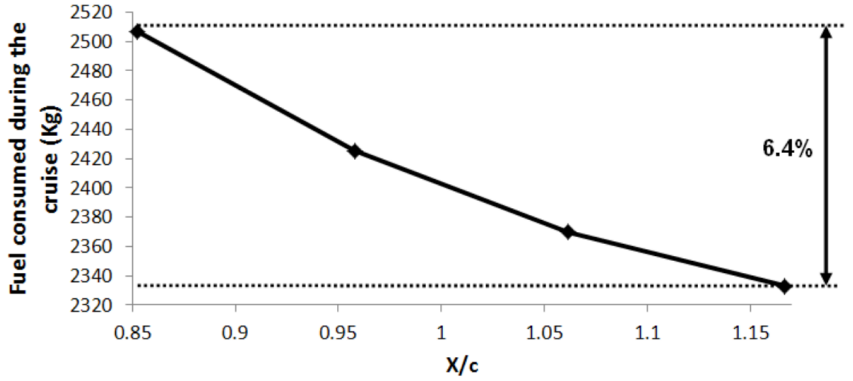

(b) Changes in cruise fuel burn as a function of horizontal installation location for the short range aircraft.[50]

FIGURE 2.22: Changes in cruise fuel burn as a function of horizontal installation location.[50] X and c are the horizontal distance from the cowl edge to the wing trailing edge and the mean aerodynamic wing chord respectively.

ranged from 4 to 5 for the lower technology level and 4 to 6 for the higher.[59]

Another aircraft-engine synthesis study[60] simulated a direct drive two-spool turbofan aero engine with PROOSIS[62]. This was linked to an aircraft model, an in house nacelle drag prediction tool based on ESDU 81024[13] and WEICO[63] an engine weight model.

Similarly it has been used as a standalone tool in a study[61] which evaluated the characteristics of a general turbofan engine and its integration in a flying-wing aircraft conceptual design. This study brought together TURBOMATCH[64] as an engine performance model,

ESDU 81024[13] as a nacelle drag assessment tool and a spreadsheet based aircraft performance model A comparison was made between a conventional engine and a geared turbofan and it was found that the nacelle drags accounts for about 3% and 4% of net thrust respectively.[61]

2.3 Thrust and drag bookkeeping

To separate forces on an aircraft into thrust and drag a bookkeeping system must be used.[65] This may be necessary due to the compartmentalisation of an aircraft design, where engine and airframe design are carried out quasi-independently. This segregation can arise with separate airframe and engine manufacturers or with distinct design teams within the same company. In both cases a robust thrust and drag bookkeeping is required. Interfaces between design team responsibilities must be explicit.[14] The accounting system must facilitate the comparison of different measurement and estimation techniques allowing actual performance to be compared to estimated performance[66] The fidelity and practicalities of the estimation method, either numerical or experimental, influences the choice of thrust drag interfaces. The bookkeeping process must also be consistent across different aircraft-engine configurations so that interference drag can be calculated.[51]

The industry standard for thrust and drag bookkeeping has been set out in a number of guides.[4,14,66] The most comprehensive reference on this topic was the result of a study set up in 1971 by Dr. J. Seddon.[14] This document sets out a thrust and drag bookkeeping system and different decompositions of net propulsive force (NPF) based on differing thrust and drag interface choices.

2.4 Drag extraction methodology

To understand engine installation effects, it is necessary to be able to quantify the effects on the parameters of interest. In conjunction with a clear and robust thrust and drag accounting system a reliable method to extract lift and drag forces must be employed. A brief review of drag extraction theory is presented in this section..

The "mid-field" drag extraction method was proposed by Van der Vooren and Slooff[67] and developed by Destarac and Tognaccini[68]. A summary of the method is given by Vos et

al..[69] This approach relies on the use of cut-off constants to define viscous and wave drag components. There is no consensus in the literature on the exact value that these sensors should take. A previous study[50] investigating installation effects for a wing-body-nacelle type configuration found that reasonable agreement could be found with experimental data by tuning these cut-off sensors. However, for different configurations different cut-off sensors were required for reasonable experimental agreement. For this reason this method was deemed not robust or reliable enough for the current research.

Drag can be found by comparing the fluid momentum ahead of the body with the momentum downstream of the body.[28] This approach is suited to experimental work where a pitot-static rake can be used to measure local static and total pressures. This approach is discussed in more detail in Appendix B. In CFD calculations two implementations of this approach can be employed. The outer edge of the wake can be defined by a percentage of total head loss. This is the approach commonly utilised in experimental programs.

Determination of the force on a body by the integration of pressure and shear forces which act upon it is known as the "Near-Field Method".[70] However forces calculated with the near-field method from a CFD calculated flow field can be inaccurate. This can be due to numerical diffusion and discretisation error.[70] [16,49–52,55,56,59–61,71]

Chapter 3

Performance modelling

The overall research aim is to develop a preliminary design framework for the assessment of powerplant aerodynamic installation effects. This framework will be used to assess the impact of nacelle size, geometry and installation on mission performance. A Propulsion System Integration Modelling (PSIMOD) framework has been developed. PSIMOD couples Cranfield University's in house engine (Turbomatch [10]) and aircraft (Hermes [11,12]) performance codes with a nacelle drag prediction model based on ESDU 81024 [13]. The ESDU drag prediction method is used to predict nacelle drag as a function of flight Reynolds number, Mach number, nacelle shape and intake MFCR. Corrections are then applied to this drag prediction to take into account nacelle local upflow effects and nacelle and propulsion system integration effects based on CFD simulations. This nacelle drag is integrated within PSIMOD in a drag build up method at each point in the flight. The development and operation of this framework will now be discussed.

3.1 Baseline method

HERMES V5B[12] is used as the baseline code. This aircraft aerodynamic and performance model can be used in conjunction with Turbomatch,[10] an engine simulation code. Typical inputs include aircraft and mission specifications as well as engine specifications (Figure 3.1). The code then outputs predicted performance of the aircraft and engine throughout the whole mission and in each segment of the mission. Hermes V5B can be run in two modes, starting with fixed fuel to calculate the maximum range and fixed range to calculate the fuel required. However neither of these are suited to the comparison of aircraft performance when different nacelle drag calculations are implemented. Of the two, the fixed range to calculate the fuel required is most suited to this task. This mode starts with a guess for fuel required, flies the mission, calculates remaining fuel and uses this as an iteration variable to converge on a flight solution where all fuel is consumed. When different nacelle drag calculation methods are implemented the aircraft flies with different drag and hence different fuel burn. This results in different take off weights for different nacelle drag calculation methods which does not allow direct comparisons to be made between methods. It was for this reason that a third mode was implemented. This mode allows for both fixed fuel and range allowing a clearer comparison of nacelle drag calculation methods and their effects to be made. This however is not a final solution as the same aircraft model flying in this mode but with different nacelle drag calculation methods will fly slightly different trajectories. For example the aircraft model with less drag will climb and reach its cruise altitude quicker. This results in it spending less time in climb and possibly, depending on the descent spending more time in cruise where the required thrust will be different. This leads to a difference in overall fuel burn and as such not all differences in fuel burn can be solely attributed to the different nacelle drag calculation method used.

The solution for this is to set fixed trajectory (Mode 4). This fixed trajectory would define, distance, altitude, velocity, acceleration, time and flight path angle at each point in the

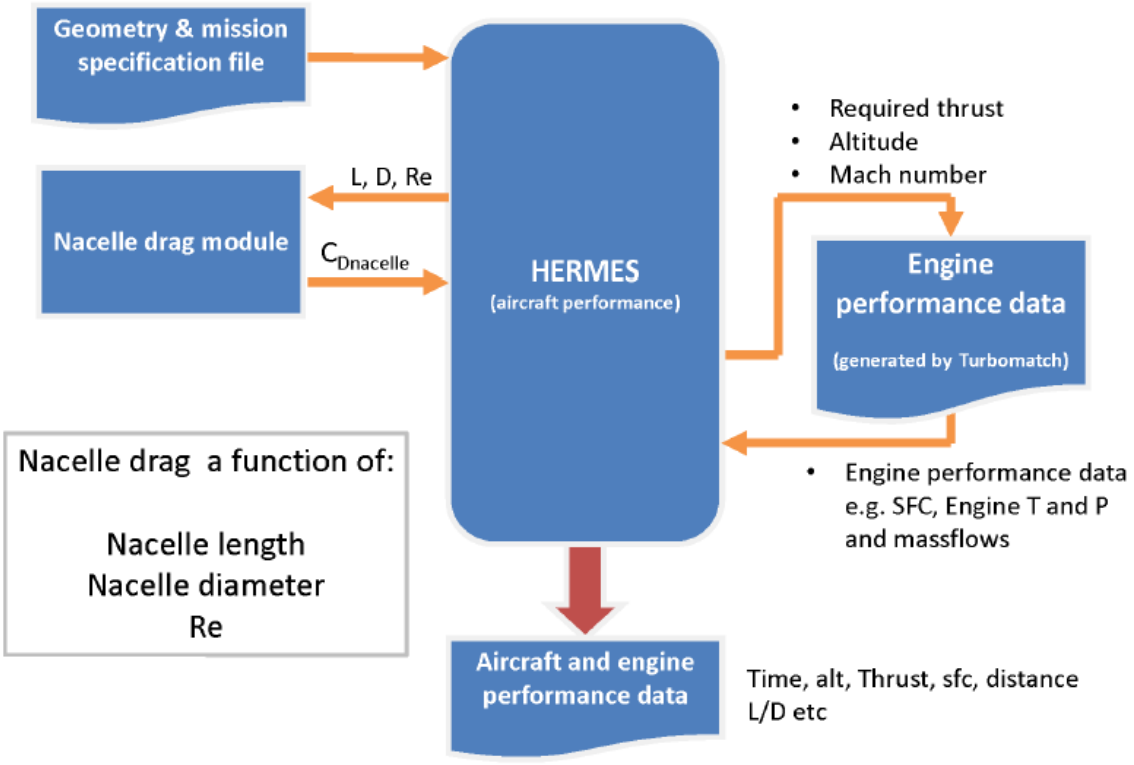

FIGURE 3.1: Overview of the baseline code[12]

mission. The point mass model outlined below, comprising six equations is commonly used to model aircraft dynamic behaviour (Equation 3.1)[72].

$$\begin{pmatrix} \dot{x} \\ \dot{y} \\ \dot{H} \\ \dot{\gamma} \\ \dot{\chi} \\ \dot{V} \end{pmatrix} = \begin{pmatrix} V\cos\gamma_{air,ang}\cos\chi_{air,ang} \\ V\cos\gamma_{air,ang}\cos\chi_{air,ang} \\ V\sin\chi_{air,ang} \\ \frac{g}{V}(n\cos\phi_{air,ang} - \cos\gamma_{air,ang}) \\ \frac{g}{V}\frac{n\sin\phi_{air,ang}}{\cos\gamma_{air,ang}} \\ \frac{T-D}{m} - g\sin\gamma_{air,ang} \end{pmatrix} \tag{3.1}$$

Where:

x, y and H are the coordinates of the aircraft centre of gravity in the Earth Axes (3.2), $\phi_{air,ang}$, $\chi_{air,ang}$ and $\gamma_{air,ang}$ are the bank, heading and flight path angles respectively defined with the same reference axes(3.2),

T and D are respectively the thrust and drag of the aircraft(3.2),

g is acceleration due to gravity,

V is the ground speed velocity ($V = \sqrt{\dot{x}^2 + \dot{y}^2 + \dot{z}^2}$).

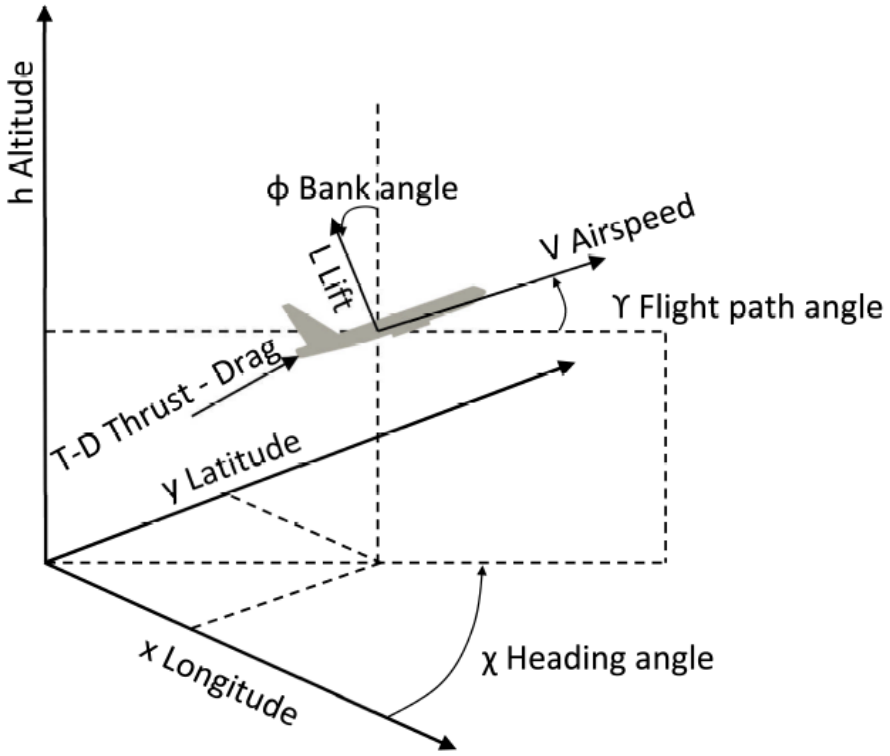

FIGURE 3.2: Point mass model angle definitions

HERMES V5B works in the cruise phase by calculating the required thrust then looking up the engine performance data provided by Turbomatch[10] and interpolating for the required engine performance parameters.[12] Taking the last equation from Equation set 3.1 and rearranging for thrust results in Equation 3.2.

$$T = m\dot{V} + mg\sin\gamma + D \tag{3.2}$$

All terms in Equation 3.2 are provided by the fixed trajectory except for thrust and drag. HERMES V5B[12] can then calculate drag allowing to then calculate the required thrust. If two identical aircraft models, with different engine installations, are then flown in this

mode their trajectories will be identical in time and space (if it is physically possible for them to do so). Effectively the thrust setting will be increased to overcome any increased drag and vice versa. This mode allows the most direct comparison of different nacelle drag calculation methods, however it is not the most realistic as it is not necessarily what a real aircraft would do. For situations where more realism is required Mode 3 (fixed fuel and range) is more appropriate.

3.1.1 Description of baseline code

3.1.1.1 Hermes-Turbomatch interaction

Hermes V5B[12] requires engine performance data. In this case this data is generated by Turbomatch.[10] The user must prepare two files for Tmatch-CallsV3.[12] The first file is an engine design point file which contains the design point of the engine and some off-design points if required (e.g. engine degradation). The second file required is the geometry, mission and engine specification file. This file acts as the main input file for both TMatchCallsV3 and HermesV5B. When all the input files are prepared TMatchCalls[12] creates the final off-design input file which is passed to Turbomatch. The Turbomatch results are then processed by TMatchCallsV3 and an engine performance data required for Hermes V5B is extracted and formatted into an engine performance data file (Figure 3.3).

3.1.1.2 Hermes V5B input files

The main input file for Hermes V5B is *GeomMissionEngineSpec.txt*. Divided into several parts this file defines the geometry and configuration of the aircraft and definitions for all flight phases.

The first section in the specification file defines the aircraft geometry and high lift systems. This is followed by a section defining the mission and weight breakdown of the

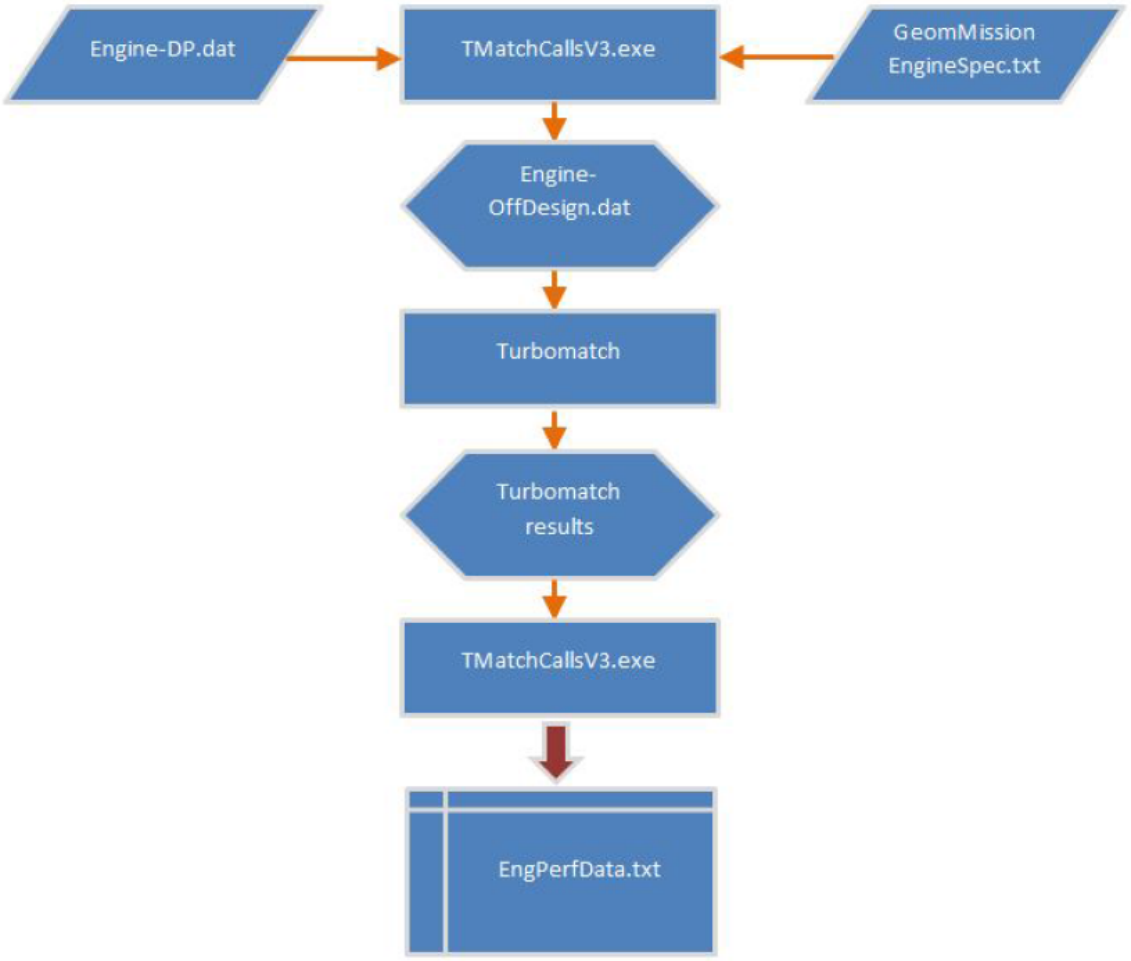

FIGURE 3.3: Operating procedure for TMatchCallsV3 [12]

aircraft. Then the flight profile is defined in three sections, the cruise climb and descent phases (Figures 3.4, 3.5 and 3.6). Multiple cruise altitudes can be specified to create a stepped cruise profile. Hermes V5B then automatically selects the altitude with the highest aerodynamic efficiency.

The climb phase is split into segments. For each segment the user must specify the altitude, temperature deviation from ISA, the equivalent airspeed and the power setting of the engine.

The descent phase is defined identically to the climb phase except that the altitude of each segment is calculated by the code. This is because the last cruise altitude is not known

```
!CRUISE MAIN/DIVERSION AND HOLDING DATA
1              ! number of cruise altitudes and Mach numbers
1              ! number of cruise Temperature Deviations from ISA day
1              ! number of diversion cruise altitudes
5.             ! Cruise small segment time Interval in (min).
10668.         ! Cruise altitudes in [m] (WARNING: THE ALTITUDES CANNOT BE THE SAME!!!!!!!!!!)
0.81           ! Cruise Mach numbers, the same number with cruise altitudes
0.             ! Cruise ambient temperature deviation from ISA, in [K]
6096.          ! Diversion cruise altitudes (m)
0.65           ! Diversion cruise Mach numbers,
0.             ! Diversion cruise ambient temperature deviation from ISA, in [K]
457.0          ! Holding altitude (m)
30.            ! Hold Time in (min)
```

FIGURE 3.4: Cruise specifications in GeomMissionEngineSpec.txt

before the calculation if the user has specified multiple cruise altitudes.

```
!CLIMB DATA
22                ! Climb segments Number
! Altitudes(m)        | DTisa(K) | EAS(knots) | Power(0.-1.)
557.20 0. 250. 1.
900.00 0. 250. 1.
1500.00 0. 250. 1.
1981.20 0. 250. 1.
2438.40 0. 250. 1.
2743.20 0. 250. 1.
3048.00 0. 250. 1.
3048.10 0. 320. 1.
3657.60 0. 320. 1.
4267.20 0. 320. 1.
4876.80 0. 320. 1.
5486.40 0. 320. 1.
6096.00 0. 320. 1.
7620.00 0. 320. 1.
8077.20 0. 320. 1.
9144.00 0. 320. 1.
10058.00 0. 320. 1.
10668.00 0. 320. 1.
11227.00 0. 320. 1.
11887.00 0. 320. 1.
12000.00 0. 320. 1.
12496.8 0. 320. 1.
```

FIGURE 3.5: Climb specifications in GeomMissionEngineSpec.txt

3.1.1.3 HERMES V5B output files

Hermes V5B[12] outputs three files, a log file and aircraft and engine performance files.

```
!DESCENT DATA
10                ! Descent segments Number
! The altitudes are dependant on the final cruise altitude.They are calculated by the code.
! DTisa(K)        | TAS(knots) | Power(0.-1.) *The last 3 power settings use the Approach rating
0. 233.1 0.3                                 ! Flight Idle Rating
0. 221.5 0.3                                 ! Flight Idle Rating
0. 202.9 0.3                                 ! Flight Idle Rating
0. 195.0 0.3                                 ! Flight Idle Rating
0. 183.1 0.3                                 ! Flight Idle Rating
0. 164.7 0.3                                 ! Flight Idle Rating
0. 150.9 0.3                                 ! Flight Idle Rating
0. 140.0 0.3                                 ! Approach Rating
0. 135.0 0.3                                 ! Approach Rating
0. 135.0 0.3                                 ! Approach Rating
```

FIGURE 3.6: Descent specifications in GeomMissionEngineSpec.txt

Engine performance output file

The engine performance file contains engine performance data throughout mission. This file contains the operating conditions of the engine (altitude, temperature deviation and Mach number) as well as thrust and additional engine performance data. Specific fuel consumption and temperature, pressure and mass flow at various engine stations are included in this data.

Aircraft performance output file

The aircraft performance file contains performance information for the whole flight and for each segment. It describes the performance of the integrated aircraft-engine. For each segment parameters such as distance, time, aerodynamic performance and fuel consumed are output. The complete mission is described in terms total fuel consumption, distance covered and flight duration.

3.1.1.4 Description of HERMES V5B nacelle drag calculation

The nacelle drag calculation utilised in HERMES V5B [12] is a simple equivalent flat plate skin friction estimate. Profile drag and interference drag are accounted for using a form factor. Flat-plate skin friction depends on the type of flow over the surface, laminar or turbulent. In HERMES V5B a turbulent flow assumption has been made. As such the flat plate skin friction coefficient is:

$$C_{fn} = \frac{0.455}{\log_{10} Re_{Lnac}(1 + 0.14M^2)^{0.65}} \tag{3.3}$$

Where:

Re_n is the Reynolds number based on overall nacelle length as given in Equation 3.4

$$Re_{Lnac} = \frac{UL_{nac}}{\nu_\infty} \tag{3.4}$$

Nacelle drag is then given by:

$$D_{nac} = C_{fn} F_n (S_{wet}) \tag{3.5}$$

Where:

S_{wet} is the nacelle wetted area and

F_n is the form factor

3.2 ESDU 810024 drag estimation method

As part of this research the skin friction drag estimate used by HERMES needed to be updated. It was decided base the replacement module on an ESDU drag estimation methodology[13] which will now be discussed.

3.2.1 The ESDU drag calculation method

ESDU 81024 is a procedure for estimating the drag of axisymmetric cowls with sharp trailing-edges at zero incidence and at subsonic free-stream Mach numbers[13]. The nacelle geometry is separated into three sections a forebody, cylindrical midbody and afterbody, however a midbody is not essential (Figure 3.7). The application procedure is outlined in Figure 3.8. The method is based on series of nacelle windtunnel experiments[28,73–85] using empirical form factors to estimate profile spillage and wave drag.

3.2.2 The limitations of the ESDU drag calculation method

ESDU 81024 is limited to axisymmetric nacelles at zero incidence. This situation however is very rare[49]. The Reynolds number range is limited to $10^6 < Re_{D_{max}/L_{nac}} < 3 \times 10^6$. When the initial forebody radius is different to that of the equivalent NACA-1 series forebody the method is restricted to a maximum Mach number of 0.6.

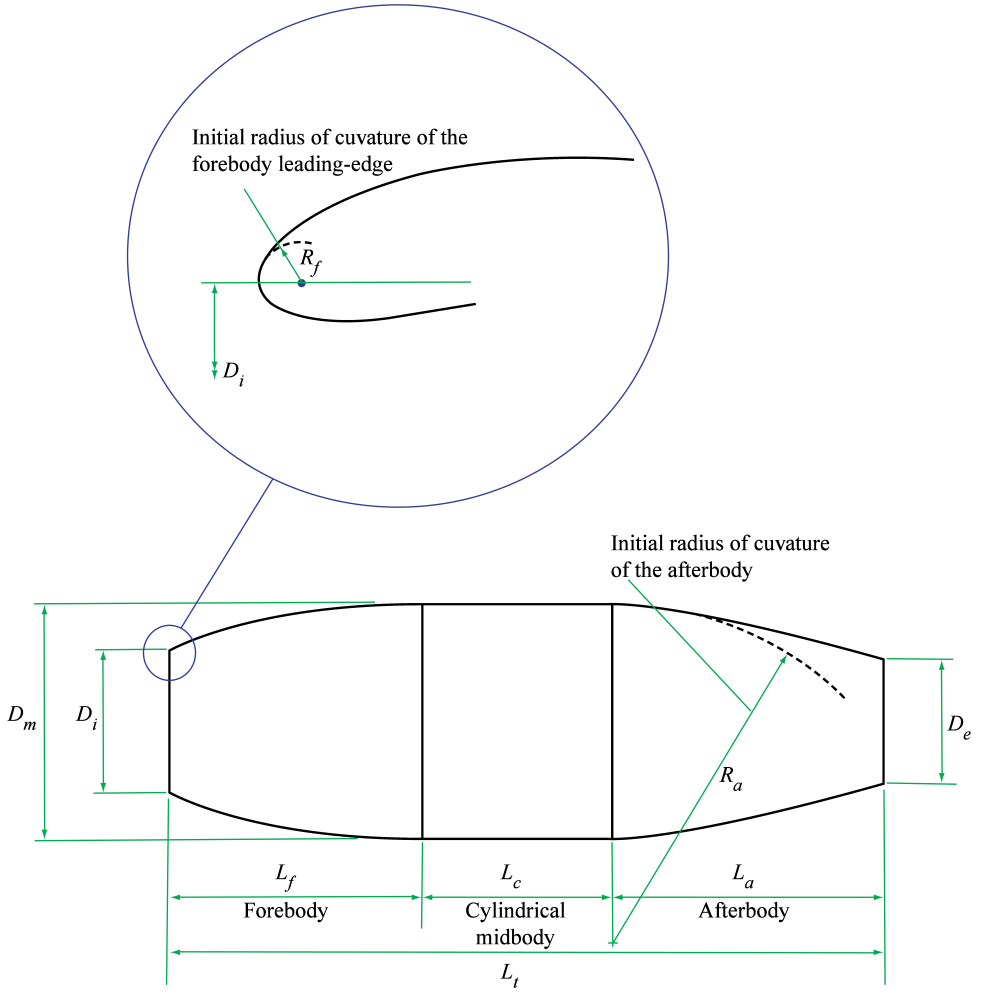

FIGURE 3.7: ESDU definition of nacelle geometry [13]

3.2.3 What does the ESDU method calculate?

The ESDU drag estimation method [13] complies with the thrust and drag accounting system used across this project. The method makes the assumption that the jet efflux is pressure matched and as such the post-exit streamtube force is zero. Drag calculated using this method therefore comprises the pre-entry streamtube force and the profile drag on the nacelle surface bounded the pre-entry streamtube and the nacelle trailing edge. This

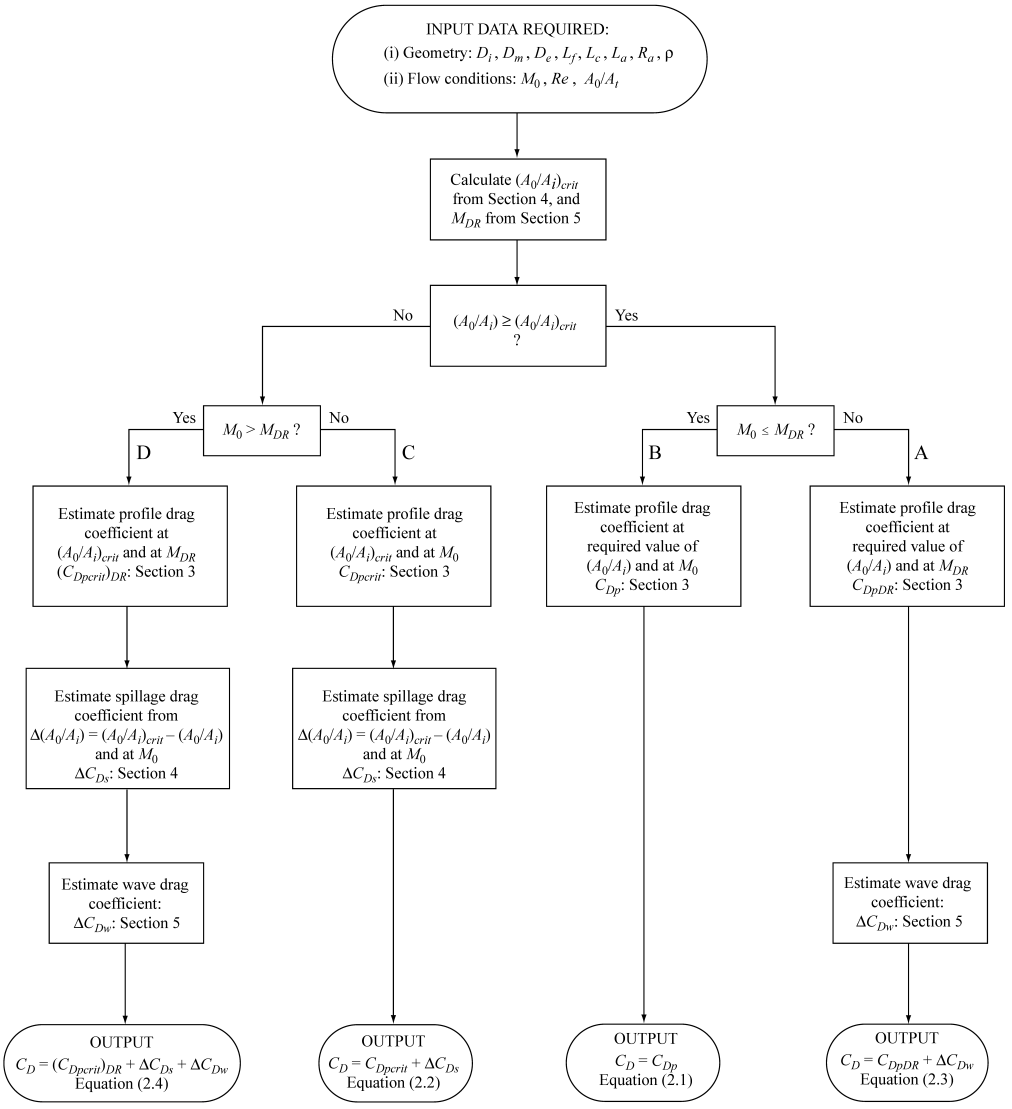

Note: (i) Path A is the high-speed case with wave drag.
(ii) Path B is the moderate-speed case without spillage or wave drag.
(iii) Path C is the low-speed case with spillage drag.
(iv) Path D is the unlikely case of high-speed with both wave and spillage drags.

FIGURE 3.8: ESDU 81024 application procedure[13]

neglection of the post-exit streamtube force is common practice in experimental investigations due to the difficulty in its quantification caused by its entrainment by the external flow. In practice the post-exit streamtube force is not usually equal to zero.

3.2.4 Validation and accuracy of the ESDU drag calculation method

"ESDU 81024 Drag of axisymmetric cowls at zero incidence for subsonic Mach numbers" [13] is the open literature standard for the calculation of nacelle drag at zero incidence.[71] It has been used extensively as part of engine performance analysis assessments.[59–61] Previously it has been incorporated into "in-house" codes and used to evaluate optimum engine bypass ratios[59] and the impact of engine aerodynamic losses on overall mission performance.[60] Similarly it has been used as a standalone tool in a study which evaluated the characteristics of a general turbofan engine and its integration in a flying-wing aircraft conceptual design.[61] The ESDU 81024 method nacelle drag estimation approach has also been used to calculate nacelle profile drag in a substantial aircraft-engine conceptual design study.[55] Another study used it as a tool against which to assess the accuracy of CFD estimations of nacelle drag.[49]

There is no single figure for the accuracy of nacelle drag coefficients estimated using the ESDU 81024 method because of the differing characteristics of the various drag components. Profile drag predictions are estimated to be accurate to within approximately 8%. Spillage drag estimations have an error figure of 25% while wave drag has an error figure of 20%.[13] To assess the accuracy of the ESDU nacelle drag prediction method as it is applied within the PSIMOD frame a comparison has been made with experimental data (Figure 3.9). As discussed in § 2.1.1.1 experiments have been carried out at which focus on flow development over the nacelle exterior flow.[28] Tests were carried out at Mach numbers ranging from 0.4 to 0.95 to capture both subsonic and transonic flow regimes. To test the ability of the ESDU method[13] to capture the drag rise characteristics of a nacelle, variation of drag calculated with Mach number, at a MFCR=0.7, has been compared to experimental data.[28] Data is presented in terms of aircraft drag counts calculated using the CRM nacelle and wing areas to put the accuracy of the predicted drag in context. The maximum difference occurred at MFCR=0.7 where nacelle drag was over-predicted

by the ESDU method by 0.8 aircraft drag counts. On average the difference between the empirical method and the experimental results was 0.5 aircraft drag counts.

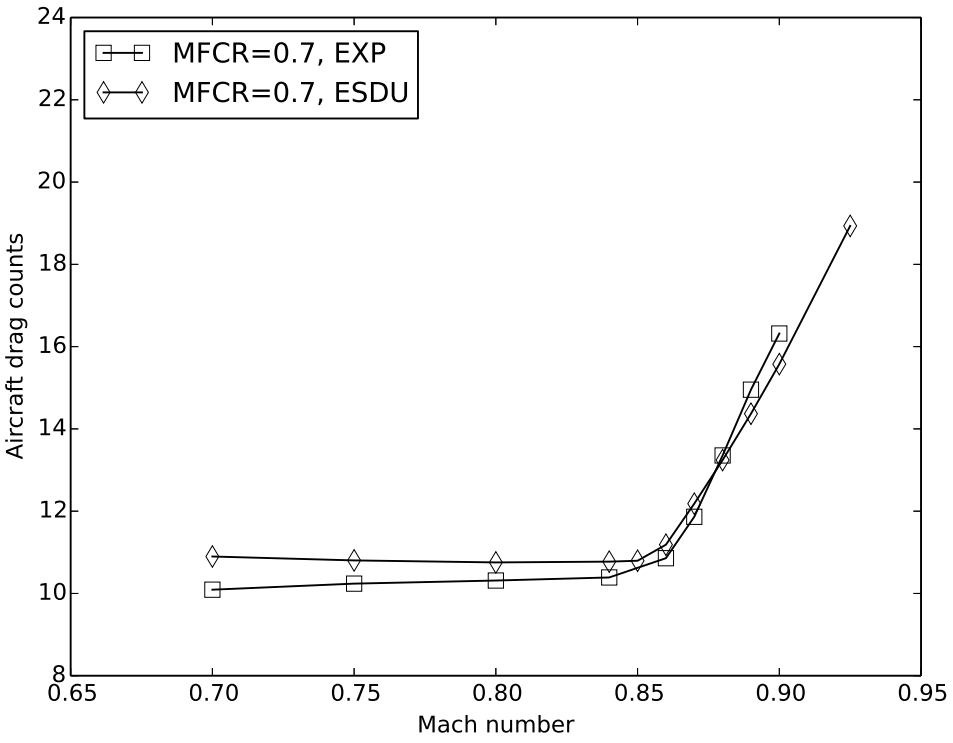

FIGURE 3.9: Variation of drag calculated by the ESDU method[13] with Mach number for the ARA Cowl 1 compared to experimental data[28]. Aircraft drag counts calculated using the CRM nacelle and wing areas. Variation of $C_{D,nac\,max}$ with Mach number at MFCR=0.7

3.3 PSIMOD

3.3.1 Nacelle drag prediction

PSIMOD integrates the ESDU method[13] into HERMES V5B's architecture.[12] This is achieved by replacing the nacelle drag module in the baseline code (Figure 3.10) with a modified nacelle drag module (Figure 3.11). This alteration means that nacelle drag is now a function of engine geometry, flight conditions and mass flow capture ratio (MFCR). This dependency of drag on MFCR introduces an added complexity. Nacelle drag is dependent

on engine mass flow, which is dependent on thrust, but the assumption is that thrust is equal to drag in the cruise condition. This complexity is overcome by an iteration carried out on thrust. An initial guess is made for thrust. The MFCR associated with this thrust and the current flight conditions is calculated. Drag is then calculated using this MFCR. Thrust is then set equal to this new drag and used as the second guess. This iteration is carried out until the thrust guess equals the new drag.

The ESDU method is only available in a compiled executable which is controlled with an input file. The modified drag module prepares this input file and passes it to the ESDU executable. The output from the ESDU executable (a text file) is then processed by a Perl script. This script extracts the required drag coefficient from the text file and formats it into a format readable by the modified drag module. The rest of the calculation is carried out identically to the baseline code.

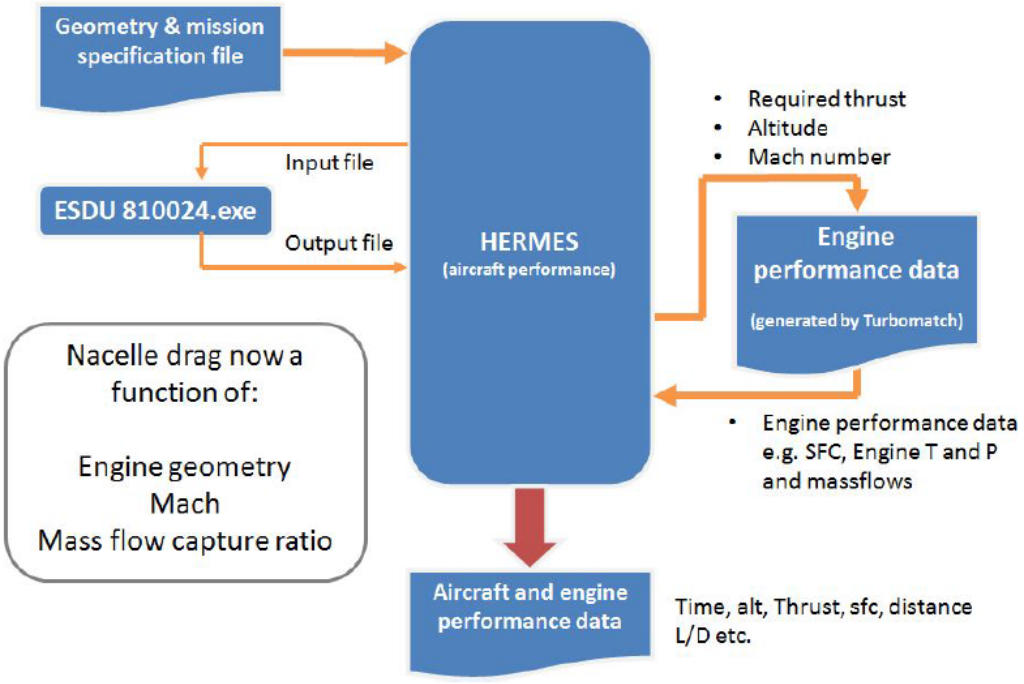

FIGURE 3.10: Overview of PSIMOD

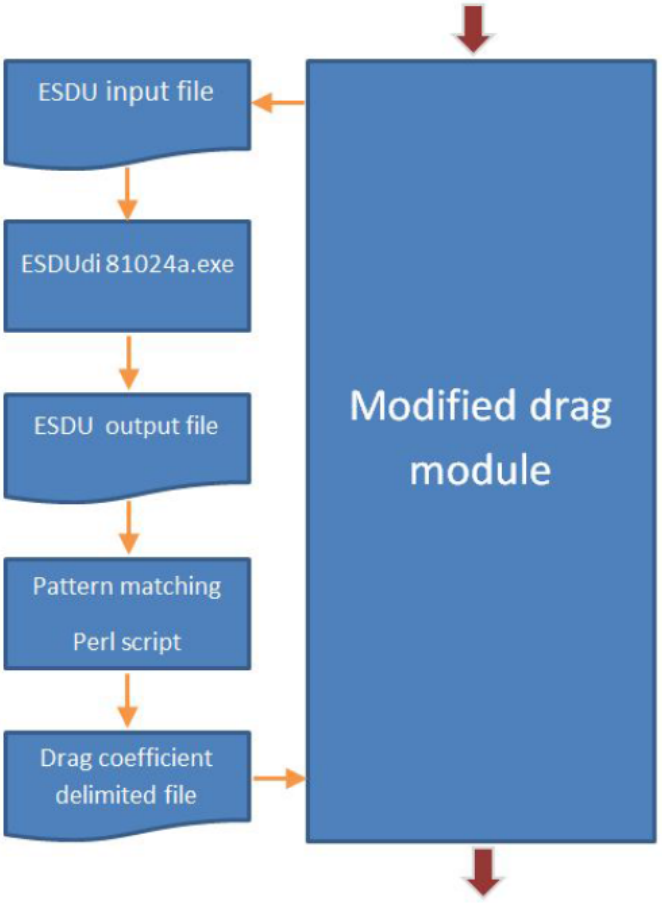

FIGURE 3.11: Overview of the modified nacelle drag module in PSIMOD

3.3.2 Modelling nacelle incidence

Up to this point all nacelle drag prediction methods have neglected the influence of angle of attack. This section describes a method whereby these effects can be taken into account. Firstly for clarity, aircraft and engine angle nomenclature will be defined.

3.3.2.1 Angle definitions

Aircraft angles

The standard definitions of the primary aircraft angles are used. The pitch angle (θ) is the angle of the thrust vector (and the aircraft longitudinal axis) to the horizontal while the flight path angle (γ) is the angle of the velocity vector to the horizontal. The angle of attack (α) is then the difference between these two angles (Figure 3.12).

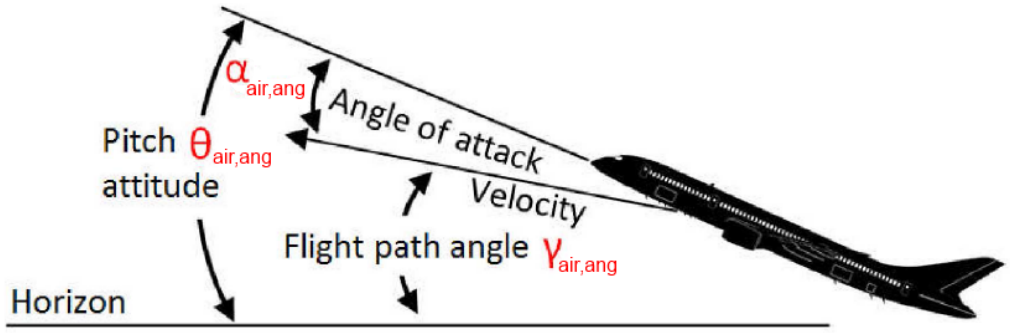

FIGURE 3.12: Definition of aircraft angles

Engine angles

The definition of the engine angles used in this report are outlined in Figure 3.13. The total upflow angle (A) is the angle from the direction of local relative velocity to the nacelle centreline axis. α_w is the wing angle of attack and in this study is assumed to be equal to the aircraft angle of attack (α). ϵ denotes the angle of upwash measured from the direction of local relative velocity. Finally nacelle inclination (γ_n) is the angle from the wing chord line to the nacelle longitudinal axis.

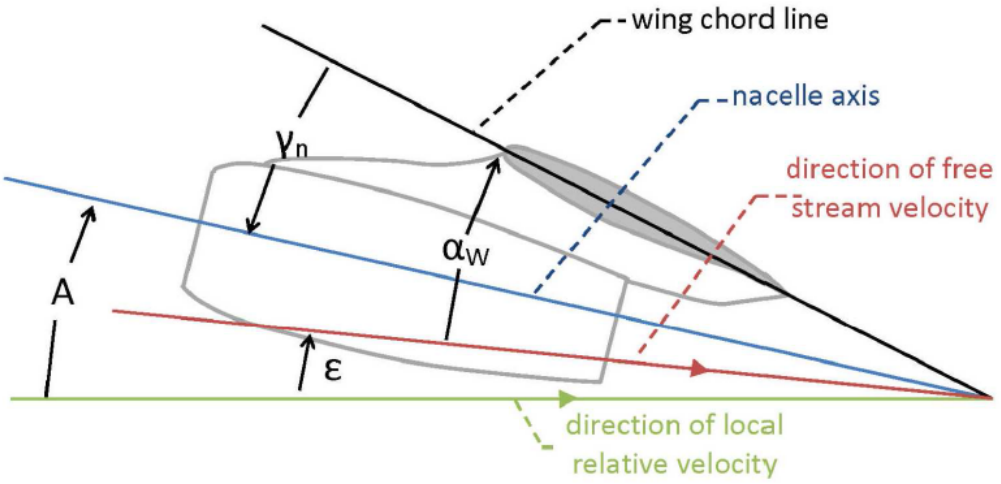

FIGURE 3.13: Definition of engine angles

3.3.3 Correction for incidence

The effects of nacelle incidence are taken into account through modifications made to the nacelle drag module. These modifications are outlined in Figure 3.14.

PSIMOD V2 (Figure 3.14) works the same as PSIMOD where nacelle drag is calculated using the ESDU method. The difference between the codes is that there is then a modification to this ESDU predicted drag in order to model the effects of angle of attack. Firstly as HERMES never directly deals in angle of attack, a method had to be developed to work this out. HERMES calculates aircraft C_L so if the relationship between C_L and α can be quantified, α can be found. This relationship was modelled using DATCOM[86] (further information can be found in Section 3.3.3.1). Now that α is known the next step is to translate this into A the total engine upflow angle. As seen in Figure 3.13 this is the sum of α_w and γ_n. Both α_w and γ_n are known so it is only left to quantify ϵ. The relationship between α and ϵ was found using JAVAFOIL.[87] Now the total engine upflow angle is known. Isolated nacelle CFD studies then give correlations between A and C_L and between A and C_{di}. This finally allows the nacelle drag coefficient taking into account the effects of nacelle incidence to be calculated using Equation 3.6.

$$C_{Deng} = C_{D0eng} + (C_{Dieng})(C_{Leng})^2 \tag{3.6}$$

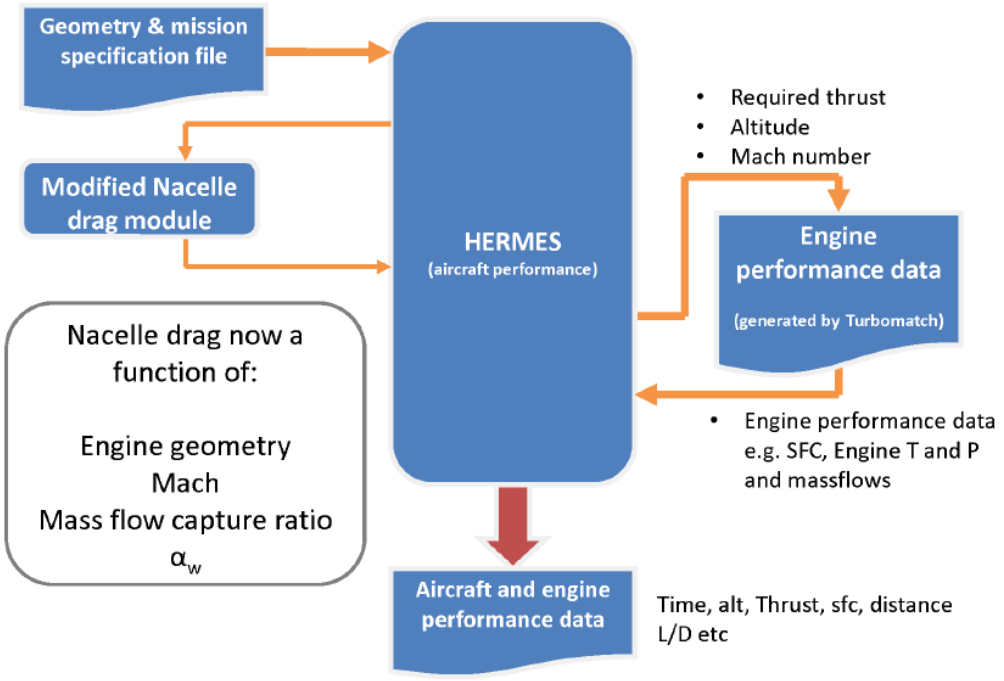

FIGURE 3.14: Overview of PSIMOD V2

3.3.3.1 DATCOM

DATCOM[86] is an aircraft design and performance tool based on semi-empirical methods. It can deal with subsonic, supersonic, hypersonic, transonic flight conditions. It can model a variety of aircraft configurations including symmetric fuselage, wing, vertical and horizontal tailbconfigurations. Twin vertical tails can also be modelled but for subsonic speeds only. A large range oateral control surfaces can be modelled. However no directional control surfaces can be simulated. Ground effect can also be taken into consideration.

Basic DATCOM outputs

An extract from a DATCOM[86] output file is shown in Figure 3.16. Available parameters can include aerodynamic force and moment coefficients as well as their derivatives.

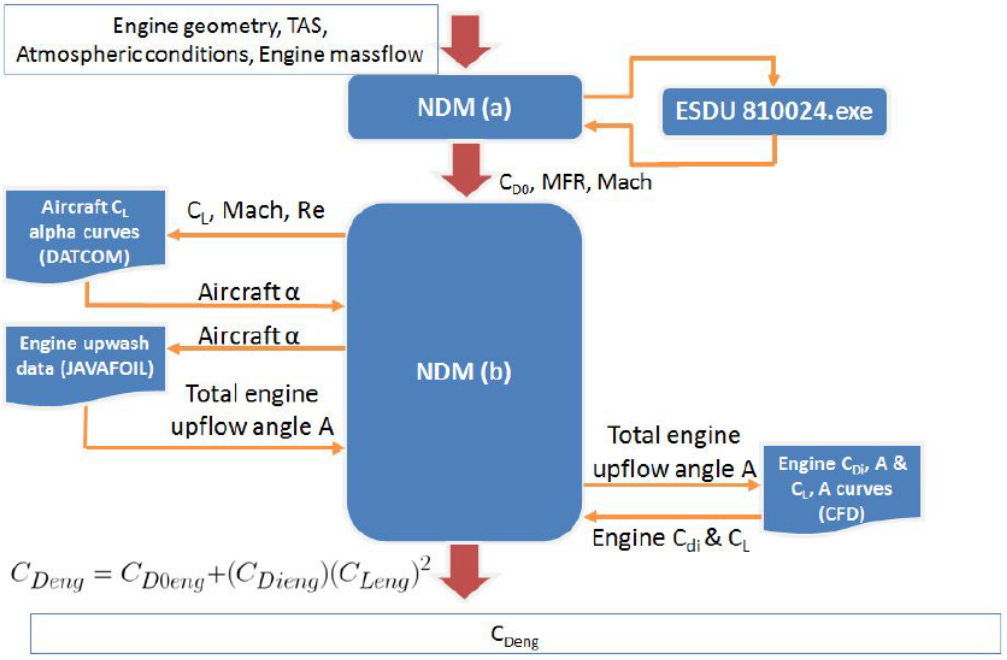

FIGURE 3.15: Nacelle drag module modified to take into account nacelle angle of attack

ALPHA	CD	CL	CM	CN	CA	XCP
-6.0	.024	-.377	.3209	-.378	-.015	-.850
-5.0	.021	-.291	.2821	-.292	-.004	-.968
-4.0	.019	-.205	.2441	-.206	.005	-1.186
-3.0	.018	-.121	.2071	-.121	.012	-1.706
-2.0	.017	-.037	.1704	-.038	.016	-4.482
-1.0	.017	.045	.1344	.045	.018	2.994
.0	.018	.129	.0975	.129	.018	.757

FIGURE 3.16: Extract from DATCOM ouptut file

3.3.3.2 Javafoil

JavaFoil[87] is a potential flow solver. It is based on a linear varying vorticity distribution panel method.[87] The tool is limited by the fact that it cannot model flow separation or laminar separation bubbles. Therefore results are inaccurate for flow-fields which contain these phenomenon. The boundary layer model used by JAVAFOIL is uncoupled.

Wing section choice

The NASA Common Research Model (CRM[34]) was chosen as the aircraft from which to extract a realistic wing section as it is based on a transonic transport configuration and highly detailed geometry was freely available. The wing taken in-line with engine centreline (Figure 3.17).

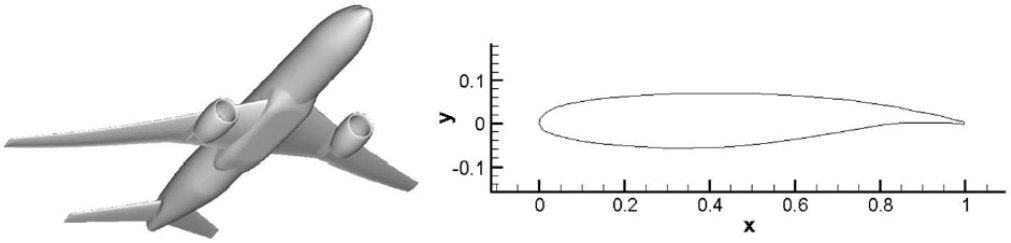

FIGURE 3.17: Wing section choice

Javafoil results

This wing section was then modelled in JavaFoil[87] (example in Figure 3.18). These results were then imported into Tecplot (example in Figure 3.19). This allowed the velocity vector at the centre of the engine highlight area to be extracted. This point was defined from the CRM geometry. This analysis was repeated for a series of α_w allowing Upwash angle (ϵ) and nacelle up flow angle (A) as a function of wing angle of attack to be found (Figure 3.20).

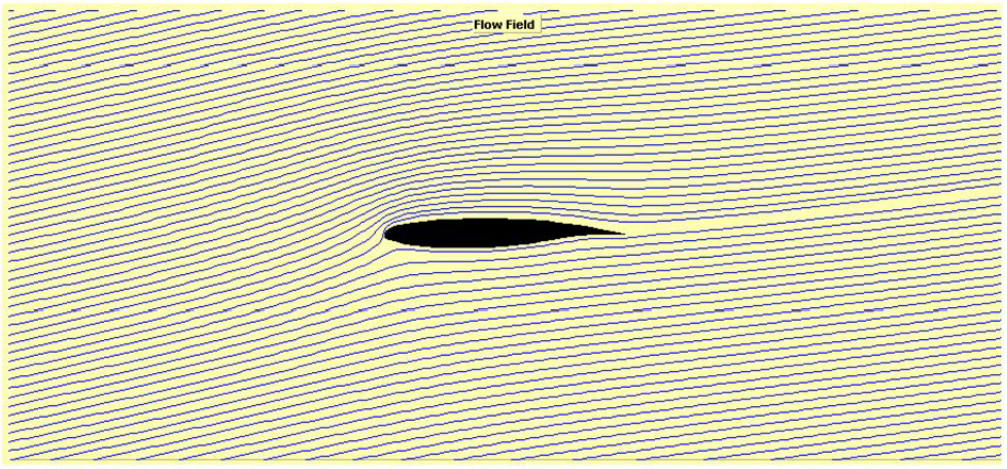

FIGURE 3.18: Example JavaFoil[87] flow field

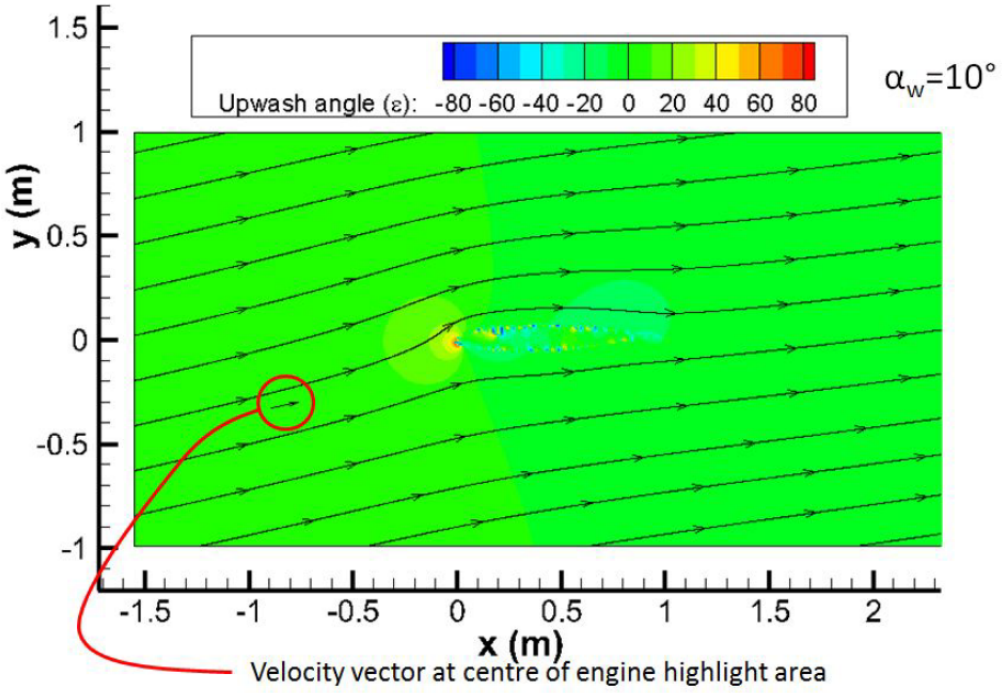

FIGURE 3.19: Example JavaFoil flow field imported into Tecplot, showing interrogation point

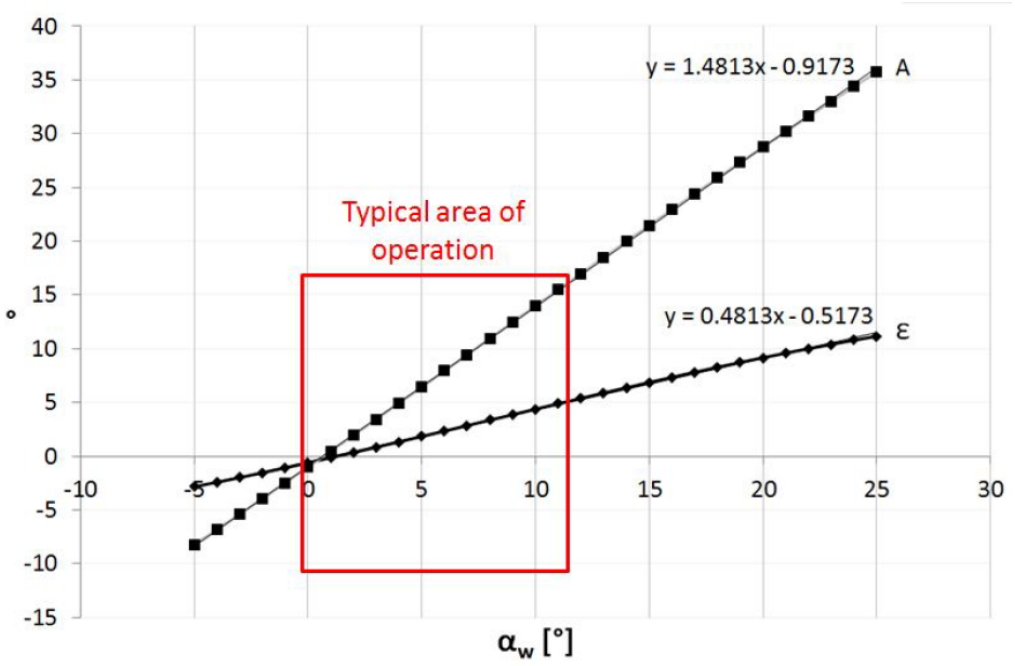

FIGURE 3.20: Upwash angle (ϵ) and nacelle upflow angle (A) as a function of wing angle of attack

3.3.4 Correction for installation effects

Increasing the by-pass ratio (BPR) of engines is key to improving their propulsive efficiency. This leads to larger diameter nacelles which are expected to have a stronger effect on engine-airframe integration. There is a risk that performance gains from increased BPR could be lost due to this interference. It is therefore essential that these effects be quantified. A module is integrated into the HERMES architecture to take these effects into account. An overview of this architecture is provided in Figure 3.21. Nacelle drag is now a function of engine geometry, flight conditions, MFCR, α_w and installation location. The installation drag module takes the form of a series of correlations extracted from CFD work.

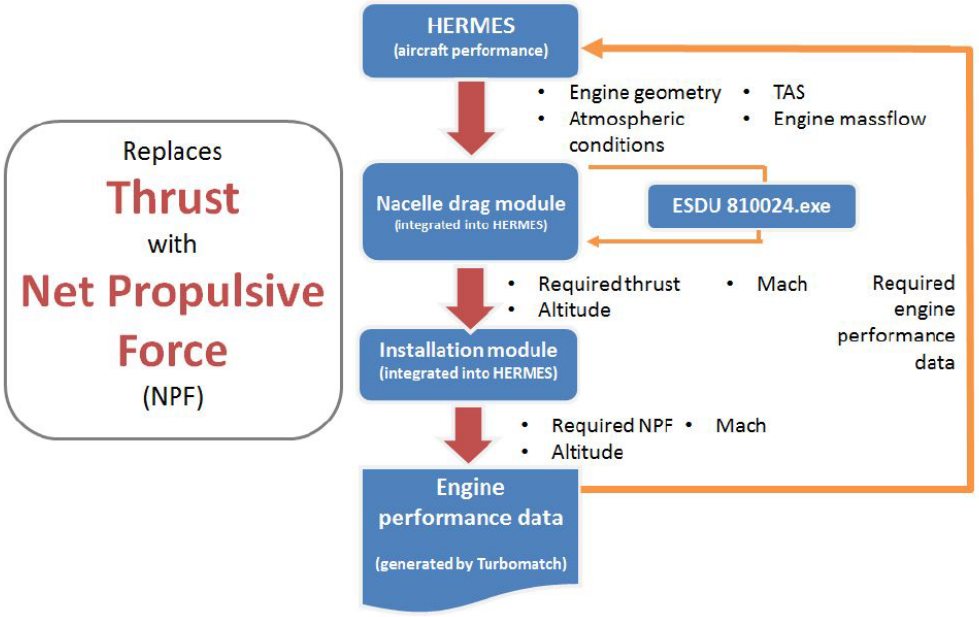

FIGURE 3.21: The integration of a nacelle interference module into the HERMES architecture

Chapter 4

Numerical Methodology

A short description of the numerical methodologies employed in this research will now be discussed. Section 4.2 to 4.4 discuss CFD related methodologies. Subsequently nacelle geometry generation (4.5) and drag extraction (4.6.1) methodologies are described.

4.1 Meshing approach

All meshes used in this thesis were created with the commercial meshing software ICEM CFD.[88] The grid structure is of a multi-block structured type. The grids consist exclusively of hexahedrons. For the isolated through ow nacelles an o-grid surrounds the nacelle. When the nacelle is powered or is mounted on a sting a c-grid structure was used. The first cell height was set to ensure a $Y+ < 1$. Further details of the gridding approach are given for each configuration simulated in Chapters 5 and 7.

4.2 Solver

CFX[89] uses an unstructured finite-element-based volume method using shape functions to describe a variable changes across each element. All solution variables are stored at the nodes. A control volume is constructed around each mesh node. Mass and momentum are conserved over each control volume.[90] The rationale behind CFX as the flow solver of choice and a summary of some problems encountered and their solutions is provided in Appendix C.

4.3 Turbulence model

4.3.1 Shear-stress transport model

The shear-stress $k-\omega$ turbulence model (SST) was developed in 1994.[91] The SST model combines two other turbulence models: the $k-\epsilon$ model and the $k-\omega$ model. Flowfields which feature regions of moderate adverse pressure gradients close to solid surfaces are better modelled with the $k-\omega$ model as opposed to the $k-\epsilon$. However of the two models, the $k-\epsilon$ turbulence model better approximates the development of turbulent boundary layers up to the point of separation. These two turbulence models are blended together in the SST model. In the vicinity of solid surfaces $k-\omega$ is used while away from solid surfaces the $k-\epsilon$ is employed.[91] This ensures that the SST model is appropriate for a wide range of flow problems including flowfields which feature pressure gradient induced flow separations and full aircraft simulations.

4.4 Error and uncertainty in CFD calculations

In the context of CFD calculations uncertainty is defined as inadequacies in the calculation due to a lack of knowledge.[92] All other calculation deficiencies are termed errors.[92]

Common CFD uncertainties can include geometrical inaccuracies due either to simplification or a lack of knowledge. Uncertainties in flow modelling can arise from simplifications such as a steady flow assumption or turbulence modelling. Errors associated with CFD calculations can include numerical errors and human error.[92] The treatment of iterative convergence and grid convergence, which are both sources of numerical error is discussed in §4.4.1 and §4.4.2. For the CFD calculations carried out in this thesis all other errors and uncertainties were considered to be negligible.

4.4.1 Iterative convergence

Levels of iterative convergence were assessed throughout this work by monitoring the standard CFX[89] residuals and the forces acting upon all walls throughout the calculation.

4.4.2 Grid convergence

For each CFD configuration mesh independence was assesed by a grid convergence study. The methodology used in these studies is presented below. Grid convergence study results are discussed in 5.2.5 and 7.4.

The normal and axial forces acting upon all surfaces (C_Z and C_X) were the parameters selected for these studies. For every grid convergence study a grid refinement ratio (r, Equation 4.1) of 2 was used.

$$r = \frac{N_{g=1}}{N_{g=2}} \tag{4.1}$$

Where N is the number of cells in a mesh and g is the level of refinement.

$$p_{con} = \frac{\ln\left(\frac{C_{X,g=4} - C_{X,g=2}}{C_{X,g=2} - C_{X,g=1}}\right)}{\ln r} \tag{4.2}$$

The magnitude of the force coefficients for a mesh with infinitesimal spacing (g=0) were calculated using Richardsons Extrapolation.[93]

$$C_{X,g=0} \cong C_{X,g=1} + \frac{C_{X,g=1} - C_{X,g=2}}{r^{p_{con}} - 1} \tag{4.3}$$

The Grid Convergence Index (GCI) could then be calculated for each force coefficient using Equation 4.4.[93] As the mesh was refined three times a factor of safety (F_s) was applied.[93]

$$GCI_{g=1,2} = \frac{F_s \left| \frac{C_{X,g=1} - C_{X,g=2}}{C_{X,g=1}} \right|}{r^{p_{con}} - 1} \tag{4.4}$$

$$GCI_{g=2,4} = \frac{F_s \left| \frac{C_{X,g=2} - C_{X,g=4}}{C_{X,g=2}} \right|}{r^{p_{con}} - 1} \tag{4.5}$$

If the calculated GCIs satisfy Equation 4.6 then the solutions can be deemed to lie in the asymptotic range.

$$AR \cong \frac{GCI_{g=2,4}}{GCI_{g=1,2} r^{p_{con}}} \cong 1 \tag{4.6}$$

4.5 Nacelle geometry generation

One of the main tasks of this research was the assessment of nacelle installation effects with changes in nacelle size. To achieve this task it was essential to be able to generate representative nacelle geometries. An Excel based tool was developed by the Author during this research based on nacelle design rules from the open-source literature.[94] Given some basic information about the engine cycle and some engine hard-points, a representative spinner, intake and fan cowl afterbody is constructed. This tool is discussed in § 4.5.1.

This Excel based tool was used as a proof of concept in the initial stages of this project. The tool has been further developed by a fellow PhD student into Cranfield University's Geometric Engine Modeller (GEM)[95]. This update allows allows the generation of profiles

which are more representative of modern transonic nacelles using Class Shape Transformation (CST) curves. CST parameteristaion will be discussed in § 4.5.2. GEM has been used to create the parametric nacelle geometries used in Chapters 5 and 7.

4.5.1 Excel based nacelle geometry definition tool

An engine conceptual design study was carried out on a blended wing body (BWB) cargo freighter (Figure 4.1) by NASA[96]. Two configurations were designed, a podded design (N2A) and an embedded design (N2B). The N2A was proposed for a 2020 timeframe as its design was considered lower risk. This engine has been chosen for simulation as it is representative of a realistic future design. The general cycle characteristics and internal geometric design (Figure 4.2) has been completed[96]. However the nacelle shape has not been fully designed. The following sections shows how the nacelle was designed.

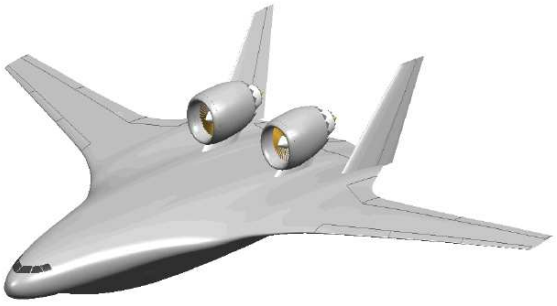

FIGURE 4.1: The NASA N2A BWB aircraft with podded nacelles[96]

4.5.1.1 Nacelle geometry generation

Initial calculations were performed in Microsoft Excel. Parametric equations were used to define the geometry completely to allow changes to be easily made. These parametric equations were then used to model the engine in Pro Engineer[97] (Figure 4.5). This model was also completely defined by parametric equations so if a parameter such as nacelle maximum diameter was changed the whole model would be automatically updated. This

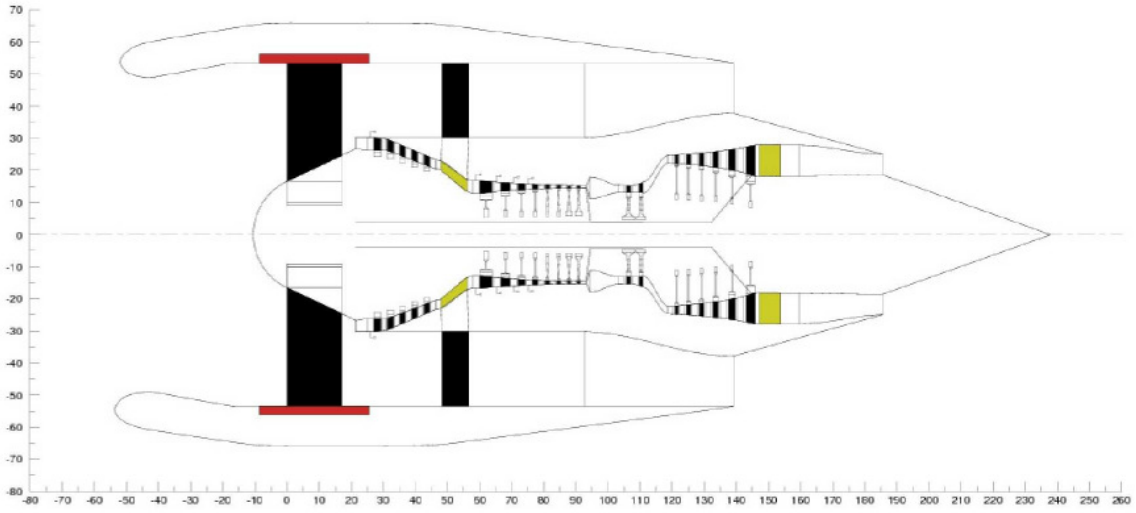

FIGURE 4.2: FPR 1.6 podded engine internal layout (dimensions in inches) [96]

Pro Engineer model was then exported as a parasolid to ICEM CFD [88] were the geometry could be meshed. This workflow pattern is illustrated in Figure 4.3. The nacelle geometry is divided into sections as defined in Figure 4.4. The fan front face, bypass duct inlet, core duct inlet and plug are constructed from straight lines and are completely defined by Table 4.1. The methods by which the remaining nacelle geometry were defined are described in the following sections.

Engine points	L_{axial}	L_{radial}	Units
Fan Front Face Inner	1.3240	0.4200	m
Fan Front Face Outer	1.3240	1.3510	m
Highlight Radius	0.0000	1.3610	m
Nacelle Max Radius	1.7940	1.6680	m
Nacelle Trailing Edge	4.8607	1.3498	m
Fan Back Face Inner	3.6773	0.7678	m
Fan Back Face Outer	3.6773	1.3502	m
Hot Afterbody Trailing Edge	6.0369	0.6329	m
Core Duct Inlet Inner	5.3791	0.4584	m
Core Duct Inlet Outer	5.3791	0.7091	m
Engine length	7.3653	0.0000	m

TABLE 4.1: Engine geometrical constraints

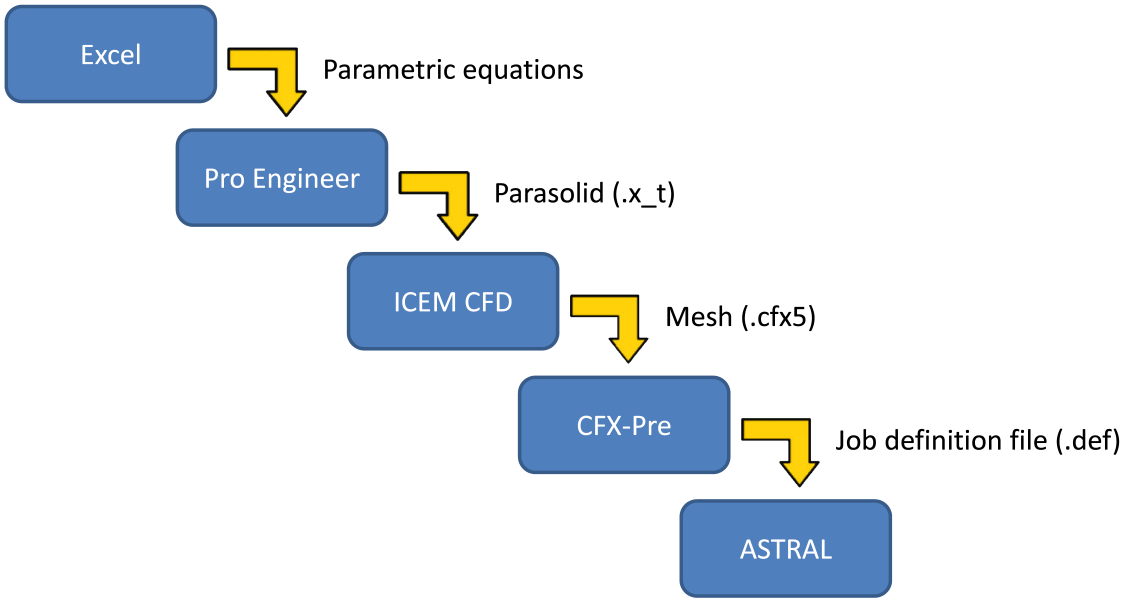

FIGURE 4.3: FPR 1.6 podded engine geometry generation workflow

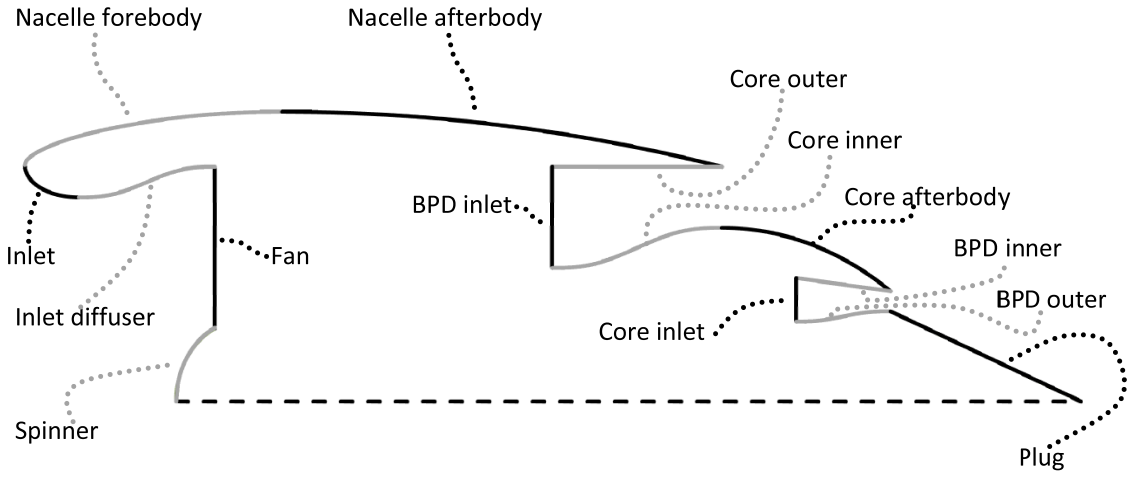

FIGURE 4.4: Nacelle sections

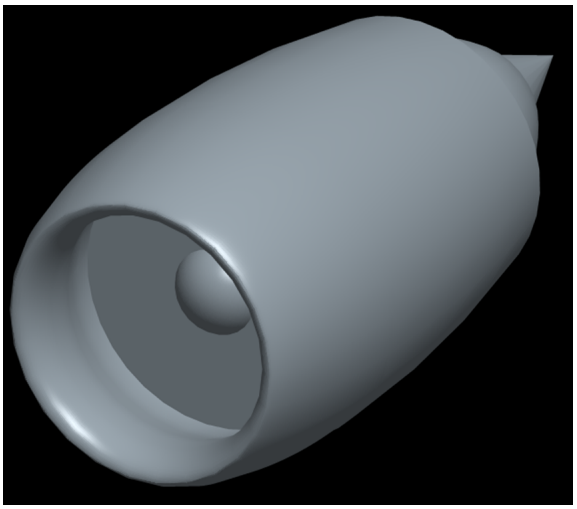

FIGURE 4.5: NASA 2A podded engine modeled in Pro Engineer[97]

4.5.1.2 Inlet diffuser, by-pass duct and core duct

The Inlet diffuser, by-pass duct and core duct are defined by a fifth order polynomial (Equation 4.7). This equation is usually used to minimise total pressure losses in wind-tunnel contraction sections.

$$\begin{aligned} h &= (-10\psi^3 + 15\psi^4 - 6\psi^6)(h_i - h_o) + h_i \\ \psi &= x/L \end{aligned} \tag{4.7}$$

Where L is the total length of the converging section, h is the distance from the centerline at position x and h_i and h_i are the distances from the centerline at the inlet and outlet respectively[98].

4.5.1.3 Nacelle forebody

The nacelle forebody was modeled using a NACA-1 series forebody. Specifically the smooth approximation to the profile was utilised[99] as described in Equation 4.8.

$$\begin{aligned}\frac{z}{L_{f,max}} = c_{naca}\left(\frac{x}{L_f}\right)^{1/2}\Bigg[\frac{1}{c_{naca}} - \left[\left(\frac{x}{L_f}-\right)\frac{1}{2c_{naca}}\right] \\ + \left[\left(1-\frac{1.5}{c_{naca}}\right)\left(\frac{x}{L_f}-1\right)^{1/2}\right]\Bigg] \\ + \left[\sum_{n=0}^{7}(-1)^{n+1}A_n\left(\frac{x}{L_f}\right)^n\right]\left[\frac{\left(\frac{x}{L_f}\right)^{3/2}\left(1-\frac{x}{L_f}\right)^2}{\left(b_{naca}+\frac{x}{L_f}\right)^2}\right]\end{aligned} \tag{4.8}$$

c_{naca}	1.044988
b_{naca}	0.05
An0	0.009466
An1	0.378874
An2	1.709298
An3	7.731339
An4	22.79108
An5	40.64622
An6	38.05716
An7	14.23322

TABLE 4.2: NACA 1-Series Smooth Approximation Coefficients

4.5.1.4 Nacelle and core afterbodies, spinner and inlet

The spinner and nacelle and core afterbodies were defined as circular arcs while the inlet was defined as an ellipse with a 2:1 aspect ratio.

4.5.2 CST approach

Class Shape Transformation (CST) parameterisation[100] represents a geometry by the product of a class function, $C(\psi)$, and a shape function, $S(\psi)$. The start and end points of all curves constructed with a class and shape function have equal ordinates. An additional term, $(\psi\Delta\xi_{te})$, is included to modify the end-point's ordinate[100]:

$$\xi(\psi) = S(\psi)C(\psi) + \psi\Delta\xi_{te} \;\; ; \;\; \xi = \frac{y}{c} \;\; , \;\; \psi = \frac{x}{c} \tag{4.9}$$

The basic profile is defined by the class function. One set of class functions which describes basic external aerodynamic shapes through different exponent combinations takes the form[100]:

$$C_{N_2}^{N_1}(\psi) = \psi^{N_1}[1-\psi]^{N_2} \;\; for \;\; 0 \leq \psi \leq 1 \tag{4.10}$$

Equation 4.10 can be used to describe bi-convex ($C_{1.0}^{1.0}$), ellipitic ($C_{0.5}^{0.5}$) and round-nosed ($C_{0.5}^{1.0}$) airfoil shapes as well as other common external aerodynamic shapes such as a Sears-Haack body ($C_{0.75}^{0.75}$) or a cone ($C_{0.+}^{1.0}$). The class function is modified by the shape function. Bernstein polynomials (Eqn. 4.11) are commonly employed as the shape function[100–102].

$$BP(\psi) = \sum_{i=0}^{N} \left[K_{i,n} \cdot \left(\psi^i \cdot (1-\psi)^{n-1} \right) \right] \;\; ; \;\; K_{i,n} = \frac{n!}{i!(n-1)!} \tag{4.11}$$

They are stable, robust and importantly form a partition of unity, i.e., the $n+1$ Bernstein polynomials of order n sum to one. The shape function can then be manipulated by the variation of Bernstein polynomial coefficients (Eqn. 4.12) which in turn modifies the final profile (Figures 4.6 and 4.7).

$$S(\psi) = \sum_{i=0}^{N} \left[bp_i \cdot K_{i,n} \cdot \left(\psi^i \cdot (1-\psi)^{n-1} \right) \right] \tag{4.12}$$

The mathematically smooth behaviour of Bernstein polynomial shape functions and their inherent curvature continuity make this system ideal for aerodynamic optimisation work.

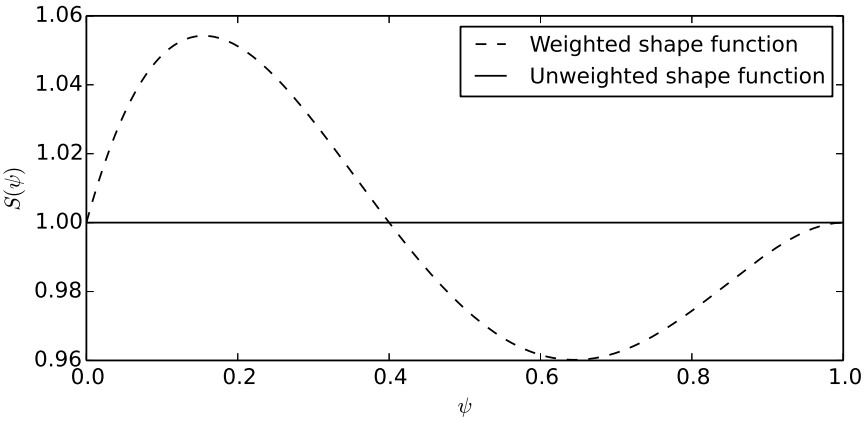

FIGURE 4.6: Perturbation of the shape function by variation of the Bernstein polynomial weighting coefficients

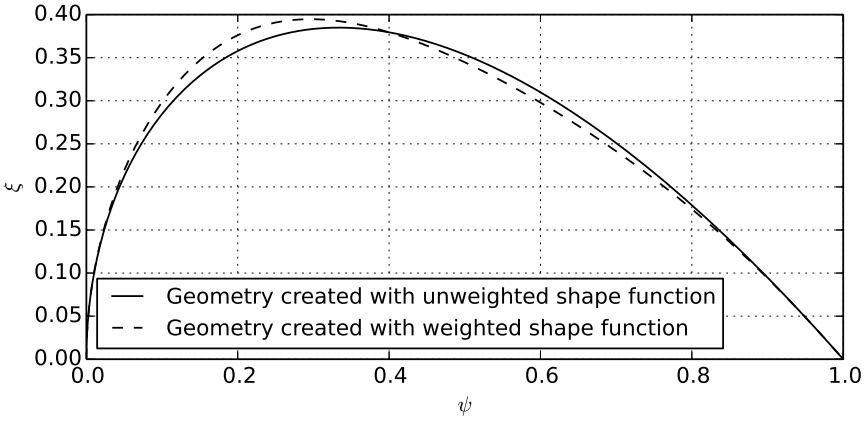

FIGURE 4.7: Geometry formed using a unit shape function and a shape function perturbed by bernstein polynomial weighting coefficients (Figure 4.6)

However the design relies on the manipulation of the Bernstein polynomial weighting coefficients which are not aerodynamically intuitive. To allow a design engineer to explore the design space and set up constraints for optimisation process the design parameters need to be physically intuitive. The Bernstein polynomial coefficients can be analytically calculated from intuitive variables through the construction of a transformation matrix.

4.6 Drag extraction

The importance of a clear and robust thrust and drag bookkeeping methodology has been highlighted in § 2.3. The forces acting on an uninstalled nacelle assuming 1-dimensional flow are shown in Figure 4.8. Here rearwards forces on a streamtube or solid surface are denoted by ϕ while gauge stream forces are represented by F_G. The net propulsive fore (NPF) is the sum of all forces acting upon it (Equation 4.13)[14]. A standard convention for air breathing engines is that thrust is equal to the sum of the forces imparted by the flow internal to the engine.[66] The sum of forces imparted by the external forces can be resolved into lift and drag. An equation for nacelle drag (Equation 4.14) be defined by applying this convention to Figure 4.8.

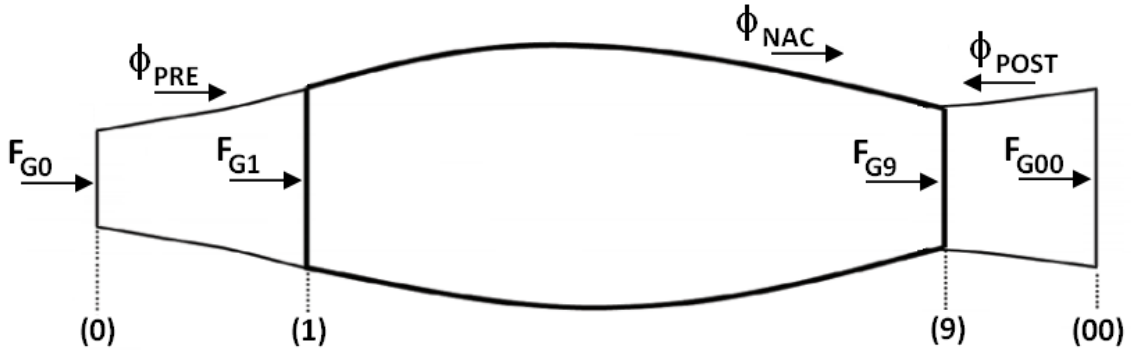

FIGURE 4.8: Forces acting on a single stream nacelle[14]

$$NPF = F_{G9} - F_{G1} + \phi_{nac} \tag{4.13}$$

$$D_{nac} = \phi_{pre} + \phi_{nac} + \phi_{post} \tag{4.14}$$

The calculation of the post exit streamtube force ϕ_{post} is non-trivial due to mixing and momentum transfer between the exhausted and external flow. If downstream infinity is chosen as a bookkeeping interface ϕ_{post} can be estimated using ideal flow assumptions.[103]

Another approach is to employ a datum nozzle for which $\phi_{post} = 0$.[13] In reality this condition is impossible. For this condition to exist the nozzle environmental pressure and freestream pressure would have to be equal. In CFD simulations this condition can be approximated by minimising ϕ_{post}. This is achieved by setting the nozzle exit total conditions equal to the freestream values and the nozzle internal walls to free slip walls. This approach is compatible with the ESDU nacelle drag estimation methodology.[13]

Initially the wake integral method was employed to calculate drag. In testing this approach it was found that calculated drag values were highly dependent on the definition of the wake outer boundary. To mitigate this CFD domain boundary was used as the integration region extreme. However in assessing this approach it was found to be highly sensitive to minor numerical fluctuations in the flowfield. This approach was deemed not robust or reliable enough for the current research.

It was then decided that the near-field drag extraction method should be employed. But this approach is not suited to CFD data as the calculation of the pre-entry force ϕ_{pre} can also be non-trivial, especially at high angles of attack or with the presence of intake flow separation. To ensure a robust and reliable drag calculation a new approach has been developed as part of this PhD thesis. This method, known as the Modified Near-field method is expounded upon in § 4.6.1.

4.6.1 Modified near-field drag extraction method

In line with the standard thrust and drag bookkeeping definition,[14] nacelle drag is given by the summation of the forces on the pre-entry and post-exit streamtubes and the nacelle surface wetted by external flow (Equation 4.15 and Figure 4.9).

$$D_{nacelle} = \phi_{pre} + \phi_{nac} + \phi_{post} \tag{4.15}$$

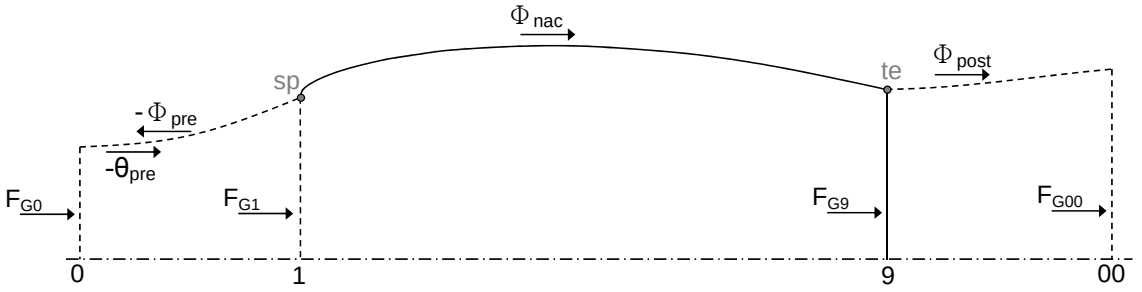

FIGURE 4.9: Decomposition of the Nearfield Method forces acting upon the pre-entry and post-exit streamtubes and the nacelle. Forces imparted by the external flow on the streamtubes and the nacelle are denoted by Φ, while Θ represents forces imparted by the internal flow. F_G designates the stream force at a station within the streamtube. Station 1 is the highlight plane and Station 9 is the nacelle trailing edge plane. The upstream and downstream planes are denoted by Station 0 and Station 00 respectively. The stagnation point on the nacelle lip is marked by the point "sp" while the trailing edge is identified by point "'te".

The ESDU nacelle drag method assumes that post-exit forces are equal to zero.[13] All CFD calculation carried throughout this body of research set the engine nozzle boundary conditions to minimise any post-exit force to be compatible with the ESDU method. To do this the nozzle total temperature and total pressure were set to be equal to freestream values. Therefore in the context of this work Equation 4.15 can be restated as Equation 4.16.

$$D_{nacelle} = \phi_{pre} + \phi_{nac} \tag{4.16}$$

Directly evaluating ϕ_{pre} and ϕ_{nac} involves extracting the stagnation line on the nacelle and separating surfaces into those inside and outside of the streamtube. While this method is practical for simple axisymmetric cases, at zero-incidence it becomes non-trivial at more complicated conditions. It is therefore desirable to find a method which allows drag to be calculated easily for all conditions. The force which acts upon the nacelle from the fan face (ff) to the trailing edge (te) can be calculated by integrating the pressure and viscous forces that act upon it (Equation 4.17 and Figure 4.10).

$$\theta_{nac} + \Phi_{nac} = \int_{ff}^{te} (P - P_\infty) \sin\theta_{surf} \partial S + \int_{ff}^{te} \tau_w \cos\theta_{surf} \partial S \tag{4.17}$$

The forces which act upon a surface in a real flow are illustrated in Figure 4.12. These

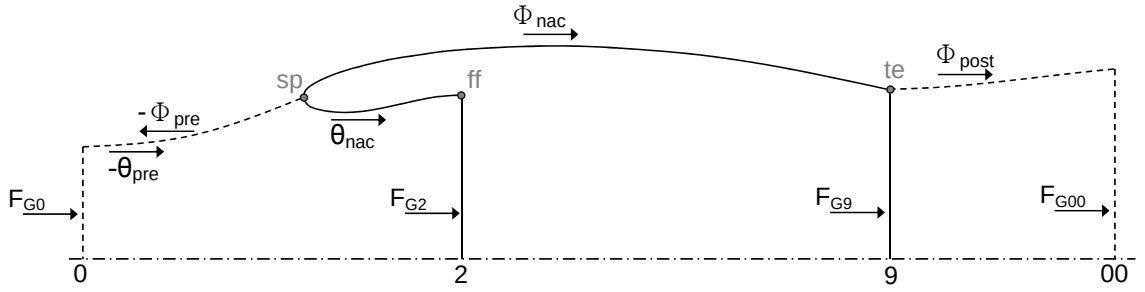

FIGURE 4.10: Decomposition of the "Modified Nearfield Method" forces acting upon the pre-entry and post-exit streamtubes and the nacelle. Forces imparted by the external flow on the streamtubes and the nacelle are denoted by Φ, while Θ represents forces imparted by the internal flow. F_G designates the stream force at a station within the streamtube. Station 2 is the fan face plane and Station 9 is the nacelle trailing edge plane. The upstream and downstream planes are denoted by Station 0 and Station 00. The juncture between the intake and the fan face, the stagnation point on the nacelle lip and the trailing edge are identified by point "'ff", "sp" and "te" respectively.

elemental forces can be resolved into the axial direction to give the rearwards force acting upon it (Equation 4.18 and Figure 4.11).

$$\partial\Phi = (P\sin\theta_{surf} + \tau_w\cos\theta_{surf})\partial A \tag{4.18}$$

When Newton's Second law of motion is applied to the volume of fluid within a streamtube

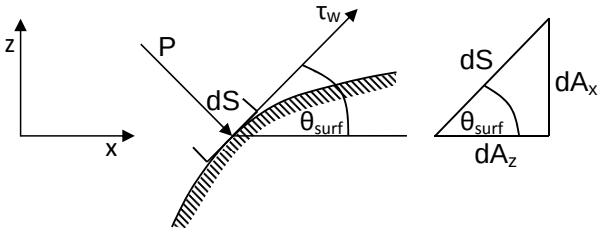

FIGURE 4.11: The pressure (P) and viscous (τ_w) forces acting upon a surface in a real flow flow and the decomposition of the elemental surface area (∂S) into the axial (x-direction) and normal (z-direction) projected areas (∂A_x and ∂A_z).

it can be shown that the total force on the streamtube surface is equal to the time rate of change of linear momentum.[14] Applied to the volume of fluid within the intake streamtube from upstream infinity (Station 0) to the fan face (Station 2) this results in Equation 4.19. Addition of Equations 4.17 and 4.19 gives D_{nac} (Equation 4.20). This methodology is

ideal for use with CFD data because all required data can be evaluated from the CFD domain bounds. However one disadvantage is that the individual terms, ϕ_{pre} and ϕ_{nac} are inextricable. This "Modified-Nearfield approach"has allowed the development of a robust methodology to automatically extract nacelle drag from CFD calculations in a manner compatible with standard thrust and drag accounting methodology.

$$\begin{aligned} F_{2,0} &= F_2 - F_0 \\ &= (W_2V_2 + P_2A_2) - (W_0V_0 + P_0A_0) \\ &= (-\Phi_{pre}) + \Phi_{nacelle} \end{aligned} \tag{4.19}$$

$$D_{nac} = \theta_{nac} + \Phi_{nac} + F_{2,0} = \Phi_{nac} + \theta_{pre} \tag{4.20}$$

Thrust and drag accounting methodology is usually only reported for zero degree angle of attack cases. The modified nearfield method has been extended to allow the extraction of lift and drag non-zero angles of attack. When an engine is at an incidence of α_{eng} the normal and axial forces which act upon the nacelle (Figure 4.12) can be resolved into the lift and drag forces acting upon it with Equations 4.22 and 4.21.

$$D_{nac} = N_{nac}\sin\alpha_{eng} + A_{nac}\cos\alpha_{eng} \tag{4.21}$$

$$L_{nac} = N_{nac}\cos\alpha_{eng} - A_{nac}\sin\alpha_{eng} \tag{4.22}$$

Equation 4.20 showed that D_{nac} can be calculated by the addition of the forces acting on the nacelle surface from the fan face to the trailing edge ($\theta_{nac} + \Phi_{nac}$) and the difference in the gauge stream forces at Station 2 and Station 0 ($F_{2,0}$). In the same way the axial force (A_{nac}) and the normal force (N_{nac}) which act upon a nacelle at incidence have a surface force and stream force component (Equations 4.23 and 4.24)

$$A_{nac} = A_{surf} + A_{stream} \tag{4.23}$$

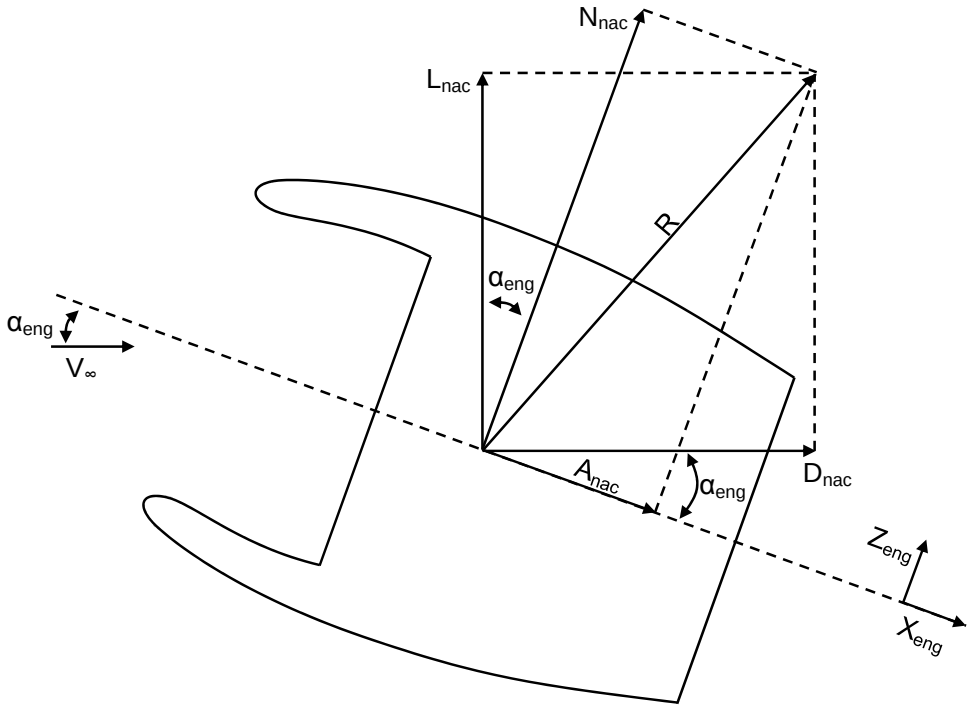

FIGURE 4.12: Schematic showing the definitions of nacelle lift, drag, normal and axial forces for an engine at an incidence of α_{eng}.

$$N_{nac} = N_{surf} + N_{stream} \tag{4.24}$$

The pressure and viscous forces acting upon the nacelle surface from the fan face and the highlight in the axial and normal directions are given by Equation 4.25 and Equation 4.26 respectively.

$$A_{surf} = \int_{ff}^{te} (P - P_\infty) \sin\theta_{surf} \partial S + \int_{ff}^{te} \tau_w \cos\theta_{surf} \partial S \tag{4.25}$$

$$N_{surf} = \int_{ff}^{te} (P - P_\infty) \cos\theta_{surf} \partial S + \int_{ff}^{te} \tau_w \sin\theta_{surf} \partial S \tag{4.26}$$

Equation 4.19 can be resolved into normal and axial forces when applied to a nacelle at incidence (Equations 4.27 and 4.28).

$$A_{stream} = \int_0^{r_{fan}} \left[(V_x \rho V - V_\infty) + (P - P_\infty) \right] \partial A_x \tag{4.27}$$

$$N_{stream} = \int_0^{r_{fan}} \left[(V_z \rho V - V_\infty) + (P - P_\infty) \right] \partial A_z \tag{4.28}$$

Equations 4.21 and 4.22 can then be expanded with Equations 4.25 to 4.28 to give the "Modified Nearfield Method"definitions of nacelle drag and lift applied to a nacelle at incidence (Equations 4.29 and 4.30).

$$\begin{aligned} L_{nac} = & \left[\int_{ff}^{te} (P - P_\infty) \cos\theta_{surf} \partial S + \int_{ff}^{te} \tau_w \sin\theta_{surf} \partial S \right. \\ & \left. + \int_0^{r_{fan}} \left[(V_z \rho V - V_\infty) + (P - P_\infty) \right] \partial A_z \right] \cos\alpha_{eng} \\ & - \left[\int_{ff}^{te} (P - P_\infty) \sin\theta_{surf} \partial S + \int_{ff}^{te} \tau_w \cos\theta_{surf} \partial S \right. \\ & \left. + \int_0^{r_{fan}} \left[(V_x \rho V - V_\infty) + (P - P_\infty) \right] \partial A_x \right] \sin\alpha_{eng} \end{aligned} \tag{4.29}$$

$$\begin{aligned} D_{nac} = & \left[\int_{ff}^{te} (P - P_\infty) \cos\theta_{surf} \partial S + \int_{ff}^{te} \tau_w \sin\theta_{surf} \partial S \right. \\ & \left. + \int_0^{r_{fan}} \left[(V_z \rho V - V_\infty) + (P - P_\infty) \right] \partial A_z \right] \sin\alpha_{eng} \\ & + \left[\int_{ff}^{te} (P - P_\infty) \sin\theta_{surf} \partial S + \int_{ff}^{te} \tau_w \cos\theta_{surf} \partial S \right. \\ & \left. + \int_0^{r_{fan}} \left[(V_x \rho V - V_\infty) + (P - P_\infty) \right] \partial A_x \right] \cos\alpha_{eng} \end{aligned} \tag{4.30}$$

Chapter 5

Isolated nacelles numerical campaign

This chapter describes the isolated nacelle CFD calculations that were performed to generate correlations to correct the ESDU nacelle drag prediction method [13] for incidence effects. To validate the CFD method comparison cases were also performed. These validation cases are discussed first.

5.1 Validation cases

The 1968-73 ARA nacelle test program [28] has been chosen to assess the numerical method. This allows comparison to measured external drag in terms of Mach number and MFCR.

5.1.1 Test matrices

The chosen simulations are shown in Table 5.1. ARA nacelle 1 [28] has been chosen. Mach 0.4 and Mach 0.85 were chosen to simulate both fully subsonic and transonic flow regimes.

Mach 0.85 is also a typical cruise Mach number. For each nacelle grid and domain sensitivity studies were carried out at the MFCR extreme values.

$M = 0.40$	$0.2 \leq MFCR \leq 1$
$M = 0.85$	$0.2 \leq MFCR \leq 1$
$MFCR = 0.70$	$0.7 \leq M \leq 0.925$

TABLE 5.1: Uninstalled nacelle validation test matrix

5.1.2 Grid and boundary conditions

The axisymmetric nature of the problem meant that it could be simulated by a 2-dimensional grid with periodic faces. However CFX[89] is solely a 3-dimensional solver. This necessitated a quasi-2d approach where a thin, one element thick 3-d grid was used. For this axisymmetric case a 2° wedge was used. The boundary conditions used are illustrated in Figures 5.1.

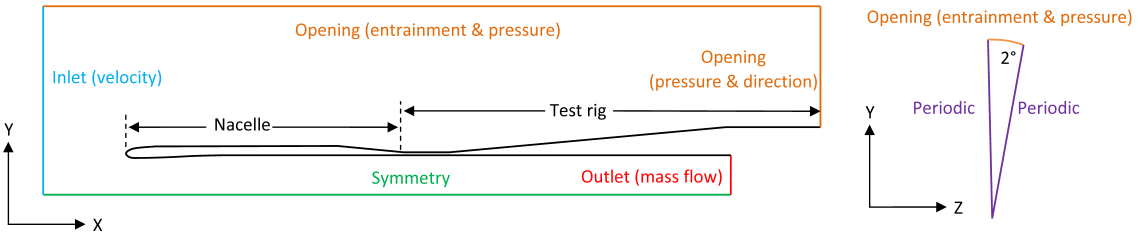

FIGURE 5.1: ARA boundary conditions showing periodic faces

Freestream conditions were set by the upstream velocity inlet and the MFCR was controlled by the massflow outlet. Values applied at these boundaries are given in Tables D.1, D.2, D.3 and D.4. An example grid created in ICEM CFD[88] is shown in Figure 5.2, which shows close-up of the airfoil nose.

5.1.3 Solver settings

Simulations were performed as Reynolds-Averaged Navier-Stokes Simulations (RANS) with the commercial code ANSYS CFX 12.1SP1.[89] The Shear Stress Transport model

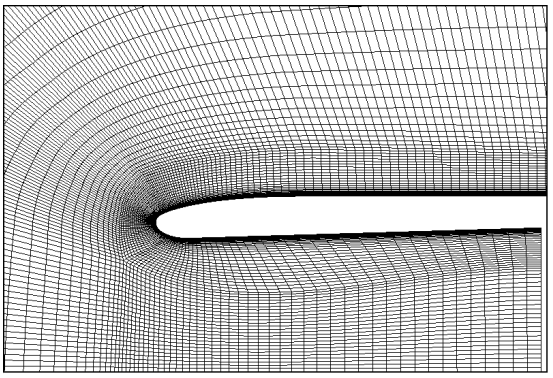

FIGURE 5.2: Close-up of mesh around nacelle nose

with transitional correlations (SST $k-\omega$ model) and automatic wall function was implemented. The fluid domain was modeled as a continuous ideal gas. Heat transfer was simulated by the "Total Energy" model with the viscous work term included. CFX's "high resolution" numerical schemes were used for both the turbulence numerics and the advection scheme. The standard momentum and mass, heat transfer, turbulence and wall scale residuals were monitored during the calculation. In addition, mass-flow through all inlets and outlets and forces on all surfaces were monitored to ensure adequate convergence was reached.

5.1.4 Grid independence study

The initial "coarse" grid consisted of 107,897 elements. This grid was the refined three times with an approximate refinement factor of two. This resulted in four grids a coarse, a medium, a fine and an extra-fine grid as outlined in Table 5.2.

Grid #	# Elements	Description
1	44,359	Coarse
2	89,769	Medium
3	180,328	Fine
4	360,849	Extra-fine

TABLE 5.2: Grid sizes for ARA nacelles calculations

As both the viscous and pressure forces are non-monotonic when plotted for Grids 2-4 Richardson's extrapolation[104] could not be used to generate a higher order estimate. Instead the level of grid independence was ascertained by looking at the percentage difference between forces calculated with the extra-fine grid (4) and the fine grid (3). This difference was $5.6 \times 10^{-4}\%$ and $2.5 \times 10^{-2}\%$ for the pressure and viscous forces respectively. This was deemed to be an adequate level of grid independence.

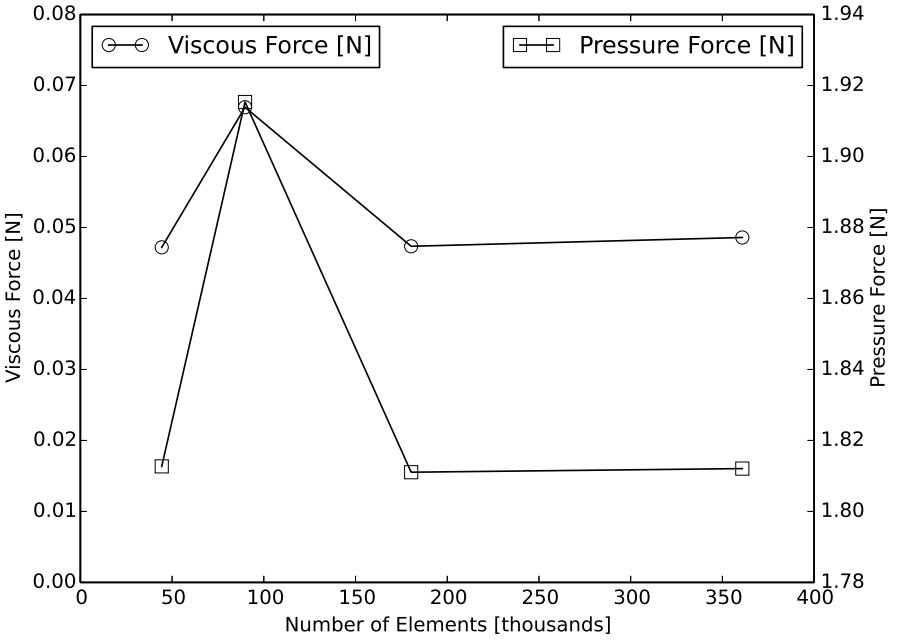

FIGURE 5.3: Variation of axial force with grid size for ARA cowl 1

5.1.5 Results

External drag has been calculated by extracting local flow values at the experimental measurement points and using the same method that would have been used in the experimental tests to calculate drag from these local values. This method is outlined in § 2.4. The results of this drag extraction are presented in Figure 5.4 and Figure 5.5. Here the extracted drag is compared to the experimentally measured drag. Good agreement between

the CFD calculation and experimental values was found. Typical differences between the experimental and numerical data were of the order of 2 drag counts.

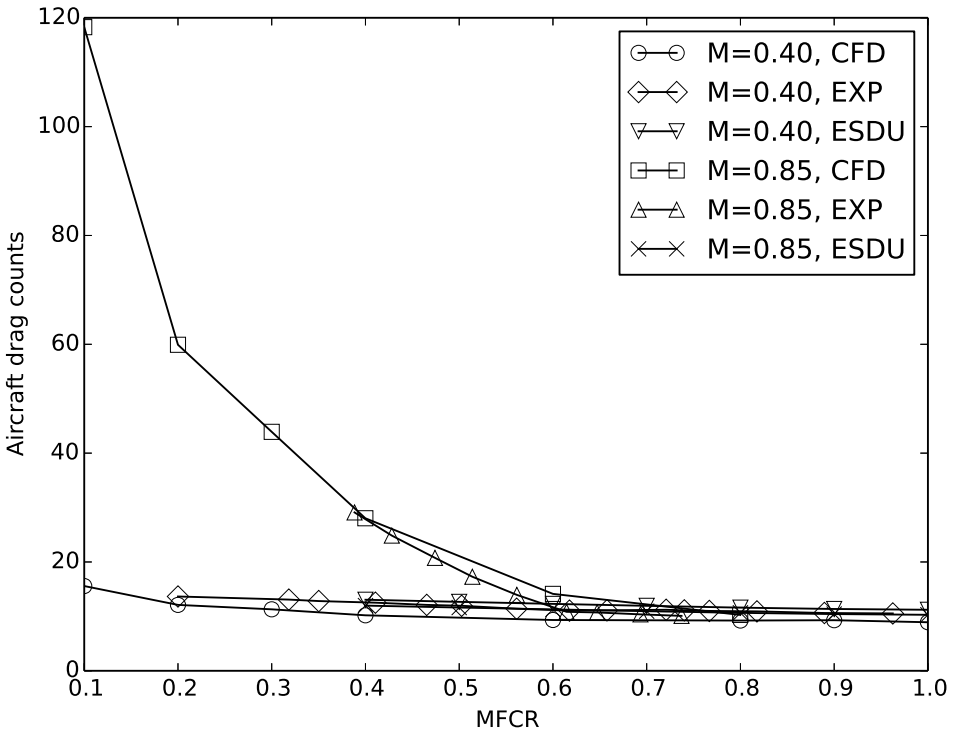

FIGURE 5.4: Variation of drag with Mach number and MFCR for the ARA Cowl 1 compared to experimental data[28]. Aircraft drag counts calculated using the CRM nacelle and wing areas. Variation of $C_{D,nac\,max}$ with MFCR at constant Mach numbers

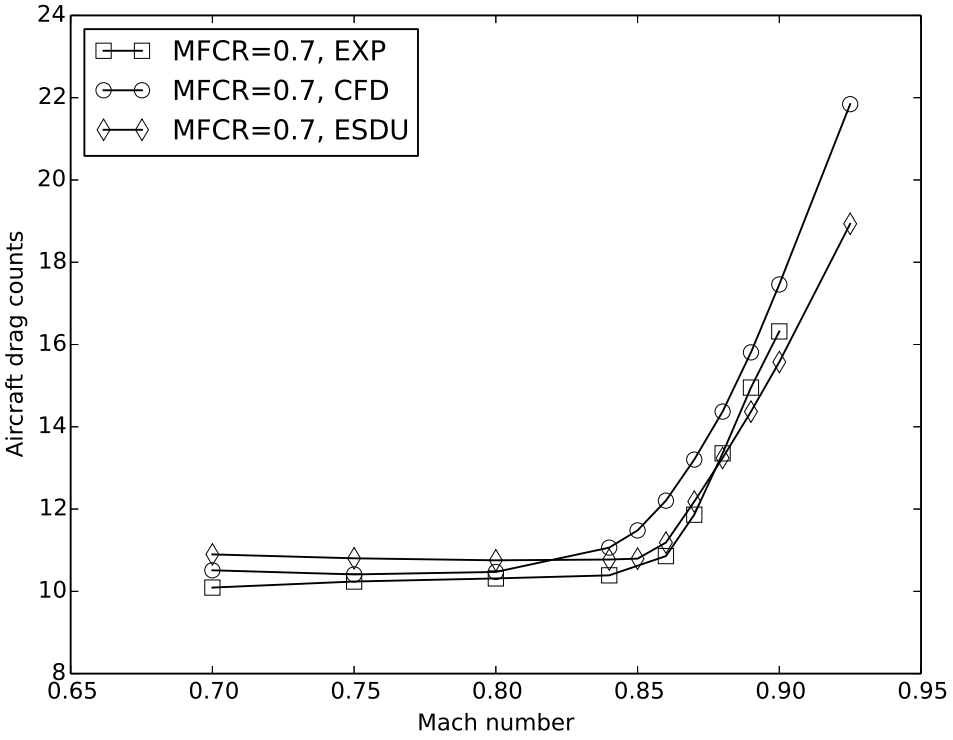

FIGURE 5.5: Variation of drag with Mach number and MFCR for the ARA Cowl 1 compared to experimental data[28]. Aircraft drag counts calculated using the CRM nacelle and wing areas. Variation of $C_{D,nac\,max}$ with Mach number at MFCR=0.7

5.2 CRMfit test cases

The simulation of an isolated nacelle at a range of Mach numbers, MFCRs and angles of attack was motivated by the need to apply corrections to the ESDU 810024 drag estimation method[13] to take into account angle of attack effects. Further CFD studies were then carried out with this nacelle installed on an aircraft so that installation effects could be accounted by a further correction to ESDU method. Of the available open source geometries the NASA Common Research Model (CRM, see §2.1.1.3 for more details) is the most representative of modern transonic transport aircraft. The CRM nacelle is similar to that of the GE CF6-80E1 A3 (Table 5.3).

	CRM TFN[34]				
	subscale	full scale	Trent 700[105]	PW 4000[105]	GE CF6-80E1 A3[105]
D_{fan} [m]	0.78	2.878	2.474	2.718	2.896
L_{eng} [m]	-	-	3.912	4.143	4.267
L_{tot} [m]	0.154	5.719	7.32	6.17	7.95

TABLE 5.3: A comparison of the CRM through flow nacelle with nacelles of a similar size

The ESDU method is only applicable to axisymmetric nacelles,[13] however the CRM nacelle is a non-axisymmetric through-flow nacelle. The exhaust diameter of the CRM through flow nacelle is sized to give the a representative intake MFCR at its design point. This means that the exhaust diameter is relatively smaller than for a real nacelle. Using NACA guidelines and the afterbody length, forebody curvature radius and boattail angle the exhaust diameter was set. These properties and Cranfield University's GEM tool[95] were then used to create an axisymmetric nacelle based on the CRM nacelle known as the CRMfit nacelle. The non-dimensional nacelle properties of the CRMfit required by the ESDU method are provided in Table 5.4.

5.2.1 Test matrices

To investigate Mach number, MFCR and angle of attack effects on uninstalled engine drag a series of simulations have been carried out. Mach number was varied from 0.1 to 0.85 to capture both the incompressible regime and a typical maximum cruise Mach number for a modern transonic transport aircraft. MFCR capture ratio was varied from 0.25 to 1.5 and the angles of attack varied from 0^o to 10^o (Table 5.5). This range covers most MFCRs and aircraft angle of attacks normally seen throughout a flight.

	$M = 0.10$			$M = 0.40$			$M = 0.60$			$M = 0.85$		
α / MFCR	0^o	5^o	10^o	0^o	5^o	10^o	0^o	5^o	10^o	0^o	5^o	10^o
0.25	1.1.1	1.1.2	1.1.3	2.1.1	2.1.2	2.1.3	3.1.1	3.1.2	3.1.3	4.1.1	4.1.2	4.1.3
0.50	1.2.1	1.2.2	1.2.3	2.2.1	2.2.2	2.2.3	3.2.1	3.2.2	3.2.3	4.2.1	4.2.2	4.2.3
0.75	1.3.1	1.3.2	1.3.3	2.3.1	2.3.2	2.3.3	3.3.1	3.3.2	3.3.3	4.3.1	4.3.2	4.3.3
1.00	1.4.1	1.4.2	1.4.3	2.4.1	2.4.2	2.4.3	x.x.x	x.x.x	x.x.x	x.x.x	x.x.x	x.x.x
1.50	1.5.1	1.5.2	1.5.3	x.x.x	x.x.x	x.x.x	x.x.x	x.x.x	x.x.x	x.x.x	x.x.x	x.x.x

TABLE 5.5: CRMfit test case matrix

5.2.2 Grid and boundary conditions

At the domain farfield velocity, static temperature and static pressure were specified (Figure 5.7). The intake MFCR was controlled by the massflow outlet. Exhaust total conditions were set equal to freestream to form a pressure matched nozzle and minimise post

L_f/L_t	0.300
L_a/L_t	0.600
L_f/D_{max}	0.708
L_a/D_{max}	1.417
D_i/D_{max}	0.723
D_e/D_{max}	0.656
A_i/A_{th}	1.244

TABLE 5.4: CRMfit nacelle non-dimensional parameters (Figure 5.6)

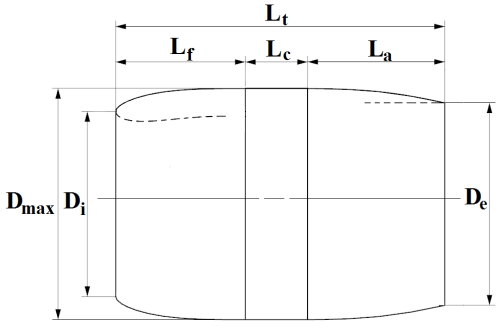

FIGURE 5.6: Non-dimensional CRMfit nacelle parameters (Figure 5.6)

exit streamtube drag. A grid and domain independence study were carried out which resulted in a fully structured mesh with 4.8×10^6 cells (Figure 5.8). To ensure mesh quality a cell minimum 2x2x2 determinant of 0.62 and maximum cell expansion rate of 1.2 were maintained.

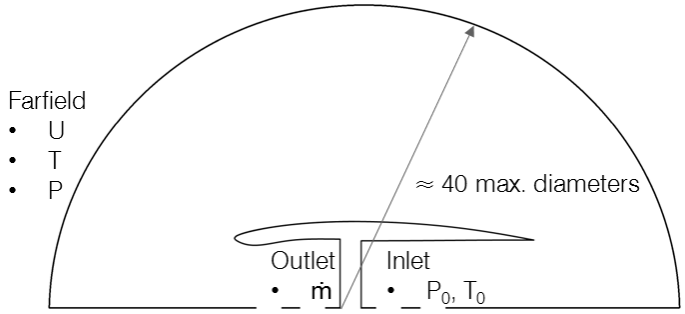

FIGURE 5.7: Domain and boundary conditions for the isolated nacelle CFD cases (not to scale)

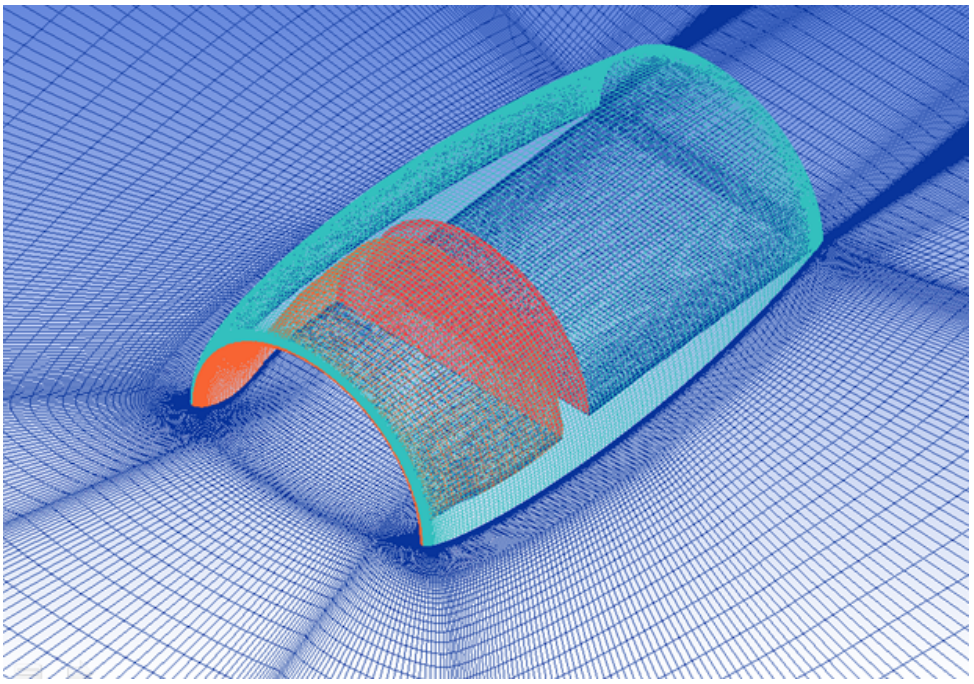

FIGURE 5.8: Mesh for the isolated nacelle CFD cases

5.2.3 Solver settings

The CFD calculations have been performed using a steady RANS approach and an implicit, nominally second-order compressible flow solver. The calculations were performed following detailed studies of domain size, grid independence and iterative convergence.

5.2.4 Domain independence study

The CFD domain sensitivity study was carried out using four different domain sizes while the inner mesh topology was kept constant. The domain diameter (D_D) was modified as a function of the nacelle maximum diameter (D_{max}) over a range of $60D_{max} \leq D_D \leq 90D_{max}$. Distances from the nacelle to the far-field were changed by adding external layers to the smaller domain, with the internal topology unaltered. A domain with $D_D = 80D_{max}$ was chosen. For this mesh the absolute difference in calculated $C_{D,nac}$ from a mesh with $D_D = 90D_{max}$ was below 0.01%.

5.2.5 Grid independence study

Once the domain size was defined, grid convergence analysis was performed using Richardsons extrapolation and Grid Convergence Index (GCI), as suggested by Roache.[93] A coarse, medium and fine grid were produced (Table 5.6). The GCI for nacelle drag for the coarse and fine meshes are 0.73% and 0.05%, respectively. This meant that the medium grid was within a band of error, with regards to nacelle drag, greater than 0.05% and below 0.73% and resulted in a mesh size of 4.8 million elements.

Grid	# Elements
Coarse	2.4×10^6
Medium	4.8×10^6
Fine	9.6×10^6

TABLE 5.6: The size of grids created during the isolated nacelle mesh independence study

The impact of mesh refinement was seen primarily in subtle changes in the flow physics over the nacelle forebody. An example of this is given in Figure 5.9 for an isolated nacelle with a freestream Mach number of 0.8 and a MFCR of 1.0. As the mesh is refined the supersonic region over the forebody is altered. The intake flow, stagnation point and the shape of the pre-entry streamline were insensitive to mesh refinement across the investigated meshes. Prediction of the supersonic region as the flow accelerates around the forebody is sensitive to the mesh refinement in this region. These changes in velocity distribution and the corresponding changes in the pressure distribution alter the forebody suction force. As the stagnation point remained in the same location and the shape of the pre-entry streamline was unchanged it can be seen that the changes in the calculated nacelle drag were primarily caused by changes in the forebody suction force.

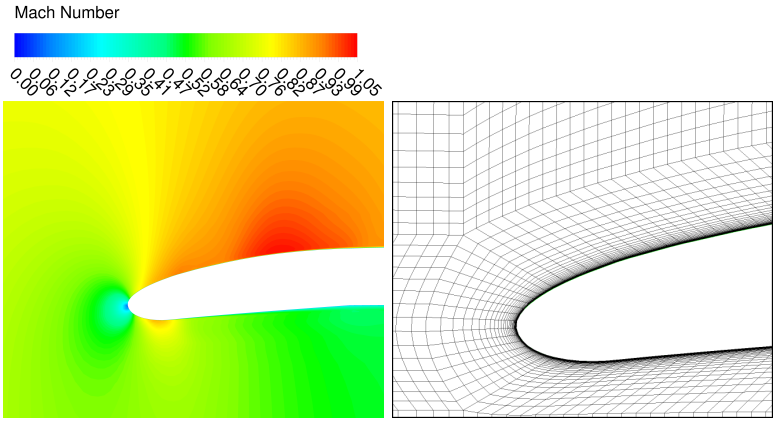

(a) Mach number on the symmetry plane around the intake and forebody of the coarse, isolated nacelle mesh ($M_\infty = 0.8$, $MFCR = 1.0$).

(b) Detail of the coarse, isolated nacelle mesh (2.4×10^6 cells) around the nacelle intake and forebody.

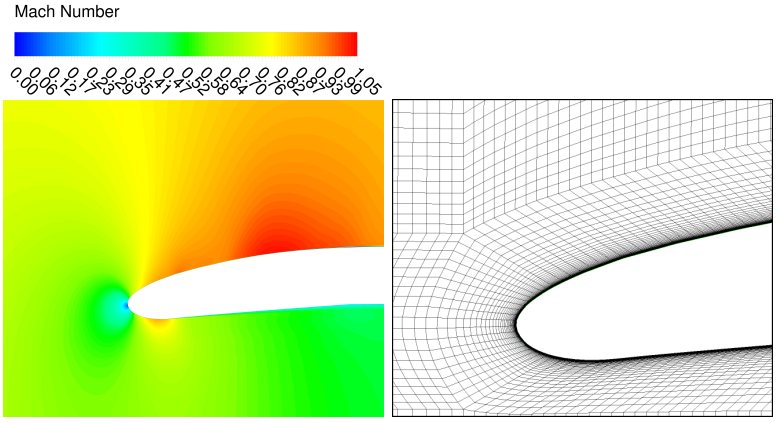

(c) Mach number on the symmetry plane around the intake and forebody of the medium, isolated nacelle mesh ($M_\infty = 0.8$, $MFCR = 1.0$).

(d) Detail of the medium, isolated nacelle mesh (4.8×10^6 cells) around the nacelle intake and forebody.

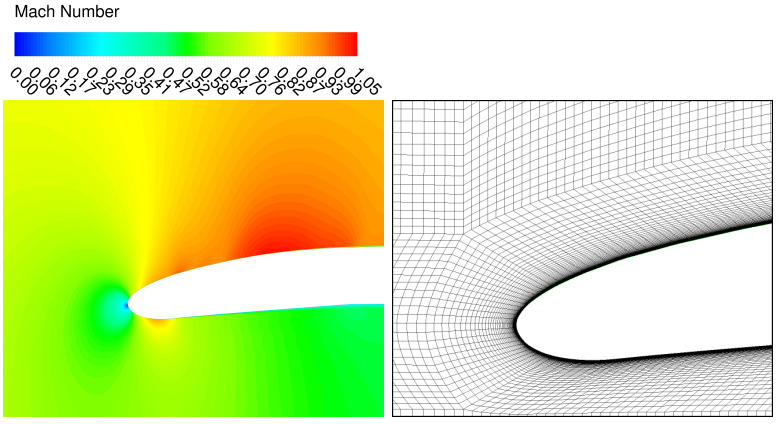

(e) Mach number on the symmetry plane around the intake and forebody of the fine, isolated nacelle mesh ($M_\infty = 0.8$, $MFCR = 1.0$).

(f) Detail of the fine, isolated nacelle mesh (9.6×10^6 cells) around the nacelle intake and forebody.

FIGURE 5.9: The impact of mesh refinement on the Mach number distribution around the intake and forebody of an isolated nacelle ($M_\infty = 0.8$, $MFCR = 1.0$).

5.3 Results and discussion

Changes in $C_{D,nac\,max}$ with changes in nacelle total upflow angle were investigated (Figure 5.10). As Mach number was increased the choking MFCR ratio of the nacelle reduced. This meant that the maximum MFCR investigated for the M=0.4 configurations was 1 while for the M=0.6 and M=0.85 cases the maximum MFCR=0.75. The coefficient of nacelle drag based on nacelle cross-sectional area.

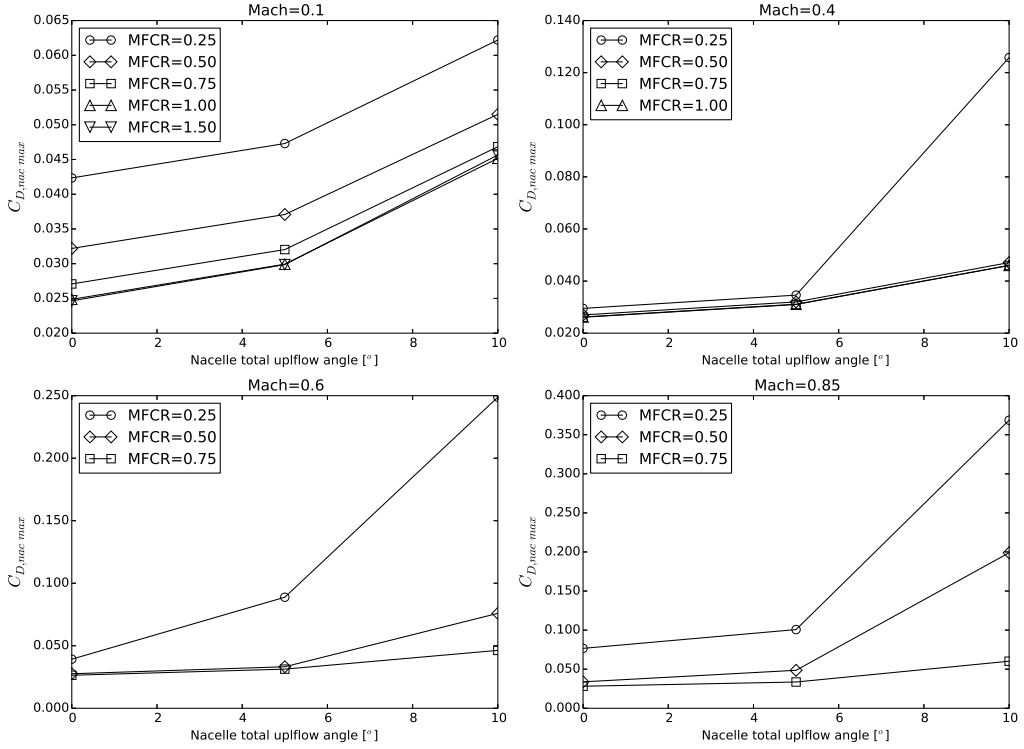

FIGURE 5.10: Variation of nacelle drag with Mach number & MFCR for the CRMfit

The influence of Mach number on the flowfield is illustrated by Figures 5.11 and 5.12. Between the two lowest Mach numbers, (0.1 and 0.4), at all angle of attacks, (0^o, 5^o and 10^o), little change in the shape of the Mach number and pressure coefficient distributions occurred. This was to be expected as the $M = 0.4$ cases are only just into the compressible regime.

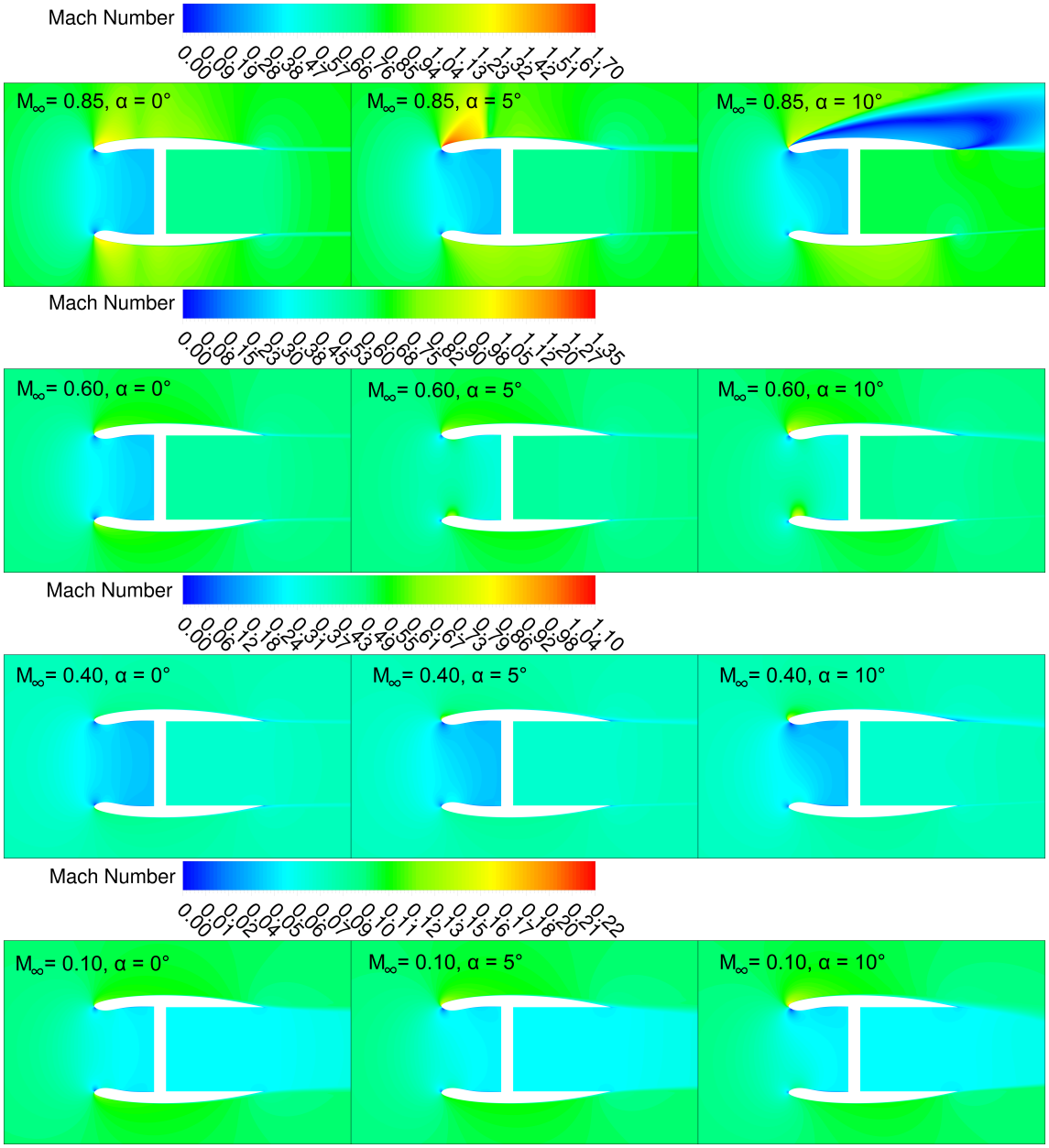

FIGURE 5.11: Changes in the distribution of Mach number on the symmetry plane for an isolated nacelle with changes in freestream Mach number (M) and angle of attack (α). In all cases the MFCR was set to 0.75.

At $M = 0.6$ and $\alpha = 10^o$, (Config. 2.3.3), flow acceleration around the forebody is sufficient to generate a small shock with a pre-shock Mach number of 1.33. This can also be seen in the altered C_P distribution in Figure 5.12(c). When the freestream Mach number was further increased to $M = 0.85$ supersonic flow around the forebody was present at all angles of attack with $MFCR = 0.75$ (Figure 5.11). However for the $\alpha = 0^o$ case, (Config. 4.3.1), though a peak Mach number of 1.4 was reached no shock was predicted. This can be seen in the smooth decay of C_P from its maximum value of -0.98 to -0.28 before a small re-acceleration takes place just forward of the nacelle maximum diameter (Figure 5.12(d)).

When the angle of attack is increased to 5^o, (Config. 4.3.2), the peak Mach number increases to 1.7. The flow the decelerates to a Mach number of 1.2 before a shock is formed. The additional wave drag caused by this shock increases $C_{D,nac\,max}$ by 0.006 (from 0.028 for Config. 4.3.1 to 0.034 for Config. 4.3.2). At 10^o, (Config. 4.3.3), flow acceleration around the forebody results in a stronger shock much closer to the highlight (pre-shock Mach number of 1.7). As this shock occurs in a region with greater local curvature the flow is unable to reattach. This strong shock induces a large separation which extends along the full length of the fan cowl. $C_{D,nac\,max}$ increases from 0.034 for Config. 4.3.2 to 0.060 for Config. 4.3.3 as a result.

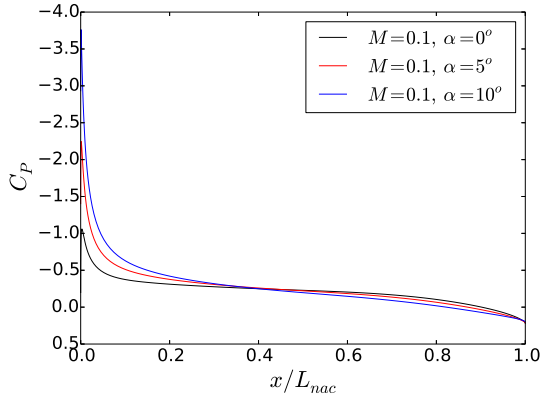

(a) Differences in the distribution of pressure coefficient (C_P) on the fan cowl centreline for an isolated nacelle with changes in α, (M=0.1, MFCR=0.75).

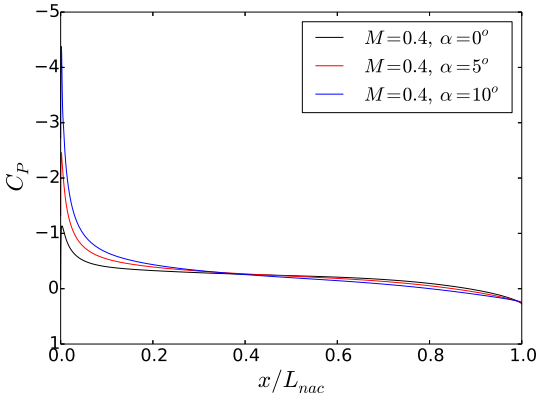

(b) Differences in the distribution of pressure coefficient (C_P) on the fan cowl centreline for an isolated nacelle with changes in α, (M=0.4, MFCR=0.75).

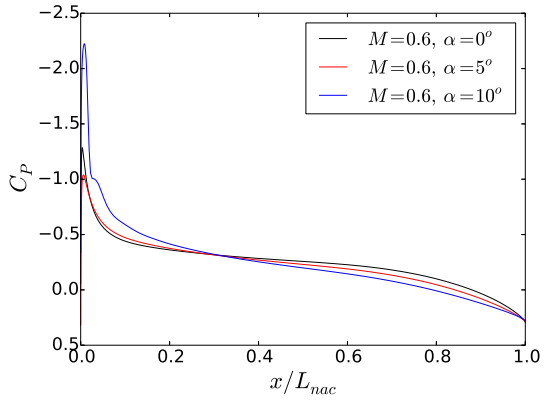

(c) Differences in the distribution of pressure coefficient (C_P) on the fan cowl centreline for an isolated nacelle with changes in α, (M=0.6, MFCR=0.75).

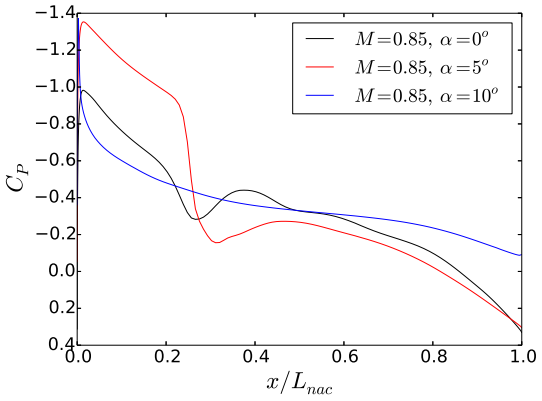

(d) Differences in the distribution of pressure coefficient (C_P) on the fan cowl centreline for an isolated nacelle with changes in α, (M=0.85, MFCR=0.75).

FIGURE 5.12: Changes in the distribution of pressure coefficient (C_P) on the fan cowl centreline for an isolated nacelle with changes in freestream Mach number (M) and angle of attack (α). In all cases the MFCR was set to 0.75.

As expected there was an increase in $C_{D,nacmax}$ as MFCR was reduced. For the $M = 0.1$ case the $\Delta C_{D,nacmax}$ between the $MFCR = 0.25$ and $MFCR = 0.75$ cases was approximately constant at 0.015 for all angles of attack. This is equivalent to 4.4 aircraft drag counts when non-dimensionalised by the CRM wing reference area. This sensitivity

increased when the freestream Mach number was increased. At $M = 0.4$, for the $MFCR = 0.25$ and $\alpha = 10^o$ case the combination of flow acceleration due to the low MFCR, angle of attack and the freestream Mach number led to a shock on the nacelle forebody and a corresponding increase in nacelle drag. The $\Delta C_{D,nac\,max}$ between the $MFCR = 0.25$ and $MFCR = 0.75$ cases was 1 aircraft drag counts for $\alpha = 0^o$ and $\alpha = 5^o$ but rose to to 23 aircraft drag counts for $\alpha = 10^o$.

For larger MFCRs at M=0.4 flow over the forebody lip stayed subsonic. As MFCR decreases the projected area of the pre-entry streamtube along the engine axis increases. This leads to an increase in the rearwards force on the pre-entry streamtube. However as MFCR and the projected area decreases, flow acceleration around the forebody increases. This flow acceleration is associated with a reduction in the local static pressure which manifests itself as an increase in the forebody suction force and a decrease in nacelle drag. In potential flow changes in the pre-entry force would balance with changes in the nacelle rearwards force and nacelle drag would be unchanged. However as this is viscous flow this is not the case due to losses caused by viscous effects such as skin friction and at higher Mach numbers shock losses. Losses due to viscous effects increase with increases in Mach number, hence sensitivity to MFCR is increases with increases in Mach number.

Further increases in freestream Mach number continued the trend of decreased MFCR and increased nacelle total upflow angles to result in increased nacelle drag. At $M = 0.85$ and $\alpha = 10^o$ (Figure 5.13(a)) a strong shock was present on the forebody. When MFCR=0.75 (Figure 5.13(b)). This shock was present at about 1/4 of the nacelle length and it caused caused a small region of separation on the nacelle crown. A small shock was also present on the lower intake lip. This shock induced a large area of separation (Figure 5.13(c)).

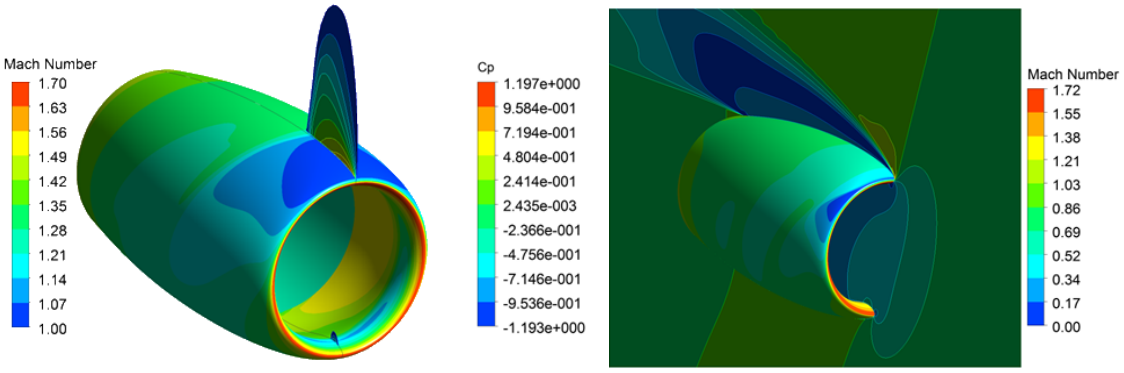

(a) $Mach = 0.85$, $\alpha = 10^o$ & $MFCR = 0.75$, Pressure coefficient on surface, Mach contours clipped to those above $Mach = 1$

(b) $Mach = 0.85$, $\alpha = 10^o$ & $MFCR = 0.50$, Pressure coefficient on surface, Mach contours on the plane of symmetry

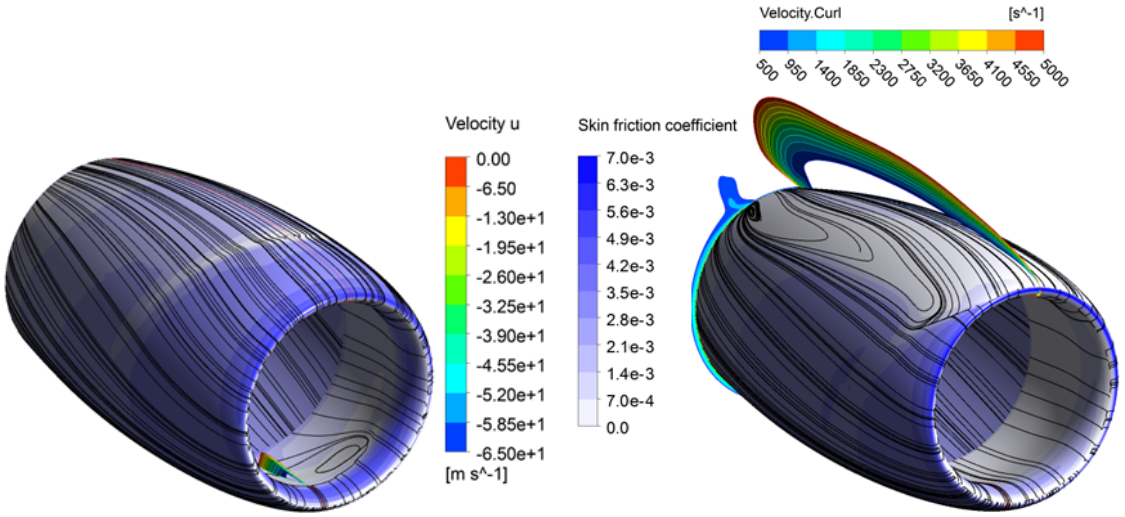

(c) $Mach = 0.85$, $\alpha = 10^o$ & $MFCR = 0.75$. Contours of skin friction coefficient overlaid with streamlines on the nacelle surface. Axial velocity clipped to negative values on the plane of symmetry.

(d) $Mach = 0.85$, $\alpha = 10^o$ & $MFCR = 0.50$. Contours of skin friction coefficient overlaid with streamlines on the nacelle surface. Axial velocity clipped to negative values on the plane of symmetry. Contours of velocity curl in the nacelle trailing edge plane.

FIGURE 5.13: Local flowfield for configurations 4.2.3 and 4.3.3

However when the MFCR was reduced to 0.5 a flow separation the full length of the nacelle topside occurred. This separation resulted in a loss of lift and increase in drag which is apparent in the nacelle drag polars (Figure 5.14). Nacelle drag increased by 41 aircraft drag counts over the MFCR=0.75 case (Figure 5.10). The intake separation was however removed (Figure 5.13(d)). This was caused by a reduction in the local flow angle on the bottom lip due to the decrease in MFCR. The flow did not accelerate around the lip as much with a resultant decrease in the local maximum Mach number eliminating the shock which was causing the separation.

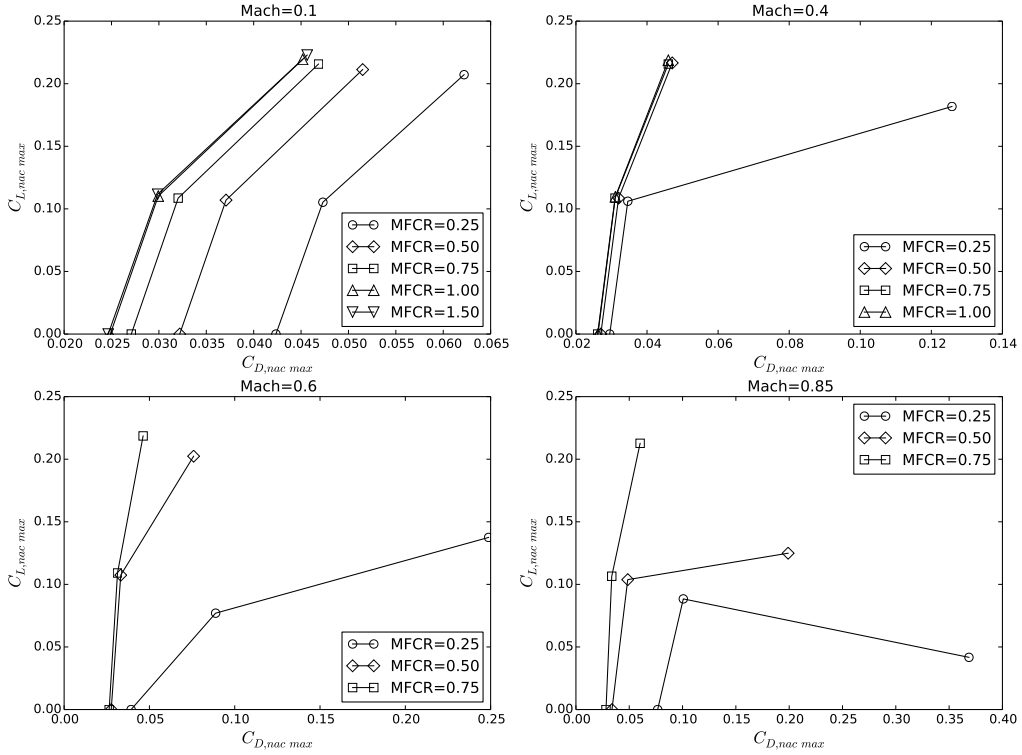

FIGURE 5.14: Variation in drag polar with Mach number & MFCR for the CRMfit

5.4 Correction for incidence extraction

A simple scaling factor is used to correct for incidence effects ($C_D/C_{D=0}$). A Barycentric interpolation routine has been added to PSIMOD to interpolate between data points. The extracted corrections for 5^o and 10^o angles of attack are provided in Figure 5.15. Here the data points are represented by the triangular grid and the contour fill is created from interpolated values.

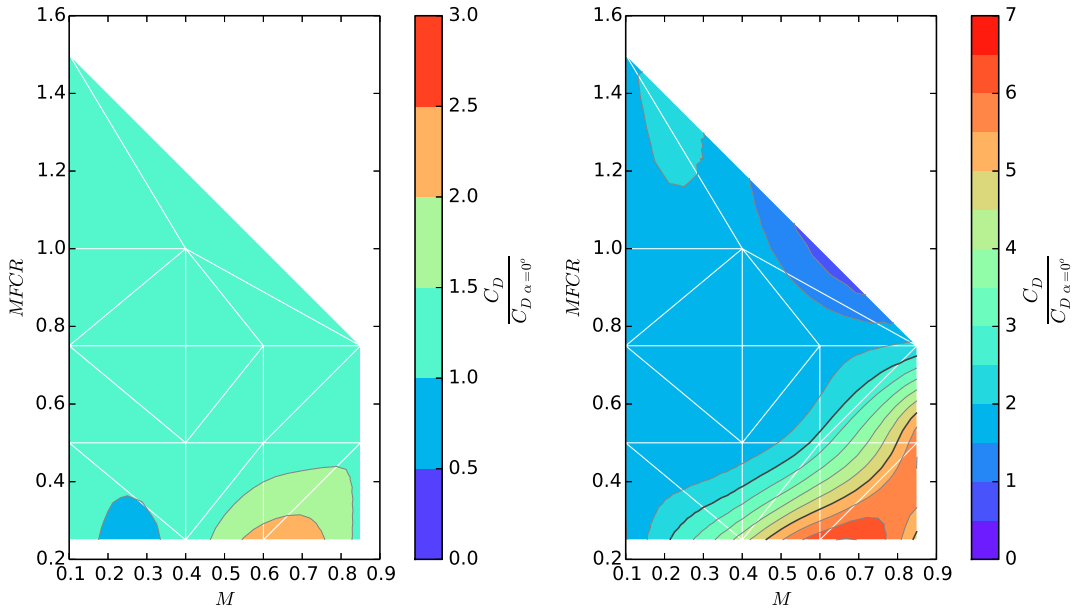

(a) $\alpha = 5^o$ (b) $\alpha = 10^o$

FIGURE 5.15: Extracted uninstalled correlations

Chapter 6

Mission performance sensitivity studies

An initial assessment of nacelle drag prediction methods using the BADA tool[106] is discussed in §6.3. PSIMOD is then used to assess the effects of nacelle size, weight, local upflow angle and installation quality. To assess these effects separately the effects of local upflow angle and installation quality were initially neglected (§6.4, §6.5 & §6.6). Subsequently these effects were modelled and are discussed in §6.7 and §6.8 respectively. These assessments necessitated the development of two aircraft models for a short haul and a long haul mission. In conjunction with these a series of engine models were developed to enable mission performance sensitivity to nacelle size to be assessed. The development of these models is discussed in the following sections.

6.1 Engine models

The engine thermodynamics were simulated with Turbomatch, which is the gas-turbine performance simulation program developed by Cranfield University [64,107]. The baseline engine simulations for the CFM56-7B27 and Trent 892 were validated with publicly available information about their cycles. Engine models are based on the known engine cycle characteristics and were refined so that the main parameters of thrust, massflow and specific fuel consumption agreed with the published data to typically within $1 \times 10 - 2\%$.

Additional engines with larger BPRs were computed to take into account the impact of the nacelle size on the mission performance (Table 6.2). The bypass ratio increase leads to larger fan diameters and consequently to larger nacelle diameters (Table 6.2). All the nacelles studied had the same non-dimensional geometry (Table 6.1) and were scaled by the D_i required to match the baseline engine MFCR at design point. For the cycles based on these larger engines the core was unaltered from the baseline engines and the BPR was increased to 7.6 and 8.5 on the CFM like engine and 8.3 and 11 for the larger versions of the Trent 892 type engine (Table 6.2).

L_f/L_t	0.3
L_a/L_t	0.6
L_f/D_max	0.708
L_a/D_max	1.417
D_i/D_max	0.723
D_e/D_max	0.656
A_i/A_th	1.244

TABLE 6.1: Non-dimensional nacelle parameters

Two different philosophies were followed to create the thermodynamic model of the bigger engines; matching the baseline thrust and matching the baseline TET, while the core was kept the same (Table 6.2). In general, matching TET and increasing BPR led to an increase engine thrust, which implies that the climb phase could be completed in less time and that the engines would operate derated during cruise or for a stretch development of

the same aircraft. For the other design philosophy, matching thrust and increasing BPR decreased TET. This meant that climb to cruise altitude took longer because the increase in nacelle drag was not accompanied by an increase in thrust. However, lower TET could result in a lower life cycle cost for the engines.

Engine Model	BPR	T-O Thrust	Dmax	Description
		[kN]	[m]	
Short haul mission engines				
CUTF-BPR5.1-120K	5.1	121.43	2.222	Baseline similar to CFM56-7B27
CUTF-BPR7.6-120K	7.6	121.43	2.689	Larger versions, thrust matched
CUTF-BPR8.5-120K	8.5	121.43	2.826	”
CUTF-BPR7.6-140K	7.6	144.37	2.683	Larger versions, TET matched
CUTF-BPR8.5-150K	8.5	150.63	2.822	”
Long haul mission engines				
CUTF-BPR5.8-410K	5.8	407.52	3.907	Baseline similar to Trent 892
CUTF-BPR8.3-410K	8.3	407.49	4.407	Larger versions, thrust matched
CUTF-BPR11-410K	11	407.49	5.011	”
CUTF-BPR8.3-430K	8.3	428.04	4.407	Larger versions, TET matched
CUTF-BPR11-450K	11	451.09	5.011	”

TABLE 6.2: Engine models used to evaluate the engine size effect on the aircraft mission performance

The changes of dry weight on bigger engines, caused by the modifications of the cycles were accounted with a correlation extracted from the NASA WATE++ model[108]. This statistical method computes engine weight as a function of overall pressure ratio, bypass ratio and core massflow. Evaluating this method for known engine configurations an uncertainty of approximately 20% on the estimation of the baseline engine weight was found. This is a relatively modest uncertainty given that the model is based on just three required variables.[109] Nacelle weight changes were computed with a database correlation method[110]. This statistical method is established on a range of engines and the main independent variable is the maximum engine thrust at take-off. Predicted nacelle weight for a range of known nacelles was found to be within an uncertainty band of 10%.

The main focus of this research is the development of a methodology for use in preliminary

aircraft-engine design. This methodology has been demonstrated using aircraft and engine information based on current technology levels and can be viewed as a re-engining feasibility exercise. This application differs somewhat from other aircraft-engine synthesis studies in the literature.[50,55,56] Previous studies have tended to focus on future conceptual design with assumptions on future engine technologies built in. This has previously been achieved by basing engine performance on future engine technologies.[55] For example a study carried out in 2003 assumed that engine technologies such as advanced contra-rotating fans, geared turbofans and variable area nozzles would be mature in 2015.[55] Another study used a more conventional engine layout (two-spool, direct drive fan engine).[56] However future advances in engine technology were approximated by increasing the aerodynamic efficiencies of individual engine components. It is important to note these differences in approach when considering the results presented in this Chapter. This is especially true regarding predicted optimum BPRs as these will likely be higher for future engine technology levels.

6.2 Aircraft models

Two baseline aircraft models were utilised for the analysis using PSIMOD of the engine integration effect on the mission performance. A short haul (Table 6.3) flight was considered based on an aircraft based on the Boeing 737-800, with two engines similar to the CFM56-7B27 over a mission distance of 1,000 km and with a payload of 10,660 kg. The long haul (Table 6.3)) mission was assessed using an aircraft based on a Boeing 777-300 configuration, whose engines were similar to the Trent 892 over a range of 6,000 km and with a payload weight of 33,370 kg. Both flights were computed at a cruise altitude of 10,668m and cruise Mach numbers of 0.81 for the short haul and 0.84 for the long haul (Table 6.3)). PSIMOD also requires a model of the $C_L - \alpha$ curve of the aircraft to compute the mission performance. For the Boeing 777-300 type aircraft this was obtained[111], a vortex lattice method[112] with compressibility corrections for high subsonic Mach numbers.

This same method was used to compute the lift coefficient curve of the Boeing 737-800 type aircraft.

		Short haul mission	Long haul mission
Aircraft based on		Boeing 737-800	Boeing 777-300
Altitude	[m]	10,668	10,668
Cruise Mach number	[-]	0.81	0.84
Range	[km]	1,000	6,000
Weights			
Maximum T-O	[kg]	79,016	299,370
Maximum landing	[kg]	66,361	237,680
Usable fuel	[kg]	20,894	135,880
Maximum payload	[kg]	21,319	66,740
Mission payload	[kg]	10,660	33,370
Mission fuel	[kg]	4,080	69,600
Baseline engine	[kg]	2,763	10,108
Airframe	[kg]	35,887	137,585
Mission T-O	[kg]	56,153	260,770

TABLE 6.3: Mission specification for the aircraft and engine performance model

Wing circulation affects the velocity field in its close proximity, which modifies the direction of the engine inlet flow. It was envisioned that intake incidence angle may have an important effect on nacelle drag. Therefore, the local flow angle at the engine intake was computed. The upwash at the centreline of the engines inlet was estimated from the 2D velocity field calculated using a potential flow solver based on a higher order panel method[87]. The Kármán-Tsien approximation was used to correct local surface pressure to account for compressibility effects. This method required the definition of the wing airfoil coordinates, which were extracted from an open source database[113] for the Boeing 737 and from the NASA Common Research Model (CRM)[114] for the Boeing 777 class of aircraft. The CRM airfoil was chosen because it is aerodynamically similar to the Boeing 777,[114] whose coordinates are not publicly available. Here only the upwash effect of the wing was taken into account. Disturbances to the flowfield in front of and around the nacelle due to the presence of the fuselage were not accounted for. Validation exercises were carried out to compare the payload range diagram to published data (Appendix E).

The aircraft models were created to be representative of existing transonic civil transport aircraft not to model them exactly. A closer match with the real aircraft could be achieved by manual iteration of the aircraft model inputs in PSIMOD. To show that the created aircraft models are representative of real aircraft the payload range diagram calculated for the long haul aircraft is compared to that of a Boeing 777-300.[115] For the long haul case when no nacelle drag was modelled the maximum range was over-predicted by 1.1%. However when the skin-friction estimate (SFE) and ESDU methods were used to calculate nacelle drag the maximum range was underpredicted by 3.1% and 5.7% respectively. For the short haul aircraft, in this case when no nacelle drag was modelled the maximum range was over-predicted by 2.2%. The SFE and ESDU nacelle drag methods underpredicted nacelle drag by 3.4% and 7.6% respectively. Based on this comparison the aircraft models were deemed to be representative enough to be used as PSIMOD models to assess the impact of engine integration effects on overall mission performance.

The low order methodology for the estimation of wing upwash at the intake centreline was evaluated with computational studies. Three dimensional computations with the full-scale CRM with clean wing were used to estimate the wing effect on the flow angle. The potential flow solution mostly overpredicted the value of the local flow angle when compared to CFD results. For the operational envelope, the difference went from 0.75^o at an angle of attack of 0^o to -0.05^o at an angle of attack of 3^o.

In a similar way to the approach to engine modelling, aircraft modelling has been based on current aircraft and can be viewed as a re-engining exercise. Previous studies have made assumptions about future airframe performance particularly regarding wing performance.[55,56] For example, one airframe-engine synthesis study[55] used a composite wing and it assumed that this wing geometry would be re-optimised for every engine installation position so as to regain any aerodynamic performance lost due to the presence of the engine. Engine installation position was based on input from industrial partners and was based on best practice.[55] Another study applied technology scaling factors to the wing to

account for assumed future aerodynamic improvements.[55] Detailed wing geometry appropriate to this research is not commonly available in the open literature. This was the main motivation behind the use of the NASA CRM geometry in the CFD study in Chapter 7, as it features a transonic wing. It is also beyond the scope of this research to carry out an aerodynamic re-optimisation of the wing for each engine installation configuration. The exposition of PSIMOD in this Chapter can be viewed from the point of view of an engine manufacturer where detailed wing geometry may not be available.

6.3 Comparison of nacelle drag prediction methods

The difference in nacelle drag predicted by the ESDU drag prediction method[13] and the simple equivalent flat plate skin friction approach which is used in HERMES[12] was quantified by comparing the methods at discrete points throughout a flight profile. The BADA Eurocontrol model[106] was used to generate a flight profile. A Boeing 737-800 with an initial weight of 65,300kg[116] was modelled. Climb, cruise and descent segments were calculated using the BADA model. The climb profile (Figure 6.1) was calculated using BADA nominal values of a constant airspeed of 300kts to an altitude of 35,000ft and a cruise Mach number of 0.81. Similarly the descent profile (Figure 6.1) was calculated by descending from cruise conditions with the BADA nominal constant airspeed of 290kts[106]. Cruise length was iterated until the total mission length equalled 1,000km. Due to the limitations of the ESDU drag prediction method, the engines are assumed to be at 0^o angle of attack. For this initial calculation, the engine massflow rate was not known as it is not calculated by the BADA model so the engine massflow capture ratio (MFCR) could not be calculated. A typical cruise MFCR of 0.73 was selected for the whole flight.

Results from this preliminary evaluation using the ESDU drag prediction method are presented in Figure 6.2. Throughout the climb phase the contribution of nacelle drag increases from 1.9% at take-off to approximately 4.8% in cruise (Figure 6.2). Nacelle

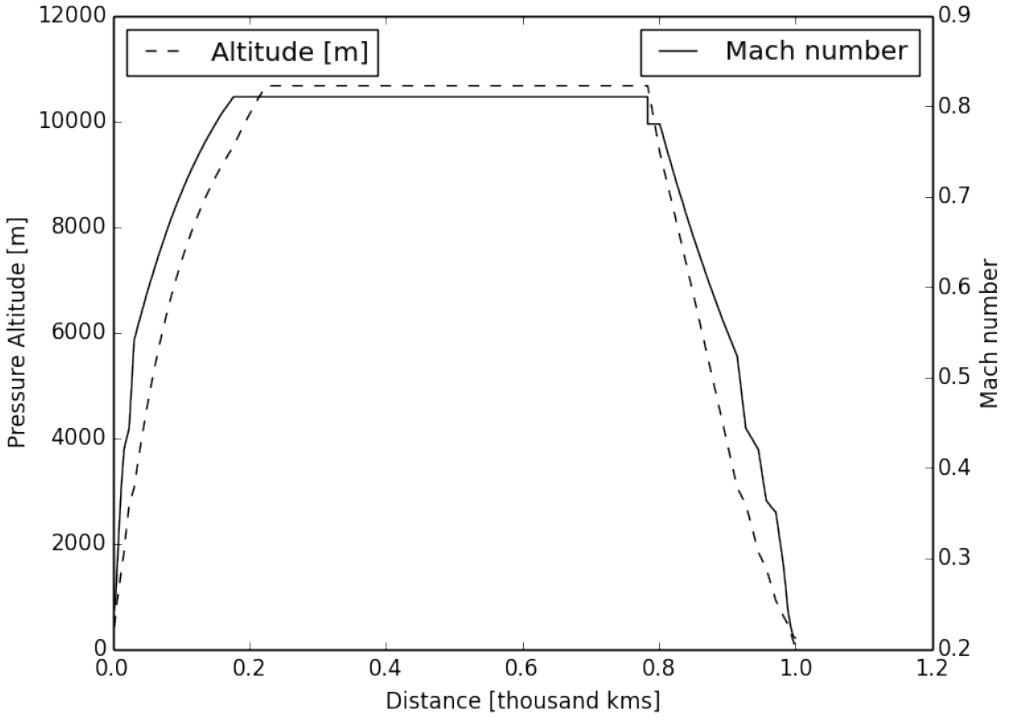

FIGURE 6.1: BADA calculated flight trajectory for a Boeing 737-800 with an initial weight of 65,300kg

drag makes its biggest contribution at top of climb. Throughout the descent phase this contribution reduces from a maximum of 4.9% to 0.9% of total aircraft drag (Figure 6.2).

To see how these contributions change as engine sizes increase in relation to aircraft size this calculation was repeated with engine size scaled to a factor of 1.5 in factor increments of 0.1. Only the nacelle drag calculation was recalculated. Total aircraft drag for these aircraft with larger diameter engines was calculated using Equation (6.1):

$$D_{a,tot} = [D_{BADA} - D_{nac,baseline}] + D_{nac} \tag{6.1}$$

where D_{BADA} is the BADA predicted aircraft drag, $D_{nac,basline}$ is the predicted nacelle drag for the baseline engine and D_{nac} is predicted nacelle drag.

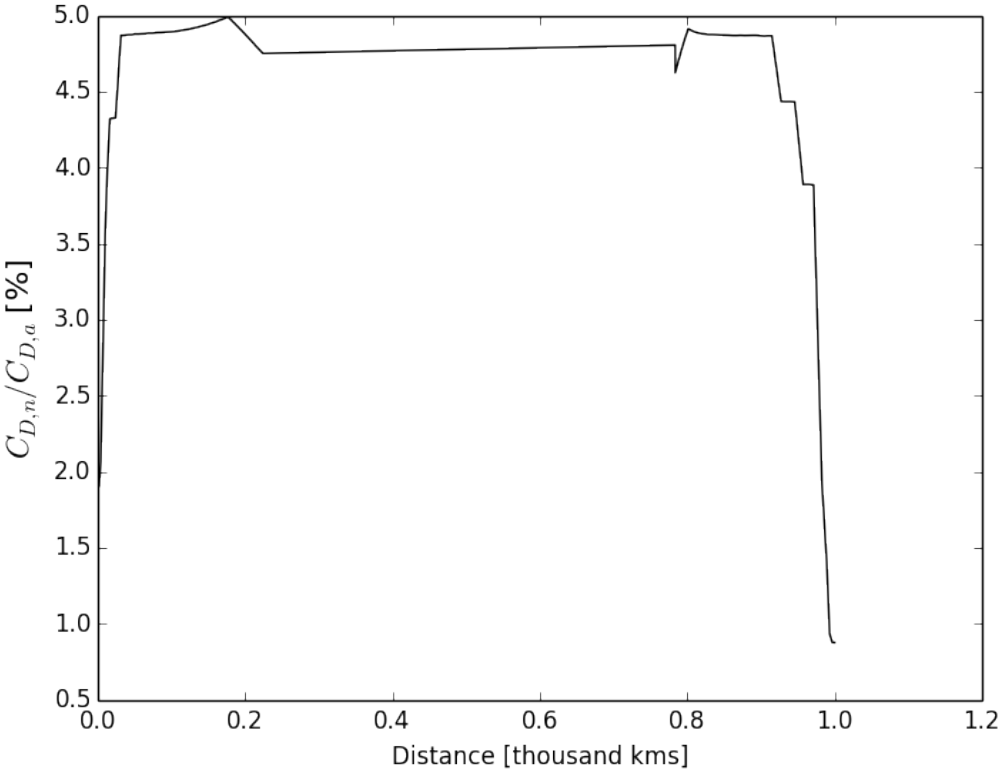

FIGURE 6.2: Percentage contribution of nacelle drag to overall aircraft drag throughout a flight profile (Figure 6.1) calculated using the ESDU drag prediction method

The percentage contribution of ESDU predicted nacelle drag to overall aircraft drag remained almost constant throughout the trajectory. For this level of modelling using the ESDU drag prediction method nacelle drag contribution does not significantly change throughout the mission. This is a due to the fact that this method does not account for nacelle local flow incidence and highlights a shortcoming in using the ESDU method throughout a flight. The effects of nacelle local flow incidence are quantified in §6.7.

The percentage contribution of nacelle drag increases almost with the square of engine scale from 4.4% for the baseline engine up to 9.5% for an engine scaled up by a factor of 1.5 (Figure 8). This is because the nacelles have the same non-dimensional geometry and hence the same drag coefficient and their reference area scales with the square of their diameter with a slight reduction in drag due to increases in nacelle Reynolds number.

Up until this point in the discussion nacelle drag was calculated using the ESDU drag prediction method as implemented in PSIMOD. This method was compared to the skin friction estimation (SFE) in HERMES[12] as engine size increases relative to aircraft size (Figure 8). The SFE method under predicts nacelle drag in comparison with the ESDU method by approximately 54%. As the engine scale factor increased from 1 to 1.5 the disparity between the methods increases. This difference is the justification for the implementation of the ESDU nacelle drag method into PSIMOD method instead of the simple skin friction estimate. However as the ESDU method does not take into account nacelle local flow angle and installation effects corrections need to be applied to take these aspects into account. In §6.7 and §6.8 these aspects will be discussed and developed further.

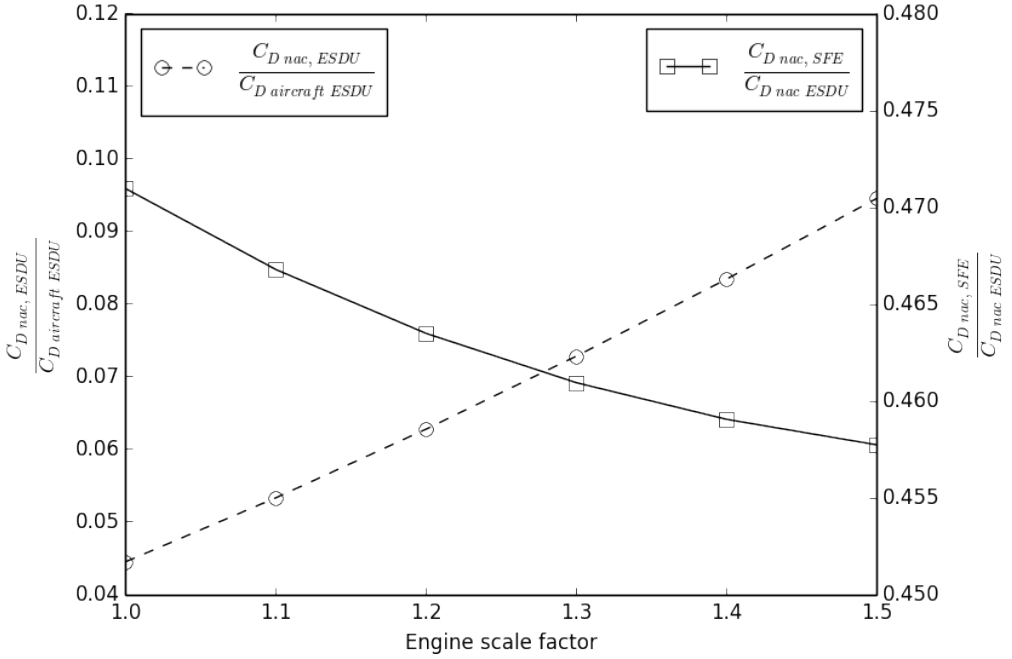

FIGURE 6.3: The effect of increasing nacelle size relative to aircraft size on nacelle drag averaged over a flight profile (Figure 6.1) calculated using the ESDU and SFE drag prediction methods. Engine scale factor is the engine maximum diameter non-dimensionalised by the baseline engine maximum diameter

To see how the nacelle drag calculated using the ESDU drag prediction method as implemented in PSIMOD compares to the skin friction estimation (SFE) in HERMES as engine sizes increase relative to aircraft size this analysis was repeated using SFE nacelle drag

(Figure 6.3). The SFE method under predicts in comparison to the ESDU method by approximately 40%. As the nacelle maximum diameter increased from 3.389m to 5.084m the disparity between the methods increases. This difference is the justification for the implementation of the ESDU nacelle drag method into the revised HERMES method instead of the simple skin friction estimate. However as the ESDU method does not take into account nacelle local flow angle and installation effects it on its own is not sufficient. In § 6.7 and § 6.8 these aspects will be discussed and developed further.

6.4 The importance of modelling nacelle drag

The contribution of nacelle drag to fuel burn was investigated by comparing the skin friction estimation (SFE) and ESDU models to the case where the effect of nacelle drag is neglected (NND). PSIMOD links the calculation of the trajectory with the engine thermodynamics, aircraft performance and nacelle uninstalled drag models. Results using the PSIMOD framework have been calculated for short haul and long haul missions (Table 6.3) with the reference baseline engines (Table 6.2).

The reduction in overall drag on both missions due to the omission of nacelle drag means that the aircraft climb and reach their cruise altitude quicker as the aircraft are climbing at maximum available thrust (Figure 6.4). Overall, when the nacelle drag is modelled by the ESDU method, relative to the zero-drag nacelle, there is an increase in fuel burn of 6.5% on the long haul and 9.3% on the short haul (Table 6.4) and the nacelle drag contributes significantly to the overall fuel burn.

Relative to this ESDU estimate, the impact of the simpler SFE method predicts a lower nacelle drag penalty across the missions of 5.3% and 3.9% (Table 6.4). For these particular configurations and flights, the difference between these two methods for nacelle drag estimation is shown to have an important impact on the overall fuel burn. The ESDU method is more accurate when compared to experimental data[28] because it takes into

account nacelle geometry and MFCR, which are key influences on nacelle drag generated from the nacelle.

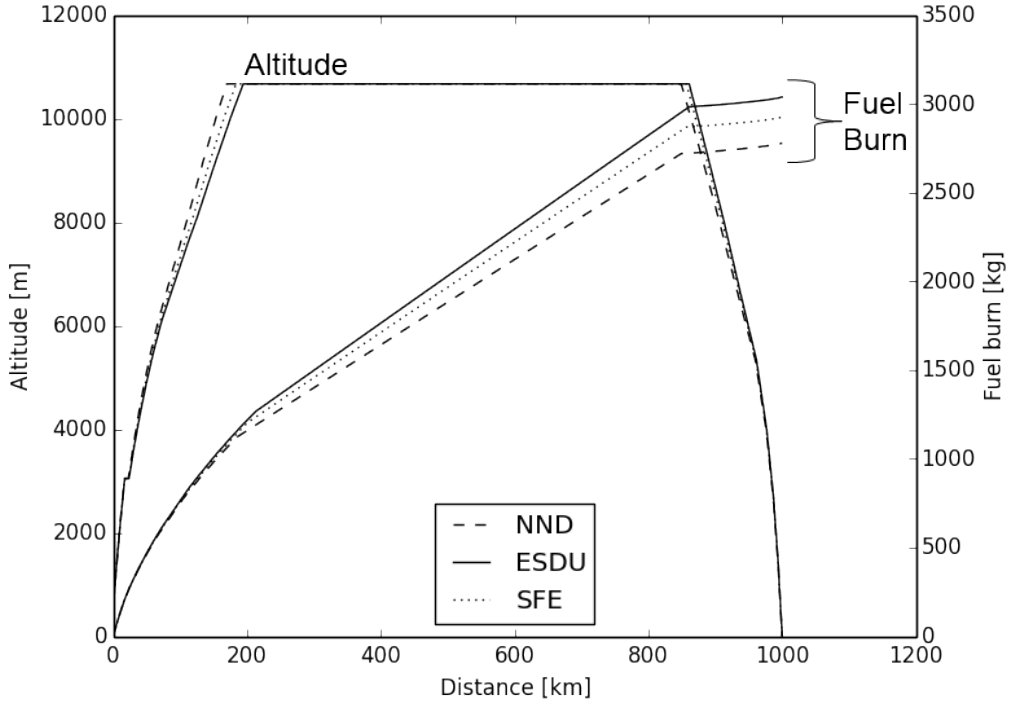

FIGURE 6.4: Comparison of nacelle drag estimation methods for baseline engines throughout the short haul mission (Table 6.4)

It was found that nacelle drag had a greater relative impact on the performance of the aircraft for the short haul mission. The main reason for this is the lower contribution of the engines to the overall aircraft drag on the long haul mission. While 6.4% of the mid cruise drag on the Boeing 777 type aircraft on a long haul mission is due to the presence of the nacelle, it is about 8.6% on the short haul flight. This is because the maximum nacelle cross-sectional area on the CUTF-BPR5.1-120K is about 4% of the aircraft wing area, whereas the nacelle on the CUTF-BPR5.8-410K is just 2.8%. The contribution of nacelle drag to overall aircraft drag will therefore be larger for the short haul aircraft and its mission fuel burn will be more sensitive to changes in nacelle drag.

In the previous section the effects of modelling nacelle drag on overall mission fuel burn have been quantified. To ascertain how these effects are translated into changes in the

		Short haul			Long haul		
		NND Value	ESDU Δ	SFE Δ	NND Value	ESDU Δ	SFE Δ
Climb	Distance [km]	186	14.60%	8.30%	259	12.00%	6.70%
	Fuel burn [kg]	1,124	12.60%	7.20%	4,917	10.40%	5.70%
	Time taken [hr]	0.24	13.60%	7.80%	0.33	11.20%	6.20%
Cruise	Distance [km]	663	-2.30%	-1.20%	5,563	-0.30%	-0.20%
	Fuel burn [kg]	1,595	7.60%	4.30%	43,159	6.10%	3.80%
	Time taken [hr]	0.77	-2.30%	-1.20%	6.2	-0.30%	-0.20%
Descent	Distance [km]	151	-7.90%	-5.10%	178	-7.20%	-4.40%
	Fuel burn [kg]	59	-7.10%	-4.50%	185	-6.70%	-4.00%
	Time taken [hr]	0.22	-7.60%	-4.80%	0.26	-7.00%	-4.20%
Total	Distance [km]	1,000	0.00%	0.00%	6,000	0.00%	0.00%
	Fuel burn [kg]	2,778	9.30%	5.30%	48,260	6.50%	3.90%
	Time taken [hr]	1.23	-0.10%	-0.10%	6.79	0.00%	0.00%

TABLE 6.4: Comparison of nacelle drag estimation methods for baseline engines throughout short haul and long haul. NND indicates no nacelle drag. ESDU evaluates the drag using ESDU 81024 and SFE evaluates nacelle drag using the baseline skin friction estimate

	Short haul	**Long haul**
Maximum payload capacity [kg]	21,319	66,739
Maximum fuel capacity [kg]	20,894	135,880
Max. break release weight, baseline engine ($W_{MAX,BR,baseline}$) [kg]	78,751	299,300
Operating empty weight, baseline (OEW_{base}) [kg]	41,145	157,801
Max. combined payload & fuel capacity ($W_{MAX,BR,baseline-OEWbase}$) [kg]	37,603	141,499

TABLE 6.5: Mission settings used for the comparison of the payload-range diagrams for different methods of nacelle drag estimation

extents of the payload range diagram both the short haul and long haul aircraft with baseline engines (Table 6.5) have been modelled for a series of missions.

To construct a payload range diagram (example in Figure 10) three bounding numbers are required. For low ranges the payload range diagram is typically bounded by the maximum payload capacity of the aircraft. Longer ranges are then achieved by increasing the mission fuel. This can continue until the maximum break release weight of the aircraft is reached

(Point A, Figure 10). To further increase the range of the aircraft payload must be traded for fuel. Range can continue to be increased using this method until the maximum fuel capacity of the aircraft is reached (Point B, Figure 10). Range can continue to be increased by reducing the aircraft payload until maximum range of the aircraft is achieved with no payload and maximum fuel (Point C, Figure 10).

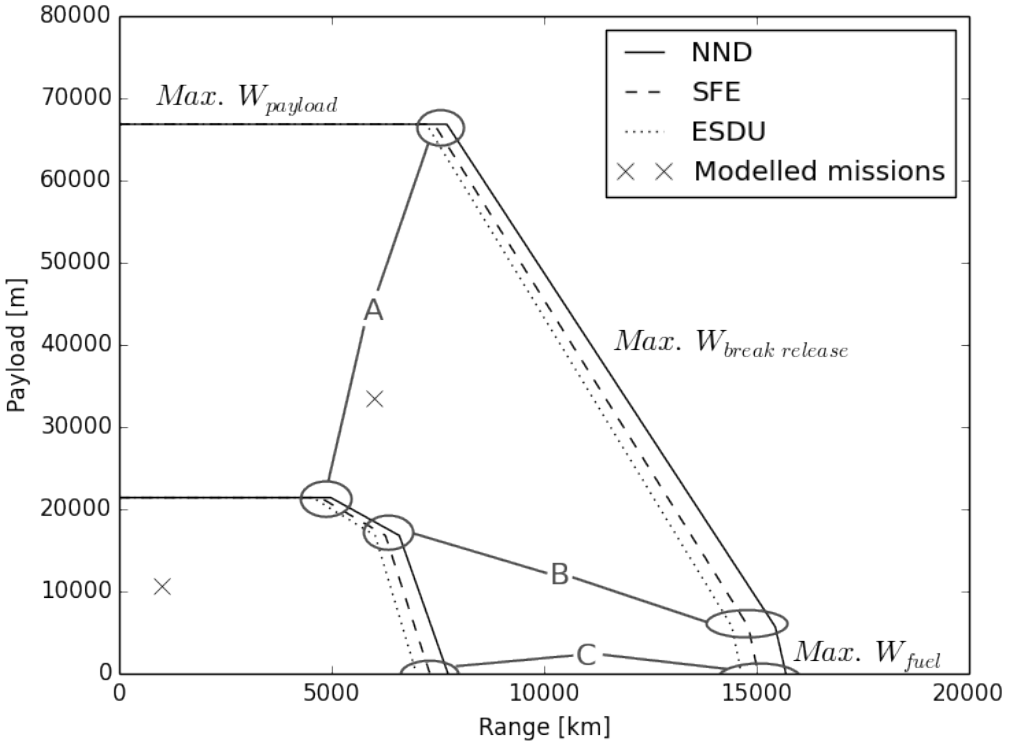

FIGURE 6.5: Comparison of the payload-range diagrams for different methods of nacelle drag estimation

6.5 Influence of nacelle size on short haul mission performance

The impact of the installation of larger diameter engines on a Boeing 737 like mission was undertaken to assess the relationship between improvements in uninstalled engine SFC and overall fuel burn. New engines were modelled (Table 6.2) with the same core as the

baseline engines but with an increase in BPR which leads to larger nacelle diameters with maximum increases of approximately 28% relative to the baseline (Table 6.2, Table 6.6). The missions were also modelled for the configurations where the increase in engine weight was neglected to allow the effects of drag and weight to be separately identified. The effect of the changes in fan and nacelle weight was evaluated by considering the cases where the weight increase was not modelled (WINM) as well as models using Jenkinsons[110] and WATE++[108] correlations for nacelle and engine weight, respectively.

Mission calculations were carried out by linking the Turbomatch simulations for baseline and larger BPRs with the aircraft models through the PSIMOD framework. Hermes computations for flight performance included the nacelle drag estimated by ESDU method.

The $WATE++$ method was evaluated using known engine configurations and an uncertainty of approximately 20% on the estimation of the baseline engine weight was found. To understand how this uncertainty translated into uncertainty on fuel burn a study was carried out using the CUTF-BPR8.5-150K (Table 6.2) engine model. Combined engine and nacelle weight was varied from that of the baseline engine (2763 kg) to 10% greater than that predicted by the $WATE++$ method (4543kg). This variation was carried out across a set of mission ranges and the fuel required to fly the exact same trajectory with no fuel remaining was calculated. To put this in context a 10% variation in combined engine and nacelle weight was equivalent to 0.7% change in aircraft weight which affects the aircraft lift and drag characteristics through the flight. The $\pm 10\%$ variation in combined engine and nacelle weight resulted in a variation of $\pm 0.8\%$ in mission fuel. Although there is a significant change in magnitude of the predicted fuel burn with changes in combined engine and nacelle weight the overall changes were linear with aircraft weight and range and as such the weight prediction method was found to be adequate to predict trends in mission fuel burn.

The improvements in the cruise SFC for the uninstalled engines from baseline BPR to the cycles with larger BPR ranged from 6% to 7% (Figure 6.6). Within the assumptions

used in this model, although there are clear benefits in the cruise part of the flight, this does not always translate into improved installed fuel burn across the full mission. When the drag increase due to the larger nacelle diameter was modelled and the weight increase neglected, the cycle benefits of the increased BPRs was offset (Figure 6.6).

L_f/L_t	0.3
L_a/L_t	0.6
L_f/D_m	0.708
L_a/D_m	1.417
D_i/D_m	0.723
D_e/D_m	0.656
A_i/A_t	1.244

TABLE 6.6: Non-dimensional nacelle parameters

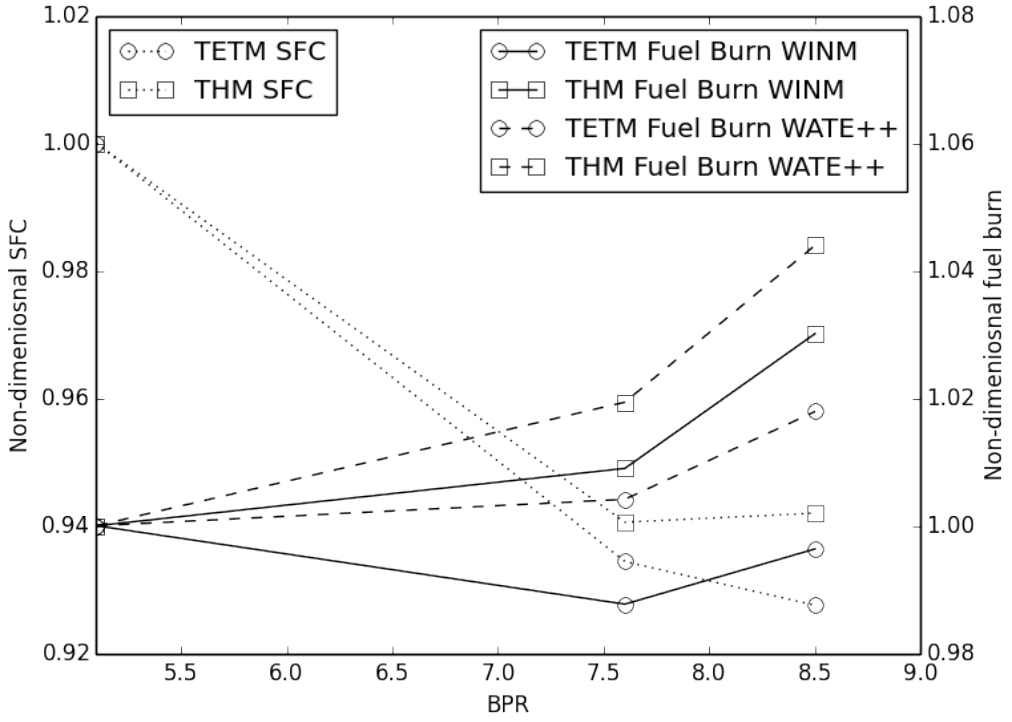

FIGURE 6.6: The influence of nacelle size and weight on mission fuel burn for the short haul trajectory

When the increase in weight is neglected (WINM), the fuel burn results are different for both cycle matching processes. The larger BPR engines with matched TET generated improvements in fuel consumption up to a maximum of 1.2% (Figure 6.6). However, when

the thrust matched engines are simulated, the fuel burn increases for BPRs of 7.6 and 8.5. The difference in results between the two matching philosophies comes mainly from the time spent on cruise in both trajectories (Table 6.7). As the TET matched engine has more thrust available it can reach cruise altitude about 18% faster than the baseline (Table 6.7) and then fly at its design point for longer. Whereas the thrust matched engine has the same available thrust as the baseline, but the overall aircraft drag is greater due to the increase in the engine size. This impacts the climb time and increases it by 14% compared to the baseline trajectory (Table 6.7). Therefore, the thrust matched engines on the short haul mission fly a relatively shorter period of time at their design point and hence have an increased overall fuel burn during the studied mission.

		Baseline	BPR 7.6 TETM CUTF-BPR7.6-140K		BPR 7.6 ThM CUTF-BPR7.6-120K	
		Value	Value	Δ from BL	Value	Δ from BL
Climb	Distance [km]	213	173	-18.80%	244	14.50%
	Fuel burn [kg]	1,266	1,095	-13.50%	1,333	5.30%
	Time taken [hr]	0.27	0.22	-17.90%	0.31	14.20%
Cruise	Distance [km]	648	694	7.00%	622	-4.00%
	Fuel burn [kg]	1,716	1,852	7.90%	1,670	-2.70%
	Time taken [hr]	0.75	0.8	7.00%	0.72	-4.00%
Descent	Distance [km]	139	133	-4.10%	134	-3.70%
	Fuel burn [kg]	55	53	-3.10%	62	13.20%
	Time taken [hr]	0.2	0.2	-3.90%	0.2	-3.50%
Total	Distance [km]	1,000	1,000	0.00%	1,000	0.00%
	Fuel burn [kg]	3,038	3,000	-1.20%	3,065	0.90%
	Time taken [hr]	1.22	1.22	-0.30%	1.23	0.10%

TABLE 6.7: Comparison between the mission fuel burn on the short haul aircraft for engines obtained with TET matching and Thrust matching philosophies. The Baseline engine is CUTF-BPR5.1-120K.

When the increased nacelle and engine weight were also accounted for the fuel burn increased by up to 2% (Figure 6.6), relative to the case where no weight increase was modelled. It resulted in the loss of the potential gains found on the TET matched engines when the combined effect of nacelle drag and weight are taken into account.

For both engine modelling approaches (TETM and THM) and when both weight and drag were modelled, in all cases mission fuel burn was greater than that of the baseline configuration. This indicates that the optimum BPR for these engines is less than 7.6 with further engine models required to find the exact value. A previous study [56] carried out on an aircraft similar to a Boeing 737-800 with a two-spool direct drive turbofan engine found an optimal BPR of 7.1. Though there are differences between the exact aircraft and engine models as well as the methods used these results are consistent.

As discussed in §6.4, the influence of the nacelle drag was evaluated on the limits of the payload range diagram (Figure 6.5). The assessment was made for missions with and without the engine and nacelle weight increase modelled (Figure 6.7). The baseline engines and the larger engines with TET matched philosophy were used for the mission analyses (Table 6.2). The relative change in range from that achieved by the baseline engine with the same fuel and payload (Equation 6.2) was defined to study installation impact on the payload range diagram. With ΔR_{BL} it is possible to evaluate the change in the boundaries of the payload range diagram due to the installation of larger engines.

$$\Delta R_{BL} = \frac{R - R_{BL}}{R_{BL}} 100\% \tag{6.2}$$

An increase in range between 1.1% and 0.6% over the baseline mission was found for the largest engines (BPR=8.5) at maximum $W_{breakrelease}$ (Point A to B, Figure 6.7) with baseline weight. This increase rose to 1.8% at Point A and 1.4% at Point B for the engines with a BPR=7.6. For short flights (Points A and B Figure 6.7) the increase in BPR has a positive effect if the weight penalty is not taken into account. However, for missions with maximum range (point C Figure 6.7) the sensitivity to nacelle drag increases. This is partly due to the relative participation of the nacelle drag on the overall drag of the aircraft. As the mission with no payload is flown with less weight it requires a lower C_L, which implies a lower overall C_D. In the short haul aircraft the nacelle drag is 11% of

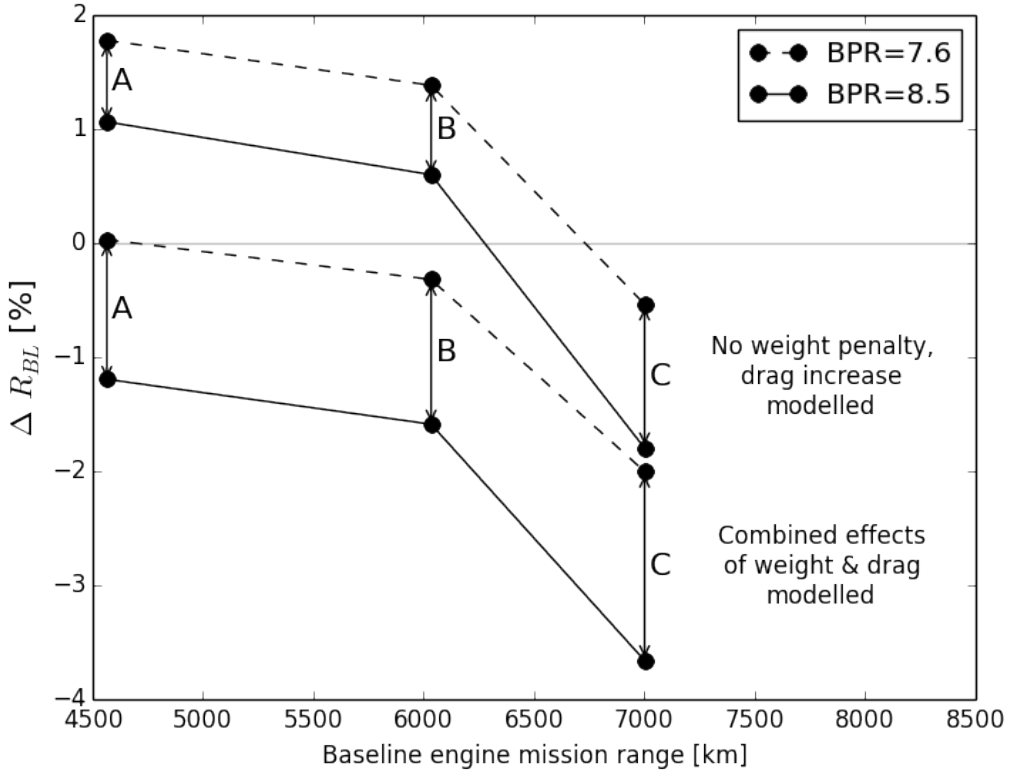

FIGURE 6.7: Influence of the nacelle size and weight on the limits of the payload range for the short haul mission

total C_D at mid-cruise for the short range (point A Figure 6.7) and approximately 12% for long range (point C Figure 6.7). The change in the range sensitivity is also explained by relatively smaller climb and descent phases on longer flights. As discussed previously, the gains obtained due to excess of thrust in these phases become relatively smaller for longer missions.

Even though the largest engine has the lowest uninstalled SFC (Figure 6.7) it does not produce the best mission performance (Figure 6.7). This is due to the fast increase in drag compared to the decrease in uninstalled SFC between the BPRs of 7.6 and 8.5. The SFC decrease due to this increase of BPR is approximately 0.7% (Figure 6.7) while the drag increase scales with D^2_{max}. Nacelle drag increased by 8.8% when the BPR was increased from 7.6 and 8.5.

When the combined effect of weight and drag penalties is modelled, the gains from uninstalled SFC are negated on the B737 like mission (Figure 6.7). The effect of increased drag and weight for the larger engines overcome the benefits of the lower uninstalled SFC.

6.6 Influence of nacelle size on long haul mission performance

Similar trends to those discussed in §6.5 were found for the engines on the long haul aircraft (Figure 6.8). Increased BPR on the B777 like aircraft resulted in gains on uninstalled cruise SFC of approximately 3% to 5% (Figure 6.8). These gains in uninstalled SFC resulted in approximately 1.5% lower installed fuel consumption if the weight increase is not taken into account (Figure 6.8).

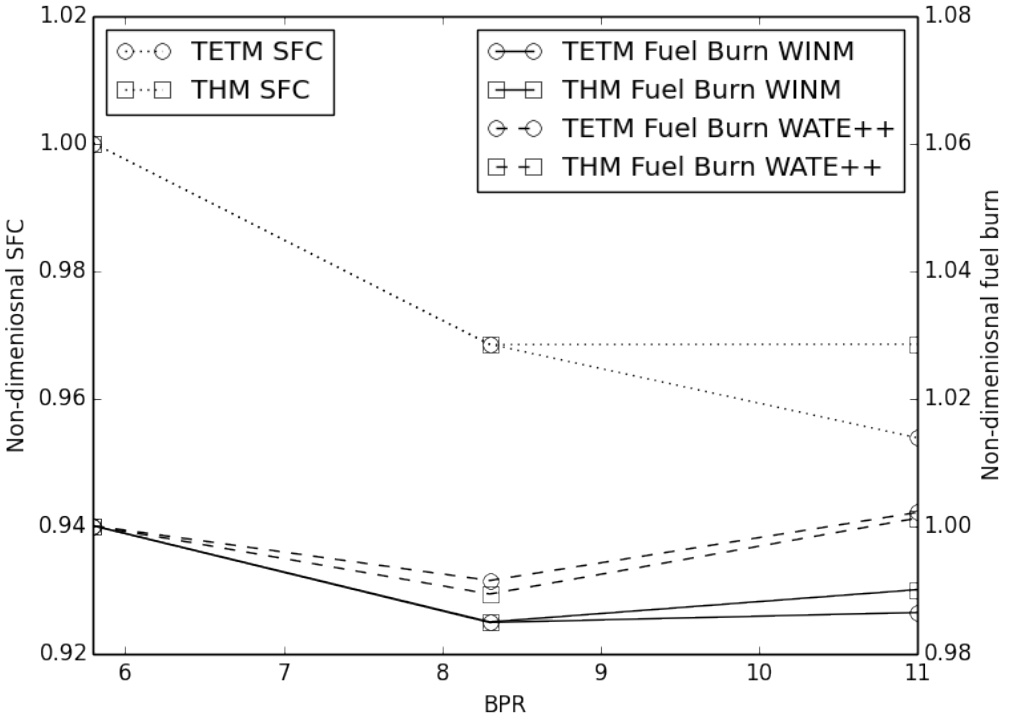

FIGURE 6.8: The influence of nacelle size and weight on mission fuel burn for the long haul trajectory

When the penalties of increased nacelle and engine weight was also taken into account the fuel burn increased by up to 1%, relative to the WINM case (Figure 6.8). Improvements in fuel consumption were achieved by increasing the BPR up to a maximum decrease of 1% in fuel burn (Figure 6.8). From that maximum a further increase in BPR starts to increase mission fuel burn due to the combined action of the increased nacelle drag and weight. As it was found on the short haul case (§6.5), the nacelle drag increased by a higher rate than the uninstalled SFC gains for a BPR change from 8.3 to 11.

For the engines with a BPR=8.3 there was reduction in overall mission fuel burn when compared to the baseline engine. However when the BPR was increased to 11 the influence of weight and drag eroded any gains. Therefore the optimal BPR for these engines is between that of the baseline, 5.8 and 11. A similar study[55] of optimum BPRs for a a long haul civil transport aircraft (based on a Boeing 777-200 with technology improvements) found optimal BPRs of 11 and 14.5 depending on the engine manufacturer and the assumed engine technologies. These results are not inconsistent however with the results presented here. This is due to the differences in assumptions on technology levels particularly with respect to engine technology. The modelling within this research is based on current technology levels while the similar study[55] assumed the use of future engine technologies such as advanced contra-rotating fans, geared turbofans and variable area nozzles.

When the impact on the payload range is studied (Figure 6.9), the long haul mission produced approximately the same trends found for the short haul aircraft (§6.5). The baseline mission range was increased by 2% when only drag penalty was taken into account. If the combined effect of increased weight and drag is modelled, the gains in range compared to the baseline are reduced to 0.5% to 1% (Figure 6.9). The engine with a BPR of 11 generates smaller gains in range at Points B and C than the engine with a BPR of 8.3 (Figure 6.9). This was also the case for the short haul mission. As discussed for the short haul case (§6.5), this effect is due to the faster increase in drag compared to the SFC improvement. However for Point A (Figure 6.9), the maximum break release weight

point CUTF-BRR-11-450K has a larger increase in range over the baseline engine than CUTF-BPR8.3-430K (2.16% as opposed to 1.9%). This result is an outlier and is the only case in which the largest BPR engines had the largest increase in range over the baseline mission. This was due to the fact that CUTF-BRR-11-450K has a larger thrust CUTF-BPR8.3-430K. This means that it can climb quicker and hence spend less time than in this high drag configuration. However CUTF-BRR-11-450K has more drag in cruise than CUTF-BPR8.3-430K. It is the balancing of these two effects which causes a crossover point in Figure 6.9. At higher take-off weights and lower ranges CUTF-BRR-11-450K wins out due to its larger thrust and less time spent in climb. At lower take-off weights and higher ranges CUTF-BPR8.3-430K gives a larger increase in range over the baseline due to the fact that it has less drag in cruise than CUTF-BRR-11-450K. This crossover point occurs at a range of 12,505km.

When only drag is modelled the potential increase in range due to larger engines are of similar order for both types of aircraft on payload limits from A and B (Figure 6.7 and Figure 6.9). However, when the weight is taken into account the short haul aircraft is notably more sensitive. Engine weight increase has a stronger impact on the B737 type mission because it represents a relatively higher portion of the maximum take-off weight. The weight increase on the short haul aircraft due to larger engines goes from 2.6% to 3.5% of the maximum take-off weight, while it increases from 0.9% to 2.2% on the long haul mission.

Overall, results show that potential gains in uninstalled efficiency can easily be lost due to the combined effect of drag and weight. Therefore, these results highlight the importance of the nacelle drag and weight considerations at different parts of the flight and underline the need for accurate nacelle and engine weight estimates within the context of the expected notable increases in fan diameters.

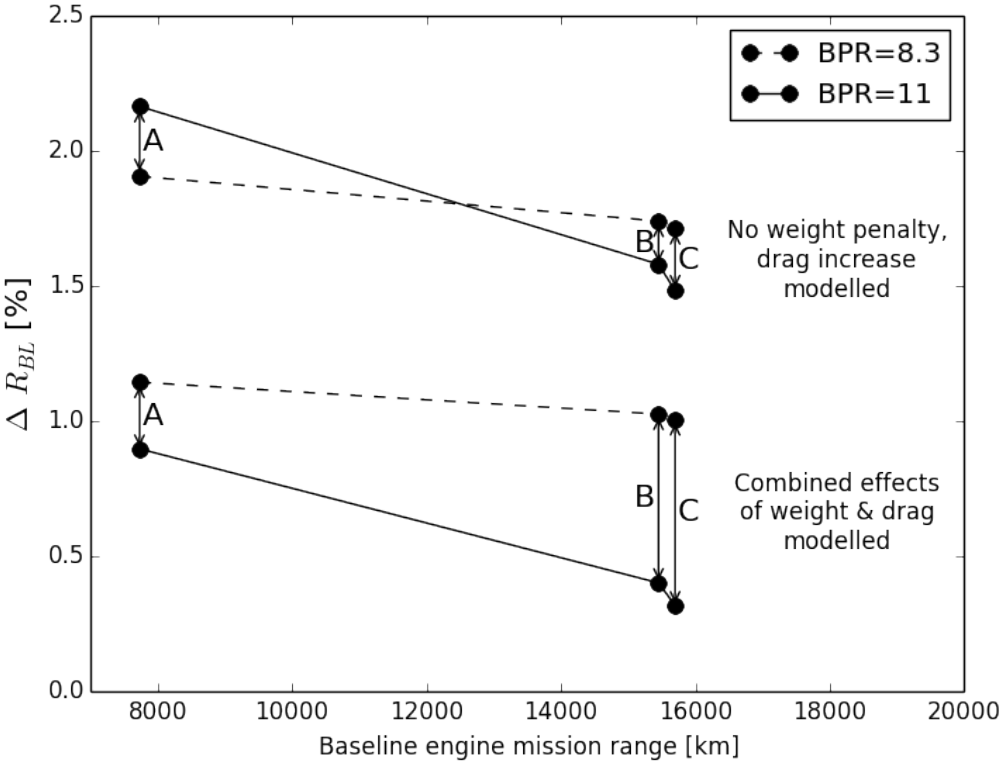

FIGURE 6.9: Influence of the nacelle size and weight on the limits of the payload range for the long haul mission

6.7 The influence of nacelle local flow angle

Nacelle total upflow angle (A) is the result of nacelle incidence, upwash angle and nacelle offset angle (Figure 3.13). As described in 6.3, a correction has been made to the ESDU estimated drag to take into account the effects of local incidence, with correlations which relate the local nacelle flow incidence with the nacelle C_L and C_D. These correlations were extracted from CFD which was carried out with Mach number varied from 0.1 to 0.85, MFCR from 0.25 to 1.5 and nacelle total upflow angle (A, Figure 3.13) varied from -10^o to 10^o. The calculations were performed with $Re_{FAN} = 16.4 \times 10^6$. These correlations are applied as a correction to the ESDU drag prediction method within PSIMOD. For this analysis PSIMOD used these correlations and calculated nacelle drag at each point in the mission as a function of engine geometry, nacelle shape, flight conditions, Reynolds

number, MFCR and local nacelle incidence.

The effect of nacelle incidence has been quantified by evaluating the percentage change in mission fuel burn from the baseline mission (Figure 6.10). The engine inclination relative to the local chord line (γ, Figure 3.13) for the baseline mission was defined such that the nacelle total upflow angle at mid-cruise was equal to zero. Variations to the nacelle inclination angle were applied to evaluate the fuel burn sensitivity to changes in γ from the baseline value. Both baseline engines and the two largest engines with TET matched philosophy (Table 6.2) were assessed for the short and long haul missions described in Table 6.3.

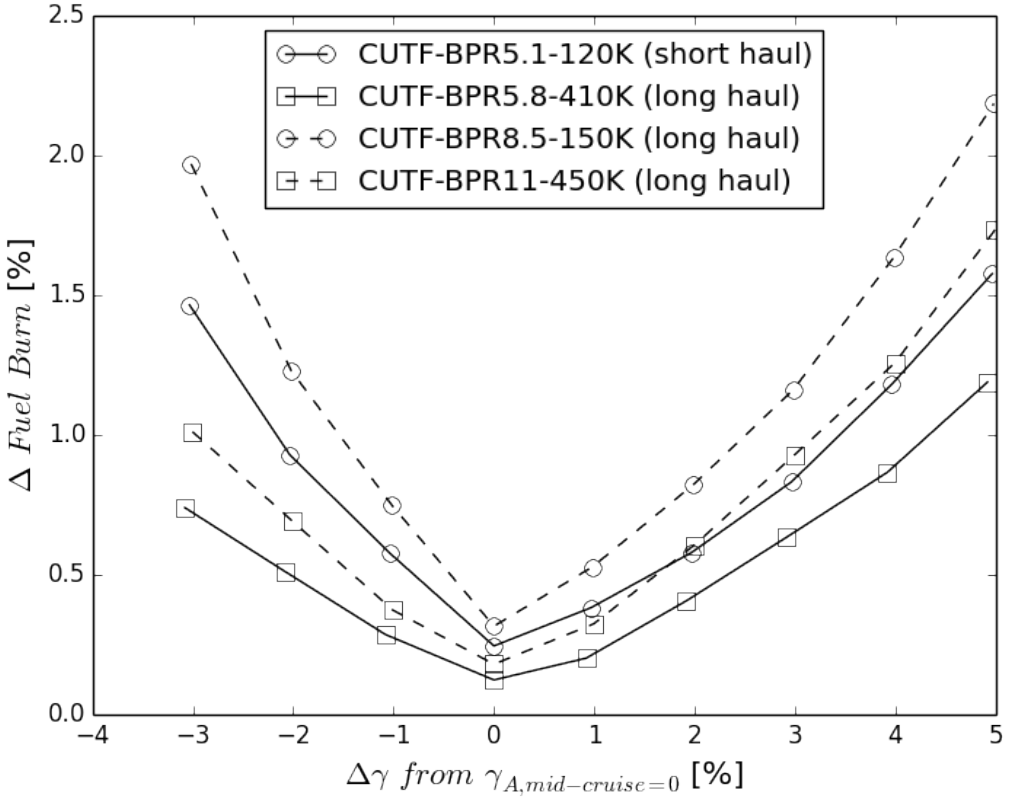

FIGURE 6.10: Influence of modelling nacelle total upflow angle on the flight performance calculation

It was found that the correction for local flow angle applied to PSIMOD increased the calculated fuel burn on both the short and long haul missions (Figure 6.10). In all cases

the modelling of A led to an increase in overall mission fuel burn, whose sensitivity to nacelle offset angle was different for the range of scenarios studied. As expected from previous results (§ 6.4, § 6.5 and § 6.6), the short haul aircraft was more sensitive to $\Delta\gamma$. The percentage increase in fuel burn on the B737 type aircraft with baseline engines reached a maximum of 1.6% for the range studied, while the maximum increase on the B777 type aircraft with baseline engines was around 1.2% (Figure 6.10). This difference is mainly an effect of relative engine size, as discussed in § 6.4.

The effect of modelling A becomes stronger when larger engines are taken into account. For the study of short haul mission with CUTF-BPR8.5-150K engines (Table 6.2), it was found that the increase in mission fuel burn had a maximum value of 2.2% within the range studied. A similar result was found for the long haul mission with CUTF-BPR11-450K engines, whose maximum increase was 1.7% for a change in nacelle inclination of 5^o (Figure 6.10). Results show that the increase in fuel burn due to variations of the engine inclination angle is not linear. Fuel burn sensitivity varies differently depending on the type of mission and relative size of the engine on the aircraft. All the cases showed a small increase when $\Delta\gamma = 0$, which ranged from 0.12% to 0.31% (Figure 6.10). However, as γ was changed to the maximum extents analysed, the results on mission fuel increase ranged from 1.2% to 2.2% (Figure 6.10).

As mission range is increased the same trends and sensitivities were found (Figure 6.11). The only notable change is the increase in $\Delta\gamma$ at which minimum fuel burn occurs with increases in range. This is because the engine inclination relative to the local chord line (γ, 3.13) was defined such that the nacelle total upflow angle at mid-cruise was equal to zero for the baseline missions (1000km for the short haul and 6000km for the long haul). As mission range is increased from these distances the mission distance at which the mission mid-cruise occurs. As all flights were modelled with the same take-off payload and fuel, aircraft weight at the mid-cruise point decreases with mission range. This decrease in mid-cruise weight results in a decrease in aircraft angle of attack at this point. This decrease

in conjunction with a reduction in upwash angle due to a decrease in the lift generated by the wing leads to a decrease in A at mid-cruise.

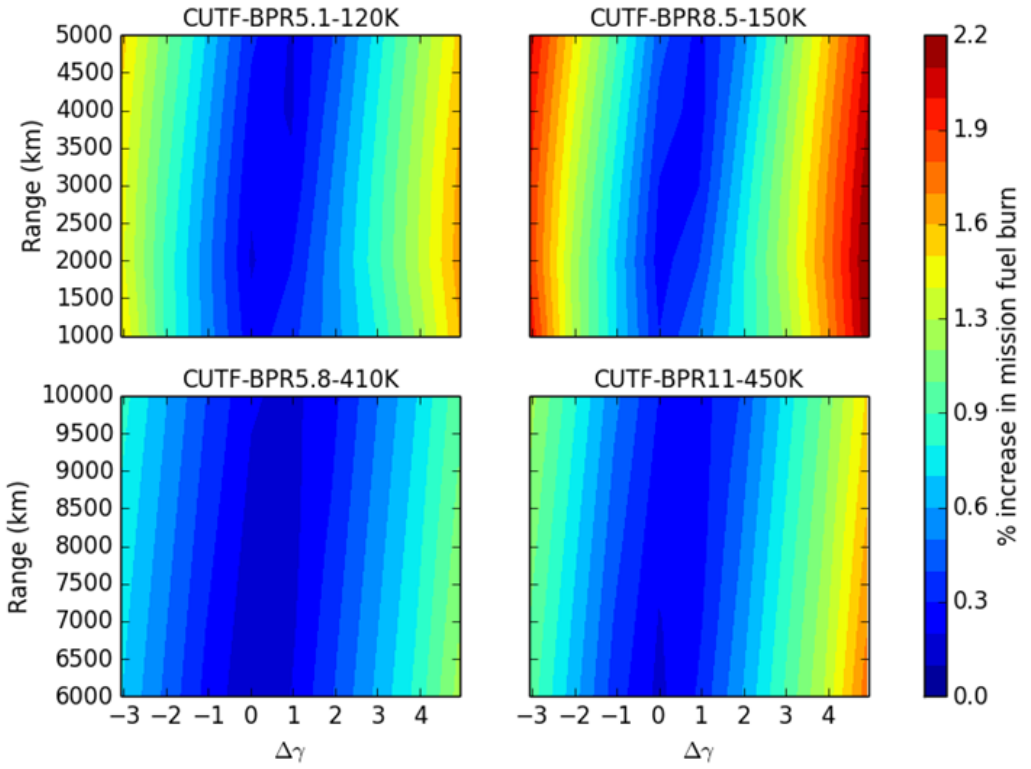

FIGURE 6.11: Influence of modelling nacelle total upflow angle on the flight performance calculation over a series of ranges

These results highlight the importance of an adequate modelling of nacelle upflow angle especially for modern and future installations, which will tend to integrate engines with larger fan diameters and lower specific thrust to the airframe. It is shown that the ESDU drag prediction method on its own is not adequate and corrections need to be made to account for nacelle total upflow angle in preliminary design.

6.8 The effect of propulsion system installation quality on overall flight performance

To investigate mission fuel burn sensitivity to the quality of propulsion system integration a correction has been made to the ESDU estimated drag to take into account the installation drag effect. The nacelle drag increment due to nacelle installation can range from 1 to 1.5 times the drag of the isolated nacelle[117]. This factor allows the comparison of fuel burn between two missions with different types of installations. This factor was varied from 1 to 1.5 and the effect of propulsion system installation quality on overall flight performance was quantified. Mission fuel burn was non-dimensionalised by baseline mission fuel burn (Figure 11). The CUTF-BPR5.1-120K and CUTF-BPR8.5-150K engines on the short haul and the CUTF-BPR5.8-410K and CUTF-BPR11-450K engines on the long haul (Table 6.2) were flown for the missions described in Table 6.3. In all cases there was a linear increase in mission fuel burn with increases in installation drag factor (Figure 6.12). The results showed that the rate of change of mission in fuel burn with the quality of installation is a function of the engine size. With a larger engine, the fuel burnt in the short haul mission increased from 4.4% to 6% on the worst installation quality modelled, whereas it increased from 3.1% to 4.6% on the long haul mission (Figure 6.12). As discussed in §6.4, the short haul aircraft is more sensitive to the installation effects, because its engines are bigger relative to the airframe than in the long haul case.

With an installation factor of 1.5, the combined effect of nacelle drag and installation quality increased the calculated mid cruise C_D of the aircraft by 8 drag counts (dc) on the B777 type aircraft and by 12 on the B737 type aircraft, whose missions were studied with their respective baseline engines (Table 6.2). When the effect of the same installation factor on the mid cruise CD was analysed with larger engines the computed drag increase was relatively greater. The calculated mid cruise CD of the long haul aircraft with the CUTF-BPR11-450K engine increased by 13 dc compared to the case of installation factor

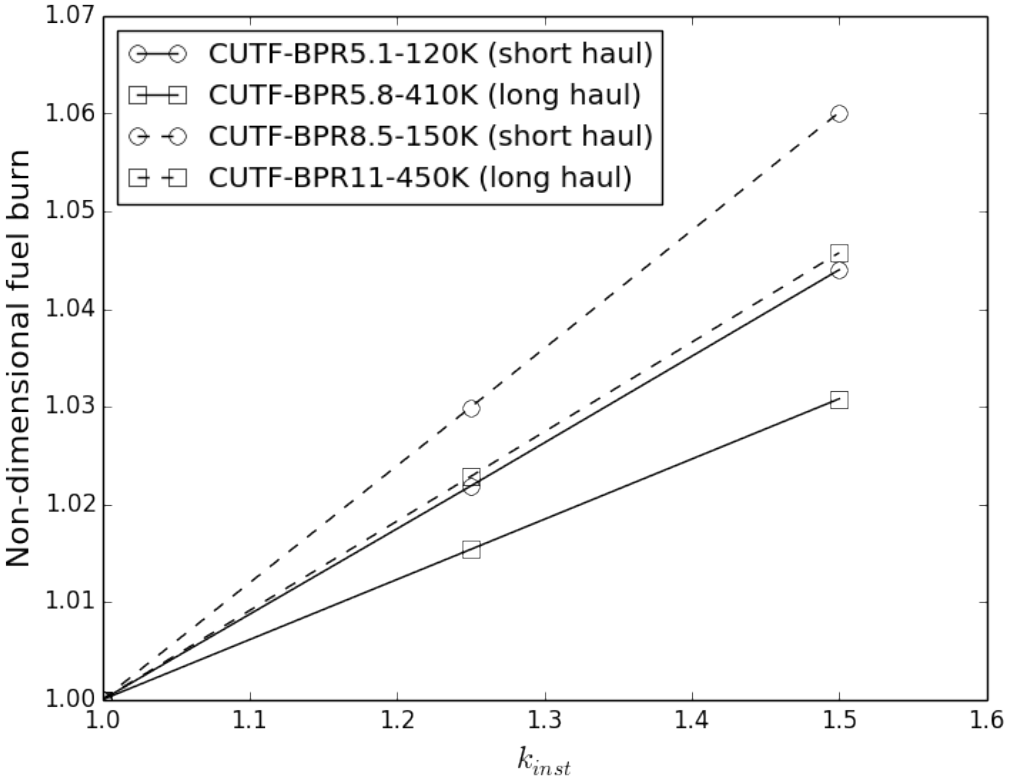

FIGURE 6.12: The influence of installation quality on mission fuel burn. Results are shown for two different engine sizes in each mission

equal to 1. The same comparison resulted in an increase of 19 dc for the short haul aircraft with the CUTF-BPR8.5-150K engine. These are important quantities if they are compared to van Dams[118] statement that one drag count could decrease the payload of a twin engine subsonic aircraft on a long-range mission by approximately one passenger. The greater sensitivity of larger engines to installation factor is expected due to their larger uninstalled drag.

This analysis assumes that the installation drag factor is constant throughout the mission. This is a simplification and is not true in reality. However, this analysis is enough to show that installation drag effects are significant and need to be taken into account. Correlations should be extracted from CFD to account for the variation in installation drag factor at different flight conditions (for example typical climb, cruise and descent conditions) and

these correlations should then be implemented as a correction to the ESDU drag prediction within the installation drag module of PSIMOD.

Chapter 7

Underwing installed nacelles numerical campaign

In the previous Chapter, (Section 6.8), the sensitivity of mission fuel burn to installation quality was assessed through the use of an installation drag factor. This drag factor was kept constant throughout a mission. In reality installation drag will vary throughout a mission and this variation will lead to different optimum powerplant installations for missions which spend relatively shorter or longer times in certain flight segments. Also the installation drag factor used in the previous Chapter was not a function of known installation parameters like nacelle size or installation location. The aim of this Chapter is to address these issues by extracting installation drag factors from complex full aircraft CFD as a function of nacelle size and installation position for three flight conditions which are representative of a typical mission. These factors will be extracted from mid-climb, mid-cruise and mid-descent configurations.

7.1 Test matrices

The NASA Common Research Model (CRM[34]) was chosen as a suitable airframe. As described in § 2.1.1.3, the CRM airframe has a supercritical wing and a fuselage that is typical of a civil transport aircraft. It is designed to cruise at a Mach number of 0.85 with a lift coefficient of 0.5. These properties makes it representative of modern transonic aircraft. For this reason, and the wealth of available experimental data for both installed and clean-wing configurations, it was chosen as the airframe upon which to study nacelle installation effects.

The CRM aircraft is most similar to an Airbus A330. To have the correct airframe to engine ratio the datum installed engine was based on the Trent 700. Due to computational constraints it was decided that only two nacelle sizes could be investigated which will be referred to as the datum installed nacelle and larger installed nacelle. The aim of the underwing installed nacelle CFD exercise was to extract installation drag factors to improve PSIMOD's installation drag modelling capability. In the long-haul aircraft PSIMOD modelling, detailed in Chapter 6, the largest engine (CUTF-BPR11-450K) modelled had a maximum diameter 1.28 times that of the smallest engine (CUTF-BPR5.8-410K). The larger installed nacelle was therefore scaled from the datum installed nacelle by the same factor. This resulted in two nacelles with a maximum diameter of 3.133m and 4.018m. The CRMfit, described in § 5.2, has been scaled to these sizes.

To put the choice of installation positions in context a review was carried out. Data has been extracted from published papers[55] and aircraft manufacturer's ground handling manuals[105,115,119–127] with assistance from a fellow PhD student.[128] Industrial powerplant installation trends have been assessed based on the vertical offset from wing trailing edge and the horizontal offset from wing leading edge (Figure 7.1). These offsets are non-dimensionalised by the local wing chord in the engine installation plane, c. Positive values of x/c indicate overlap between the wing and nacelle trailing edge. The accuracy of this

study was limited by the quality and resolution of publicly available aircraft sketches, however the exercise is still useful in that it allows the the overall industrial trends and differing approaches by different aircraft manufacturers to be observed. Also annotated on Figure 7.1 is an interference drag "keep out" boundary[45,117,129] based on Boeing wind-tunnel data.

Early Pratt and Whitney low bypass ratio turbofans on Boeing aircraft (Points 11 to 12 in Figure 7.1) were positioned close to the wing with significant wing-nacelle horizontal overlap. As BPR increased with the PW JT9D on the Boeing 747 (Point 15 in Figure 7.1) the engine was moved further forwards and vertically down from the wing. In general engines on Boeing aircraft seem to be installed vertically closer than those installed on Airbus aircraft with some installations crossing the interference drag "keep out" boundary. The trend is more dependent on aircraft manufacturer than engine manufacturer. The Trent 1000 and GE90-94, both high by-pass ratio turbofan engines fitted on the Boeing 787-9 and Boeing 777-200 respectively cross this notional boundary.

Key	Airframe	Engine	Key	Airframe	Engine
1	NASA CRM	NASA CRM	15	B747	PW JT9D
2	A300B	CF6-50	16	B777-200	PW STF 1173
3	A321	CF56-5B1	17	B777-200	PW STF 1174
4	A330-300	CF6-80E1	18	DC10-30	CF6-50
5	A340-500	Trent500 (IB)	19	C5A	TF39
6	A340-500	Trent500 (OB)	20	B747	CF6-50
7	A350-900	TrentXWB	21	B777-200	GE90-94
8	A380-800	Trent900 (IB)	22	B777-300ER	GE90-115B
9	A380-800	Trent900 (OB)	23	B737-800	CFM56-7
10	A320neo	PW1000	24	B737max	CFM LEAP-1B
11	DC8-10	JT3C-6	25	B777	Trent800
12	DC8-60	JT3D	26	B787-9	Trent1000 / GE NX
13	B707-320	JT4-3	27	Bombardier CS100	PW 1500G
14	B720	PW JT3C-7	28	Bombardier CS300	PW 1500G

TABLE 7.1: The key for Figure 7.1, a summary of engine installation locations for existing aircraft.

The datum installation location (Position 1, Table 7.2) was chosen to be equal to that of the Boeing 777 with Trent 800 engines. Traditionally larger engines are accommodated

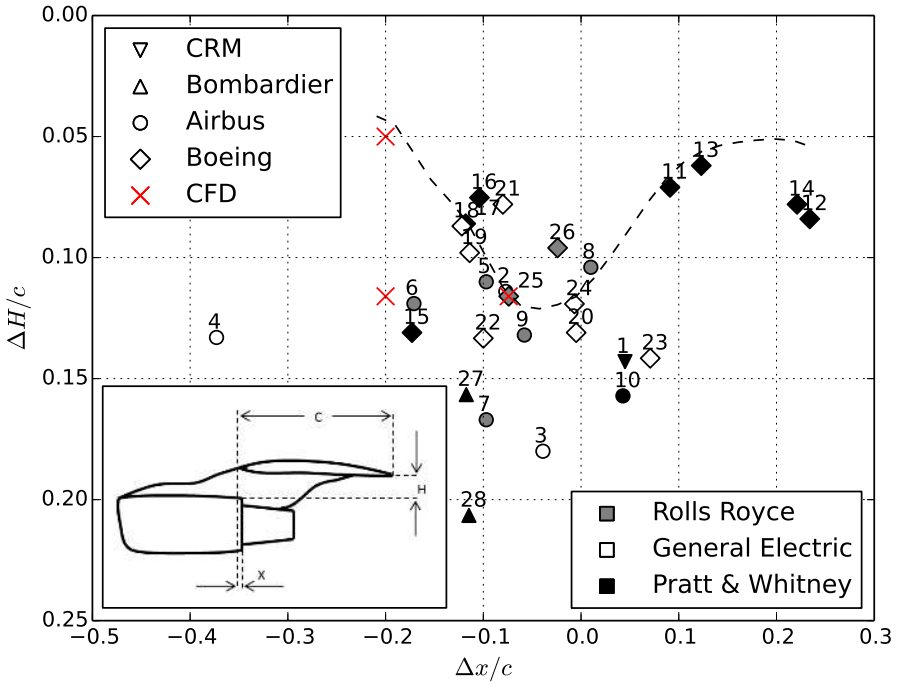

FIGURE 7.1: A summary of engine installation locations for existing aircraft. The vertical offest from the wing trailing edge and the horizontal offset from the leading edge are denoted H and x respectively. Distance is non-dimensionalised by the wing chord, c. Positive values of x/c indicate overlap between the wing and nacelle trailing edge. The key for aircraft and engine manufacturers is provided in Table 7.1

by a decrease in the vertical offset between the wing and engine, this often necessitates an increase in the horizontal offset.[130] Nacelle installation Position 2 and 3 have been chosen in line with this design thought process. Position 2 is a solely horizontal displacement from Position 1, while, Position 3 is a vertical displacement from Position 2. The nacelle inclination and toe-in angles, (Figure 7.2), have been set to 1.5^o and 2.7^o respectively. These angles correspond those of the CRM TFN and have been kept constant for each nacelle size and position studied.

To have representative climb, cruise and descent conditions and to ensure compatibility with PSIMOD a mission profile for a Boeing 777-300 generated with PSIMOD. Mid-climb, mid-cruise and mid-descent conditions have been extracted (Table 7.4).

Position	1	2	3
Delta x/c	-0.074	-0.200	-0.200
Delta H/c	-0.116	-0.116	-0.050

TABLE 7.2: The three engine installation locations selected for the CFD study

Condition	**Altitude**	**Mach**	α
Climb	10,000ft	0.46	2.7^o
Cruise	35,000ft	0.84	1.2^o
Descent	17,500ft	0.57	0.7^o

TABLE 7.3: Installed CFD flight configurations

Config. #	Flight Config.	Installation Position	Nacelle Size
1	Cruise	1	Datum
2	Cruise	1	Large
3	Cruise	2	Datum
4	Cruise	2	Large
5	Cruise	3	Datum
6	Cruise	3	Large
7	Climb	1	Datum
8	Climb	1	Large
9	Climb	2	Datum
10	Climb	2	Large
11	Climb	3	Datum
12	Climb	3	Large
13	Descent	1	Datum
14	Descent	1	Large
15	Descent	2	Datum
16	Descent	2	Large
17	Descent	3	Datum
18	Descent	3	Large

TABLE 7.4: Installed CFD cases test matrix

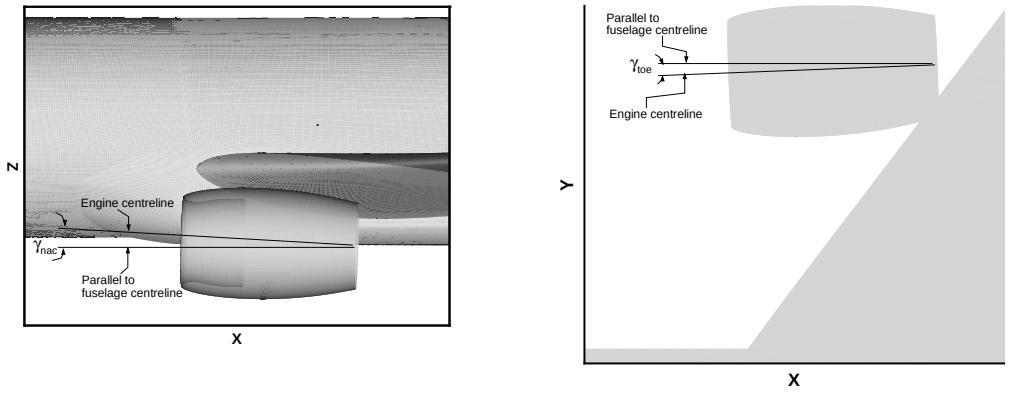

(a) Nacelle inclination angle definition

(b) Nacelle toe angle definition

FIGURE 7.2: Nacelle installation angle definitions

7.2 Grid and boundary conditions

A fully structured multi-block grid was created using ANSYS ICEM 14[88] (Figure 7.3). To ensure mesh quality a cell minimum 2x2x2 determinant of 0.2 and maximum cell expansion rate of 1.5 were maintained. The boundary layer block had 35 cells normal to the wall with a constant cell expansion rate of 1.2. The first cell height was set such that $y^+ \approx 1$. The maximum cell size on the fan cowl was set to 0.9% of nacelle length while the cell size at the nacelle trailing edge was set to 0.15% of nacelle length. To ensure adequate refinement around the nacelle leading edge, 30 nodes were employed. The domain size was defined by a radius of $100c_{ref}$ in line with the fourth Drag Prediction Workshop (DPW IV)[131] meshing guidelines. The final mesh composed 30.5×10^6 cells. This figure resulted from a mesh sensitivity study outlined in § 7.4.

In the same way that was implemented for the isolated cases to allow a back to back comparison "datum" nozzle exit conditions were imposed. The nozzle outlet boundary condition sets the total pressure and total temperature equal to that of the freestreeam. The nozzle walls are modelled with inviscid slip walls. In the isolated engines cases this is

to ensure that the nozzle efflux streamlines area approximately parallel to the nacelle axis and post-exit forces are minimised. At the domain farfield velocity, static temperature and static pressure were specified. The intake MFCR was controlled by the massflow outlet.

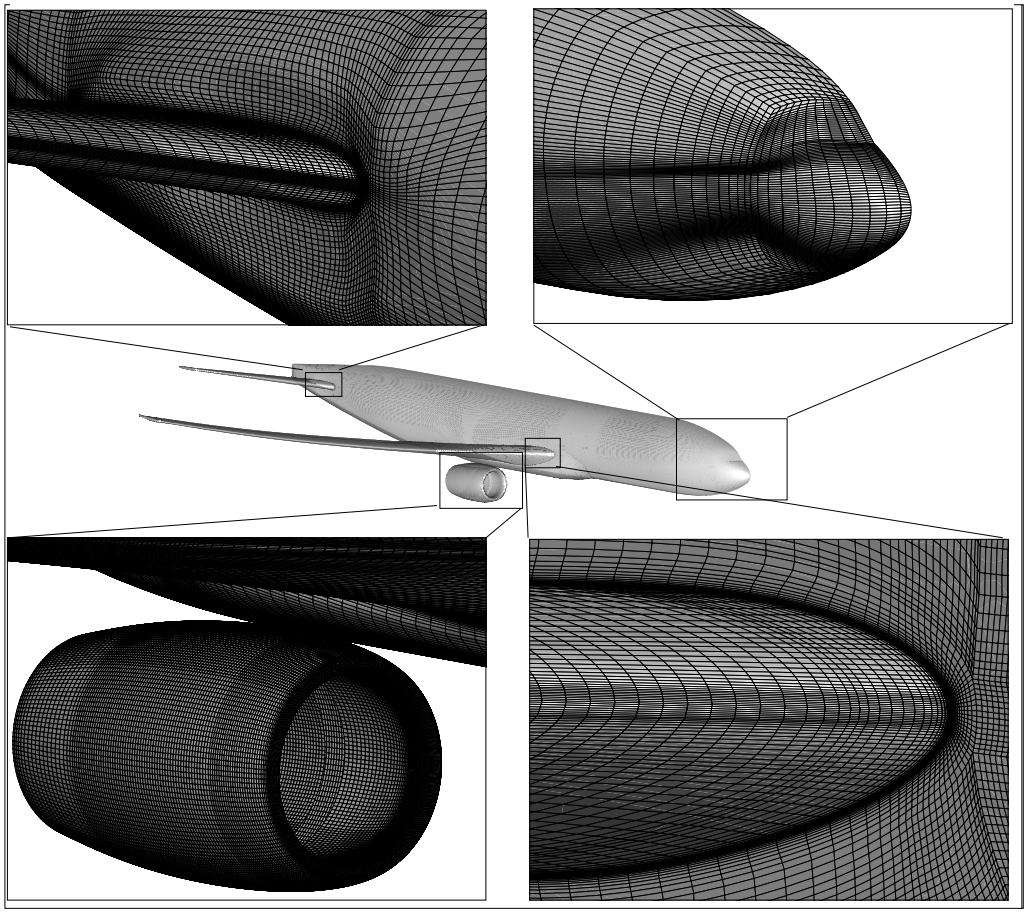

FIGURE 7.3: Mesh for a 3D fuselage, wing, tail and installed nacelle configuration

7.3 Solver settings

All simulations were run in double precision. ANSYS CFX[89] was used as the flow solver as described in Section 4.2. Air was modelled as a calorically, perfect, ideal gas with a constant specific heat capacity at constant pressure of $1.0044 \times 10^3\,[J\,kg^{-1}\,K^{-1}]$ and a molar mass of $28.96\,[kg\,kmol^{-1}]$. Viscosity was modelled with Sutherlands's Law.

The flowfield was initialised with the cartesian velocity components, static pressure and static temperature which correspond to freestream conditions. Turbulence levels were initialised with an eddy viscosity ratio of 3 and fractional intensity of 0.02. To ensure convergence the following strategy was employed. Initially the solution was run with a first order scheme for turbulence numerics and a first order upwind scheme for advection terms for 1000 iterations with a timescale factor of 0.02. Subsequently the timescale factor was increased to 1 and the solution progressed for a further 1000 iterations. Then CFX's high resolution schemes[89] were employed for both the turbulence numerics and the advection terms for 3000 iterations with a timescale factor of 0.02.

7.4 Grid independence study

The initial mesh consisted of 7.5×10^6 cells. This grid was then refined twice with an approximate refinement factor of two. This resulted in three meshes (Table 7.5). The symmetric nature of the domain meant that the airframe was not subjected to any net side force. The coefficient of lift and drag were therefore chosen as the criteria used to assess mesh independence as outlined in Section 4.4.2. The grid convergence index for these meshes is given in Table 7.6. For the fine mesh the drag coefficient is converged within an acceptable limit.

Coarse	7.5×10^6
Medium	1.5×10^7
Fine	3.0×10^7

TABLE 7.5: The number of elements in the installed nacelle meshes

The grid convergence index or Richardson's extrapolation could not be calculated for this metric as the solutions for the lift coefficient from the three grids were non-monotonic. Further mesh refinement, which would have resulted in a mesh of 6×10^7 elements, was deemed computationally too expensive. The percentage difference in lift coefficient between the fine mesh and a Richardson's extrapolated lift coefficient or a lift coefficient

calculated from a further refined mesh. However, there was a difference of 0.155% for the lift coefficient between the fine and medium mesh. Assuming that C_L continues to converge as mesh resolution increases in line with C_D the difference between the C_L calculated by the fine mesh and the mesh independent C_L is less than 0.155%. As a result of the mesh independence assessment the fine mesh (3×10^7 cells) was chosen.

	Coarse (g=4)	Medium (g=2)	Fine (g=1)	(g=0)	$GCI_{1,2}$	$GCI_{2,4}$	AR	P_{con}	$\%dif_{1,2}$	$\%dif_{0,1}$
C_D	0.0345	0.0335	0.0330	0.0326	0.015	0.032	0.99	1.1	-1.37	-1.21
C_L	0.6058	0.6128	0.6118	NM	NM	NM	NM	NM	-0.155	NM

TABLE 7.6: Grid Convergence Indices calculated as part of the installed CFD mesh sensitivity analysis study. NM stands for non-monotonic.

7.5 Results and discussion

As described in § 7.1 a series of complex 3D CFD calculations have been carried out to assess the impact of nacelle size, installation location relative to the wing on nacelle drag for three flight configurations; mid-climb, mid-cruise and mid-descent. This activity is motivated by the desire to improve the installation drag modelling methodology in PSIMOD.

7.5.1 Installed nacelle drag

This section describes the evaluation of installed nacelle drag and its variation with nacelle size, installation location and flight condition. Eighteen wing-body-engine CFD calculations have been carried out. These comprise a datum engine ($D_{fan} = 3.133$) and a larger engine ($D_{fan} = 4.018$) installed in three underwing positions (Table 7.2) in climb, cruise and descent flight configurations (Table 7.4). For each configuration the engine drag coefficient ($C_{D,eng}$) has been calculated using the modified nearfield method (§ 4.6.1).

The variation of nacelle drag with flight condition, installation position and engine size is shown in Figure 7.4. Changes in nacelle drag between installation position, flight condition and nacelle size are determined primarily by the balance of two wing induced phenomenon. An increase in wing C_L modifies the local static pressure field which increases the pressure force on the nacelle afterbody which reduces nacelle drag. An increase in wing C_L also induces an increase in upwash angle ahead of the wing which can significantly impact upon the forebody suction force and nacelle shock formation, especially on the nacelle topline. For example, in Position 1, the position closest horizontally to the wing, the larger engine ($D_{max} = 4.015m$) experiences higher drag at all tested flight conditions than the datum size nacelle ($D_{max} = 4.015m$) as expected. However, this increase is noteworthy for the mid-cruise condition where drag increased by a factor of 2.1. The highlight plane of the datum nacelle is closer to the wing than the larger nacelle and experiences a higher local incidence due to wing upwash effects. This higher local incidence for the datum nacelle increases flow acceleration around the nacelle forebody. For the datum size nacelle the flow reaches a maximum Mach number 1.2 compared to 1.02 for the larger nacelle (Figures 7.5(a) and 7.5(b)). This results in a lower surface static pressure peak and a higher forebody suction force for datum nacelle (Figure 7.5(c)).

The wing influence on the static pressure distribution on the nacelle afterbody can be seen when nacelle drag in the climb configuration is compared to the cruise and descent configurations (Figure 7.6). For all but one configuration nacelle drag was lowest in the climb configuration. On the surface this may be a surprising result as in the case of the isolated nacelle, drag increases with increases in angle of attack. However once installed, wing flowfield effects dominate and increased pressure on the nacelle after body as the wing C_L increases overcomes this effect. When nacelle drag is decomposed into momentum flux, stream pressure, skin friction and pressure force it can be seen that this is primarily caused by an increase in pressure force. The wing modifies the local static pressure field and increases the pressure force on the nacelle afterbody (Figure 7.6).

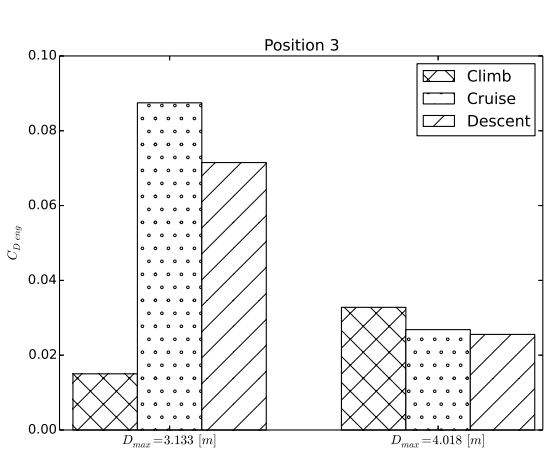

(a) Variation of nacelle drag calculated using the modified nearfield method with flight condition and engine size for installation position 3.

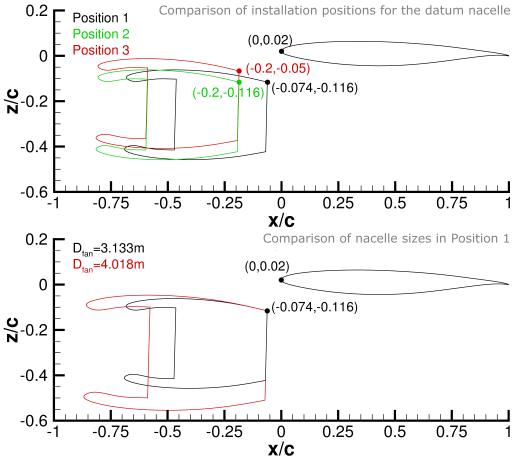

(b) Comparison of engine sizes and installation positions relative to the local wing cross-section.

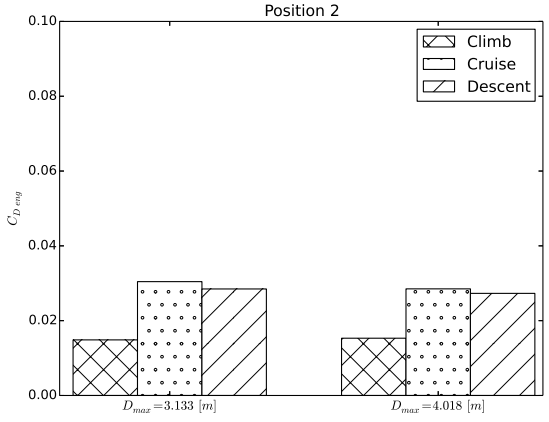

(c) Variation of nacelle drag calculated using the modified nearfield method with flight condition and engine size for installation position 2.

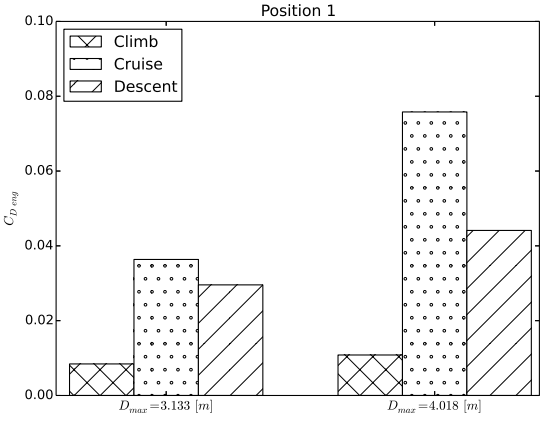

(d) Variation of nacelle drag calculated using the modified nearfield method with flight condition and engine size for installation position 1.

FIGURE 7.4: Variation of nacelle drag calculated using the the modified nearfield method with flight condition, installation position and engine size.

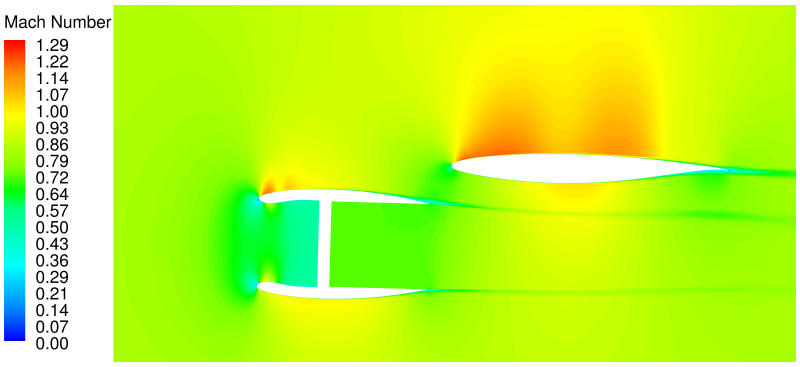

(a) Contours of Mach number on the symmetry for installed Config. 1, datum size nacelle, installed in Position 1, at cruise conditions (Altitude=35,000ft, M=0.84, $\alpha = 2.7^o$).

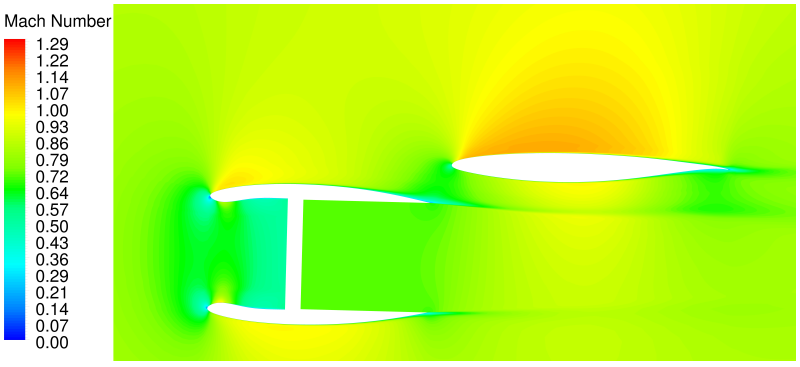

(b) Contours of Mach number on the symmetry for installed Config. 2, large nacelle, installed in Position 1, at cruise conditions (Altitude=35,000ft, M=0.84, $\alpha = 2.7^o$).

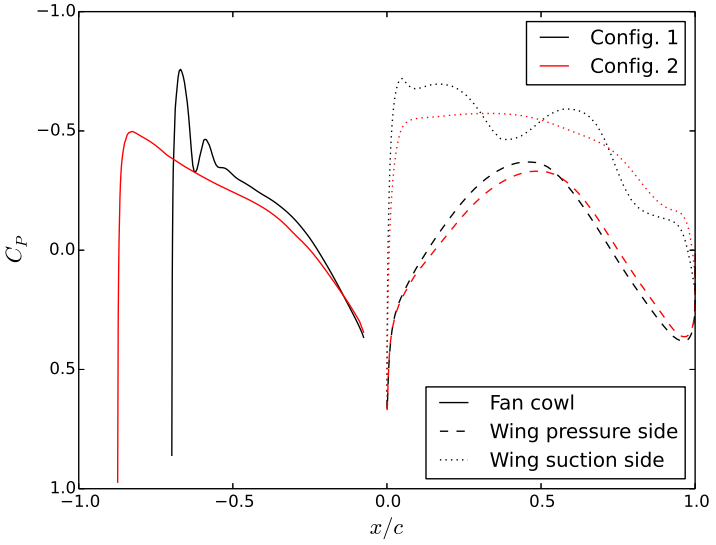

(c) A comparison of fan cowl and wing pressure coefficient, (C_P), distributions, for the datum and large nacelles installed in Position 1, at cruise conditions (Altitude=35,000ft, M=0.84, $\alpha = 2.7^o$).

FIGURE 7.5: A flowfield comparison, for the datum and large nacelles installed in Position 1, at cruise conditions (Altitude=35,000ft, M=0.84, $\alpha = 2.7^o$).

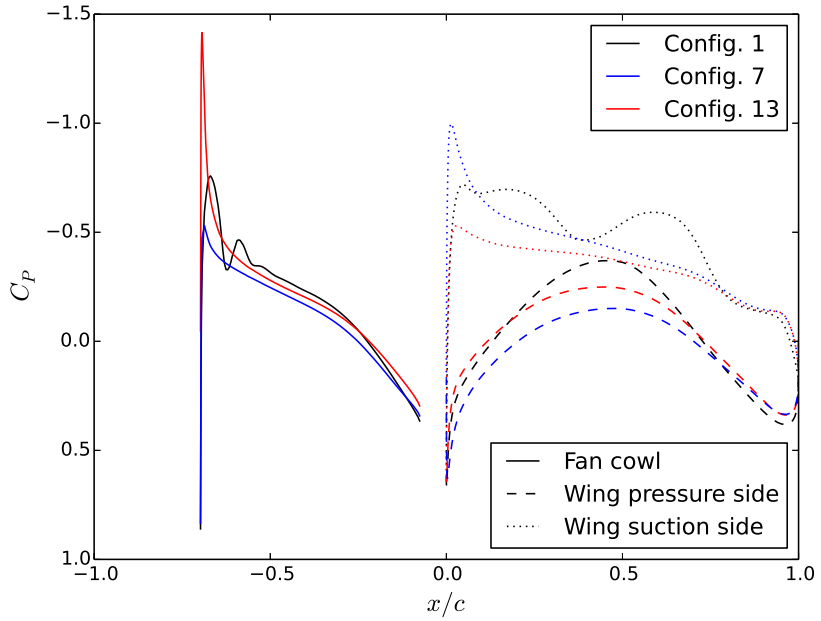

FIGURE 7.6: A comparison of fan cowl and wing pressure coefficient, (C_P), distributions, for the datum engine installed in Position 1, at cruise climb and descent conditions, Config. 1, 7 and 13 respectively (Table 7.4).

When the nacelle is moved from Position 1 to Position 2, a forwards movement of $x/c = 0.126$ parallel to the fuselage axis, nacelle drag decreases for both engine sizes in all flight configurations except for the climb configuration for which nacelle drag increases by 108% and 76% for the datum and larger nacelles respectively. Wing influence on the nacelle is highest in the mid-climb configuration and the forward movement of the nacelle from Position 1 to 2 reduces this beneficial drag reduction. An example of the C_P distribution on the nacelle surface is given in Figure 7.7(a). For both the datum and large nacelles installed in position 1 and 2 (Table 7.2) this distribution remains almost constant (a full comparison is provided in Appendix F, Figure F.2). Changes in nacelle drag are a result of a subtle change in C_P on the upper surface of the aft-nacelle. This change can more clearly be seen when the pressure coefficient distribution on the topline of the fan cowl ($\theta = 0^o$) is plotted (Figure 7.7(b)). This C_P difference is on average approximately 0.05 over the aft-nacelle between position 1 and 2. The equivalent figure which also shows the

wing C_P distribution is provided in Appendix F (Figure F.1).

Detailed flow field analysis is outside the scope of this work and the primary aim was to generate a set of results from which nacelle drag installation drag factors as a function of engine size, position and flight condition could be extracted to improve the installation drag modelling within PSIMOD. This is dealt with in the subsequent section.

7.5.2 Installed nacelle drag factors

The aim of this section was to extract nacelle drag installation drag factors as a function of engine size, position and flight condition. These factors could then be applied to the nacelle drag calculated by PSIMOD. The calculation of nacelle drag installation factors for each configuration required the simulation of an isolated nacelle at the same conditions. To make a fair comparison nacelles should be compared at the same local flow incidence. A clean wing CFD calculation was performed for the mid-climb, mid-cruise and mid-descent configurations. The upflow angle at a point equivalent to the center of the nacelle highlight was extracted to estimate the upwash effects of the wing. This point in space and the extracted upflow angle change with both installation location and nacelle size. When nacelle size is increased it is scaled around the trailing edge point of the nacelle topline and as such the highlight plane of the nacelle moves forward away from the wing. The variance of upflow angle with nacelle size and position was assessed (Table 7.7). This variance was small when the upflow angle for each configuration was compared to the upflow angle for the datum size nacelle in installation position 1. The maximum discrepancy ($\Delta 0.16^o$) was found for the larger nacelle in the climb configuration at installation position 1. These variances were deemed to be small enough that three isolated nacelle CFD simulations, one for each flight configuration, were sufficient to allow a back to back comparison with the eighteen different installed configurations.

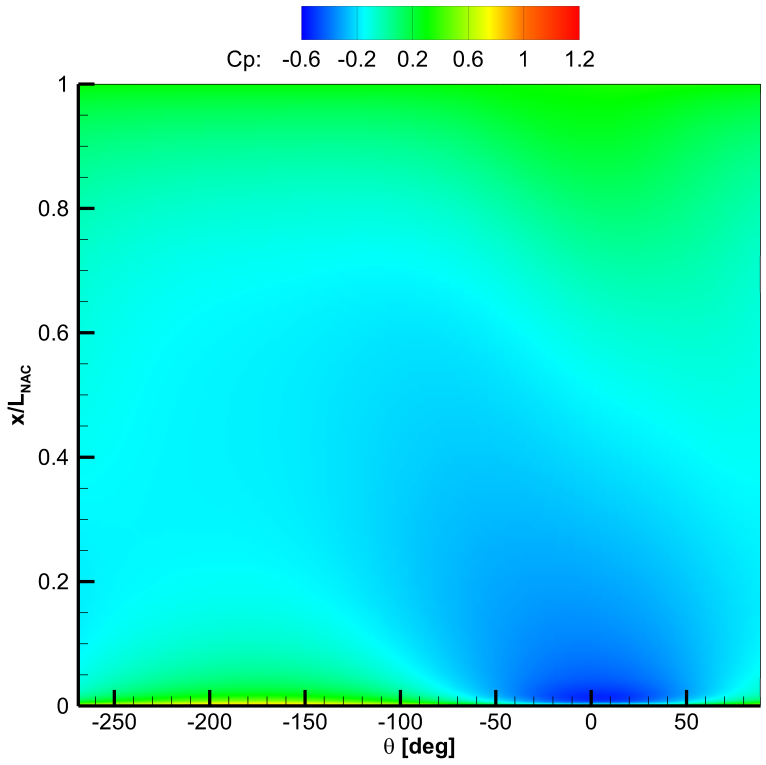

(a) The C_P distribution on the surface of the datum nacelle installed in position 1 in the climb configuration (Config. 7). The axial coordinate (x) is non-dimensionalised by the nacelle length L_{nac} is the nacelle length such that x/L_{nac} is the nacelle trailing edge. θ is the nacelle azimuthal angle from the nacelle topline.

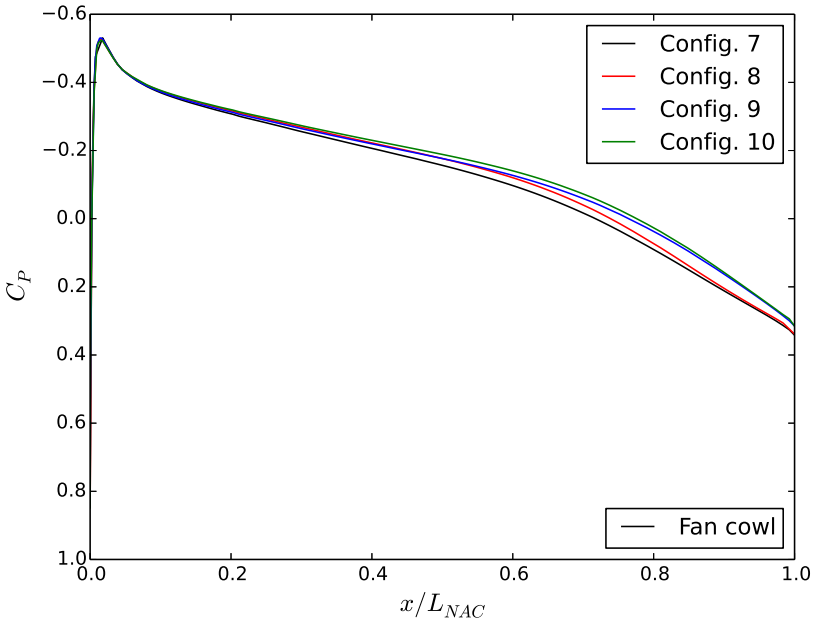

(b) The C_P distribution along the fan cowl topline for datum nacelle and large nacelle installed in positions 1 and 2, Configurations 7, 8, 9 and 10 respectively (Table 7.4).

FIGURE 7.7: Fan cowl pressure coefficient distributions in the climb configuration.

Config. #	Flight Config.	Installation Position	Nacelle Size	Upwash Angle (ϵ)	$\Delta\epsilon$ from Datum size nacelle in pos. 2
1	Cruise	1	Datum	1.44	0.05
2	Cruise	1	Large	1.41	0.08
3	Cruise	2	Datum	1.48	0.00
4	Cruise	2	Large	1.43	0.05
5	Cruise	3	Datum	1.54	0.06
6	Cruise	3	Large	1.50	0.02
7	Climb	1	Datum	3.83	0.09
8	Climb	1	Large	3.58	0.16
9	Climb	2	Datum	3.74	0.00
10	Climb	2	Large	3.52	0.22
11	Climb	3	Datum	3.81	0.08
12	Climb	3	Large	3.61	0.13
13	Descent	1	Datum	1.03	0.01
14	Descent	1	Large	0.95	0.09
15	Descent	2	Datum	1.04	0.00
16	Descent	2	Large	0.95	0.08
17	Descent	3	Datum	1.10	0.06
18	Descent	3	Large	1.02	0.02

TABLE 7.7: The variance of upflow angle extracted from clean wing CFD cases with changes in nacelle size and installation position for different flight configurations. The difference between the upflow angle for each configuration and the upflow angle for the datum size nacelle in installation Position 2 is also shown.

The nacelle total upflow angle was then calculated from the nacelle inclination angle and the upwash angle derived from the clean wing CFD cases. The calculated nacelle drag (Figure 7.4) was then expressed as a factor of the calculated isolated nacelle drag (Figure 7.8).

Generally scaling the installed drag coefficients by isolated nacelle drag did not change the overall trends with respect to changes in position and flight configuration. However in all cases the installation drag factors are less than one, which indicates that in all cases the presence of the airframe acts to reduce nacelle drag. The greatest influence, an 87% reduction, is seen by the datum size nacelle installed in Position 1 in the climb configuration. This indicates that changes in nacelle drag are not the dominant installation drag component and that the application of nacelle drag installation factors alone in PSIMOD

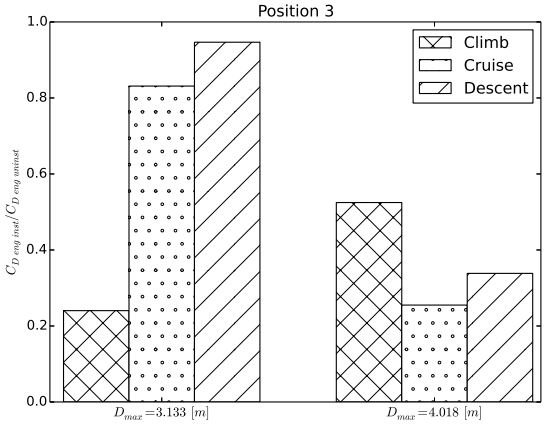

(a) Variation of installed nacelle drag expressed as a fraction of isolated nacelle drag at the same conditions with flight condition and engine size for installation position 3.

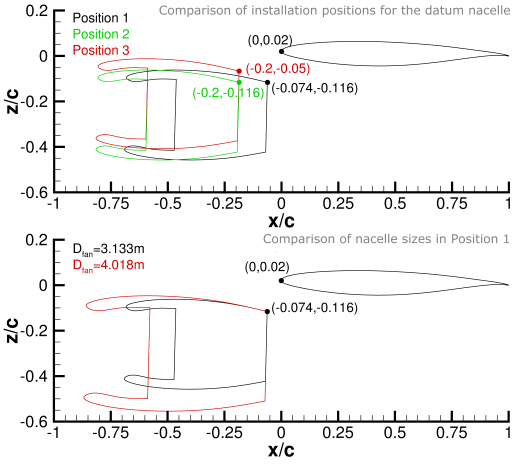

(b) Comparison of engine sizes and installation positions relative to the local wing cross-section.

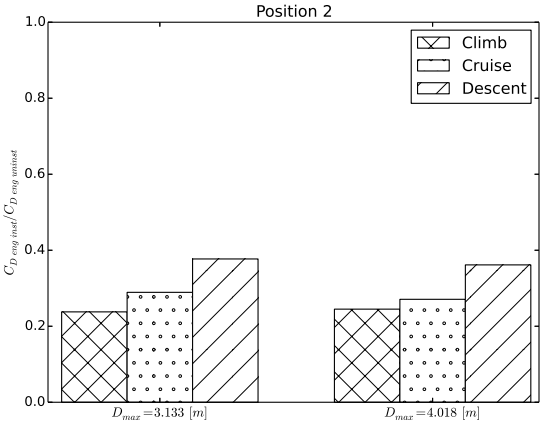

(c) Variation of installed nacelle drag expressed as a fraction of isolated nacelle drag at the same conditions with flight condition and engine size for installation position 2.

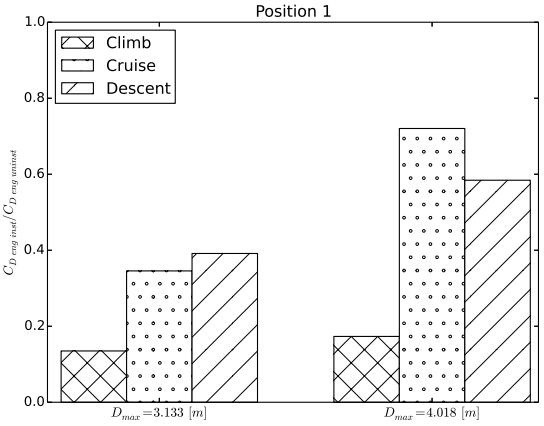

(d) Variation of installed nacelle drag expressed as a fraction of isolated nacelle drag at the same conditions with flight condition and engine size for installation position 1.

FIGURE 7.8: Variation of installed nacelle drag expressed as a fraction of isolated nacelle drag at the same conditions with flight condition, installation position and engine size. Drag is calculated with the modified nearfield method.

to model installation effects is not adequate. The complimentary effect of the nacelle on the airframe must also be considered. Including these effects in PSIMOD is outside the scope of the current work but possible approaches are discussed in Chapter 8 (Future Work).

7.5.3 Breakdown of installed drag components

The preceding section concluded that the assessment of installation effects by solely looking at changes in nacelle drag was inadequate. To fully evaluate a power plant installation the complementary effects of the nacelle on the airframe must be considered. To this end, drag was decomposed into installation drag (Eq. 7.1) and airframe and nacelle interference drag (Eq. 7.2 and Eq. 7.3) and expressed as a percentage of overall aircraft drag.

$$\Delta D_{inst} = D_{a/c} - (D_{a/f,iso} + D_{eng,iso} N_{eng}) \tag{7.1}$$

$$\Delta D_{a/f} = D_{a/f,inst} - D_{a/f,iso} \tag{7.2}$$

$$\Delta D_{eng} = D_{eng,inst} - D_{eng,iso} \tag{7.3}$$

In the majority of cases installation drag was found to be negative. However in two cases for the larger size installed nacelle a large increase in airframe drag was calculated. In Position 1, for the cruise configuration an increase in airframe drag when compared to isolated airframe drag ($\Delta D_{a/f}$) resulted in a large positive installation drag (37% of $D_{a/c}$). Similarly in Position 3, for the climb configuration a large increase in airframe drag (36% of $D_{a/c}$) resulted in a similarly large installation drag (30% of $D_{a/c}$). In both cases the presence of the nacelle significantly altered the shock pattern on the inboard section of the wing. An example of this is shown in Figure 7.9. Acceleration over the wing in the vicinity of the engine is reduced and the shock structures have been altered with the inboard shocks moving forwards. This has the effect of reducing the suction force on the wing leading edge, particularly in the inboard section (Figure 7.9(b)) which in turn leads to an increase in airframe drag over the clean-wing configuration.

In conjunction with this the jet is exhausted at approximately freestream static pressure which is higher than the nozzle environmental static pressure in the installed case. This is especially pronounced in the climb configurations. The jet efflux therefore increases wing drag. These jet efflux effects would be markedly different when realistic nozzle exit boundary conditions are simulated. The need for this approach is discussed in Chapter 8 (Future Work).

For the datum size nacelle installation drag was, on average, -13%, -9% and -6% of $D_{a/c}$ for the mid-climb, mid-cruise and mid-descent configurations respectively In the climb configuration $\Delta D_{a/f}$ was of the same order of magnitude as ΔD_{eng} for the datum size nacelle but of opposite sign.

It is obvious from these results that the presence of the nacelle is having a significant impact upon wing performance. As this is the case it is not enough to look at changes in drag alone, lift installation effects must also be considered to fully evaluate a powerplant installation. An assessment of the impact on aircraft lift will now be made in the following section along the same lines as the drag breakdown discussed here.

7.5.4 Breakdown of installed lift components

Section 7.5.3 concluded that to properly evaluate a powerplant installation the effects on total lift must be evaluated. In this section changes in lift will be decomposed into installation lift and changes in airframe and nacelle lift (Eq. 7.4, Eq. 7.5 and Eq. 7.6).

$$\Delta L_{inst} = L_{a/c} - (L_{a/f,iso} + L_{eng,iso} N_{eng}) \tag{7.4}$$

$$\Delta L_{a/f} = L_{a/f,inst} - L_{a/f,iso} \tag{7.5}$$

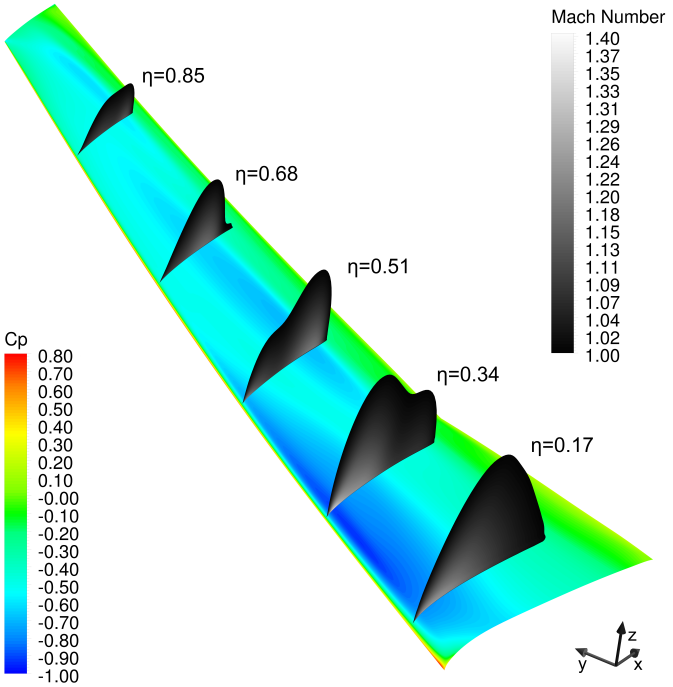

(a) The clean wing geometry in the cruise condition.

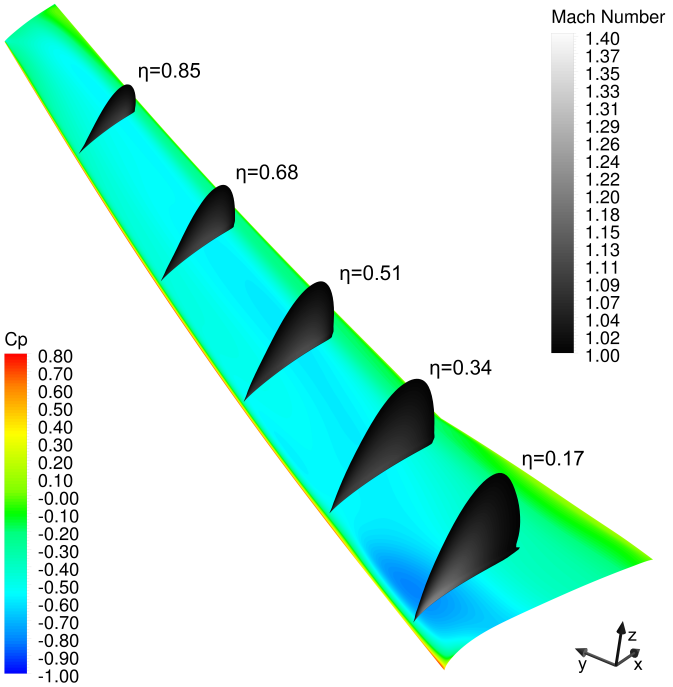

(b) Config 1 (datum sized nacelle installed in position 1) in the cruise condition

FIGURE 7.9: A comparison of the flowfield over the wing in Config. 1 (datum sized nacelle installed in position 1) with the clean-wing configuration in the cruise condition ($M = 0.84$, $\alpha = 1.2^o$). Contours of pressure coefficient (C_P) on the wing upper surface and a series of planes parallel to the symmetry plane coloured by Mach number and limited to $1.0 \leq M \leq 1.4$. η is the non-dimensional wing span.

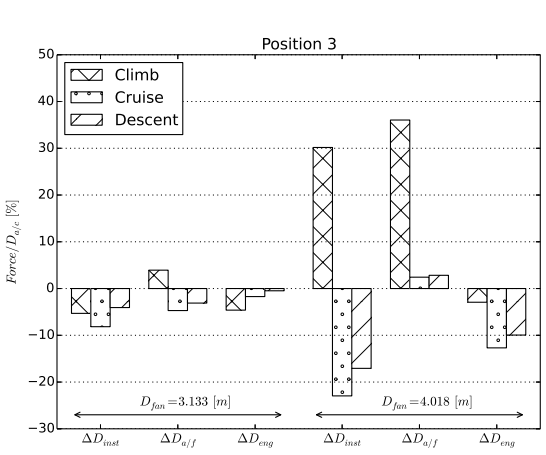

(a) Variation of drag components expressed as a fraction of overall aircraft drag with flight condition and engine size for installation position 3.

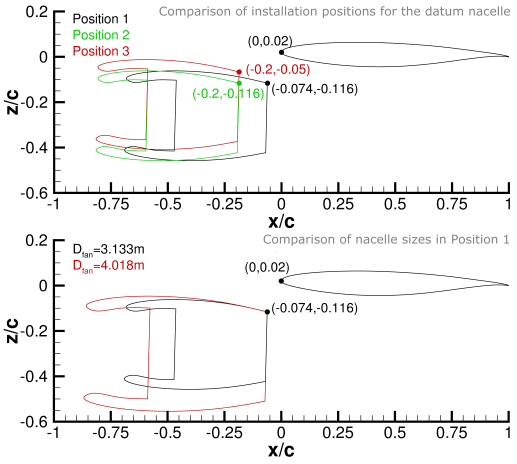

(b) Comparison of engine sizes and installation positions relative to the local wing cross-section.

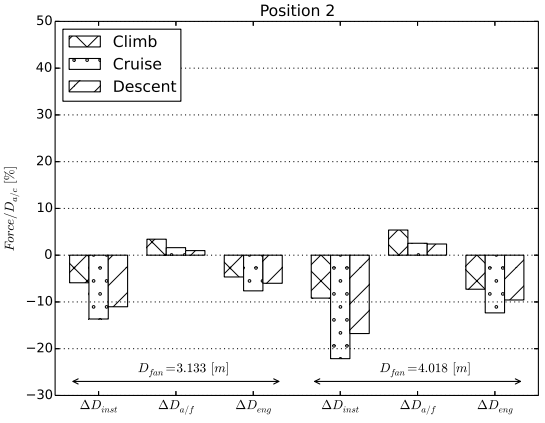

(c) Variation of drag components expressed as a fraction of overall aircraft drag with flight condition and engine size for installation position 2.

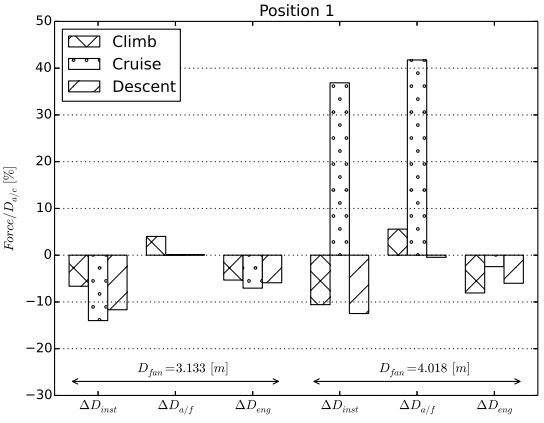

(d) Variation of drag components expressed as a fraction of overall aircraft drag with flight condition and engine size for installation position 1.

FIGURE 7.10: Variation of drag components expressed as a fraction of overall aircraft drag with flight condition, installation position and engine size. Nacelle drag is calculated with the modified nearfield method.

$$\Delta L_{eng} = L_{eng,inst} - L_{eng,iso} \tag{7.6}$$

The presence of the nacelle changes the pressure distribution of the wing. Primarily the suction side of the wing is affected through the change shock positions at inboard sections (Figure 7.11). Further outboard the presence of the nacelle shields which results in a local flow angle reduction. The higher jet efflux of the larger engine effects a greater area of the wing pressure side that that of the datum engine. The pressure matched nozzle condition is matched to freestream conditions but the nozzle environmental static pressure had been accelerated by the presence of the fuselage. The jet efflux reduces flow velocity under the wing directly behind it (Figure 7.11(b)).

In all cases the effect of the presence of the nacelle was to reduce overall lift. To regain this lost lift either an increase in aircraft angle of attack is required or the wing needs to be redesigned. An increase in aircraft angle attack would lead to an increase in drag. So to properly evaluate a powerplant installation changes in total aircraft drag need to assessed at a constant lift coefficient. The increase in drag associated with a percentage increase in wing C_L can be estimated with the CRM experimentally measured drag polar. For the cases simulated the typical cruise C_L calculated was 0.24. To recover the average loss of lift for the datum nacelle installation (-2.9%) $C_{D\,a/c}$ increases by 1.5%. This increase is less than the negative installation drags calculated (Figures 7.10) for the datum sized nacelle. The equivalent calculation for the larger installed nacelle, which suffers an average loss of lift of 3.9% in the cruise configurations results in a $C_{D\,a/c}$ increases of 1.9% which is typically less than the negative installation drags calculated. These figures are only estimations based on an experimental drag polar. Ideally the installed CFD cases would be re-run to enable a drag breakdown comparison at equal C_L.

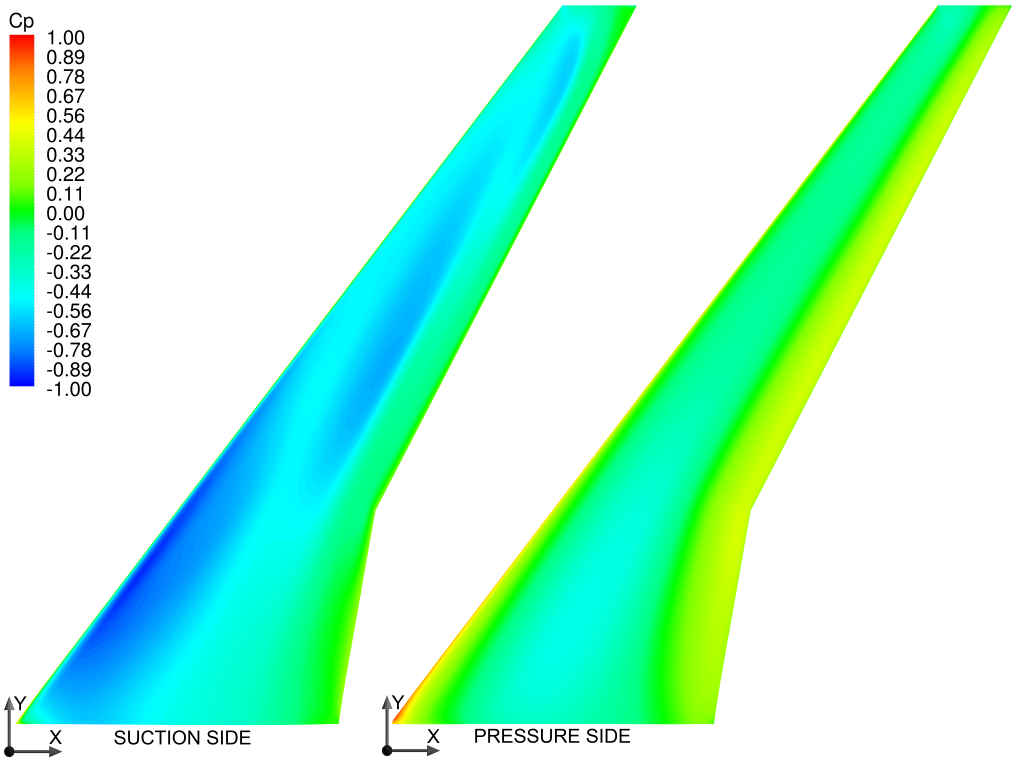

(a) The clean wing geometry in the cruise condition

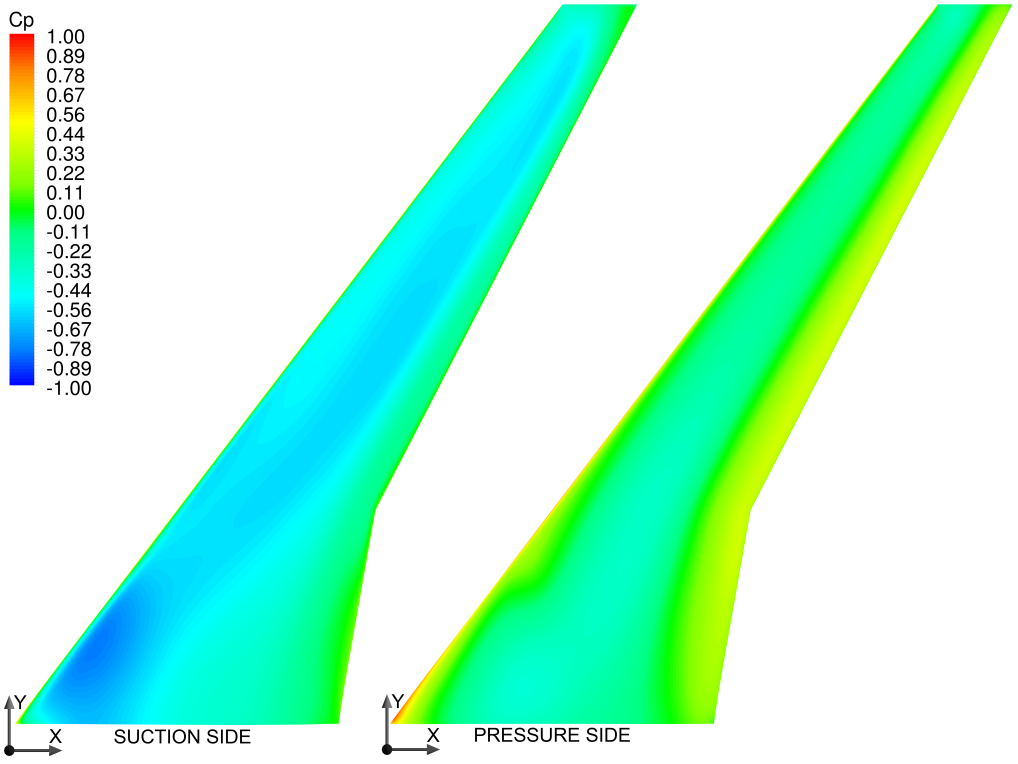

(b) Config 1 (datum sized nacelle installed in position 1) in the cruise condition

FIGURE 7.11: A comparison of pressure coefficient distribution on the wing in Config. 1 (datum sized nacelle installed in position 1) with the clean-wing configuration in the cruise condition ($M = 0.84$, $\alpha = 1.2^o$). Contours of pressure coefficient (C_P on the suction and pressure sides of the wing.

(a) Variation of lift components expressed as a fraction of overall aircraft lift with flight condition and engine size for installation position 3.

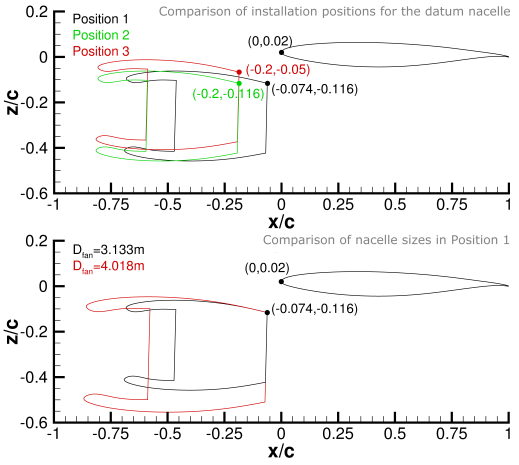

(b) Comparison of engine sizes and installation positions relative to the local wing cross-section.

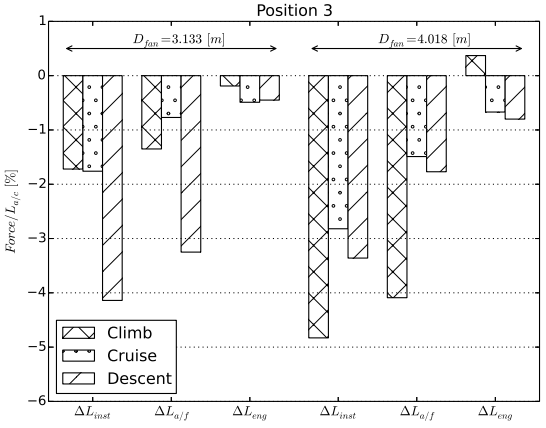

(c) Variation of lift components expressed as a fraction of overall aircraft lift with flight condition and engine size for installation position 2.

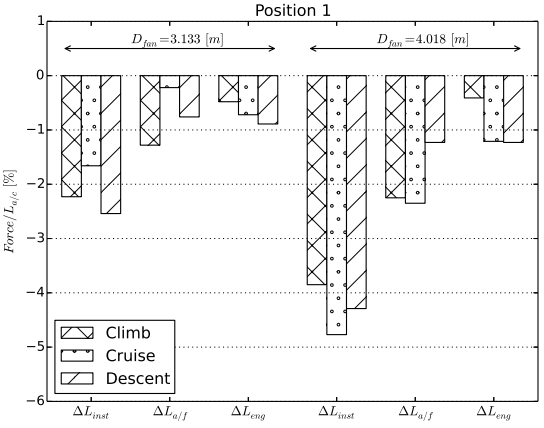

(d) Variation of lift components expressed as a fraction of overall aircraft lift with flight condition and engine size for installation position 1.

FIGURE 7.12: Variation of lift components expressed as a fraction of overall aircraft lift with flight condition, installation position and engine size. Nacelle lift is calculated with the modified nearfield method.

Chapter 8

Future Work

A framework to assess propulsion system integration has been developed Based on this research it is possible to identify some ways by which this framework could be further developed.

1. It was found that the impact of an installed nacelle on an airframe forces can be of the same order as the impact of the presence of the airframe on nacelle drag. The framework should be extended so that forces on the whole system are calculated as a function of nacelle size and installation location.

2. In the assessment of individual powerplant installations or the establishment of correlations for installation drag, force comparisons should be carried out at equal total lift. This may be due to a loss of lift caused by installation effects or in an increase in weight and hence required lift.

3. It was noted in this research that the jet efflux can have a significant impact on wing performance. However unrealistic datum efflux was adopted to ensure compatibility with the ESDU 81024 drag prediction method.[13] The effect of realistic jet effluxes should be investigated. This will necessitate the definition of a robust post-exit force

lift and drag accounting methodology. Both mixed and split stream nozzles should be investigated as a function of nozzle pressure ratio.

4. A series of nacelle drag sensitivity studies carried out with PSIMOD showed that when engine size is increased the impact on mission fuel of weight can be of the same order of magnitude as nacelle drag effects. An improved engine, nacelle and pylon weight estimation method is required to account for this.

5. The airframe, wing, nacelle calculations carried out within this research investigated the influence of nacelle size, position and flight condition on installation drag. No effort was made to reduce any negative effects by the alteration of the geometry. There are multiple routes which could be investigated including the following. Can any negative installation effects be reduced by modifying nacelle inclination angle or toe angle? Can they be reduced by designing thinner nacelles with shorter intakes? Can they be reduced by non-axisymmetric nacelles?

6. For each new powerplant installation a new pylon design is required. So that installation drag results were not a function of the quality of the pylon design, pylons were omitted from the study. However pylon drag will vary with nacelle size and installation position. It should be investigated whether pylon drag just be superimposed. A pylon drag estimation model should also be investigated.

7. The installation of an engine under a wing will influence its performance. The sensitivity of engine performance and mission fuel burn to these effects should be investigated. The impact of the flowfield generated by the airframe and wing on engine cycle performance and intake performance could be investigated

8. The experimental dataset upon which ESDU 81024 drag prediction method[13] is based comprises nacelle shapes which are not representative of future high and ultra bypass ratio engine nacelles. This dataset could be expanded and the tool updated through an isolated nacelle CFD study.

Chapter 9

Summary and conclusions

9.1 Main accomplishments

9.1.1 Modified nearfield method

For CFD post-processing a robust, reliable and repeatable method is required. Standard thrust and drag accounting methodology rely on the extraction of stagnation lines. The automatic extraction of stagnation lines and the splitting of surfaces is difficult to implement especially for complex stagnation lines that may occur when the nacelle is at incidence or at extremes of mass flow capture ratio. To address this issue the modified nearfield method (§4.6.1), a thrust and drag accounting methodology compatible with CFD methods has been developed. This method eliminates the need to extract a stagnation line.and all properties that are required by the method can be acquired by the interrogation of the CFD domain boundaries. This has allowed the development of scripts to automatically extract nacelle drag in a manner compatible with standard thrust and drag accounting methodology. The modified nearfield method has been adopted and used in multiple MSc and PhD projects as in projects with industrial partners as well as in this work. Thrust and drag accounting methodology is usually only reported for zero degree angle of attack

cases. The modified nearfield method has been extended to allow the extraction of lift and drag non-zero angles of attack.

9.1.2 Nacelle geometry generation

One of the main tasks of this research was the assessment of nacelle installation effects with changes in nacelle size. In order to achieve this it was necessary to be able to generate representative nacelle geometries. An Excel based tool was developed during this research based on nacelle design rules from the open-source literature. Given some basic information about the engine cycle and some engine hard-points, a representative spinner, intake and fan cowl afterbody is constructed. This Excel based tool has been further developed by a fellow PhD student into Cranfields Geometric Engine Modeller (GEM).[95]

9.1.3 PSIMOD

A Propulsion System Integration Modelling (PSIMOD) framework has been developed. PSIMOD couples Cranfield University's in house engine (Turbomatch[10]) and aircraft (Hermes[12]) performance codes with a nacelle drag prediction model based on ESDU 81024.[13] The ESDU drag prediction method is used to predict nacelle drag as a function of flight Reynolds number, Mach number, nacelle shape and intake MFCR. Corrections are then applied to this drag prediction to take into account nacelle local upflow effects and nacelle and propulsion system integration effects based on CFD simulations. This nacelle drag is integrated within PSIMOD in a drag build up method at each point in the flight.

9.2 Conclusions

Methods for the estimation of nacelle external drag have been developed. ESDU method 81024,[13] a method for the estimation of nacelle drag has been incorporated into a Propulsion System Integration Modelling (PSIMOD) framework. This has replaced a simple skin friction drag estimation methodology for nacelles which was part of Cranfield Universitys aircraft modelling tool HERMES.[12] The simple skin friction based estimate of nacelle drag was found to under predict nacelle drag by approximately 40% with respect to the ESDU method which takes into account nacelle geometry, Mach number, Reynolds number and MFCR effects

It is important to accurately model nacelle and engine weight in preliminary design as its effects on mission fuel burn are of the same order of magnitude as nacelle drag. For the short haul mission when weight increases were not modelled some engines showed an uninstalled SFC improvement over the baseline engine. When the additional weight of these larger engines was included in the modelling these uninstalled SFC improvements were completely negated. For the long haul mission when engine and nacelle weight increases were not modelled all engines showed an improvement in mission fuel burn over the baseline engine. However when the weight increases were modelled only the engines with a BPR=8.3 maintained a mission fuel burn improvement. This showed that for the engine design approach adopted in this paper there is an optimum increase in BPR after which further increases increase mission fuel burn. In preliminary design it is important to take into account both nacelle total upflow angle and installation drag. This has been achieved with the PSIMOD framework which uses the ESDU drag prediction method[13] to predict nacelle drag as a function of flight Reynolds number, Mach number, nacelle shape and intake MFCR. Corrections are then applied to this drag prediction to take into account nacelle local upflow effects and nacelle and propulsion system integration effects. This nacelle drag is integrated within PSIMOD in a drag build up method at each point in

the flight as part of an aircraft and engine performance model. PSIMOD and its sensitivity to propulsion system drag components has been demonstrated.

A large number of isolated nacelle CFD calculations at a range of Mach numbers, MFCRs and angles of attack were carried out. Corrections to nacelle drag due to incidence effects were extracted from the CFD data. The CFD method has been validated against experimental data with typical discrepancies being of the order of two drag counts.

Methods for the estimation of angle of attack effects on nacelle drag have been developed. Corrections to nacelle drag due to incidence effects which were extracted from CFD have been applied to PSIMOD.

Nacelle total local upflow angle can have a significant effect on mission fuel burn with increases in mission fuel burn of up to 2.2% seen for non-optimum nacelle offset angle. This showed that the ESDU method which does not take nacelle total local upflow angle into account is inadequate for calculating nacelle drag throughout a mission in preliminary design.

A method to assess the impact of nacelle installation effects has been developed. An installation drag factor has been added to PSIMOD in order to assess the impact of installation quality on overall mission performance. A sensitivity study to nacelle installation quality was undertaken across a range of installation drag factors from the literature. Engine installation quality can have a significant effect on mission fuel burn. For a poor propulsion system integration which may have an installation drag penalty of 50% of the isolated nacelle drag mission fuel burn can increase by up to 6%. The rate of change of mission fuel burn with installation quality is a function of nacelle size. Installation effects are not taken into account by the ESDU method.[13]

An airframe, wing, nacelle CFD campaign was carried out with the aim of extracting installation drag factors as installation drag factors as a function of nacelle size and installation position for three flight conditions which are representative of a typical mission.

The extracted installation drag factors were all less than one indicating that influence of the airframe and the wing in particular act to reduce nacelle drag at equal angle of attack. The primary mechanism by which this occurs is imposition of an increased pressure field on the aft of the nacelle. The assessment of installation effects by solely looking at the effect of the airframe on nacelle drag is inadequate. The effect of presence of the airframe on nacelle drag is of the same order of magnitude as the effect the nacelle on airframe drag. In addition the presence of a nacelle alters the lift generated by the airframe. In all cases investigated the effect was to reduce lift, by up to 4% in some cases. The increase in aircraft angle of attack to recover this loss in lift will lead to a corresponding increase in drag. This demonstrates that assessments of nacelle integration effects should be carried out at equal lift and not at equal angles of attack.

References

[1]Green, J., "Civil aviation and the environmental challenge," *Aeronautical Journal*, Vol. 107, No. 1072, 2003, pp. 281–300.

[2]Argüelles, P., Lumsden, J., Bischoff, M., Ranque, D., Busquin, P., Rasmussen, S., Droste, B., Reutlinger, P., Evans, R., Robins, R., et al., "European Aeronautics: A vision for 2020," *Advisory Council for Aeronautics Research in Europe, Report*, 2001.

[3]Krein, A. and Williams, G., "Flightpath 2050: Europe's Vision for Aeronautics," *Innovation for Sustainable Aviation in a Global Environment: Proceedings of the Sixth European Aeronautics Days, Madrid, 30 March-1 April, 2011*, 2012.

[4]Laban, M., "Aircraft Drag And Thrust Analysis (AIRDATA), Publishable Synthesis Report," NLR-TP-2000-473, National Aerospace Laboratory, NLR, 2001.

[5]Méheut, M. and Bailly, D., "Drag-breakdown methods from wake measurements," *AIAA journal*, Vol. 46, No. 4, 2008, pp. 847–862.

[6]Nalianda, D., Kyprianidis, K., Sethi, V., and Singh, R., "Techno-economic viability assessments of greener propulsion technology under potential environmental regulatory policy scenarios," *Applied Energy*, Vol. 157, 2015, pp. 35–50.

[7]Jupp, J., "The design of future passenger aircraft–the environmental and fuel price challenges," *The Aeronautical Journal*, Vol. 120, No. 1223, 2016, pp. 37–60.

[8]Sehra, A., Whitlow, W., et al., "Propulsion and power for 21st century aviation," *Progress in Aerospace Sciences*, Vol. 40, No. 4-5, 2004, pp. 199–235.

[9]Hegen, G. and Kiock, R., "Experiences with ultra-high-bypass simulators from calibration and isolated engine testing," NLR-TP-1996-193, NLR, March 1996.

[10]Palmer, J., "The TURBOMATCH scheme for aero/industrial gas turbine engine design point/off design performance calculation," Unpublished Internal Report, Cranfield University, 1999.

[11]Laskaridis, P. and Pilidis, P., "An integrated engine - aircraft performance platform for assessing new technologies in aeronautics," *International Society for Air Breathing Engines*, ISABE Paper 2005-1165, September 2005.

[12]Cranfield University, *HERMES V5 and TmatchCalls V3 User Manual*, 2009, Unpublished, Internal Manual.

[13]ESDU, "Drag of Axisymmetric Cowls at Zero Incidence for Subsonic Mach Numbers," Data item 81024, IHS ESDU, London, 1981.

[14]Ministry-Industry Drag Analysis Panel Study Group and others, "Guide to in-flight thrust measurement of turbojets and fan engines," AGARD-AG-237, AGARD, January 1979.

[15]Christie, R., Ramirez, S., and MacManus, D., "Aero-engine installation modelling and the impact on overall flight performance," *Advanced Aero Concepts, Design and Operations Conference, Vol. 27*, July 2014.

[16]Stańkowski, T., MacManus, D., Sheaf, C., and Christie, R., "Aerodynamics of aero-engine installation," *Journal of Aerospace Engineering*, Vol. 230(14), 2016, pp. 2673–2692.

[17]Hoheisel, H. and von Geyr, H. F., "The influence of engine thrust behaviour on the aerodynamics of engine airframe integration," *CEAS Aeronautical Journal*, Vol. 3, 2012, pp. 79–92.

[18]Kettle, D. J. and Kirby, D. A., "Low-Speed Wind-Tunnel Tests on the Effects of Tailplane and Nacelle Position on the Superstall Characteristics of Transport Aircraft," R. & M. No. 3571, Aeronautical Research Council, August 1967.

[19]Küchemann, D. and Weber, J., *Aerodynamics of Propulsion*, Vol. 2, McGraw-Hill, 1953.

[20]Bangert, L. H., Krivec, D. K., and Segall, R. N., "Effects of Nacelle Configuration/Position on Performance of Subsonic Transport," NASA-CR-3743,NASA, NASA Langley Research Center, Hampton, VA, United States, November 1983.

[21]Abeyounis, W. K. and Patterson Jr, J. C., "Effect of underwing aft-mounted nacelles on the longitudinal aerodynamic characteristics of a high-wing transport airplane," NASA-TP-2447, NASA, NASA Langley Research Center, Hampton, VA, United States, December 1985.

[22]Henderson, W. P. and Patterson Jr, J. C., "Propulsion Installation Characteristics for Turbofan Transports," *21st Aerospace Sciences Meeting*, AIAA Paper 83-0087, January 1983.

[23]Whitcomb, R. T., "Special Bodies Added on a Wing to Reduce Shock Induced Boundary-layer Separation at High Subsonic Speeds," NASA-TN-4293, NASA, NASA Langley Research Center, Hampton, VA, United States, June 1958.

[24]Carlson, J. R. and Compton, W. B., "An Experimental Investigation of Nacelle-Pylon Installation on an Unswept Wing at Susbonic and Transonic Speeds," NASA-TP-2246, NASA, NASA Langley Research Center, Hampton, VA, United States, Febuary 1984.

[25]Lee, E. E. and Pendergraft Jr, O. C., "Installation Effects of Long-duct Pylon-mounted Nacelles on a Twin-jet Transport Model with Swept Supercritical Wing," NASA-TP-2457, NASA, NASA Langley Research Center, Hampton, VA, United States, December 1985.

[26]Lamb, M. and Abeyounis, W. K., "Integration effects of underwing forward-and rearward-mounted separate-flow, flow-through nacelles on a high-wing transport," NASA-TM-87627, NASA, NASA Langley Research Center, Hampton, VA, United States, April 1986.

[27]Convair Aerospace Division of General Dynamics, "Experimental Investigation of Parametric Models in Support of a NASA Advanced Transport Technology Program," NASA-CR-112133, NASA, NASA Langley Research Center, Hampton, VA, United States, October 1972.

[28]Langley, M., "The Design of Axisymmetric Cowls for Podded Nacelles for High By-pass Ratio Turbofan Engines," Reports and Memoranda No. 3846, Aircraft Research Association Ltd, Bedford, May 1979.

[29]Lamb, M. and Abeyounis, W. K., "Natural Laminar Flow Nacelle for Transport Aircraft," NASA-N88-14949, NASA, NASA Langley Research Center, Hampton, VA, United States, December 1988.

[30]Laflin, K. R., Klausmeyer, S. M., Zickuhr, T., Vassberg, J. C., Wahls, R. A., Morrison, J. H., Brodersen, O. P., Rakowitz, M. E., Tinoco, E. N., and Godard, J.-L., "Data summary from second AIAA computational fluid dynamics drag prediction workshop," *Journal of Aircraft*, Vol. 42, No. 5, 2005, pp. 1165–1178.

[31]Redeker, G., Schmidt, N., and Muller, R., "Design and experimental verification of a transonic wing for a transport aircraft," *Proceedings of the FDP Symposium on Subsonic/Transonic Configuration Aerodynamics*, AGARD-CP-285, 1980, pp. 1–7.

[32]Rossow, C.-C., Godard, J.-L., Hoheisel, H., and Schmitt, V., "Investigations of propulsion integration interference effects on a transport aircraft configuration," *Journal of Aircraft*, Vol. 31, No. 5, 1994, pp. 1022–1030.

[33]Keye, S., Sitzmann, M., Brodersen, O., and Heinrich, R., "Fluid-Structure Coupled Loads Analysis of DLR's F6 Wing-Body Configuration," *46th AIAA Aerospace Sciences Meeting and Exhibit*, AIAA Paper 2008-0675, January 2008.

[34]Vassberg, J. C., Sclafani, A. J., and DeHaan, M. A., "A wing-body fairing design for the DLR-F6 model: a DPW-III case study," *23rd AIAA Applied Aerodynamics Conference*, AIAA Paper 2005-4730, June 2005.

[35]Vassberg, J. C., Tinoco, E. N., Mani, M., Rider, B., Zickuhr, T., Levy, D. W., Brodersen, O. P., Eisfeld, B., Crippa, S., Wahls, R. A., et al., "Summary of the Fourth AIAA CFD Drag Prediction Workshop," *Journal of Aircraft*, Vol. 51(4), 2010, pp. 1070–1089.

[36]Levy, D. W., Laflin, K. R., Tinoco, E. N., Vassberg, J. C., Mani, M., Rider, B., Rumsey, C., Wahls, R. A., Morrison, J. H., Brodersen, O. P., et al., "Summary of data from the fifth AIAA CFD drag prediction workshop," *51st AIAA Aerospace Sciences Meeting including the New Horizons Forum and Aerospace Exposition*, AIAA Paper 2013-0046, January 2013.

[37]Gatlin, G. M., Rivers, S. M., Goodliff, S. L., Rudnik, R., and Sitzmann, M., "Investigation of the DLR-F6 Transport in the National Transonic Facility (Invited)," *26th AIAA Applied Aerodynamics Conference*, AIAA Paper 2008-6917, August 2008.

[38]Pauley, G., "Interim Note on Tests with a Wing-Mounted Fan Nacelle with the Fan Jet Simulated by Cold Air Blowing and Alternatively by a Gas Generator Shroud," C.P. No. 1111, Aeronautical Research Council, Bedford, March 1968.

[39]Levart, P., "Experimental Study of the Interaction between the Wing of a Subsonic Aircraft and a Nacelle of a High By-pass Ratio Engine," NASA-TM-76606, NASA, NASA Langley Research Center, Hampton, VA, United States, July 1981.

[40]Harrington, D. E., "Jet Effects on Boattail Pressure Drag of Isolated Ejector Nozzles at Mach Numbers from 0.60 to 1.47," NASA-TM-X-1785, NASA, NASA Langley Research Center, Hampton, VA, United States, May 1969.

[41]Wells, O. D., Lopez, M. L., Welge, H. R., Henne, P. A., and Sewell, A. E., "Wind Tunnel and Analytical Investigation of Over-the-wing Propulsion/Airframe Interferences for a Short-haul Aircraft at Mach Numbers from 0.6 to 0.78," NASA-CR-2905, NASA, NASA Langley Research Center, Hampton, VA, United States, September 1977.

[42]Burgsmuller, W. and Hoheisel, H., "ENIFAIR - EU Research into Engine Integration on Future Transport Aircraft," *Air and Space Europe, No. 2*, 2000, pp. 81–85.

[43]von Geyr, H. F. and Rossow, C.-C., "A correct thrust detemination method for turbine powered simulatiors in wind tunnel testing," *41st AIAA/ASME/SAE/ASEE Joint Propulsion Conference &Exhibit*, AIAA Paper 2005-3707, July 2005.

[44]Levy, D. W., Zickuhr, T., Vassberg, J., Agrawal, S., Wahls, R. A., Pirzadeh, S., and Hemsch, M. J., "Summary of Data from the First AIAA CFD Drag Prediction Workshop," *Journal of Aircraft*, Vol. 40(5), 2002, pp. 875–882.

[45]Rudnik, R., Rossow, C.-C., and von Geyr, H. F., "Numerical simulation of engine/airframe integration for high-bypass engines," *Aerospace Science and Technology*, Vol. 6, No. 1, 2002, pp. 31 – 42.

[46]Kroll, N., Rossow, C.-C., Becker, K., and Thiele, F., "The MEGAFLOW project," *Aerospace Science and Technology*, Vol. 4, No. 4, 2000, pp. 223–237.

[47]Brodersen, O., "Drag prediction of engine-airframe interference effects using unstructured Navier-Stokes calculations," *Journal of Aircraft*, Vol. 39, No. 6, 2002, pp. 927–935.

[48]Rakowitz, M., Eisfeld, B., Schwamborn, D., and Sutcliffe, M., "Structured and unstructured computations on the DLR-F4 wing-body configuration," *Journal of Aircraft*, Vol. 40, No. 2, 2003, pp. 256–264.

[49]Trapp, L. G. and Argentieri, H. G., "Evaluation of nacelle drag using computational fluid dynamics," *Journal of Aerospace Technology and Management*, Vol. 2, No. 2, 2010, pp. 145–153.

[50]Sibilli, T., *Modelling the aerodynamics of propulsive system integration at cruise and high-lift conditions*, Ph.D. thesis, Department of Power and Propulsion, Cranfield University, 2012.

[51]Zhang, Y., Chen, H., Fu, S., Zhang, M., and Zhang, M., "Drag prediction method of powered-on civil aircraft based on thrust drag bookkeeping," *Chinese Journal of Aeronautics*, Vol. 28, No. 4, 2015, pp. 1023–1033.

[52]Zawislak, M., *Experimental and RANS-CFD Study of Nacelle Drag*, Master's thesis, Department of Mechanical and Materials Engineering, Queens University, Kingston, Ontario, Canada, 2016.

[53]AGARD, "A selection of experimental test cases for the validation of CFD codes," AGARD-AR-303 Vol. I, AGARD, August 1994.

[54]Vassberg, J. C., Tinoco, E. N., Mani, M., Brodersen, O. P., Eisfeld, B., Wahls, R. A., Morrison, J. H., Zickuhr, T., Laflin, K. R., and Mavriplis, D. J., "Abridged summary of the third AIAA computational fluid dynamics drag prediction workshop," *Journal of Aircraft*, Vol. 45, No. 3, 2008, pp. 781–798.

[55]Daggett, D. L., Brown, S. T., and Kawai, R. T., "Ultra-Efficient Engine Diameter Study," NASA/CR-2003-212309, NASA, NASA Langley Research Center, Hampton, VA, United States, May 2003.

[56]Seitz, A., *Advanced methods for propulsion system integration in aircraft conceptual design*, Ph.D. thesis, Faculty of Mechanical Engineering, Technical University of Munich, 2012.

[57]GasTurb GmbH, "GasTurb 12 Manual," *GasTurb GmbH, www.gasturb.de/manual (last accessed: 05 Febuary 2017)*, 2007.

[58]Lissys Limited, "PIANO website," *Lissys Limited, UK www.piano.aero (last accessed: 05 February 2017)*, 2017.

[59]Lacava, P. T. and Ribeiro, R. F. G., "Investigation of Optimum Turbofan Engine Bypass Ratio For a Large, Long Range Business Jet," *22nd International Congress of Mechanical Engineering*, COBEM Paper 2013-1874, November 2013.

[60]Thulin, O., Rogero, J.-M., and Grönstedt, T., "A mission assessment of aero engine losses," *22nd ISABE Conference*, ISABE Paper 2015-20121, October 2015.

[61]Miao, Z., *Aircraft engine performance and integration in a flying wing aircraft conceptual design*, Master's thesis, School of Engineering, Cranfield University, 2012.

[62]Bala, A., Sethi, V., Lo Gatto, E., Pachidis, V., and Pilidis, P., "PROOSISA Collaborative Venture for Gas Turbine Performance Simulation Using an Object Oriented Programming Schema," *ISABE 2007 Proceedings*, ISABE Paper 2007-1357, May 2007.

[63]Kyprianidis, K., Dax, A., Ogaji, S., and Grönstedt, T., "Low Pressure System Component Advancements and Its Impact on Future Turbofan Engine Emissions," *XIX International Symposium on Air Breathing Engines (ISABE)*, ISABE Paper 2009-1276, September 2015.

[64]Palmer, J., "The TURBOMATCH scheme for gas turbine performance calculations," Unpublished Internal Report, Cranfield University, 1983.

[65]Covert, E. E., *Thrust and Drag: Its Prediction and Verification*, Vol. 98 of *Progress In Astronautics and Aeronautics*, AIAA, 1985.

[66]ESDU, "Introduction to the Measurement of Thrust in Flight. (Air Breathing Ducted-flow Engines)," Data item 69006, IHS ESDU, London, 1981.

[67]Van Der Vooren, J. and Sloof, J., "CFD-based drag prediction: State-of-the-art, theory, prospects," NLR-TP-90247, NLR, August 1990.

[68]Destarac, D. and Van Der Vooren, J., "Drag/thrust analysis of jet-propelled transonic transport aircraft; Definition of physical drag components," *Aerospace Science and Technology*, Vol. 8, No. 6, 2004, pp. 545–556.

[69]Vos, J. B., Sanchi, S., and Gehri, A., "Drag prediction workshop 4 results using different grids including near-field/far-field drag analysis," *Journal of Aircraft*, Vol. 50, No. 5, 2013, pp. 1615–1627.

[70]Brodersen, O., Rakowitz, M., Amant, S., Larrieu, P., Destrac, D., and Sutcliffe, M., "Airbus, ONERA, and DLR Results from the 2nd Drag Prediction Workshop," *42nd AIAA Aerospace Sciences Meeting and Exhibit*, AIAA Paper 2004-0391, January 2004.

[71]Tomita, J. T., Bringhenti, C., Pozzani, D., Barbosa, J. R., de Jesus, A. B., de Almeida, O., and Oliveira, G. L., "Overview on Nacelle Design," *18th International Congress of Mechanical Engineering*, COBEM Paper 2005-0972, November 2005.

[72]Bicchi, A. and Pallottino, L., "On optimal cooperative conflict resolution for air traffic management systems," *IEEE Transactions on Intelligent Transportation Systems*, Vol. 1, No. 4, 2000, pp. 221–231.

[73]Baals, D., Smith, N., and Wright, J., "Development and Application of High-critical-speed Nose Inlets," NACA Rep. 920, 1945.

[74]Palmer, C., "Tests on Pods with Short Forebodies in the Aircraft Research Association Wind Tunnel." Tech. Rep. DMB/WFW.10/CHB, Rolls-Royce Ltd, 1964.

[75]Sutherland, W., "The Results of Model Tests on Intake Cowlings for Ducted Fan Engines," Tech. Rep. P.D. 1369, Bristol Siddeley Engines Ltd, 1965.

[76]Hitchcock, M., "The Spillage Drag of NACA 1-Series Intake Cowlings," Tech. Rep. G.W. 10260, Bristol Siddeley Engines Ltd, 1967.

[77]Stanhope, F., "The performance of NACA 1-series intakes," Tech. Rep. IAR-85002, Rolls-Royce Ltd, 1968.

[78]Jones, A., "Engine Pod Drag Model Tests to Show the Effect of Intake Shape on the Drag and Airflow Characteristics of Pod Intakes," Tech. Rep. IAR 85001, Rolls-Royce Ltd, 1968.

[79]Horton, H., "Calculation of compressible turbulent boundary layers by the entrainment history method," Tech. Rep. 1048/HPH, Hawker Siddeley Aviation (Hatfield), 1969.

[80]Cook, T., "Measurement of the Boundary Layer and Wake of Two Aerofoil Sections at High Reynolds Numbers and High Subsonic Mach Numbers." Reports and Memoranda No. 3722, Aeronautical Research Council, June 1971.

[81]Langley, M., "Measurements of External Drag and Surface Pressure Distributions on Six Cowls Designed for High Subsonic Mach number," Model test note M.31/l, Parts l, 2 and 3, Aircraft Research Association, Bedford, 1971.

[82]Reubush, D., "Effects of fineness and closure ratios on boattail drag of circular-arc afterbodies having closure ratios of 0.50 with jet exhaust at Mach numbers up to 1.30," NASA-TN-D-7163, NASA, NASA Langley Research Center, Hampton, VA, United States, May 1973.

[83]Re, R., "An Investigation of Several NACA 1-Series Inlets at Mach Numbers from 0.4 to 1.29 for Mass Flow Ratios near 1.0," NASA-TM-X-3324, NASA, NASA Langley Research Center, Hampton, VA, United States, December 1975.

[84]Reubush, D.E. Putnam, L., "An Experimental and Analytical Investigation of the Effect on Isolated Boattail Drag of Varying Reynolds Numbers up to 13,000,000," NASA-TN-D-8210, NASA, NASA Langley Research Center, Hampton, VA, United States, May 1976.

[85]Reid, J., "Interference on axisymmetric bodies in subsonic flow," Tech. Rep. 77185, Royal Aerospace Establishment, Bedford, 1977.

[86]Galbraith, B., "DATCOM Predicted Aerodynamic Model," *Holy Cows, www.holycows.net, (last access: 05 February 2017)*, 2004.

[87]Hepperle, M., "JAVAFOIL users guide," *MH-AeroTools, http://www.mh-aerotools.de/airfoils/javafoil.htm (Last accessed: 06 July 2016)*, 2011.

[88]ANSYS, Inc., "ANSYS CFX-Solver Modeling Guide Release 12.0," ANSYS, Inc., Canonsburg, PA 15317, November 2009.

[89]ANSYS, Inc., "ICEM CFD User Manual Release 12.0," ANSYS, Inc., Canonsburg, PA 15317, November 2011.

[90]ANSYS, Inc., "ANSYS CFX-Solver Theory Guide Release 12.0," ANSYS, Inc., Canonsburg, PA 15317, November 2009.

[91]Menter, F., Langtry, R., Likki, S., Suzen, Y., Huang, P., and Völker, S., "A correlation-based transition model using local variables Part I: model formulation," *Journal of Turbomachinery*, Vol. 128, 2006, pp. 413.

[92]Versteeg, H. K. and Malalasekera, W., *An Introduction to Computational Fluid dynamics: The Finite Volume Method*, Pearson Education, 2007.

[93]Roache, P., *Verification and Validation in Computational Science and Engineering*, Hermosa Publishers, 1998.

[94]Christie, R., "PhD 9 Month Progress Review," School of Engineering, Cranfield University, 2011.

[95]Stańkowski, T., "PhD 21 Month Progress Review," School of Engineering, Cranfield University, 2014.

[96]Tong, M., Jones, S., Haller, W., and Handschuh, R., "Engine Conceptual Design Studies for a Hybrid Wing Body Aircraft," *ASME Turbo Expo 2009: Power for Land, Sea, and Air*, ASME Paper GT2009-59568, June 2009.

[97]PTC, "Creo Parametric | PTC," *PTC, http://www.ptc.com/cad/creo/parametric (Last accessed: 07 May 2016)*, 2016.

[98]Bell, J. H. and Mehta, R. D., "Contraction Design for Small Low-Speed Wind Tunnels," NASA-CR-177488, NASA, NASA Langley Research Center, Hampton, VA, United States, August 1988.

[99]ESDU, "NACA 1-series geometry representation for computational fluid dynamics," Data item 94013, IHS ESDU, London, 1994.

[100]Kulfan, B. M. and Bussoletti, J. E., "Fundamental parametric geometry representations for aircraft component shapes," *11th AIAA/ISSMO Multidisciplinary Analysis and Optimization Conference*, AIAA Paper 2006-6948, September 2006.

[101]Kulfan, B. M., "Universal parametric geometry representation method," *Journal of Aircraft*, Vol. 45, No. 1, 2008, pp. 142–158.

[102]Zhu, F. and Qin, N., "Intuitive Class/Shape Function Parameterization for Airfoils," *AIAA Journal*, Vol. 52, No. 1, 2013, pp. 17–25.

[103]Aeronautical Research Council, "Report of the Definitions Panel on the Definitions of the Thrust of a Jet Engine and of the Internal Drag of a Ducted Body," C.P. No. 190, Aeronautical Research Council, May 1954.

[104]Roache, P., "Perspective: a method for uniform reporting of grid refinement studies," *Journal of Fluids Engineering*, Vol. 116, No. 3, 1994, pp. 405–413.

[105]Airbus, "A330 Aircraft characteristics airport and maintainance planning," *Airbus S.A.S., Customer Services, Technical Data Support and Services, 31707 Blagnac Cedex, France*, January 2014.

[106]EUROCONTROL, "Base of aircraft data (BADA)," *BADA, www.eurocontrol.int/eec/public/standard_page/proj_BADA.html, (Last accessed: 05 March 2014)*, 2014.

[107]MacMillan, W. L., *Development of a modular type computer program for the calculation of gas turbine off design performance*, Ph.D. thesis, School of Mechanical Engineering, Cranfield University, 1974.

[108]Greitzer, E. M., Bonnefoy, P. A., de la Rosa Blanco, E., Dorbian, C. S., Drela, M., Hall, D. K., Hansman, R. J., Hileman, J. I., Liebeck, R. H., Lovegren, J., Mody, P., Pertuze, J. A., Sato, S., Spakovszky, Z. S., Tan, C. S., Hollman, J. S., Duda, J. E., Fitzgerald, N., Houghton, J., Kerrebrock, J. L., Kiwada, G. F., Kordonowy, D., Parrish, J. C., Tylko, J., Wen, E. A., and Lord, W. K., "N+3 Aircraft Concept Designs and Trade Studies, Final Report. Volume 2: Appendices Design Methodologies for Aerodynamics, Structures, Weight, and Thermodynamic Cycles," NASA/CR-2010-216794/VOL2, NASA, NASA Langley Research Center, Hampton, VA, United States, December 2010.

[109]Lolis, P., Giannakakis, P., Sethi, V., Jackson, A., and Pilidis, P., "Evaluation of aero gas turbine preliminary weight estimation methods," *The Aeronautical Journal*, Vol. 118, No. 1204, 2014, pp. 625–641.

[110]Jenkinson, L. R., Simpkin, P., and Rhodes, D., *Civil Jet Aircraft Design*, Arnold, 1999.

[111]López, R., *Validation of software for the calculation of aerodynamic coefficients: with a focus on the software package Tornado*, Ph.D. thesis, Department of Management and Engineering, Linkopings Universitet Tekniska Hogskolan, 2010.

[112]Melin, T., *A vortex lattice MATLAB implementation for linear aerodynamic wing applications*, Master's thesis, Department of Aeronautics, Royal Institute of Technology (KTH), Stockholm, Sweden, 2000.

[113]UIUC Applied Aerodynamics Group, "UIUC Applied aerodynamics group. UIUC airfoil coordinates database, Department of Aerospace Engineering, University of Illinois at Urbana-Champaign, 2014," *UUIC, http://aerospace.illinois.edu/m-selig/ads/coord_database.html, (Last accessed: 01 July 2014)*, 2014.

[114]Vassberg, J. C., DeHaan, M. A., Rivers, S. M., and Wahls, R. A., "Development of a Common Research Model for Applied CFD Validation Studies," *26th AIAA Applied Aerodynamics Conference*, AIAA Paper 2008-6919, August 2008.

[115]Boeing, "777-200/300 Characteristics for airport planning," *Boeing Commercial Airplanes, Seattle, Washington, USA*, July 1998.

[116]Boeing, "747-400 Airplane characteristics for airport planning," *Boeing Commercial Airplanes, Seattle, Washington, USA*, 2002.

[117]Federici, F., *Group design project - Section 5 - Aerodynamics Specialist Report*, Master's thesis, University of Bristol, 2009.

[118]Van Dam, C., "Recent experience with different methods of drag prediction," *Progress in Aerospace Sciences*, Vol. 35, No. 8, 1999, pp. 751–798.

[119]Airbus, "A350-900 Aircraft characteristics airport and maintainance planning," *Airbus S.A.S., Customer Services, Technical Data Support and Services, 31707 Blagnac Cedex, France*, April 2015.

[120]Airbus, "A320 Aircraft characteristics airport and maintainance planning," *Airbus S.A.S., Customer Services, Technical Data Support and Services, 31707 Blagnac Cedex, France*, April 2012.

[121]Airbus, "A321 Aircraft characteristics airport and maintainance planning," *Airbus S.A.S., Customer Services, Technical Data Support and Services, 31707 Blagnac Cedex, France*, April 2015.

[122]Airbus, "A340-200/-300 Aircraft characteristics airport and maintainance planning," *Airbus S.A.S., Customer Services, Technical Data Support and Services, 31707 Blagnac Cedex, France*, January 2014.

[123]Airbus, "A340-500/-600 Aircraft characteristics airport and maintainance planning," *Airbus S.A.S., Customer Services, Technical Data Support and Services, 31707 Blagnac Cedex, France*, January 2014.

[124]Boeing, "747 Characteristics for airport planning," *Boeing Commercial Airplanes, Seattle, Washington, USA*, January 1984.

[125]Boeing, "757-200/300 Characteristics for airport planning," *Boeing Commercial Airplanes, Seattle, Washington, USA*, August 2002.

[126]Boeing, "767 Characteristics for airport planning," *Boeing Commercial Airplanes, Seattle, Washington, USA*, September 2005.

[127]Boeing, "787 Characteristics for airport planning," *Boeing Commercial Airplanes, Seattle, Washington, USA*, November 2014.

[128]Stańkowski, T., Personal Communication, 05 July 2015.

[129]Oliveira, G. L., Trapp, L. G., and Puppin-Macedo, A., "Integration methodology for regional jet aircraft with underwing engines," *41st Aerospace Sciences Meeting and Exhibit*, AIAA Paper 2003-934, January 2003.

[130]Tinoco, E. and Chen, A., "Transonic CFD applications to engine/airframe integration," *22nd Aerospace Sciences Meeting*, AIAA Paper 84-0381, January 1984.

[131]NASA, "4th AIAA CFD Drag Prediction Workshop Gridding Guidelines," *NASA, http://aaac.larc.nasa.gov/tsab/cfdlarc/aiaa-dpw/Workshop4/gridding_guidelines_4.html, (Last accessed: 16 November 2015)*, 2015.

[132]Langtry, R. B., Kuntz, M., and Menter, F., "Drag prediction of engine-airframe interference effects with CFX-5," *Journal of Aircraft*, Vol. 42, No. 6, 2005, pp. 1523–1529.

Appendix A

RAeS Advanced Aero Concepts, Design and Operations Conference 2014

Aero-engine installation modelling and the impact on overall flight performance[15]

Robert Christie, Santiago Ramirez, David G. MacManus

Cranfield University, Bedford, United Kingdom, MK43 0AL

Abstract

The paper describes the development of a preliminary design tool which can assess the effect of nacelle size, geometry, angle of attack and installation on flight efficiency. Various methods of predicting nacelle drag were compared. The importance of including the effect of weight, nacelle local upflow angle and installation effects in the nacelle drag calculation has been shown. A preliminary design tool (PSIMOD) has been developed which uses the ESDU drag prediction method to predict nacelle drag as a function of flight Reynolds

number, Mach number, nacelle shape and intake MFCR. Corrections are then applied to this drag prediction to take into account nacelle local upflow effects and nacelle and propulsion system integration effects. This nacelle drag is integrated within PSIMOD in a drag build up method at each point in the flight as part of an aircraft and engine performance model.

Appendix B

Wake integral method drag extraction theory

Drag can be found by comparing the fluid momentum ahead of the body with the momentum downstream of the body. This equates to profile drag and is given by Equation B.1.

$$D = \int\int \rho V \left(V_0 - V\right) dA \tag{B.1}$$

Applying Equation B.1 to a body of revolution as shown in Figure B.1 leads to Equation B.2

$$\begin{aligned} D &= \int_0^\theta \int_r^R \rho V \left(V_0 - V\right) r dr d\theta \\ &= \int_0^\theta \frac{1}{2} \rho V \left(r^2 - R^2\right) \left(V - V_0\right) d\theta \\ &= \pi \rho V \left(r^2 - R^2\right) \left(V - V_0\right) \end{aligned} \tag{B.2}$$

This is the experimental approach taken in the ARA 1968-73 nacelle tests.[28] The pitot-static rake used in these tests is shown in Figure B.2. Local P and P_0, tunnel T_0 and P_0 were known. The outer edge of wake was found by scanning rake measurements from the

outermost rake inwards until a total head loss of 0.013% was found (Figure B.2. Local mach number can be calculated using Equation B.3 which enables the local static temperature to be calculated from Equation B.4. The local velocity and density can be found using Equations B.5 and B.6 respectively. Now all the variables in Equation B.2 are known and drag can be calculated. In later numerical work this method is followed with local values extracted from the numerical solution at the measurement points. This process was automated using a Tecplot macro. This macro wrote the local values at the measurement points to a text file which then was processed by a MATLAB script.

$$M = \sqrt{\left[\left(\frac{P_0}{P}\right)^{\frac{\gamma}{(\gamma-1)}} - 1\right]\frac{2}{\gamma-1}} \tag{B.3}$$

$$T = \frac{T_0}{1 + \frac{\gamma-1}{2}M^2} \tag{B.4}$$

$$V = M \cdot \sqrt{\gamma RT} \tag{B.5}$$

$$\rho = \frac{P}{RT} \tag{B.6}$$

Then Equation B.2 can be used to calculate the drag with V_0 being is the average of all good readings outside the wake.

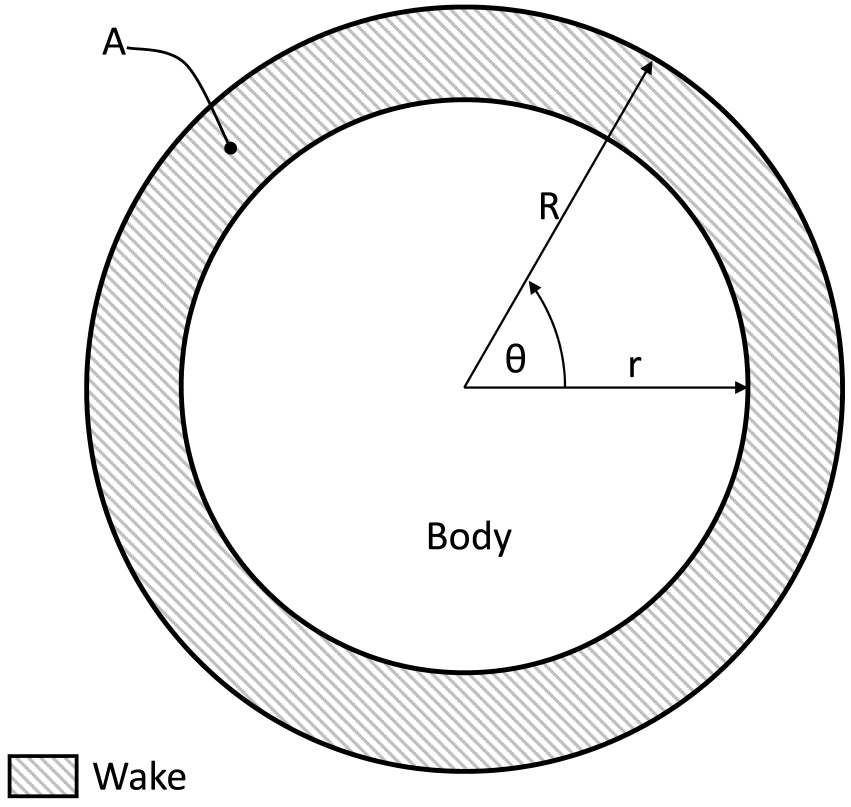

FIGURE B.1: Nomenclature for a wake integral around an axisymmetric body

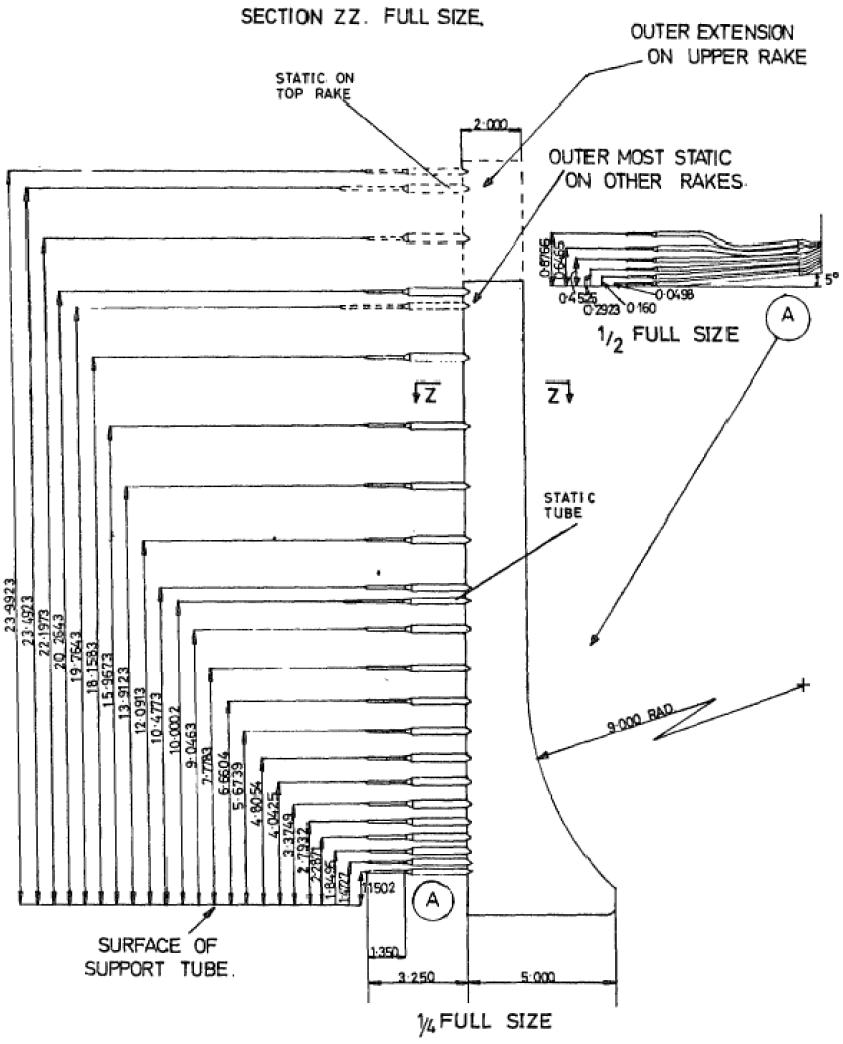

FIGURE B.2: ARA experimental pitot-staic rake[28]

Appendix C

CFD rationale

This Appendix discusses the main reasons for the use of CFX as the CFD solver, the problems encountered in running the simulations and the solutions found. Low order models, such as Euler codes do not have the required fidelity to predict the complex flowfield phenomena present in full aircraft-engine simulations. It has been shown in the literature that a steady RANS based approach is appropriate. CFX was chosen as the RANS CFD solver as it was available to the Author and has been used in the open literature for aircraft engine CFD calculations.[34,50,54,132]

The following problems encountered during the set up of robust CFD calculations were encountered:

1. Initially a rectangular cuboid domain was employed. However this lead to divergence of the solution where velocity vectors were imposed parallel to boundaries. This was solved by changing to a hemi-spherical domain.

2. CFX does not have a built in "farfield" boundary condition. The "'Opening' boundary condition was used at the farfield. Freestream conditions were imposed by setting the Cartesian components of velocity, static temperature and turbulence values. Static pressure was also imposed indirectly through global initialisation.

3. The "'Opening' boundary condition which was used at the farfield does not allow static pressure to be specified. In initial simulations of clean-wing aircraft the static pressure set correctly at the farfield to be equal to the user imposed reference pressure. However when an engine-aircraft configuration was simulated the code imposed the total pressure at the nozzle outlet as the freestream static pressure. It was found that the static pressure was automatically imposed at the farfield from other boundary conditions in the following order:

   (a) Total pressure boundary condition

   (b) Static boundary condition

   (c) User imposed reference static pressure

   Theses difficulties were overcome by carrying out a global initialisation with the relative static pressure equal to zero.

4. Difficulties were found in setting up a robust convergence strategy. This was especially different for the isolated engines simulations at incidence and the aircraft calculations in which flow separation was present. In all cases the "Automatic Timescale" was set. This was modified by adjusting the "Timescale Factor". For the wing-nacelle CFD calculations (Chapter 7) this was modified through a step function based on the "Accumulated Timestep" and the "Accumulated Iteration Number". This allowed the "Timescale Factor" to be set to 0.02 for the first 1000 iterations, then increased to 0.1 for a further 1000 iterations. It was then set to 1.0 for 3000 iterations. Next it was increased by 1 starting from 1 each iteration for 100 iterations. Finally it was increased by 100 each iteration for 10 iterations. For the clean wing

cases (Chapter 7) the "Timescale Factor" was set to 0.02, 1.0 and back to 0.02 for 1000, 1000 and 3000 iterations respectively. The isolated nacelle CFD calculations (Chapter 5) featured a large range of angles of attack ($0^o \leq \alpha \leq 10^o$) and MFCRs ($0.25 \leq MFCR \leq 1.5$). It therefore proved difficult to have a robust convergence scheme which also minimised the number of iterations required in each case. For this reason in all cases the "Timescale Factor" was set to 0.01 for all 4000 iterations.

Appendix D

ARA cowl 1 CFD boundary conditions

D.1 Boundary conditions for M=0.4 MFCR sweep

M	V (m/s)	Turbulence	T (K)
0.40	135.54	10%	285.75

Table D.1: Inlet boundary conditions

M	P (Pa)	Turbulence	T (K)
0.40	90748.13	zero gradient	285.75

Table D.2: Opening (entrainment & pressure) boundary conditions

M	P (Pa)	Turbulence	T (K)
0.40	90748.13	10%	285.75

Table D.3: Opening (pressure & direction) boundary conditions

M	MFCR	W (kg/m^2)	Mass flow update
0.40	1.0	0.0149	constant flux
0.40	0.9	0.0135	constant flux
0.40	0.8	0.0120	constant flux
0.40	0.7	0.0105	constant flux
0.40	0.6	0.0090	constant flux
0.40	0.5	0.0075	constant flux
0.40	0.4	0.0060	constant flux
0.40	0.3	0.0045	constant flux
0.40	0.2	0.0030	constant flux
0.40	0.1	0.0015	constant flux
0.40	0.0	0.0000	constant flux

TABLE D.4: Outlet (mass flow) boundary conditions

Appendix E

Payload range diagram comparison

Two baseline aircraft models were created to be representative of a short haul and long haul aircraft to be used by PSIMOD to assess the impact of engine integration effects on overall mission performance. A short haul flight was considered based on an aircraft based on the Boeing 737-800, with two engines similar to the CFM56-7B27 over a mission distance of 1,000 km and with a payload of 10,660 kg. The long haul mission was assessed using an aircraft based on a Boeing 777-300 configuration, whose engines were similar to the Trent 892 over a range of 6,000 km and with a payload weight of 33,370 kg. The cruise altitude for both aircraft was set to 10,668m with cruise Mach numbers of 0.81 and 0.84 for the short and long haul aircraft respectively. The $C_L - \alpha$ curve of each aircraft is required by PSIMOD. This was calculated using a vortex lattice method [112] with compressibility corrections for high subsonic Mach numbers.

The aircraft models were created to be representative of existing transonic civil transport aircraft not to model them exactly. A closer match with the real aircraft could be achieved by manual iteration of the aircraft model inputs in PSIMOD. To show that the created aircraft models are representative of real aircraft the payload range diagram calculated for the long haul aircraft is compared to that of a Boeing 777-300. [115] Three payload range

diagrams calculated with PSIMOD are shown (Figure E.1). These show the impact of changing the the nacelle drag prediction method upon the payload range diagram. When no nacelle drag was modelled the maximum range was over-predicted by 1.1%. However when the skin-friction estimate (SFE) and ESDU methods were used to calculate nacelle drag the maximum range was underpredicted by 3.1% and 5.7% respectively. A similar exercise was carried out for the short haul aircraft. In this case when no nacelle drag was modelled the maximum range was over-predicted by 2.2%. The SFE and ESDU nacelle drag methods underpredicted nacelle drag by 3.4% and 7.6% respectively. Based on this comparison the aircraft models were deemed to be representative enough to be used as PSIMOD models to assess the impact of engine integration effects on overall mission performance.

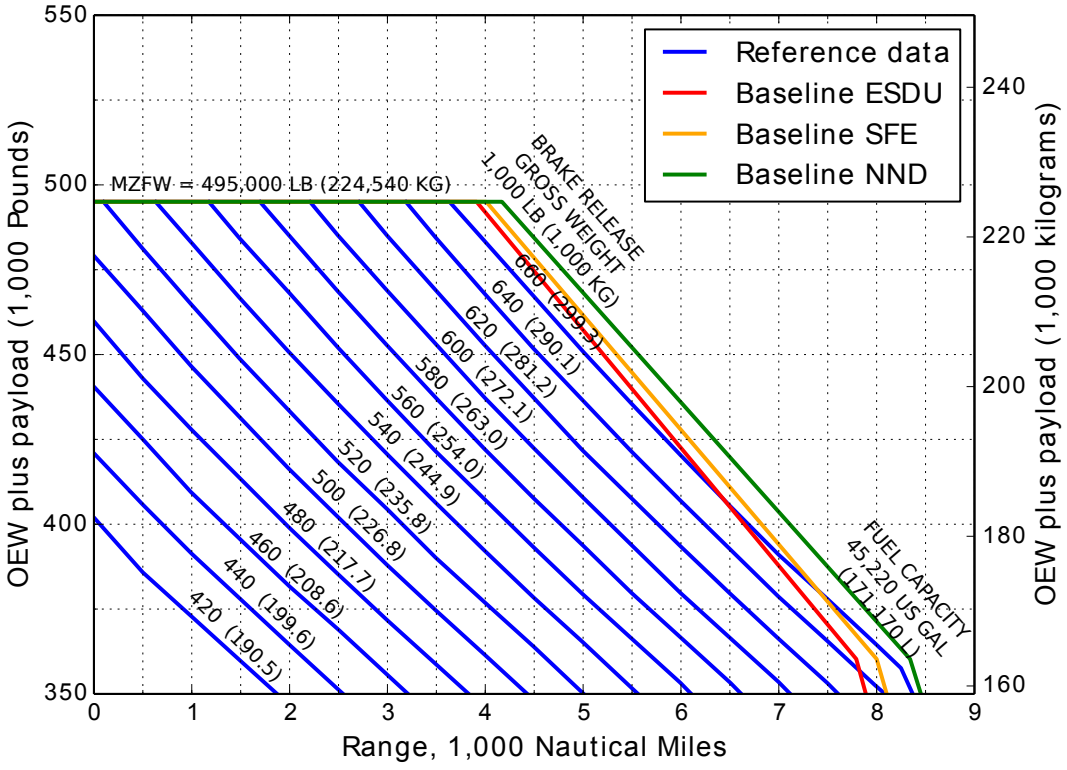

FIGURE E.1: Comparison of the payload range diagram calculated for the long haul aircraft and that of a Boeing 777[115]

Appendix F

Additional figures

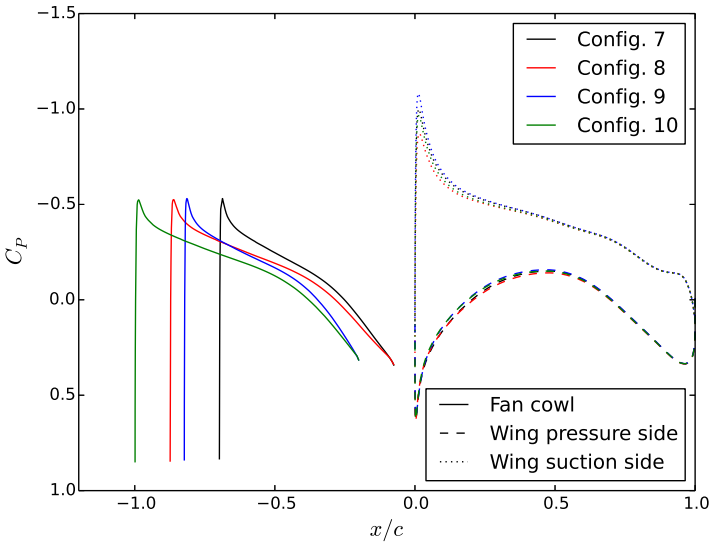

FIGURE F.1: The C_P distribution along the fan cowl topline and the wing suction and pressure surfaces for Configurations 7, 8, 9 and 10 respectively (Table 7.4).

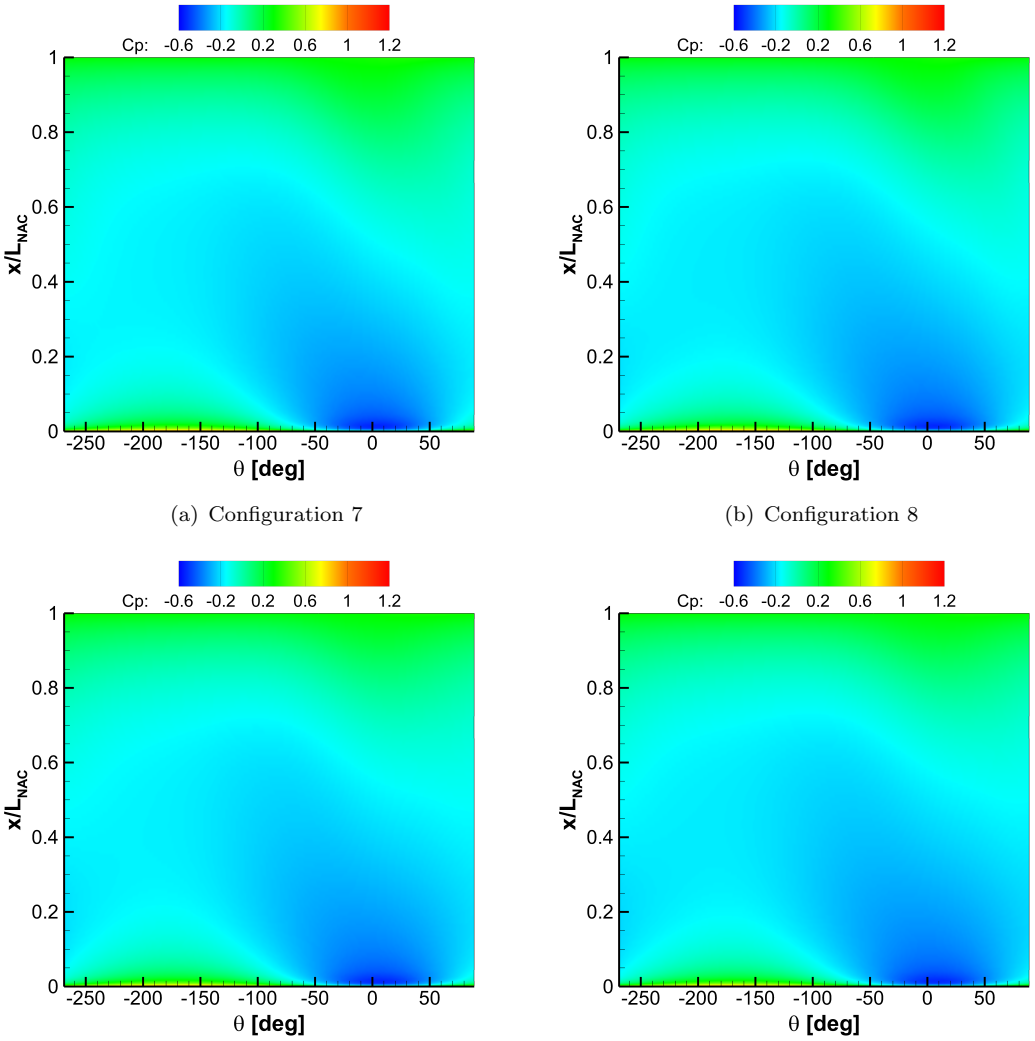

(a) Configuration 7

(b) Configuration 8

(c) Configuration 9

(d) Configuration 10

FIGURE F.2: [The C_P distribution on the unwrapped fan cowl for the datum nacelle and the large nacelle installed in positions 1 and 2, Configurations 7, 8, 9 and 10 respectively (Table 7.4).

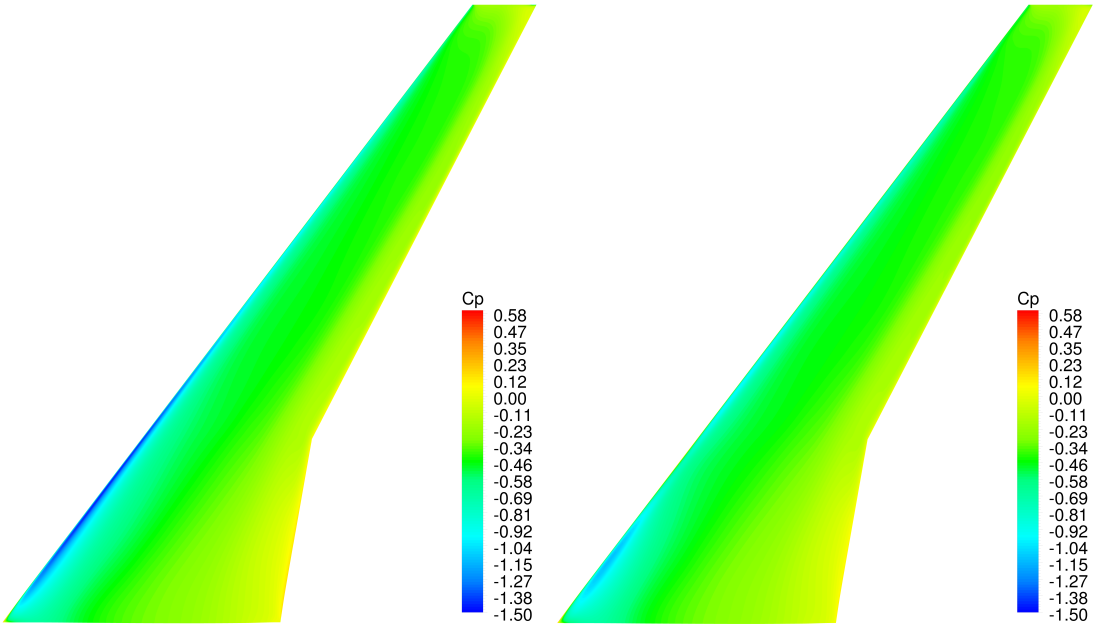

(a) Clean wing configuration

(b) Configuration 12

FIGURE F.3: Contours of C_P on the wing suction surface for the clean wing configuration and the large nacelle installed in Position 3, Configuration 12 in the climb condition (Table 7.4).